COMPUTATIONAL AND MICROHYDRODYNAMIC MODELING AND EXPERIMENTS WITH BIO-INSPIRED SWIMMING ROBOTS IN CYLINDRICAL CHANNELS

by

Ahmet Fatih Tabak

Submitted to the Graduate School of Engineering and Natural Sciences
in partial fulfillment of
the requirements for the degree of
Doctor of Philosophy.

Sabanci University

August 2012

COMPUTATIONAL AND MICROHYDRODYNAMIC MODELING AND EXPERIMENTS WITH BIO-INSPIRED SWIMMING ROBOTS IN CYLINDRICAL CHANNELS

APPROVED BY:

Assoc. Prof. Serhat Yeşilyurt .....
(Dissertation Supervisor)

Assoc. Prof. Ayhan Bozkurt .....

Assoc. Prof. Osman Uğur Sezerman .....

Prof. Dr. Hasan Güneş .....

Asst. Prof. Ahmet Onat .....

DATE OF APPROVAL: 07.08.2012

ÖZET

Yüzebilen mikro robotik sistemler, gelecekteki minimal invaziv cerrahi uygulamalar için alternatif oluşturmaktadır. Mikro boyutlardaki robotların canlı dokular içerisindeki sıvı dolu boşluk ve kanallarda verimli bir şekilde hareket edebilmesi için bakteri hücreleri gibi doğal mikro yüzücüleri taklit etmeleri gerekmektedir. Buna bağlı olarak, bakteri hücrelerinin mikro boyutlarda hidrodinamik modellemelerinin yapılması kontrol ve optimizasyon çalışmaları açısından önem taşımaktadır.

Bu çalışmada, bakterileri taklit eden santimetre boyutundaki robotik prototiplerin düzgün silindirik kanallar içerisindeki yüzme hareketleri incelenmiştir. Söz konusu prototipler taşıdıkları batarya ve kontrol devreleri ile döner sarmal kuyruklarını tahrik ederek kendilerini yüksek viskoziteli sıvılar içerisinde sevk etmektedirler. Deneylerde, yüzme hızı ile değişken kuyruk geometrisi, değişken kanal çapı ve dikey/yatay konumlarda kanal duvarlarına yakınlık ilişkileri incelenmiştir.

Daha sonra, hesaplamalı akışkanlar mekaniği metoduna dayanan benzeşim çalışmaları yapılmıştır. Benzeşim çalışmalarında, dar ve geniş kanallar içerisinde hareket eden bu yüzücü robotlar modellenmiş, ve deney sonuçları ile model doğrulamaları yapılmıştır. Doğrulanmış modeller ile sınırlandırılmamış yüksek viskoziteli sıvılar içerisinde duvar etkilerinden bağımsız olarak yüzen bakteri tipi robotların gövde ve kuyrukları arasındaki hidrodinamik etkileşim incelenmiştir. Ayrıca, değişken kanal çapının ve de kuyruk geometrisinin yüzme hızı üzerindeki etkileri de incelenmiştir.

Son olarak, direnç-kuvveti-teorisi tabanlı, zamana-bağlı altı-serbestlik-dereceli bir mikrohidrodinamik model geliştirilmiştir. Bu modelde, viskoz kuvvetler göz önüne alınarak tüm katı-cisim ve akışkan ivmeleri sıfır kabul edilmiştir. Robotun yüzme hızları sıfır-kuvvetle-yüzme kısıtlaması kullanılarak birinci dereceden bir denklemler sistemi ile hesaplanmaktadır. Mikrohidrodinamik model, dikey/yatay kanal deneyleri ve hesaplamalı akışkanlar mekaniği benzeşim sonuçları ile ayrı ayrı doğrulanmıştır. Doğrulanan mikrohidrodinamik model, örnek model-tabanlı kontrol çalışmalarında ve enerji verimliliği ile yüksek hız için gerekli sarmal kuyruk taslaklarının bulunmasında kullanılmıştır.

ABSTRACT

Modeling and control of swimming untethered micro robots are important for future therapeutic medical applications. Bio-inspired propulsion methods emerge as realistic substitutes for hydrodynamic thrust generation in micro realm. Accurate modeling, power supply, and propulsion-means directly affect the mobility and maneuverability of swimming micro robots with helical or planar wave propagation.

Flow field around a bio-inspired micro swimmer comprised of a spherical body and a rotating helical tail is studied with time-dependent three-dimensional computational fluid dynamics (CFD) model. Analytical hydrodynamic studies on the bodies of well known geometries submerged in viscous flows reported in literature do not address the effect of hydrodynamic interactions between the body and the tail of the robot in unbounded viscous fluids. Hydrodynamic interactions are explained qualitatively and quantitatively with the help of CFD-model.

A cm-scale powered bio-inspired swimmer robot with helical tails is manufactured including a payload and a replaceable rigid helical tail. The payload includes on-board power supply and remote-control circuitry. A number of helical tails with parameterized wave geometry are used. Swimmer performed in cylindrical channels of different diameters while fully submerged in an oil-bath of high viscosity.

A real-time six degrees-of-freedom microhydrodynamic model is developed and implemented to predict the rigid-body motion of the swimming robots with helical and traveling-plane-wave tails. Results of microhydrodynamic models with alternative resistance coefficients are compared against CFD simulations and in-channel swimming experiments with different tails. Validated microhydrodynamic model is further employed to study efficient geometric designs with different wave propagation methods within a predefined design space.

ACKNOWLEDGEMENTS

The author would like to express his gratitude to the people who shared their time, knowledge, equipment, data, help and patience:

His thesis supervisor, Serhat Yesilyurt,
Members of his PhD thesis jury; Ayhan Bozkurt, Ahmet Onat, Osman Uğur Sezerman, Hasan Güneş,
His professors; Kemalettin Erbatur, Asif Şabanoviç, Meriç Özcan, Melih Papila,
Lab technicians and their aids; Mükerrem İlker Sevgen, Bülent Köroğlu, Süleyman Tutkun, Muhammed Halid Taş, Erdinç Konuk,
Graduate students; Halime Didem Çilingir Doğan, Mustafa Koz, Aydek Gökçe Erman, Fatma Zeynep Temel,
Undergraduate students; Hakan Doğan Parıldar, Berna Devrim, Orçun Sabri Orhan, Talat Semih Şolt, Beste Bahçeci, Soner Ulun, Önder Erin,
Also, Bertil Waldén (COMSOL AB) and Robert Bogue (Robert Bogue & Partners, Okehampton, UK),
His close friends Elif Hocaoğlu Çetinsoy, Ertuğrul Çetinsoy,
His parents and his brother, Muharrem Tabak, Ergül Tabak, Halil Can Tabak.

This work was supported in part by

Sabanci University Internal Grant Program (contract number IACF06-00418)

and

TUBITAK (Turkish Scientific and Technological Research Council of Turkey) under the grant number 111M376.

Table of Contents

List of Figures

List of Tables

List of Symbols

{a,b,c,d,e}	Torus-Rod resistive force coefficient fit coefficients
A	Surface area
$A_{\{1,2,3\}}$	Periodic integrals of assumed flow fields used in SBT analysis
A_c	Bessel function coefficients used in in-channel flow field solutions
b	Surface binormal vector
B_{eff}	Effective viscous friction constant
B_m	Rotor friction constant
B_o	Maximum wave amplitude
$\mathbf{B}_{\{body,tail,swimmer\}}$	Fluid resistance matrix for body, tail, and entire swimmer
$B(x,t)$, $B(s,t)$	Wave amplitude function
$c_{\{x,y,z,t,n,b\}}$	Resistive force coefficients
C	Resistive force coefficient matrix
$C_{U,\Omega}$	Translation and rotation correction functions
$d_{\{1,2\}}$	Local proximity in torus-rod study
$d_{\{body,ch,tail\}}$	Proximity of body, concentric channel, tail to the bounding channel
$D_{\{ch,body,cork,c,tail\}}$	Diameter of channel, body, cork, coupling, tail
$D_{\{T,R\}}$	Translational and rotational drag coefficients of the body
$\mathbf{D}_{\{T,R\}}$	Translational and rotational drag matrices of the body
e	Position error
f_{ecc}	Eccentricity function
$f_{\{tail,magnetic\}}$	Frequency of tail and magnetic field rotations
F	Force vector
g	Gravitational pull
H	Magnetic field
$I(t)$	Motor current
$I_{\{coil,lim,no\text{-}load\}}$	Coil, limit, no-load currents
I	Identity matrix
k	Wave number
k_{wall}	Boundary (wall) stiffness

$K_{\{0,1\}}, I_{\{0,1\}}$	Bessel functions of the first kind and second kind
K_b	Back-EMF constant
K_m	Torque constant
$K_{\{p,i\}}$	Proportional and integrator gains
l	Distance of the magnetic swimmer from Helmholtz coils
ℓ	Actual length of the tail
L	Motor inductance
$L_{\{ch,body,cork,c,tail,rod\}}$	Length of channel, body, cork, coupling, tail, rod
m	Mass
$\mathbf{M}$	Magnetization
$n_{\{x,y,z,t,n,b\}}$	Surface normal vector components
$\mathbf{n}$	Surface normal vector
N	Total number of turns on each Helmholtz coil
N_λ	Number of total waves on the swimmer's tail
p	Static pressure
$\mathbf{P}$	Time-dependent local deformation vector of swimmer's tail
$q_{\{s0,v1,v2,v3\}}$	Scalar and vector components of quaternion structure
$\mathbf{q}$	Quaternion vector structure
r	Radial position
$r_{\{tail,body\}}$	Radius of tail and spherical body
$\mathcal{R}$	Rotation matrix between swimmer frame and lab frame
$R(t)$	Electrical resistance
$R_{\{torus,coil,ch,\{body,b\}\}}$	Radius of torus, Helmholtz coil, cylindrical channel, swimmer's body
S	Stokeslet function
$\mathbf{S}_{\{body,tail\}}$	Skew-symmetric matrix for cross product on body and tail
$S_{\{swimmer,torus,rod\}}$	Entire surface of the swimming robot, the torus and the rod.
$S_{\{1,2\}}$	Surfaces under effect of mutual lubrication
$\hat{S}(t)$	Swimmer trajectory
t	Time
$\mathbf{t}$	Surface tangent vector

$\mathbf{T}$	Torque vector
$T_h(t)$	Hydrodynamic load on DC-motor
$U_{\{x,y,z,s,q,r,t,n,b\}}$	Flow velocity vector components
$\mathbf{u}$	Mesh velocity vector
$\mathbf{U}$	Flow velocity vector
V	Volume
V_{pp}	Peak-to-peak voltage
$V(t)$	Battery voltage
$V_{\{x,y,z,s,q,r,t,n,b\}}$	Translational rigid-body velocity vector components in lab frame, swimmer frame, local Frenet-Serret frames
$\mathbf{V}$	Swimmer or particle velocity vector
$W_{\{x,0\}}$	Upstream in **x**-direction, DC-component of the upstream
x	**x**-position & direction
$\mathbf{x}_{\{body,tail\}}$	Position vector on swimmer's body and tail (in its frame)
$\mathbf{X}_{com}$	Position of the center of mass
α	Ratio of apparent length to actual length of the tail
β	Safety factor
γ	Angle of misalignment between magnetic fields
δ	Penetration depth (in case of surface contact)
ε, a	Upper/Lower limit to periodic integrals $A_{\{1,2\}}$ and A_3
ζ	Attack angle of helical tail
η	Hydrodynamic efficiency of the micro swimmer
θ	Tangential position in channel or around the tail
λ	Wave length of propagating helical or planar waves
μ	Kinematic viscosity
μ	Magnetic permeability of a permanent magnet body
Π	Hydrodynamic power
ρ	Liquid density
$\boldsymbol{\sigma}$	Total hydrodynamic stress tensor
$\boldsymbol{\tau}$	Shear stress tensor

$\Upsilon_{\{T,R\},\{x,y,z\}}$	Amplitude of hydrodynamic interactions for translation and rotation
ϕ	Phase of hydrodynamic interactions (complex-impedance analogy)
φ_n	Phase of piezo-stack deformations
χ	Dimensionless hydrodynamic torque in SBT method
Ψ , ψ	Velocity reduction functions in SBT method
Ψ , Ω , Π	Harmonic functions used in asymptotic in-channel solutions
$\omega_{\{\text{piezo,tail,m,upstream}\}}$	Actuation frequency (angular) of piezo-stack, swimmer's tail, DC-motor, channel upstream
ω_x	**x**-vorticity induced by the rotating helical tail
$\Omega(t)$	Fluidic (viscous) domain
Ω_x, Ω_s	Body rotation rate of the swimmer with rotating helical tail
$\mathbf{\Omega}$	Rigid-body rotation vector
$\mathbf{\Omega}_{\{body,tail\}}$	Rotation rate vectors of swimmer's body and tail

List of Abbreviations

2D	Two-dimensional
3D	Three-dimensional
AC	Alternative current
ALE	Arbitrary Lagrangian-Eulerian
BEM	Boundary element method
CCD	Charge-coupled device
CFD	Computational fluid dynamics
com	Center of mass of the swimming robot
DAC	Digital-to-analog converter
DAQ	Data acquisition
DC	Direct current
DNA	Deoxyribonucleic acid
DRIE	Deep reactive ion etching
DOS	Disk operating system
EHD	Elasto-hydrodynamics
EMF	Electromotive force
HI	Hydrodynamic interaction
HV	High voltage
IB	Immersed boundary
IC	Integrated circuit
IPMC	Ionic polymer-metal composite
IR	Infra-Red
JFET	Junction field effect transistor
LIGA	Lithographie, Galvanoformung, Abformung
Li-ion	Lithium-ion
Li-Po	Lithium-Polymer
LV	Low voltage
MD	Molecular dynamics
MEMS	Microelectromechanical systems

Mn	Magnetoelastic number
MRI	Magnetic resonance imaging
ODE	Ordinary differential equation
PARDISO	Parallel sparse direct solver
PC	Personal computer
PDMS	Polydimethylsiloxane
PECE	Predict, evaluate, correct, evaluate
PID	Proportional, integral, derivative
PVDF	Polyvinylidene diflouride
PWM	Pulse-width modulation
PZT	Lead Zirconate Titanate
RAM	Random access memory
Re	Reynolds number
RFC	Resistive force coefficient
RFID	Radio-frequency identification
RFT	Resistive-force-theory
RLC	Resistance, inductance, capacitance
RMS	Root mean square
PIV	Particle image velocimetry
RRH	Rotating rigid helix
SBT	Slender-body-theory
SEM	Scanning electron microscopy
SMA	Shape-memory-alloy
Sp	Sperm number
Sr	Strouhal number
sqr	Swimmer frame
TEM	Transmission electron microscopy
tnb	Local Frennet-Serret frame (on swimmer's tail)
TPW	Traveling plane wave
USB	Universal serial bus
xrθ, xyz	Cylindrical and Cartesian representations of the lab frame

1. INTRODUCTION

1.1. Objectives of the Thesis

The demand for minimal invasive surgery and the achievements in micro and nano-technology lead to the possibility of artificial micro robotic devices performing real-time in *vivo* therapeutic operations. The subject matter in this text is focused on bio-inspired untethered robots, which mimic the bacterial propulsion methods, swimming in channels. Furthermore, the study is expanded to include the hydrodynamic interactions between body and tail of bacteria-like swimmers.

The main objectives of this thesis are given as: to develop a hydrodynamic model for design-optimization and control, to validate the proposed hydrodynamic model with CFD-models and physical experiments, and to understand the hydrodynamic interactions within the swimming micro robot's body and tail.

Extensive CFD simulations and in-channel swimming experiments are carried out for different geometric designs and configurations. Experiments are carried out in order to study the physical scenarios, which would raise numerical complications for CFD-based analysis. Similarly, CFD simulations are carried out for physical scenarios, which are required more demanding experiments. Although the CFD-model is validated with a set of special experiments, the gap between the two is resolved with the help of a proposed reduced-order hydrodynamic model, which is based on resistive-force-theory and validated in rigid-body kinematics with experiments and CFD-models.

Furthermore, the proposed model is tested for accurate force and torque calculations in time-dependent fashion, which led to a considerable modification in resistance matrix of the swimmer robot's body.

Finally, given the speed and fidelity of the proposed hydrodynamic model, the possible future uses, such as numerical inspection for efficient geometric designs or model-based position control, are presented.

1.2. Background

The swimming artificial micro-robot concept was introduced and elaborated on by Richard F. Feynman in his celebrated lectures, i.e. "There's plenty of room at the bottom" (1959) and "Infinitesimal machinery" (1983), as a distant goal to achieve provided that several technical problems about manufacturing and precision issues are dealt with. The "swallowable surgeon" concept introduced by Feynman within the lecture in 1959. Hollywood, later on, against all scaling laws (Hsu, 2002), made an effort to present the idea for the sake of a hit at the box office by "*Fantastic Voyage*" in 1966, and another, "*Innerspace*", in 1987. Both movies were about small scale submarines with human crew inside reduced in size such that they can actually roam inside the human tissue, i.e. blood vessels and digestive system.

Progress in micro fabrication techniques and ever-increasing prospects in micro realm, lead to promising bio-inspired, micro-fluidic and micro-robotic medical applications for therapeutic purposes, (Wise, 2007). Potential advantages of micro swimming robots can revolutionize the modern medicine. Swimming micro robots are presented in literature as the candidates of minimal-invasive surgery tools to handle therapeutic operations such as kidney stone destruction or retina repair (Bogue, 2008; Martel *et al.*, 2009; Nelson *et al.*, 2010; Fountain *et al.*, 2010). It is well-established by the scallop theorem that the conventional propulsion mechanisms such as propellers are ineffective in micro realm, where the Reynolds number (Re), i.e. the ratio of inertial forces to shear forces (Batchelor, 2005), of the surrounding flow field is generally much smaller than unity rendering macro-scale propulsive methods inefficient (Purcell, 1977). Purcell articulated the inevitable requirement of "time irreversible actuation" by explaining how a motion tracing its own steps would result in almost no net displacement in micro realm, also known as "Scallop

Theorem" (Purcell, 1977). This theorem explains that being virtually independent of time; a net motion in one direction cannot be sustained by repeating a certain action because eventually the cycle would cancel out itself. Addressing to this issue, propulsion mechanisms of bacteria and spermatozoa depend on wave propagating slender tail structures (Brennen and Winet, 1977).

Inducing the desired waving action that mimics nature and controlling its behavior while interacting with the environment in micro realm would constitute a reliable propulsion system to propel a therapeutic robot introduced into the human body either via "incisions" or "natural pathways" (Fatikow, 1997). Based on observations on bacteria and spermatozoa, and through some macro and micro-scale experiments, propulsion mechanisms of natural micro swimmers are established as viable candidates for propulsion of autonomous micro swimming robots (Honda *et al*., 1996; Edd, 2003; Behkam and Sitti, 2004; Dreyfus *et al*., 2005; Behkam and Sitti, 2006a; Yu *et al*., 2006a; Yu *et al*., 2006b; Kosa *et al*., 2007; Zhang *et al*., 2009; Chen *et al*., 2010, Tabak *et al*., 2011).

The subject matter in the following section is a very brief yet comprehensive list of diverse examples in the literature from fifties to the current year. It has been chosen to eliminate most of the massive pile of work published over the years to stress some of the important results based on observation, bio-mathematical modeling, physical experimentation and finite element analysis. Each example is presented with its technique and results with emphasis on its importance to this study. More detailed reviews are presented by Young (2006) and Lauga and Powers (2009).

1.2.1. Observations on Natural Micro Swimmers

Observations on natural swimmers are carried out by fast CCD cameras and TEM analysis, mostly with dark-field method. Several specimens of spermatozoa and bacteria species are used to understand how natural micro swimmers are propelling themselves in viscous domains. The mathematical models cast to approximate the flow resistance on deforming slender surfaces are based on these visual inspections in part.

1.2.1.1. Examples of natural micro swimmers presented in literature

In 1955, Gray and Hancock introduced the resistive force coefficients for a micro swimmer's tail structure, which are based on the approximate solutions of the Stokeslet functions, and the local rotation matrix on the tail surface due to wave propagation effect. They studied the swimming behavior of "Sea-Urchin Spermatozoa" comparing it with the experimental data collated earlier on. They have compared the observational data of spermatozoa of *P. miliaris* with theoretical calculations and verified their results (Gray and Hancock, 1955).

In 1964, Brokaw, based on observations with photomicrographs, pointed out that the planar waves, which are carried out by the flagella of a sperm cell, do not consist of pure sine waves. In 1966, Brokaw presented a set of very detailed observation notes on Sea-Urchin spermatozoa motility, including numerical values of viscosity, wave length, waving frequency and propulsion velocity. This study showed that observed natural swimmers tend to decrease wave amplitude and frequency to swim more steadily (Brokaw, 1966).

In 1977, Brennen and Winet presented their work on the actual physical structures of flagellar and ciliar motors, i.e. how they are attached to the cell body and how they are actuated including a discussion on "slender-body-theory" and numerical examples obtained by observations. They presented a detailed data on morphology and propulsion means of a list of natural swimmers based on 2D observation. They also carried out a discussion on how different Stokeslet functions can be formed for varying flow field conditions (Brennen and Winet, 1977).

In 1980 and 1981, Gibbons and Gibbons studied the "wave patterns" of sea urchin spermatozoa by optical means and tabulated the "beating" forms of the flagellum under different propulsive conditions. Authors discussed how the beating form of the flagellum change when in transition, i.e. unsteady swimming effects, which will help us to find optimum non-sinusoidal beating form for different behaviors (Gibbons and Gibbons, 1980; 1981).

In 1995, Frymier *et al.* employed a "tracking microscope" to collect propulsive information and compared the results with numerical investigations concluding that hydrodynamic theories capture the change in forward propulsion behavior in case of presence of a solid boundary but not adequate to explain swimming constantly near a solid wall (Frymier *et al*., 1995). Frymier and Ford (1997) studied the effect of solid boundaries on the swimming of bacteria. Authors concluded that trajectory of a bacteria is three-dimensional without presence of a solid boundary; however, trajectory is confined to a two-dimensional path (Frymier and Ford, 1997).

In 1996, Crenshaw published his work on "3D tracking of a micro swimmer", which is important because earlier observation results are generally limited to 2D behavior as discussed by Brennen and Winet (1977), with a discussion explaining that the trajectory of most natural micro swimmers including some spermatozoa is helical instead of a two dimensional curve in space (Crenshaw, 1996).

In 1999, Armitage *et al.* presented pure observation results on maximum and average swimming speeds of R. *sphaeroids* and E. *coli* via differential interference contrast microscopy technique.

In 2000, Mahadevan and Matsudaira listed and discussed micro bacterial actuation mechanisms comparing them to macro world engines and the list included "Brownian" effect (in other words the effect of thermal noise, i.e. motion of molecules, due to the temperature of the environment), actin-myosin type fibers and "flagellar motor" giving specific power values. One of the most interesting details presented was that the specific power, i.e. in [erg s^{-1} g^{-1}], of a "flagellar motor" is found to be same order of magnitude with "typical passenger car engine" (Mahadevan and Matsudaria, 2000).

In 2001, Wooley and Vernon showed via dark field microscopy that spermatozoa of *Echinus esculentus*, a sea-urchin species, can alter the form of wave propagation from helical wave to planar wave as viscosity increases. This observation implies that some natural swimmers are equipped and able to use both wave propagation techniques up on need (Wooley and Vernon, 2001).

In 2007, Gadelha *et al.* carried out a pure observation study and focused on the planar wave propagation of three different natural swimmer specimens, i.e. *C. deanei*, *C.*

fasciculate and *L. major*, and tabulated the geometry and propulsive behavior of specimens of those species with the help of recorded images.

In 2008, Corkidi *et al.* observed the swimming behavior of spermatozoa both "confined to swim in 2D" and reconstruct their swimming path in 3D concluding that free swimmers have a higher velocity than confined ones with helical trajectory instead of 2D trajectory although they utilize planar wave propagation as propulsion method.

1.2.1.2. Actuation mechanisms of micro swimmers

Planar wave propagation of micro swimmer's tail is induced by sliding actin-myosin type fibers and tubules embedded in the tail structure. Deformations are created from base to tip and fade towards the end due to viscous dissipations. The lateral deformation on the tail actually forces the fluid slide over the surface while the viscous resistance is, in part, propelling the swimmer forward (Gray and Hancock, 1953; Brennen and Winet, 1977, Lighthill, 1975). Discussions on theoretical energy consumption calculations can be found in (Sleigh, 1962). A bull sperm uses $2.11 \cdot 10^{-7}$ erg/sec in movement at 37℃. or a sea urchin requires 1,816 erg/sec at 17℃. Both figures are calculated just to overcome the shear resistances on the tails. A further discussion on ciliar beating strategies, and power consumption for planar wave propagating natural swimmers can be found in (Sleigh, 1962). Details of inner structure of whip-like tails and natural swimmers utilizing them can be found in (Fawcet, 1970; Gibbons, 1981).

One important actuation system used by natural swimmers, particularly with bacteria species, is the bacterial motor. A bacterial motor uses Brownian motion, i.e. movements of molecules due to temperature, to induce the tail rotation. In fact, bacterial motor is a ratchet system only releasing itself with certain thermodynamic condition arises. The rotation rate and direction are controlled within the cell membrane; however, Brownian noise is the main energy source for bacterial motor (Berg, 2003). More detailed study on bacterial "rotary" motor can be found in (Childress, 1981; Ravid and Eisenbach, 1984; Washizu *et al*., 1993; Berry and Berg, 1996; Taylor and Zhulin, 1998; Berg, 2000; Lobaskin *et al*., 2008; Brown *et al*., 2011).

In 1905 Albert Einstein published his first work on Brownian motion and four other papers followed by him. Brownian motion in general is the direct result of the kinetic energy of fluid molecules. As fluid molecules affect each other via collusions they also interact with solid boundaries they come in contact with. These collusions alter the position of any microscopic particle (Einstein, 1956). Brownian effect not only forces the suspended particles to translate but also rotate in time (Berg, 1993). But the apparent viscosity of fluids in micro realm prevents sudden and long distance jumps (Einstein, 1959). Hence resultant motion can be described as small and random fluctuations in an arbitrary direction. The colliding particles can even be studied as "ballistic" in some cases (Duplanter, 2006). There are several numerical and observational studies on Brownian effect such as (Bonilla, 2007; Howse, 2007).

1.2.2. Analytical Models of Micro Swimming

Literature provides resistive force coefficients based on solely local translations of whip-like or helical tails (Gray and Hancock, 1955; Lighthill, 1976; Johnson and Brokaw, 1979) or incorporating the local proximity of bending filaments to solid boundaries (Brennen and Winet, 1977; Lauga *et al.*, 2006) as well, and drag coefficients of isolated bodies with known geometries, such as spheroids, in viscous flows (Perrin, 1934; Perrin 1936; Happel and Brenner, 1965; Berg, 1993; White, 2006). This section lists the important cornerstones of analytical models of natural swimmers presented in literature, i.e. beads with well-known geometries and tails carrying out wave propagation, either isolated in unbounded media or in interaction with another boundary in the vicinity.

1.2.2.1. Modeling local flow fields and induced local resistances

In 1951, Sir Taylor presented his work on the effects of wave propagating boundaries in contact with highly viscous fluids in micro realm. First part of his study was explicitly focused on an anchored infinite sheet carrying out planar sinusoidal wave propagation with

small amplitudes. He elaborated on the resulting flow field with a detailed analysis of relationship between waving geometry with outcome of hydrodynamic effects such as resultant fluid velocity, required energy to sustain the wave propagation. Next, he extended the analysis to large amplitude wave propagation and finally studied the propulsion forces for an unanchored sheet in contact with fluid on both surfaces. He concluded that change in propulsion velocity is linearly dependent to product of square of amplitude change and propagation frequency (Taylor, 1951).

In 1953, Hancock presented his work on the flow field around the plane wave propagating tail of a spermatozoon using local Stokeslet functions on the tail to capture the surrounding flow field and its effect on micro swimmer's overall performance. Replacing Stokeslet functions on tail instead of sole surface velocities due to local structural deformation allows modeling the fluid behavior around the moving boundary instead of assuming no flow field. This study showed that when Stokeslet functions are used the effect of wave tips pushing the surrounding fluid can be captured. Furthermore, based on approximate solutions, he formulated the resistive-force-theory (RFT) for particles undergoing quasi-static rigid-body motions in viscous flows (Hancock, 1953).

Sir J. Lighthill (1976) applied the slender-body-theory for a swimmer, composed of a single helical tail without body, using a Stokeslet velocity field and the corresponding distribution of the point forces on the tail; approximate analytical relationships for tangential and normal resistive force coefficients for an infinite-length filament are obtained in the analysis along with a sub-optimal set to calculate local viscous resistance (Lighthill, 1975; 1976). However, Lighthill pointed out that RFT ignores the long range interactions between the body and the flagellum, and between the parts of the flagellum; inclusion of the long-range interactions results in the slender-body-theory (SBT) (Lighthill, 1975).

Higdon (1978; 1979) used a numerical integration method for the integrals approximated by Lighthill in his work (Lighthill, 1976) to calculate the velocity of a swimmer with a spherical head and a helical tail, and reported the variation of the swimming velocity with the tail length, wavelength and amplitude given in dimensionless forms with respect to the diameter of the body.

In 1979, Johnson and Brokaw published their work on comparing the resistive force theory, which assumes a stationary fluid, and slender body theory, which assumes a surrounding flow field, concluding that slender body theory, hence the slender body coefficients, are more advantageous when the swimmer body is too large in dimensions comparing with the tail structure. Resistive force theory and slender body theory are simply used to predict the force on a dynamic surface immersed inside a viscous fluid in micro realm. Authors concluded that slender-body-theory is advantageous in calculating swimmers with large bodies due to the fact that resistive-force-theory approach does not account for body-tail interactions; however, computational requirements of slender body theory are considerably higher than the resistive-force-theory analysis (Johnson and Brokaw, 1979).

Johnson (1980) discussed that a nonzero lateral force is calculated by extended slender-body-theory studies based on singularity solutions on finite-length helical filaments, whereas resistive-force-theory is based on force-balance along the long axis of infinite filaments thus lacking the precision to predict lateral forces due to geometric impurities of the tail and hydrodynamic interactions between swimmer's body and tail (Johnson, 1980).

In 1996, Koehl discussed that the drag coefficient and its conditional dependence on surface morphology and the pressure distribution of a swimmer in general concluding that for different Re number regimes, e.g. especially for Re>1 where inertial forces become dominant (Batchelor, 2005), drag coefficient turns out to be related to purely form drag due to pressure distribution on the moving body (Koehl, 1996).

Sir Lighthill (1996a) presented the three dimensional flow field solution based on the Stokeslet distribution along an infinite helix. Lighthill concluded that the torque exerted on the fluid leads to vortex formation located close to the tail and perpendicular to its long axis. Moreover he demonstrated that the induced field should change its direction of flow on the plane perpendicular to the long axis near the center of the helical tail. Furthermore, he argued that the induced force field, which is signified by Stokeslets, manifests localized flow fields in the direction of wave propagation. However, Lighthill's analysis focused on an infinite length tail without a body being towed (Lighthill, 1996a).

Manghi *et al.* (2006) presented their work on a rotating elastic nano-length filaments and resultant propulsive effect solving for coupled thermal, hydrodynamic, and structural effects with Rotne-Prager Green functions.

Camassa *et al.* (2008) studied the flow field induced by rigid-body rotations of a particle. Authors studied the flow field created around a moving prolate spheroid in viscous flows, and discussed that the stokes flow assumption around a slender body undergoing rigid-body translations and rotations are valid for $Sr \cdot Re << 1$ for the surrounding flow fields and $Re << 1$ for the viscosity on the moving object, where Sr (Strouhal number) is the dimensionless frequency of the flow. Authors suggested that for rigid-body rotations satisfying $Sr \cdot Re \sim 1$, unsteady effects must be studied (Camassa *et al.*, 2008). The $Sr \cdot Re$ term, i.e. the product of Strouhal number with Reynolds number, signifies the inertial effects in oscillatory flows in viscous fluids (Laser and Santiago, 2004).

1.2.2.2. Modeling interactions with environment

Hydrodynamic interaction between a spherical body and the walls of the channel it is confined with are studied extensively in literature. Happel and Brenner (1965) argued that when two spheres undergo rigid-body-translations in tandem, the leading sphere would have to overcome higher fluid drag, thus leading to slower translational velocities. However, Nasseri and Phan-Thien (1997) studied the hydrodynamic interaction between two micro swimmers with helical tails swimming in tandem concluding that the swimmer in front attains higher velocities. Alexander and Yeomans (2010) studied the hydrodynamic interaction between two swimmers in close proximity. Authors concluded that the instantaneous position and orientation of swimmers with respect to each other is important to solve the Stokes-based representation of the problem (Alexander and Yeomans, 2010).

Blake (1974) discussed that the ratio between resistive force coefficients are subjected to the proximity to the solid boundary. Similar to Blake's arguments, the resistive force coefficients articulated by Brennen and Winet (1977) calculate the local fluid resistance on the swimmer's tail based on wave geometry and local proximity to the solid boundaries.

Keller and Rubinow (1976) presented a total six degree-of-freedom analytical model of the swimmer and pointed out that the local fluid resistance on a moving and deforming object of arbitrary shape is effected by the entire induced flow field.

De la Torre and Bloomfield (1977) modeled the helical flagellum of a micro swimmer with spherical body and studied the local effects of body-tail interactions on the rotating tail by hydrodynamic-interaction tensors. The helical tail is assumed to be composed of a series of spherical particles of the same radius that of the tail. Authors concluded that the local hydrodynamic forces acting on the tail differ dramatically near the joint between body and tail due to the interaction of the two.

Higdon and Muldowney (1995) studied the effect of proximity to channel walls on fluid resistance exerted on moving micron-sized spherical particles by means of computational fluid dynamics (CFD) simulations and lubrication solutions. Authors validated the numerical results with analytical solutions of lubrication analysis for a spherical body moving towards and parallel to a solid boundary in separate occasions. The analytical formulae show that the lubrication effect in rigid-body translations, which are parallel to the boundary, increases with the logarithm of the reciprocal of the proximity (Higdon and Muldowney, 1995).

Takano and Goto (2003) introduced a similar resistance coefficient matrix to (Spagnolie and Lauga, 2010) along with internal structural stresses to get fluid forces and studied the effect of helical wave deformation on swimming behavior combined with the forces due to structural deformation of the tail.

Lauga *et al.* (2006) used modified resistive force coefficients, similar to but simplified versions of the ones given by Brennen and Winet (1977), and modified the model presented by Keller and Rubinow (1976) to include the interactions between swimmer's body and nearby solid boundaries, in order to obtain the trajectory of micro swimmers near solid walls with appropriate approximations from the analytical solution of the hydrodynamic model.

Watari and Larson (2010) discussed that the instantaneous flow field induced around a natural swimmer is time dependent and the time average of the flow field is smaller than instantaneous magnitudes, thus capable of perturbing nearby suspended particles. Authors also added that the swimmer's body is also influenced by these flow fields.

Above conclusions of Keller and Rubinow (1976), De la Torre and Bloomfield (1977) and Watari and Larson (2010) point out that the stationary fluid assumption is not accurate and the body of a micro swimmer is under the influence of additional hydrodynamic effects on top of the fluid resistance acting due to the rigid-body motions.

Felderhof (2010) studied the swimming velocity of a body with wave-propagating surfaces in narrow channels based on the flow-field solutions for the Stokes flow based boundary-value problem of a moving body inside channels given by Happel and Brenner (1965). Author used asymptotical time-averaged solutions of harmonic functions representing the flow field induced inside infinite length cylindrical channels. However, the entire swimmer body is modeled as rotating helix and no extra payload attached.

Van der Sman (2010; 2012) studied the interaction between spheres moving along the symmetry axis of a micro channel of cross sections with known geometries. Author demonstrated that it is viable to decompose the net fluid drag exerted on spheres into pure shear force and pure pressure force (Van der Sman, 2010; 2012).

Shum *et al*. (2010) studied the force and torque efficiency of micro swimmers near solid boundaries with parameterized body and tail geometries via boundary-element-method. Author concluded that there exists an optimum geometry for efficient use of hydrodynamic power while swimming near solid boundaries which leads to similar velocity results to unbounded swimming conditions (Shum *et al*., 2010).

In 2011, Cipparrone *et al*. reported that, although it is not anticipated in microflows, the Magnus effect, i.e. induced pressure difference due to rigid-body rotation (Munson *et al*., 2002), is an important phenomenon for rotating particles without the influence of an external flow field. Authors observed the lift on the rotating particles while manipulated by optical tweezers (Cipparrone *et al*., 2011).

Spagnolie and Lauga (2012) pointed out that the gravitational pull results in rigid-body rotations or translations on natural swimmers given the fact that some are not neutrally buoyant. Furthermore, it is known that some bacteria species control the buoyancy in order to swim against gravity in order to reach a certain group of molecules or light (Li and Cannon, 1998).

1.2.3. Numerical Models of Micro Swimmers

This section deals with comparative studies on natural swimmers and the models implemented to predict their rigid-body swimming behaviors, either isolated in unbounded media or in interaction with another boundary in the vicinity.

1.2.3.1. Analytical models compared with observations

In 1996, Jordan introduced a coupled internal-external dynamics to the waving flagella structure and studied structural deformation and propulsion behavior affecting each other simultaneously. His model showed that swimming action can be modeled as a result of structural deformations and he concluded that with correct structural modeling the swimming behavior of natural swimmers can be predicted (Jordan, 1996).

In 1998, Wiggins and Goldstein coupled the fluid flow originated stresses on the deforming tail and the deflection of the tail structure using fluid stress coefficients and beam loading equations resulting in "elastohydrodynamic problems" as they called and they provided numerical solutions to these problems. Elastohydrodynamic problems assume that one end of the tail structure is inducing either oscillating or impulsive whip like motion and unless the rest of the tail is flexible the initial motion created at one end cannot result in net propulsion (Wiggins and Goldstein, 1998).

In 2003, Lagomarsino *et a*l. studied the effect of internal stress of the tail structure via a dimensionless number called Sp, i.e. ratio of fluid stresses on surface to internal structural stresses known as Sperm Number, superposing the fluid and structure problem and found that optimum propulsion effect corresponds to a bounded value of Sp via numerical methods. They have found that for Sp = 0 the motion is "reciprocal", for small amplitude beats, velocity of propulsion converges to an asymptotic value after a certain value of Sp and for large amplitude beats there exist a maximum propulsion velocity (Lagomarsino *et al*., 2003).

In 2009, Hsu and Dillon carried out 3D numerical investigations on a helical tail attached to a cylindrical body and presented the numerical algorithm and resulting velocity, force, torque with detailed analysis of flow field around the proposed swimmer geometry with a very high quality mesh and unusually small time step, i.e. on the order of (-7). Authors used a Stokeslet function for the velocity on swimmer surface and modified Stokes flow equation with local forces written in triadic coordinates added on the right hand side. Trajectory of the swimmer is found to be helical, swimming velocity is verified with observations although the computed torque is found to be higher than expected based on observations (Hsu and Dillon, 2009).

In 2009, Chattopadhyay and Wu studied the effect of flow field in long distances and concluded that both resistive force theory and slender-body-theory cannot capture the total hydrodynamic effects of the "far-field" on the swimmer presenting the differences between observational swimming forces obtained by optical tweezers. Authors calculated the hydrodynamic forces acting on the swimmer by slender-body-theory and resistive-force-theory and concluded that the former provides more accurate results. Furthermore, authors observed that body and tail of bacteria species rotate on opposite directions (Chattopadhyay and Wu, 2009) as a result of conservation of angular momentum.

Spagnolie and Lauga (2010) introduced an elasto-hydrodynamic (EHD) model of the force balance between the internal stress distribution of the solid tail and the resistive force of the surrounding viscous domain. Authors discussed the effect of body tail interactions; however, did not include this effect in their study. They carried out an overall energy efficiency study based on wave shape and concluded that the total efficiency drops rapidly for small wave numbers and large wave amplitudes.

1.2.3.2. Computational models based FEM, BEM, IB and MD approaches

Phan-Thien *et al*. (1987), using boundary-element-method (BEM) studied the effects of the geometry of helical tail and the geometry of a spheroid body on the forward velocity and hydrodynamic efficiency of the micro swimmers. Authors discussed that the interaction between rotating helical tail and the body of the swimmer decreases forward swimming

velocity and overall hydrodynamic efficiency of the swimmer. Ramia *et al*. (1993) used boundary-element-method (BEM) to obtain the motion of spheres with single rotating helical tails swimming in unbounded fluids, near plane boundaries, and between parallel plane boundaries separately. Authors studied the effect of hydrodynamic interaction on the overall propulsive and resistive behavior of the helical tail separately in detail. In both papers (Phan-Thien *et al*., 1987; Ramia *et al*., 1993), the main focus was on the forces acting on the helical tail and rigid-body swimming velocities with hydrodynamic efficiency values; results imply that the overall forward resistance of the swimmer increases with hydrodynamic interactions. Moreover, the reader may find useful information on BEM approach in (Costabel, 1986).

Fauci and McDonald, in 1995, published their numerical studies on micro swimmers, especially confined into channels, employing planar wave propagation to get thrust. Authors discussed the effect of walls by demonstrating the results changing the channel wall properties from rigid to elastic and no walls. They concluded that propulsion velocity of confined swimmers is much smaller than of free ones due to hydrodynamic interaction in between boundaries (Fauci and McDonald, 1995). Fauci, later on, built a finite element framework to conduct numerical experiments on single and multiple planar wave propagating swimmers equipped with different tail morphologies moving inside a confined liquid medium governed by full Navier-Stokes equations (Fauci, 1996).

In 1997, Nasseri and Phan-Thien proposed twisted-rigid-strip geometry for the tail and studied the optimal twist number, i.e. total number of waves and resulting surface angle, along with optimal body dimensions for such a swimmer. They concluded that for such a tail structure there exist an optimal twist number, i.e. 1.5, to get maximum propulsion velocity (Nasseri and Phan-Thien, 1997).

Goto *et al.* (2001) employed the boundary element method for the solution of Stokes equations, calculated the velocity vector of a natural micro swimmer, compared their results with observations of actual swimmers, *Vibrio Alginolyticus*, and concluded that the BEM solutions agree reasonably well with observations. However, authors could not observe tail and body rotations together accurately, thus used rotation rates of the *Vibrio Alginolyticus* specimens to predict the rotation rates of their tails (Goto *et al*., 2001).

In 2007, Rapaport employed molecular dynamics (MD) method, i.e. modeling the interactions in between fluid molecules and between solid boundaries and fluid molecules via elastic collusions, in 2D to simulate the swimming behavior of different tail combinations and presented the power and velocity results. It has been pointed out that to simplify the solution the swimmer is forced to move on a straight line which also eliminates the Brownian effect, i.e. thermal noise (Rapaport, 2007).

Tabak and Yesilyurt (2007a; 2010a; 2010b) used CFD-models based on finite-element-method (FEM) representation of the resultant fluid motion with deforming mesh, and calculated the three degree-of-freedom, i.e. forward, lateral and angular velocities of swimmers propelled by travelling-plane-wave deformation confined to a symmetry plane (Tabak and Yesilyurt, 2007a) and two degree-of-freedom motility, i.e. forward velocity and body rotation rate of swimmers propelled by helical motion of their flagella (Tabak and Yesilyurt, 2010a; 2010b). In latter study a resistive-force-theory based model is implemented to predict CFD-computed forward velocity and corresponding fluid-drag.

Qin *et al*. (2012) studied the wall effects on a swimmer based on spermatozoa undergoing translations on a plane while fully submerged in a high viscous fluid. Authors used immersed boundary (IB) method incorporating Navier-Stokes equations and deforming mesh (also see Peskin (2002)) with Newton's second law to include swimmer's rigid-body accelerations in 2D, and computed the effective hydrodynamic interaction between swimmer and parallel rigid plane walls based on the ratio of their half distance to wave length (Qin *et al*., 2012).

A similar study is carried out by Maniyeri *et al*. (2012) on the flow field induced by rotating helical tails in channels. Authors did not include a body to the analysis; however, presented the resultant flow field and swimming velocity in 3D with respect to the proximity to channel center and walls. However, authors did not report a backflow induced by the rotation of the helical tail (Maniyeri *et al*., 2012).

1.2.4. Experiments with Artificial Swimmers

Experimental studies of micro swimmers or prototypes resembling them are mainly focused on mimicking planar and helical wave propagation. Some swimmers are known to be able to use both methods based on environmental conditions (Wooley and Vernon, 2001); however, experimental work are focused on a specific method at a time due to inflexible designs used to imitate them. In some cases, experimental studies are limited with size related issues. For example, the technology to mimic a bacterial motor in nano-scales is not implemented up to date; in return, any bio-inspired robot with body and tail rotating in opposite directions are much bigger than the species it is mimicking as presented by Tabak and Yesilyurt (2012a; 2012b) in macro-scale experiments.

1.2.4.1. Micro-scale experiments

In 2005, Dreyfus *et al.* presented the very first artificial micro swimmer, which was employing travelling plane wave propagation, in the literature. The tail attached to a red blood cell was composed of magnetic materials attached to each other by genetic proteins and actuated by a combination of external dynamic magnetic fields and the resultant planar-wave propagation behavior was recorded by a camera. Planar wave propagation was carried out successfully and although the deformation was not exactly sinusoidal, they were able to present propulsion speed with respect to Sperm number and Magnetoelastic number, i.e. ratio of magnetic forces to internal structural forces known as Mn number, and stresses out that there is an optimum Sp number for different Mn numbers where swimming velocity is at its peak. The manufacturing technique used in this study is also a novel method since it employs organic material (Dreyfus *et al.*, 2005). Gauger and Stark (2006) modeled the swimmer manufactured by Dreyfus *et al.* (2005) and carried out an efficiency study based on Sp number and the cell size concluding that there exists an optimum geometry with Sp around 8.

In 2007, Hill *et al.* studied the combined effect of swimming near a solid boundary and against upstream and tested the conditions by exerting upstream velocity on E. *coli*. Authors have concluded that if the upstream velocity is faster than bacterial swimming speed and if the natural swimmer is moving near a solid boundary the resultant swimming behavior is unstable (Hill *et al*., 2007).

Ghosh and Fischer (2009) demonstrated the use of glancing angle deposition on silicon wafer in an electron beam evaporator to obtain about a micron long helical screw like structures with diameters of a few hundreds of nanometers. Helical structures are removed from the wafer, laid onto a surface and deposited by magnetic cobalt on one side. Authors manufactured chiral colloidal propellers having 200-300 nm width and 1-2 μm length made of silicon dioxide and a thin layer of ferromagnetic material (cobalt) deposited on one side. By means of a tri-axial Helmholtz coil, a rotating magnetic field is generated and modified by an open loop control scheme to navigate the micro robot on a preselected trajectory (Ghosh and Fischer, 2009).

In 2009, Zhang *et al.* presented manufacturing of a series of artificial flagella with helical shape with a few tens of micro meters in length. There are different metal and polymer layers used in the tail structure and the helical shape is obtained by the inner stress exerted by the manufacturing process. The details of manufacturing process can be found in (Zhang *et al.*, 2009; Zhang *et al*., 2010). There is a magnetic payload attached to one of end with dimensions of 4.5 μm x 4.5 μm x 200 nm which allows an external magnetic field to control the rotation. The structural integrity and swimming behavior of the helical tail is verified by SEM visualization (Zhang *et al.*, 2009; Zhang *et al*. 2010).

An unusual propulsion method, a catalytic propulsion system for micro swimmers, is presented by (Mallouk and Sen, 2009; Mirkovic *et al*., 2010; Balasubramanian *et al*., 2011). The design is based on electron and proton flux driven by gold and platinum deposited surfaces. Gold deposited surface reacts with the hydrogen-peroxide in the vicinity and produces water introducing electrons into the molecule. Platinum side simultaneously decomposes hydrogen-peroxide molecules into water, protons and electrons. The flow of electrons and protons on the surface of gold-platinum assembly induces drag on the water. Thus net propulsive force and forward motion is obtained given that that the overall shape of the deposited surface is a prolate spheroid.

1.2.4.2. Macro-scale experiments

Honda *et al.* (1996) used external actuation by rotating magnetic field to obtain propagation of a cm-long spiral swimming robot in a silicone oil filled 15-mm diameter channel. Authors demonstrated that the motion of the robot is in a linear relationship with excitation frequency and results agreed well with Sir Lighthill's (1975; 1976) slender-body-theory results.

In 2004, Behkam and Sitti carried out an experimental with a flagellum of approximately 2 cm in length carrying out helical wave propagation and presented results as a comparison between the propulsive force measured by strain gauge and propulsive force computed using the theory. Authors presented that the theoretical computations and their experimental measurements for propulsive force, although match in behavior, do not verify each other numerically (Behkam and Sitti, 2004).

In 2006, Yu *et al.* carried out an experiment employing a simple Scotch-Yoke mechanism to transform rotation into planar wave propagation in cm scale submerged in a fluid tank. The thrust force was measured by a strain gauge and the waving patterns were recorded by camera. Results were presented as a function of Sp number with an asymptotical propulsion velocity value and confirmed by earlier theoretical studies of Wiggins and Goldstein (1998).

In 2007, Kosa *et al.* proposed a swimmer with two parallel tails composed of piezoelectric laminates carrying out planar wave propagation in phase. They formulized an analytical coupled "electrical-mechanical-fluidic" model and verified their analytical model results with experimental measurements obtained from a tail made of three piezo-ceramics of different lengths driven in phase. The propulsive force is calculated from the force balance on the power lead cable hang from top. Although the model proposed in this study grasps electrical, mechanical and fluidic aspects (except Brownian effect) together, it is designed to obtain swimmer behavior as a function of frequency rather than simulation time (Kosa *et al*., 2007).

Kim *et al*. (2004) and Chen *et al*. (2010) implemented on-board powered swimming robots in cm-scales. In the former study, authors manufactured an Ionic-Polymer-Metal-Composite (IPMC) tail. IPMC systems can undergo structural deformations resembling planar wave propagation under appropriate stimulations of electric potentials. The batteries were placed in the body of the untethered tadpole-type swimmer, and it is demonstrated that, under applied voltage, the tail deforms inducing net forward thrust (Kim *et al*., 2004). In the latter study, Chen *et al*. (2010) experimented on a bacteria-like robot with four helical tails, which are placed symmetrically with respect to the long axis of the robot. Authors studied the 6 degree-of-freedom motion of the robot in a viscous reservoir and argued that the robot can be maneuvered via controlling the rotation of helical tails separately (Chen *et al*., 2010).

In 2008, Wang *et al.* introduced an experimental study on a tail in cm scale that mimics fish fin actuated by stack of shape memory alloy while introducing St number, i.e. "Strouhal number" as the non-dimensional frequency of flow, and stated that the optimal swimming takes place where St number is between 0.25 and 0.35.

Garstecki *et al*. (2009) manufactured a cm-scale artificial swimmer which is driven by external magnetic fields. The tail is actually an elastic structure, i.e. PDMS, and the body is made of a magnet. Rotations of body, which are induced by external magnetic fields, induce deformations on the elastic tail. The design is similar to the red blood cell with magnetic tail (Dreyfus *et al*., 2005); however, it is the body that is rotated in the plane (Garctecki *et al*., 2009).

Liu *et al*. (2011) studied the propulsive forces and swimming speeds of mere helical tails in Newtonian and non-Newtonian fluids separately. Authors used silicone oil with dynamic viscosity of 100 Pa·s, and Boger fluid, i.e. fluids acting as elastic medium despite having nearly constant viscosity (James, 2009), respectively. Authors concluded that the relaxation time is the key element in non-Newtonian fluids for optimum swimming velocity; thus for very low and high relaxation times the forward swimming velocity reduces and becomes smaller than the forward velocity in Newtonian fluids.

1.3. Outstanding Issues

There are several problems at hand to overcome about manufacturing limits, i.e. the question of how small it can be, application limits due to biocompatibility issues, i.e. whether it could really maneuver inside human body without interference with body itself or not, actuation mechanism, i.e. question of how to mimic the desired wave propagation, "flight time" consideration, i.e. the amount of power and total energy an artificial micro swimmer may consume and finding the answer to the question, "where am I?" to be able to control and maneuver the robotic device inside the living tissue. This section, for sake of completeness, is dedicated to list some techniques and methods addressing these issues.

1.3.1. Manufacturability

This section deals with micro manufacturing techniques used in IC and MEMS, and are briefly explained with examples to represent the achievable complexity of end products. Furthermore, given the fact that the ultimate goal of this study is to model a robotic device to perform in living tissue, the issue of biocompatibility is highlighted with possible solutions addressing important biological problems.

1.3.1.1. IC technology

A brief list of micro manufacturing techniques is presented in this section, followed by a list of micro manufactured artificial swimmers. Manufacturability limit is directly related to the micro fabrication capabilities of current techniques. This subsection will discuss the most successful micro fabrication techniques, i.e. such as "DRIE"," LIGA" and "Surface Micromachining" with some examples from literature. Details of these techniques

will not be discussed unless they have a key role in creating high dimensional ratio, i.e. aspect ratio, 3D objects in micro realm. In addition to these techniques there will be a brief discussion on packaging.

DRIE method, which exploits high energy ions directed to the surface, is utilized to manufacture "deep trenches" and almost perfectly "parallel fingers". After the photoresist material is developed under desired mask and certain light source, the geometry of the mask is printed simply by etching the surface. DRIE method allows digging out material out of the bulk of the wafer according to the mask and form etched surfaces with almost no inclination allowing producing parallel surfaces (Hsu, 2002).

LIGA, i.e. short for "Lithographie Galvanoformung Abforming" in German, method used to create more complex structures in micro realm such as micro gears. This technique utilizes X-rays for etching process and electroplating for either die production for molding or the main feature itself. Especially electroplating and molding phases allows alternative materials to be used for micro fabrication since electroplating allows a variety of metals and molding exploits plastic materials to form the smaller features of the structure (Hsu, 2002; Nguyen and Wereley, 2006).

Both ion etching and X-ray etching is used to directly subtract material from the top. Surface micromachining technique is used to eliminate "sacrificial layers" below main features via certain chemicals to create structures such as cantilever beams (Hsu, 2002). A similar micromachining technique is known as "Laser Micromachining" where the material is subtracted from the surface by laser beam "pulses" with a very high precision (Nguyen and Wereley, 2006) which could replace the X-ray etching used in LIGA possibly reducing the cost (Hsu, 2002).

Capabilities of micro manufacturing techniques can be demonstrated via examples from the literature. In year 2005, Sun *et al.* published an experimental comb drive MEMS device for force sensor applications manufactured by DRIE. Dimension of each cantilever of the comb drive was 500 μm (length) x 5 μm (thickness) x 50 μm (depth) and these dimensions were verified by SEM pictures after all manufacturing processes are done (Sun *et al.*, 2005). In 2009, Huang *et al.* published their work on manufacturing millimeter sized gears, i.e. 4 mm in diameter, using LIGA based manufacturing approach with a special molding technique (Huang *et al.*, 2009). In 1997, Döpper *et al.* manufactured a gear micro

pump based on two gears, both about 590 μm in diameters with 240 μm diameter steel shafts holding them and a channel of 500 μm deep all manufactured by LIGA (Döpper *et al*., 1997). In 2008, Loechel *et al.* manufactured micro harmonic drives with step size of 4 μm, and capable of 95 mNm "ratcheting torque" and 20 μNm "friction torque" via LIGA technology. The electroplating and molding steps in this study are presented by visual demonstrations and SEM pictures (Loechel *et al*., 2008). In the year 2001, Yang *et al.* manufactured micro "refractive lenses" with a diameter of 250 μm, again by LIGA technique. Kubby, in 2001, manufactured hinged optical structures whose orientation can be altered with respect to the operational needs via hinges with largest dimension smaller than 100 μm. In 1998, Rodgers *et al.* manufactured a complete microtransmission system actuated by "comb drive" and with gears smaller than 100 μm in diameter.

Packaging is also important as well as manufacturing. Since the proposed micro swimmer robot is supposed to perform inside fluidic environment, to avoid any contamination or malfunction, its' payload, i.e. the body, and the electrical wiring with power harvesting / generating unit must be completely sealed. This goal can be achieved by either high load or temperature application, i.e. bonding techniques, on certain contact surfaces and this type of sealing is known as Hermetic sealing where matter flow is prohibited (Cheng *et al.*, 2001; Kim *et al*., 2002; Oberhammer *et al*., 2004; Jin *et al*., 2003).

Examples on the manufacturability of tails in micro dimensions are presented in works of Dreyfus *et al.* (2005), Ghosh and Fischer (2009) and Zhang *et al.* (2009). Presented studies use novel techniques in construction of the artificial swimmer. Dreyfus *et al.* used DNA chains to attach magnetic particles to each other and to a red blood cell. This way the flexibility of tail is ensured and necessity of on-board actuation was eliminated (Dreyfus *et al*., 2005). Ghosh and Fischer (2009) and Zhang *et al*.(2009) used the similar actuation principle, i.e. applying external magnetic field but the tail structure was obtained via micro manufacturing techniques based on layer growth which is known as epitaxy, followed by DRIE as briefly described above and finally removal of sacrificial layers (Hsu, 2002).

1.3.1.2. Materials and biocompatibility

Biocompatibility is an important concern given that the main target is preservation of living tissue. Issue of biocompatibility arises due to the fact that any foreign material may lead to different allergic reactions or poisoning effect in different individuals. Assuming that the micro medical robot is supposed to perform into blood stream where these processes can be in effect the fastest, this subsection will discuss the possible pitfalls and related solutions to the issue in detail.

Blood stream directly contributes to the immune system via series of living cells generally called white blood cells. There exists a variety of white blood cells responsible of different useful and sometimes hazardous action and these cells constitute the "adaptive" part of the immune system (Mitchell, 2004). These cells, some of which are called killer cells, are responsible from killing and neutralizing the hazardous cells if detected. There also exists an "innate" part of the immunity system inside the blood stream which encompasses special proteins called "complement" proteins which create the initial reaction to hazardous intruders detected inside the blood vessels. Although "innate immunity" is considered to be very basic and primeval, it is the first to be triggered but it has a narrow range of selectiveness against foreign substances (Mitchell, 2004). Complement proteins have about 20 different types and they have the tendency to get attached to anything external and they play a key role to inflammation (Remes and Williams, 1992; Johnson, 1994; Gorbet and Sefton, 2004; Hakim, 1992).

It is common practice for the immune system, in order to protect the body, to attack suspicious molecules and cells which could result in allergic reactions. The immune system is directly responsible for this undesirable condition. There are some synthetic causes of allergic reactions such as "polymer materials, metal ions and metal salts" (Hensen-Petersen and Jacobsen, 2004) and some specific metals are known to cause allergic reactions. Allergies are known as the "over reaction to a stimuli" and can result in severe problems in some cases. Although allergenic substances may differ for each individual it is a common

practice to avoid being in contact with them since the stimuli for allergic reactions are not common (Hensen-Petersen and Jacobsen, 2004).

Furthermore, when and if the certain proteins, i.e. collagens, responsible from "coagulation" procedure, lead to a mass confrontation between the blood stream and foreign surface, it is probable that an undesired chain reaction would occur (Hanson, 2004). Once the proteins within the blood stream are accumulated on the foreign surface, platelet cells simply tend to follow this newly formed sheet of proteins. Coagulation happens after several complex chemical reactions, releasing different bio-chemicals and so on (Hanson, 2004). The most important phase in this process is the very first one where certain proteins accumulate on the surface; the rest is the natural way of cells and proteins to work which should not be interrupted for the sake of overall body safety.

To address to the problems at hand, i.e. allergy and coagulation as discussed, polymer surfaces were chemically altered such that they mimic the endothelial cell surfaces, e.g. like the inner surfaces of blood vessels, resulting in less reaction with blood elements (Bruck, 1977). These cells are located in the inner surfaces of blood vessels. This way, it is intended to avoid coagulation.

A similar surface imitation procedure is the replication of the "phospholipid ingredient" of the living membranes (Durrani *et al*., 1986). Intention is to simply hide the surface with an "engineered natural look" (Durrani *et al.*, 1986).

Another similar solution is to use hydro-gels which have "cross-linked" via in between long polymer chains (Peppas, 2000). There are several areas hydro-gels are used and they can be engineered in a way that they can imitate the elasticity of living tissue.

Instead of coating, embedding approach can be used. Polymers such as Polyethylene glycol, Polyvinyl chloride and Polye-caprolactone can be utilized via a process called "immobilization" This process makes surfaces more invisible to blood cells and blood proteins in which these long chemical chains are embedded (Merril and Salzman, 1983; Rusu *et al.*, 2006) resulting lessen coagulation (Teramura, 2008).

There are also special chemicals known as "surface additives" (Salvagnini, 2005). They are used to engineer biocompatible surfaces while preserving the physical properties of the material beneath the surface. For example, one very important organic bio compatible material, which can be used to repel cells is a polymer called heparin. This

polymer is responsible from preventing coagulation when used as coating material (Larm *et al*., 1983).

1.3.2. Actuation Methods

In this subsection actuation methods of micro robots with wave propagations or their macro scale prototype are listed in detail. Some of the methods, as already presented within the literature review on experiments, can be employed in both micro and macro experiments. It must be also noted that, carrying out wave propagations on a rigid or elastic tail is also a method of pumping in viscous fluids provided that the rigid-body translation or rotations of the micro swimmer itself are eliminated by an anchoring force (Raz and Avron, 2007). Also, there also exist different actuation methods such as obtaining forward thrust based on chemical reactions of a catalytic engine (Balasubramanian *et al*., 2011).

1.3.2.1. Invoking structural deformations on tail

One actuation method is based on exploiting the piezoelectric effect to induce travelling plane waves. The piezo effect and piezo-structure interaction is discussed in detail by Piefort (2001). Briefly, the asymmetry in crystal structure of the piezo ceramics result in deformation under applied electric field and vice versa. This effect can be harvested in different mechanical deformations if appropriate electric fields are applied and formulized by a certain constant, i.e. piezoelectric constant, in a linear manner with applied electric field (Piefort, 2001). There are several studies on exploitation of piezoelectric materials in MEMS devices but wave propagation on piezo laminates are studied in a few of them (Chakraborty *et al*., 2005). The deformation of single piezo stack was studied for active structure construction in (Yoon *et al*., 2004; Lim *et al*., 2005; Cappelleri *et al*., 2002). The propagated waves in these methods are different than sound waves where the speed is completely material dependent (Landau and Lifshitz, 2005a). There also exist polymer

materials, e.g. PVDF, with similar piezoelectric capabilities that are in use for "biomimetic applications" (Liu *et al*., 2006).

Surface deformations can also be induced based on the memory effect of chemical bonds within the material. In the year 2008, Wang *et al*., in two different studies, discussed the experimental results of implementing a fin structure in cm scale employing shape-memory-alloys (SMA) (Wang *et al*., 2008) which are metal alloys that have temperature dependent elasticity due to their matrix organization and can be used to exert local stresses on structures by applying appropriate electric voltages (Otsuka and Ren, 1999; Wang *et al*., 2008) and already in use for biomedical applications (Machadoi and Savi, 2003). SMAs are also being tested and used in order to mimic the behavior of other types of small scaled living creatures such as earthworms (Kim *et al*., 2006).

One other way to create structural deformation on a fin or tail like structure is using ionic polymer-metal composites known as IPMCs. If electric is voltage applied, these composite materials work as material pumps in aquatic environments and let molecules through their matrix structure. As molecules journey within they exert tension due to atomic interaction on the location they are passing resulting in structural deformation with lower frequencies and higher amplitudes with respect to that obtained by piezo-ceramic stacks (Newbury, 2003; Nasser-Nemat and Li, 2000; Nasser-Nemat, 2002). IPMC based tail design was employed by Arena *et al.* (2006) to study the theoretical control design of a robot employing a series of IPMC stacks driven by electric fields in phase. There is also an interest in "artificial muscle" construction based on IPMC structures (Jung *et al*., 2003) based on local contraction effect of the structural deformation, which can be utilized to mimic the sliding protein chains embedded in a flagellum. Each study requires a driving circuitry exploiting amplifiers and a medium with enough humidity to enable the pumping effect within the IPMC structure (Arena *et al*., 2006; Jung *et al*., 2003; Tadokoro *et al*., 2000).

1.3.2.2. Invoking tail rotations

Helical tail rotations are induced either by rotating external magnetic fields or on-board actuation. Swimmer robots may have either rigid or flexible tails. With rigid tails the only control on the wave propagation is rotation rate vector. However, with a flexible tail the shape of the resultant waves depend on actuation frequency and elasticity of the tail material or structure. (Wiggins and Goldstein, 1998; Belovs and Cébers, 2006; Roper *et al*., 2008; Tabak and Yesilyurt, 2012a; 2012b).

1.3.3. Energy Supply

As long as the proposed swimming micro robot is supposed to perform autonomously, i.e. without any cables attached to it to supply information or power, there must be a built in means to either consume stored energy or harvest energy from environment. This subsection deals with the solutions proposed to overcome this issue in literature.

1.3.3.1. Scavenging and harvesting

A celebrated method of energy supply is electromagnetic wave harvesting. This method is based on presence of stray waves in the environment which could be emitted from any possible source as long as strong enough. In 2006, Bhalerao *et al.* studied a system to operate on specifically "2.4 GHz band" based on an array of "patch antenna" configuration and harvest power in micro-Watts to power "wireless sensors" with minimum 1.4 μW power output. A very similar system based on "RFID technology", i.e. "radio-frequency identification", via inductive effect of fields with a comparison on distance and harvested energy relation (Jiang *et al*., 2007).

A very similar scavenging technique is harvesting energy from mechanical vibrations and one of the designs is based on transforming vibration into electrical energy via a micro-spring and a magnet with a lower aspect ratio, i.e. relatively sizeable, and presented with numerical results obtained with the help of a commercial finite-element-method (FEM) package COMSOL (Lu *et al.*, 2007). Serre *et al.* (2007) studied a similar method based on different mechanical configuration with numerical results obtained by the commercial package ANSYS yielding power in nano-Watt range with maximum of 50 nW (Serre *et al.*, 2007). Theoretical study on energy harvest from rigid-body rotations was presented by Yeatman (2006) with resultant formulae for the relation between the rotation and the power generation. Furthermore, a different mechanical vibration scavenging method based on piezoelectric effect was presented by Jeon *et al.* (2005).

Another scavenging method proposed to power MEMS devices or obtaining power is heat scavenging. This method is based on "thermovoltaic" effect, which is very similar to field emission electron gun technology. Heat energy can be used to create photon emissions from a silicon based source (Nielsen *et al.*, 2003; Goldstein *et al.*, 2007) which may also be used to harvest heat energy in body as primary or auxiliary means of energy.

Moreover, a swimming micro robot can utilize visible light to harvest energy, i.e. the "photovoltaic" effect with an output power of 4 mW for unit-centimeter square (Benjermo, 2005). However, this method is useless unless the artificial micro swimmer is operating in a location where light can be absorbed such as eyeball, otherwise photovoltaic effect cannot be exploited without an artificial light source.

1.3.3.2. On-board power supply options

One of the very interesting power source ideas is "nuclear batteries". Indeed the idea of a nuclear battery is an old one and in 1973, Braum *et al.* has studied the theory for such a power supply. The main idea was to collect the emissions from a nuclear source, i.e. "tritium", of very small quantities, e.g. in micro grams, and yet to supply energy in micro watts and pico-Amperes in the long run (Braum *et al.*, 1973). In 2000, Andreev *et al.* revisited the idea of tritium based batteries or "Betacells" as they call it but this time the

studied “Betacells” were boosted up to 35 percent in efficiency with an energy harvest of milli-Volts and nano-Amperes (Andreev *et al*., 2000). Lal *et al.* published the work on comparing three different isotopes, i.e. Ni-63, H-3 and Po-210, with a discussion on how particles emitted from are below the limit of danger (Lal *et al*., 2001). In 2002, a technical report was published by Blanchard *et al.* and proposed a new design employing Ni-63 as nuclear source and a “self-oscillating cantilever” which is the key element to the new design as both “collector” and “energy conversion unit” (Blanchard *et al*., 2002). In the year 2004, an article by Lal and Blanchard discussed the future possibilities of nuclear batteries and gave a comparison between conventional Li-ion batteries, “methanol fuel cells” and nuclear batteries, especially the ones work based on the “free oscillating beam” mechanism. Authors reported energy harvest of “3 nW with 0.1 mci (millicurie) of nickel-63” (Lal and Blanchard, 2004).

Rechargeable on board batteries are also proposed as an on board power source for MEMS applications. Bates *et al.* (1993) presented a discussion on Li batteries in micro scale, which can be recharged in need and capable of an energy density of 2.1×10^6 J/l. Author discussed the manufacturing process of such a battery with IC fabrication techniques and pointed out that the battery should be operated with low currents to prevent drastic fall in the battery voltage (Bates *et al*., 1993).

A final note on the on-board energy options is the possible utilization of living cells as propulsion means in micro robotic applications. Such an arrangement with a group of bacteria towing a payload may eliminate the necessity of energy transfer via artificial methods. The only issue about energy supply in a bacteria based propulsion would be the presence of nutritious molecules in the surrounding medium (Behkam and Sitti, 2007).

1.3.3.3. External power supply methods

External power supply options are based on either magnetic manipulation of swimmers or using acoustic waves to generate electrical power. Magnetic manipulation depends on alignment between the magnetic particles and external magnetic field; changing the orientation of magnetic vector on a particular location induces out-of alignment, which

results in reaction force and torques to move magnetic body accordingly. Magnetic field is applied either Helmholtz coil arrangement or MRI system (Beaudoin *et al*., 2006; Garstecki *et al*., 2009; Abbott *et al*., 2009).

An interesting approach to exploitation of sound waves was presented by the study of Saito *et al.* in 2002. Although the method was intended to capture and manipulate living cells by standing waves rather than propagating waves within the fluid, it has been reported that the stresses within the fluid helped altering their positions (Saito *et al*., 2002) even though the cells were already motile. Similar sound waves can be utilized to supply power to MEMS devices and mobile micro robots with proper use of piezoelectric sensors.

1.3.4. Sensing and Visualization

Determining the position and orientation of a micro swimmer is a task requiring extra computational power; however, is key element to achieve tasks in a real-time control scheme. A visual feed-back system requires high-end computational power due to intense matrix manipulation algorithms (Kragic, 2002). The environment, i.e. boundaries and obstacles, can be sensed and modeled by MRI based electromagnetic systems. In 2003, Siauve *et al*. studied modeling the visualization of human body with electromagnetic waves. Authors studied numerical models simulating visualization of the interior of human body with electromagnetic fields. They discussed that the effect of electromagnetic fields inside living tissue is dependent on the geometry and blood flow. The heat generation and varying material properties leads to a complicated problem of visualizing the targeted region given the fact than the interior of a human body differs by the subject and, furthermore, each type of tissue in human body has different electrical properties. Furthermore, the targeted tissue may not be necessarily rigid regardless of the body motion of the patient (Moireau *et al*., 2012) which also introduces complications to high resolution visualization.

In case of resolution problems of an MRI system, obstacles and openings must be physically detected with the help of auxiliary systems for a safe and sound decision making. Sensor/actuator systems mounted in swimmer's body such as piezoelectric transducers can be employed to emit and collect sound waves to detect any phase change embedded inside

the reflected waves (Jain *et al*., 2002; Xiaoming *et al*., 2007) while submerged in the fluid as proposed by Edd *et al.* in 2003.

1.3.5. Control of Micro Swimmers

Control studies on micro-robotic motility include different approaches. The very definition of micro robot changes in each experimental study depending on actuation method and selected method of control. Hence, although the notion of motion control is the same, the control approach or method may differ significantly. The following is a small list of control approaches with different micro robot designs.

1.3.5.1. Position control studies

Shechter and Martel (2010) carried out experiments controlling position and velocity of bacteria with oxygen gradient in the fluidic medium. Behkam and Sitti (2006b) discussed the possibility of employing bacteria to move a rather large payload by controlling external stimuli. In both studies (Shechter and Martel, 2010; Behkam and Sitti, 2006b) the objective is to control the position of bacteria by environmental stimuli such as the spatial gradient of oxygen, light or nutritious chemicals. If the position of bacteria can be controlled at will than a large payload attached to a group of microorganisms can be towed (Behkam and Sitti, 2006b).

Sakar *et al.* (2011) studied the direct magnetic positioning of μm-scale payloads in liquid medium by dragging the microrobot to a desired reference position via modifying an external magnetic field. Here, the robot consists of a small magnetic body and the goal is to control its position and orientation by dragging it with the help of external magnetic fields (Sakar *et al.*, 2011).

Ghosh and Fischer (2009) presented open loop position control study results on 1-2 μm long magnetic helical swimmers. Authors modified the external magnetic field actuating the robot in order to follow preselected trajectories in plane.

1.3.5.2. Velocity control studies

Chen *et al.* (2010) studied the maneuverability of a cm-scale bio-inspired robot with four independent DC-motors actuating four rigid helical tails. The body of the swimmer holds DC-motors and battery to feed them. Authors argued that by controlling the rotation of each tail separately, it is possible to control 6 degree-of-freedom motion and maneuver the robot at will (Chen et al., 2010).

Mahoney *et al.* (2011) experimented on visually assisted velocity control scheme on a magnetically driven helical micro robot with compensation for gravitational attraction. The helical robot used in this study consists of a magnetic body with a rigid helical tail glued on one side, and its total length is approximately 6 mm. Authors observed that the gravitational pull disturbs the alignment between magnetic head of a helical swimmer and the external magnetic field. To be able to overcome this problem they modified the external magnetic field with real-time visual inspection and gravity compensation.

1.4. Contribution of the Thesis

Three major tools are used in order to analyze and characterize the swimming robots in viscous fluids. Experiments provided the parameterized data sets to validate the hydrodynamic model and CFD-model. Furthermore, CFD-model is used to study the flow fields induced by the swimming robot, and particularly to study and understand the body-tail interactions. Hydrodynamic model is further improved based on the flow field and fluid resistance analysis based on CFD simulations, and utilized in design and control studies.

The contributions of the in-channel experiments with swimming untethered robotic prototype are:

- The effect of proximity to cylindrical channel walls on confined swimmer's propulsion velocity is studied in vertical and horizontal orientations with respect to gravitational pull.
- The effect of channel diameter on in-channel propulsion velocity of swimmers is inspected in horizontal channels.
- The effect of wave geometry on in-channel propulsion velocity is inspected with parameterized wave amplitude, wave length and tail length.

The contributions of the CFD simulations with bio-inspired swimmers are:

- CFD-model is validated with vertical swimming experiments.
- The effect of channel diameter on propulsion velocity of concentric swimmers is inspected with parameterized channel geometry.
- The hydrodynamic interaction between body and tail, which are rotating in opposite directions, of a bacteria-like swimmer is qualitatively and quantitatively explained with the help of varying body and tail geometry.

The contributions of the reduced-order hydrodynamic model are:

- The hydrodynamic model based on resistive-force-theory is verified with the help of experiments and CFD-model results carried out with parameterized wave geometries
- Hydrodynamic interactions between body and tail are utilized to implement a modified resistance matrix in order to achieve accurate predictions of hydrodynamic forces acting on the swimmer in time-dependent fashion.
- The uses of the proposed model as a surrogate-model in order to search for efficient swimmer geometries, and as a tool for model-based position control are presented.

2. EXPERIMENTAL PROCEDURE

In this section the experimental setup and details of the robotic prototype are discussed in detail. The robotic prototype is used in vertical and horizontal experiments in order to study the channel effects on the forward velocity (Tabak and Yesilyurt, 2012a; 2012b)

2.1. Design of the Swimmer

The bio-inspired swimmer robot is comprised of two links, which are the body and the tail and joined with a revolute joint. The design presented here is a successor to the prototype developed earlier by Erman and Yesilyurt (2011). Addition of mechanical coupler to the design led to standardized body geometry. Furthermore, the swimmer is equipped with a remote control unit and helical tails are manufactured out of copper wire, which in turn made the overall robot heavier.

2.1.1. Body (Payload) Design and Manufacturing

Overall size of the robot is subject to the available electrical components, battery pack and coreless brushed DC-motor with enough torque to rotate the helical tail under high viscous load. Body and tail are connected with a mechanical coupling, which is machined out of an aluminum alloy and has two grooves in order to transmit the mechanical power

from DC-motor to the tail. Coreless brushed DC-motor is housed in the plastic seal astern the body as depicted in Figs. 2.1b and 2.2b. Power leads of the motor are secured within the 0.75 mm thick cylindrical silica-glass cover of different lengths (see Fig. 2.1a), each of which has a hemispherical surface to the fore, while its rotor is fitted tightly into the mechanical coupling forming the revolute joint as indicated in Fig. 2.2b. DC-motor is driven by an IC board, which is salvaged from a remote controlled toy helicopter. Driver circuitry and the DC-motor, which are discussed in detail, are powered by a battery pack. The body of the robotic prototype is presented in Fig. 2.1b.

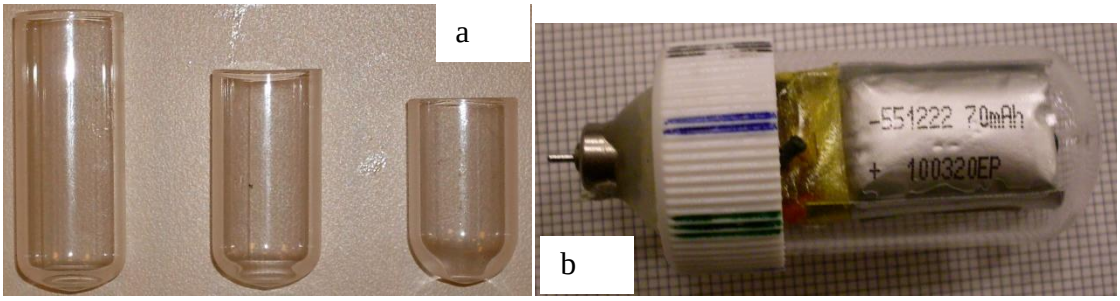

Figure 2.1: Prototype robotic swimmer's body: Silica glass casings with different length (a); assembled body without mechanical coupler (b).

2.1.2. Tail Design and Manufacturing

Right-handed helix-shaped rigid tail is manufactured by winding a 1-mm-diameter copper wire into a coil around a smooth cylinder of a certain diameter for uniform amplitude, followed by stretching evenly in order to form identical waves throughout. Actual length of the wire varies with the wave geometry but length of the helix is fixed at 60 mm. One end of the rigid tail is deformed with a steep hyperbolic tangent profile and inserted into the mechanical coupling and clamped by two setscrews. In total, sixteen helical tails with different wave geometries are manufactured (see Appendix 6 for details).

2.2. Experimental Setup

Untethered bio-inspired robot is placed inside constant-cross-section glass tubes with open ends for horizontal experiments as depicted in Fig. 2.2 and with closed ends for vertical experiments as depicted in Fig. 2.2. It is also noted that the long axis of the tails and symmetry axis of the channels are parallel to the **x**-axis of the lab frame. Furthermore, glass tubes of 350 mm in length with different inner diameters are sitting stationary at the bottom of the silicone oil tank while fully submerged (see Fig. 2.2c). As for the vertical swimming, i.e. vertical channel, experiments the channel inlets are sealed with the swimmer robot already inside while the entire volume inside is occupied with silicone oil. Swimming robot translates concentrically (see Fig 2.3a-b) and the channel is held parallel to the gravitational pull with a clamp (see Fig. 2.3b) for the duration of vertical swimming experiments.

Physical properties of the silicone oil are measured as $\rho = 985$ kg/m^3 and $\mu = 3.5$ Pa·s; a pycnometer is used in density measurement whereas the dynamic viscosity of the oil-bath is obtained by silicone oils (Cole Parmer) with viscosities of 12.5 Pa·s and 1 Pa·s mixed with a ratio of 1:3.6. It is noted that given values are independent of the temperature of the environment. Physical and geometric properties of the bio-inspired robot, the channels used in experiments and experimental design are presented in Table 2.1.

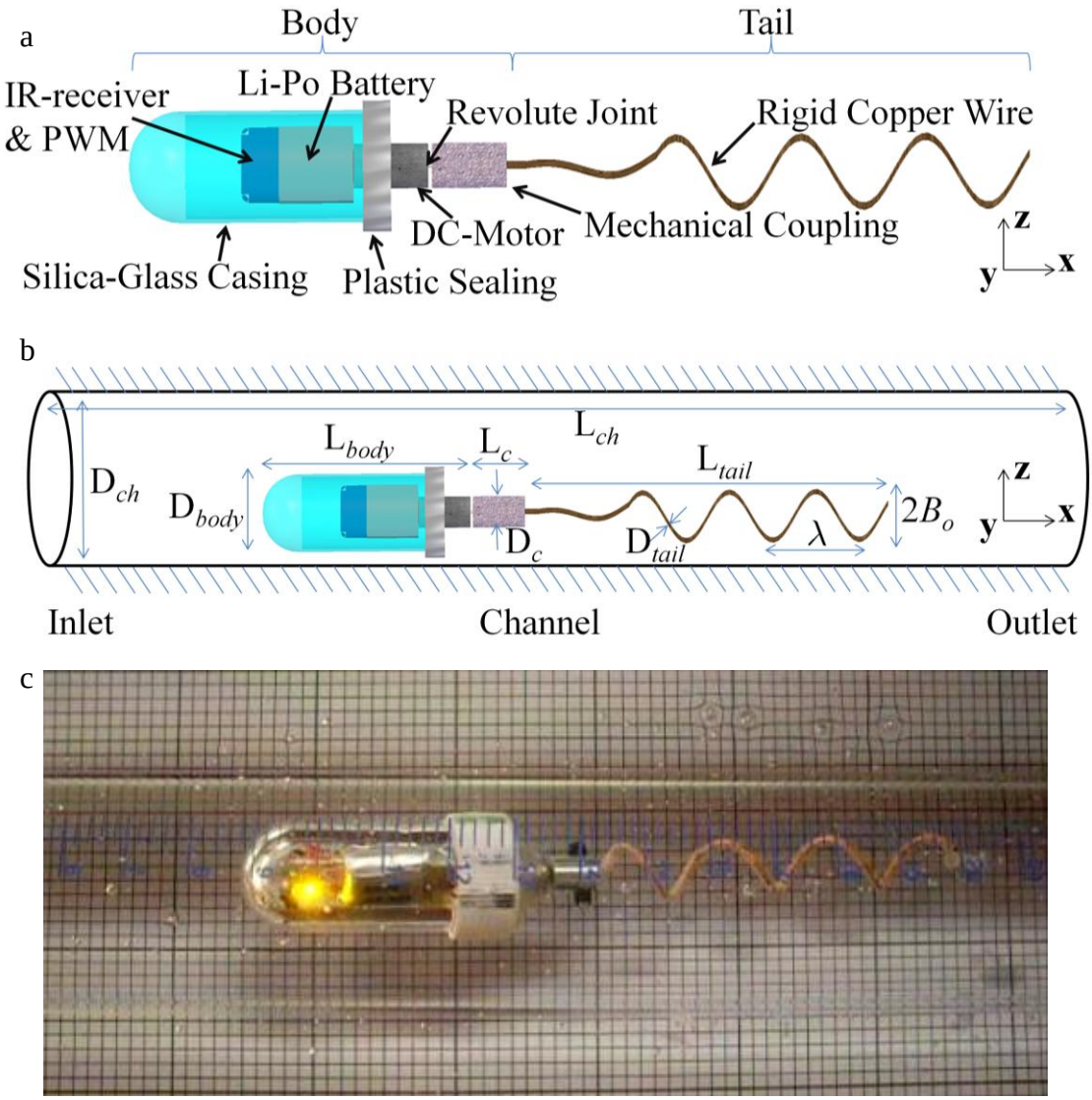

Figure 2.2: Swimmer robot design: Bio-inspired robot assembly (a); robot inside the horizontal channel presented with geometric parameters (b); robot inside channel (c).

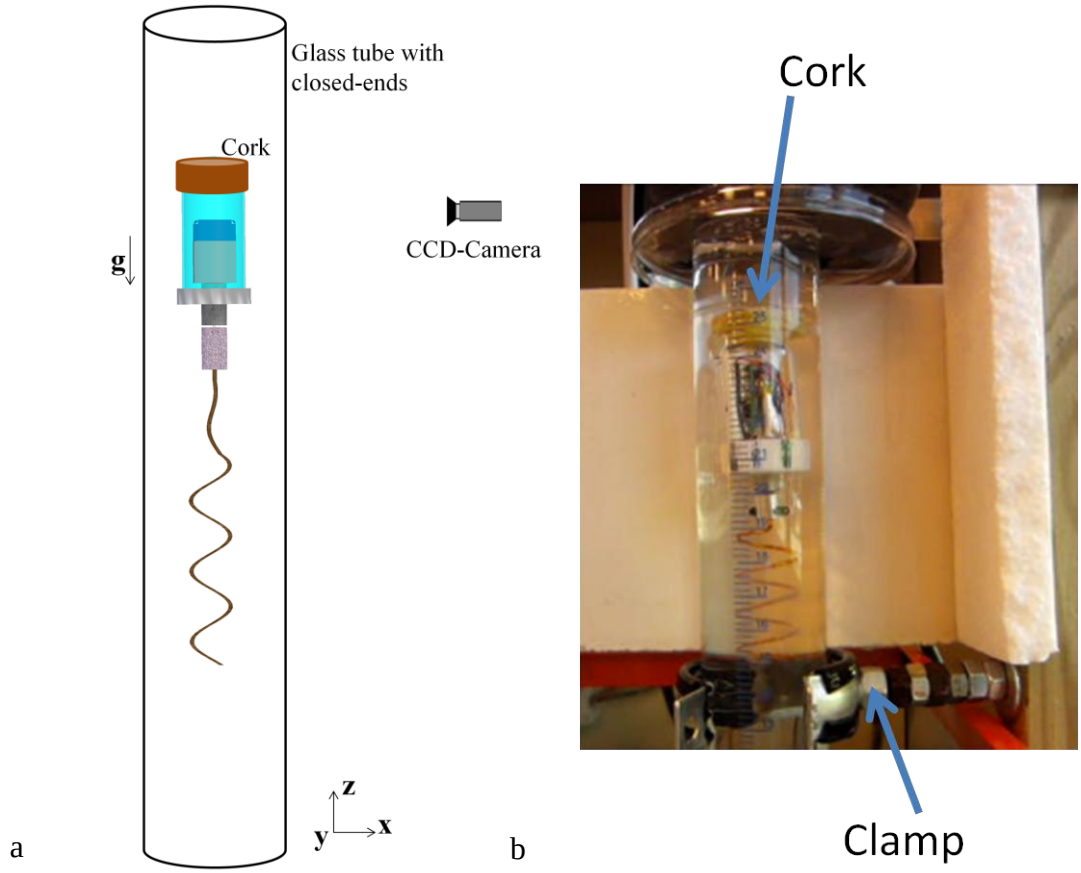

Figure 2.3: Experimental setup for vertical channel experiments: Experimental design (a); robot inside the channel (b).

Table 2.1: Bio-inspired robot and experimental setup

D_{ch}	Channel Diameter	35 mm (Wide); 30 mm (Narrow)
L_{ch}	Channel Length	350 mm
D_{body}	Body Diameter	20 mm (diameter of the plastic sealing)
D_{cork}	Cork Diameter	20 mm (only vertical experiments))
L_{cork}	Cork Length	10 mm (only vertical experiments)
L_{body}	Body Length	35 mm (Horizontal in-channel swimming experiments); 50 mm (Vertical in-channel swimming experiments)
D_c	Coupling Diameter	6 mm
L_c	Coupling Length	10 mm
L_{tail}	Helix Length	60 mm (only for horizontal in-channel swimming experiments); variable (for vertical in-channel swimming experiments (see Appendix 6))
D_{tail}	Copper Wire Diameter	1 mm
B_o	Wave Amplitude	Parameterized
λ	Wave Length	Parameterized
-	Body-Coupling Mass	10.7 g (Horizontal experiments); 11.9 g (Vertical experiments)
-	DC-motor Diameter	6 mm
-	DC-motor Length	11 mm
-	Rotor Diameter	0.8 mm
-	Li-Po Battery Volume	5.5 mm x14mm x17mm
ρ	Si-Oil Density	985 kg/m^3
μ	Si-Oil Viscosity	3.5 Pa·s
-	CCD-Camera	640-by-480 Pixels @ 30 fps
-	CCD-Camera Distance	150 mm (Horizontal experiments); 200 mm (Vertical experiments)

2.3. Actuation System and Control

The tail is rotated with a dedicated coreless brushed DC-motor, which by a 400 kHz PWM voltage controller circuit including an IR-receiver. Controller and DC-motor are powered by a single-cell rechargeable 3.7 V 70 mA·h Lithium-Polymer (Li-Po) pack. .Helical wave propagation is on-off controlled by an external IR remote controller, i.e. 'on' being full throttle and 'off' being zero motor-current. The wave length of the IR diodes is measured to be 930 nm with the help of a light spectrometer. Components listed here are

also presented in Fig. 2.4. Electromechanical and electrochemical properties of the motor and battery pack are measured and presented in Table 2.2 (also see Appendix 3). The equivalent electromechanical circuit of the system is presented in Fig. 2.5.

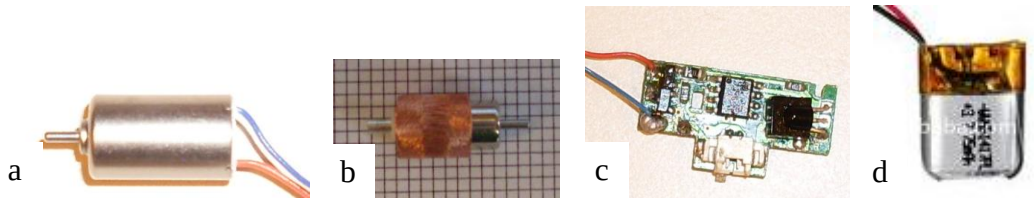

Figure 2.4: Components of the actuation system embedded in the robot's body: Coreless brushed DC-motor and its windings (a,b); PWM controller circuit with IR-diode (c); Li-Po battery pack (d).

Table 2.2: Actuation system properties

$R(t)$	Equivalent Resistance	$10.4 + 30 \exp(-54.6\, I(t)) + \exp(I(t)) - 1.555\, I(t)\ \Omega$
$V(t)$	Battery Voltage	$3.7 - 0.8\, I(t)$ V
L	Motor Inductance	0.082 H
K_m	Torque Constant	0.00045 N·m/A
K_b	Back-EMF Constant	0.004 V·s/rad
B_{eff}	Effective Friction	(variable) N·m·s/rad
B_m	Rotor Friction	$7\text{x}10^{-7}$ N·m·s/rad $@\,\omega \approx 1$ Hz
ω_m	Motor Rotation Rate	$(=\omega_{tail} - \Omega_x)$ Hz
-	Li-Po Battery Pack Rating	70 mA·h with 3.7 V
-	PWM Frequency	400 kHz
-	IR Wave Length	930 nm

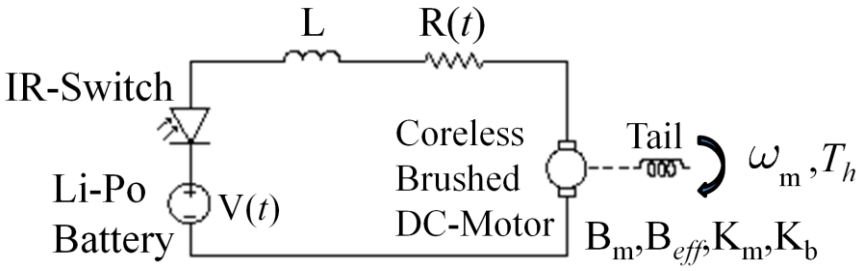

Figure 2.5: Equivalent electromechanical circuit of the actuation system.

2.4. Data Acquisition

Swimming of the autonomous robot inside the glass tube is captured by a CCD-camera, which samples 640-by-480 pixels at a rate of 30 fps, placed 15 cm away from the tank for horizontal experiments and 20 cm away from the channel for vertical experiments. The orientation of the CCD camera with respect to the glass channel is depicted in Fig. 2.6a. Eight symmetrically coded stripes of four different colors placed on the side of the plastic seal as shown Fig. 2.1b in order to determine the body rotation rates. Swimming motion is detected with the help of well illuminated grid with 2-mm-long markers (horizontal channel experiments, see Fig. 2.6b) and markers on the glass channels (vertical channel experiments, see Fig. 2.3b).

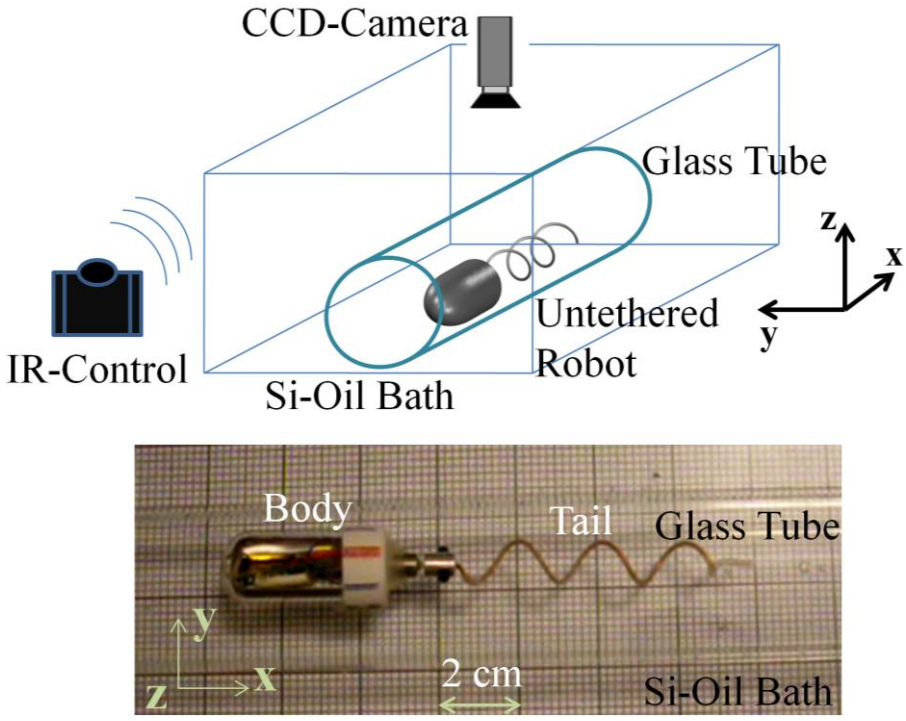

Figure 2.6: Experimental setup for horizontal channel experiments: Components of experimental setup (a); camera view of cm-scale biomimetic robot confined to glass channel (b).

3. COMPUTATIONAL FLUID DYNAMICS (CFD) MODEL

In this chapter, the CFD simulation basics are presented. The governing equations, swimmer geometry, channel geometry and corresponding boundary conditions on their surfaces are briefly discussed.

3.1. Geometry and Orientation

Figure 3.1 demonstrates the micro swimmers in viscous domain $\Omega(t)$ (see Fig. 3.2) bounded by the cylindrical channel. Consider a spherical body with a helical tail. One end of the helical tail is converging to its long axis, where the revolute joint is placed between body and tail. This geometric design is a valid representation for some bacteria species (Brennen and Winnet, 1977). Spherical body and helical tail are apart from each other with the tail radius in order to eliminate discontinuity in angular velocity boundary conditions (Ramia *et al*., 1993). It is considered that both body and helical tail are neutrally buoyant with the surrounding medium, which is bounded by a cylindrical channel. Channel has a diameter ten times that of the spherical body to eliminate the wall effects (van der Sman, 2012), thus simulating unbounded swimming conditions. Furthermore, the swimmer is placed coaxially with it at $t = 0$ as illustrated in Fig 3.2.

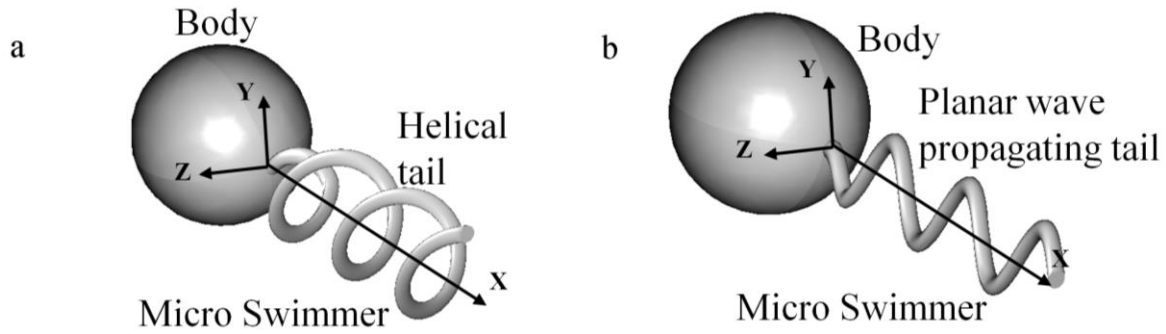

Figure 3.1: Micro swimmers with helical (a) and planar (b) wave propagating tails. Swimmer's body is designed as a perfect sphere.

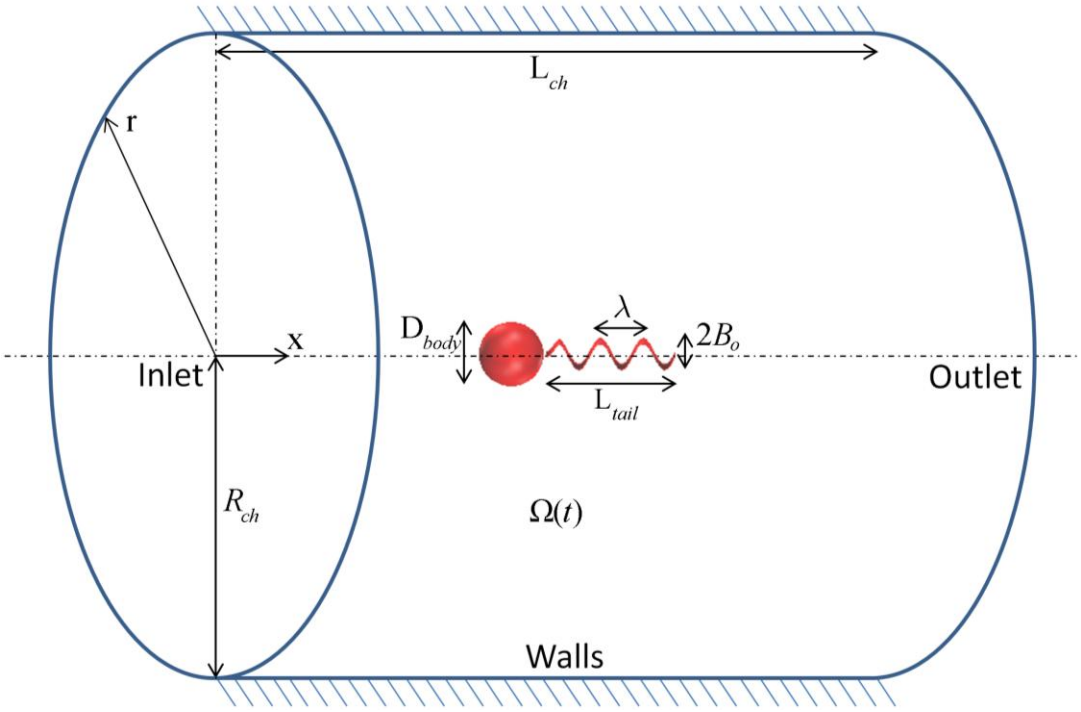

Figure 3.2: Unbounded viscous medium simulation: domain $\Omega(t)$, which is bounded by a coaxial cylindrical channel with a radius ten times that of the swimmer's body.

Figure 3.3 demonstrates the swimming robots used in-channel swimming experiments within the cylindrical channels (see Fig. 3.4). In channel experiments, robots are either placed concentrically, i.e. vertical swimming experiments, as depicted in Fig. 3.4.a, or placed eccentrically, i.e. horizontal swimming experiments with 1-mm proximity to the wall, as depicted in Fig. 3.4b.

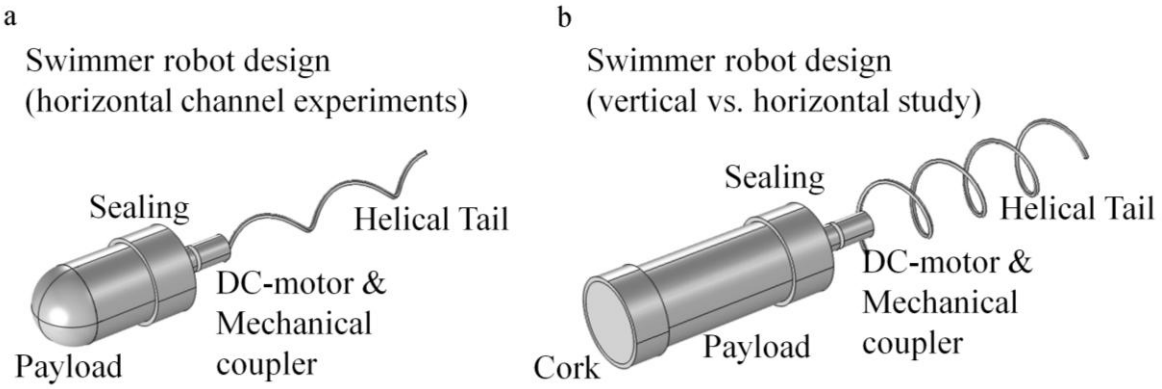

Figure 3.3: Swimming robots used in channel experiments. The body to the left is of geometry close to prolate spheroid; however, the body to the right has an unusual geometry.

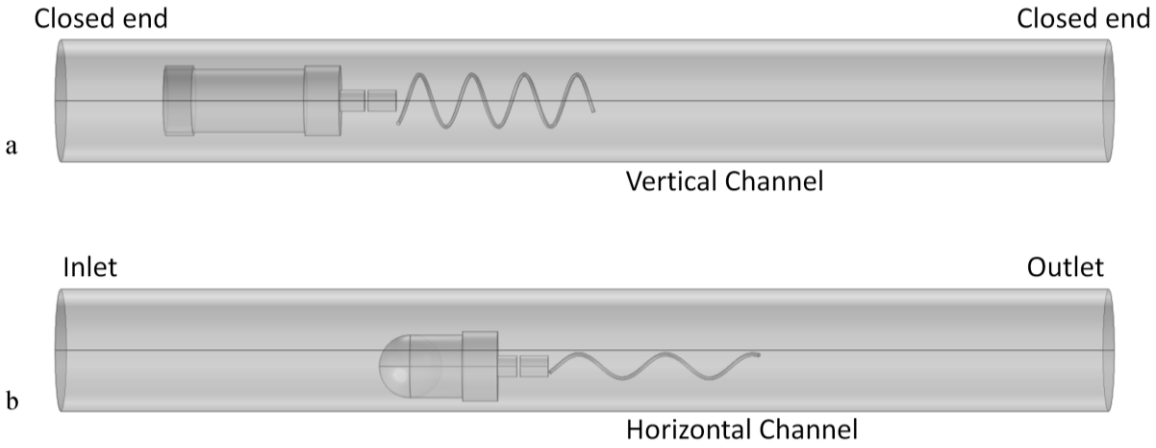

Figure 3.4: Glass channels, in which the swimmers are confined, used in experiments: Swimmer placed concentrically inside the channel (a); swimmer placed eccentrically inside the channel (b). The channel inlet and outlets are subject to experimental conditions.

3.2. Governing Equations and Boundary Conditions

In unbounded viscous medium studies, the swimmer velocity vector is computed with resolving the time-domain with a certain step-size, Δt = 0.025 s. Time-dependent incompressible Navier-Stokes equations govern the flow in $\Omega(t)$ and subject to continuity as follows:

$$\rho\left(\frac{\partial \mathbf{U}}{\partial t}+((\mathbf{U}-\mathbf{u})\cdot\nabla)\mathbf{U}\right)=-\nabla p+\mu\nabla^2\mathbf{U}\,, \tag{3.1}$$

$$\nabla\cdot\mathbf{U}=0\,. \tag{3.2}$$

Here, vectors $\mathbf{U}$ and $\mathbf{u}$ are fluid and mesh velocity vectors in $\Omega(t)$, respectively, ρ is the fluid density, μ is dynamic viscosity of the surrounding medium, and p is the hydrostatic pressure. The wave propagation, instantaneous tail shape, is imposed as mesh deformation on the tail boundaries and in $\Omega(t)$. Mesh of the swimmer robot is handled with Arbitrary-Lagrangian-Eulerian (ALE) deformation method (see Appendix 7) in order to incorporate motion of swimmer boundaries with respect to stationary channel walls (Duarte *et al.*, 2004). Furthermore, the mesh velocity term, **u**, and the explicit time derivation term in Eq. (3.1), $\partial\mathbf{U}/\partial t$, are required for time dependent Navier-Stokes solutions; however, are eliminated if the simulations are carried out for a specific time, e.g. t = 1.275 or t = 1.975.

Zero-velocity and zero-pressure initial conditions are set for Eqs. (3.1)-(3.2) at t = 0, whereas no-slip boundary condition is imposed on stationary channel walls at all times. Normal stress vectors are set to zero at channel's inlet and outlet for open-flow boundary condition in order to simulate channels with open ends. The reason being for the choice of boundary condition is that the strength of the flow field induced by the swimming robot fades drastically towards the channel inlet and outlet, where are under the influence of the same hydrostatic pressure. Moreover, no-slip boundary conditions are imposed on channel inlet and outlets to simulate swimming inside channels with closed ends (COMSOL AB 2012).

Position vector on the rotating left-handed helical tail with wavelength λ and angular rotation ω_{tail} with respect to swimmer's center of mass is specified by:

$$\mathbf{P}=\begin{bmatrix} x \\ B(x,t)\cos(\omega_{tail}t-kx) \\ B(x,t)\sin(\omega_{tail}t-kx) \end{bmatrix}, \tag{3.3}$$

and the local amplitude $B(x,t)$ on the helical tail for an unbounded swimmer is signified as:

$$B(x,t) = B_o \min(1, x/0.1)\min(1, 0.25/t) \tag{3.4}$$

in swimmer's frame of reference, i.e. **xyz**-frame depicted in Fig. 3.1. Here, B_o is the maximum wave amplitude, k is the wave number ($=2\pi L_{tail}/\lambda$) with L_{tail} being the apparent tail length in the **x**-direction as shown in Fig. 3.1, and x is the arbitrary **x**-position on tail surface with respect to swimmer's center of mass. Position-ramp in Eq. (3.4) marks the converging end of the tail, and the local amplitude stretches to its final value with a time-ramp also embedded in Eq. (3.4) to ensure smooth transition of fully-developed rotating helical tail profile for the mesh. In order to simulate the planar wave propagation, second row of **P** in Eq. (3.3) is set as zero.

On the other hand, the amplitude of swimming robots in channel experiments is modeled as B_o homogeneously throughout the helical tail without any position or time dependent ramp function. Furthermore, the swimming robots are equipped with right-handed helical tails (Tabak and Yesilyurt, 2012b).

Velocity vector on the surface of the tail, carrying out either helical or planar wave propagating is given with:

$$\frac{d\mathbf{P}}{dt} = \mathbf{\Omega}_{tail} \times \mathbf{P}, \tag{3.5}$$

where $\mathbf{\Omega}_{tail}$ is the actuation frequency vector, $\mathbf{\Omega}_{tail} = \begin{bmatrix} \omega_{tail} & 0 & 0 \end{bmatrix}'$ and the superscript ' ' ' denotes the transpose operation.

Resultant body rotation rate vector, due to conservation of angular momentum, is given as $\mathbf{\Omega}_{body} = \begin{bmatrix} \Omega_x & 0 & 0 \end{bmatrix}'$, and the corresponding fluid and mesh velocity boundary conditions on swimmer surface are given by:

$$\begin{matrix} \mathbf{U} = \mathbf{V} + \mathbf{\Omega}_{body} \times \mathbf{x}_{body} \\ \mathbf{u} = \mathbf{V} \end{matrix}, \quad \Leftarrow \mathbf{x} = \mathbf{x}_{body}, \tag{3.6}$$

for body, and

$$\mathbf{U} = \mathbf{u} = \frac{d\mathbf{P}}{dt} + \mathbf{V} \Leftarrow \mathbf{x} = \mathbf{x}_{tail} \tag{3.7}$$

for tail, where and vectors $\mathbf{x}_{body}$ and $\mathbf{x}_{tail}$ refer to an arbitrary position on body and tail surfaces with respect to swimmer's center of mass. Vector $\mathbf{V}$ signifies the resultant rigid-body translation velocity of the swimmer in **xyz-**frame, i.e. $\mathbf{V} = \begin{bmatrix} V_x & V_y & V_z \end{bmatrix}'$. Furthermore, the mesh velocity term, **u**, in Eqs. (3.6) and (3.7) is obsolete for in-channel swimming simulations. The mesh velocity, **u**, is specified only for time-dependent Navier-Stokes computations. For stationary Navier-Stokes computations, where there is no need for mesh to stretch or compress continuously, the mesh velocity term is omitted in Eq. (3.1) and Eqs. (3.6)-(3.7).

Vectors $\mathbf{V}$ and $\boldsymbol{\Omega}_{body}$ are computed with force constraint equations: in creeping flows, the fluid resistance on the entire surface of a self propelling swimmer should be zero (Taylor, 1951). Thus, one may numerically set the total instantaneous fluid force vector acting over the deforming and moving surface of the swimmer to zero in order to obtain rigid body velocities satisfying zero-net-force and zero-net-torque conditions. The constraint equations are as follows:

$$\int_{S_{swimmer}} [-p\mathbf{I} + \boldsymbol{\tau}]\mathbf{n} \, \mathrm{d}A = \mathbf{0}, \tag{3.8}$$

and

$$\int_{S_{swimmer}} \mathbf{x}_{swimmer} \times [-p\mathbf{I} + \boldsymbol{\tau}]\mathbf{n} \, \mathrm{d}A = \mathbf{0} \tag{3.9}$$

where A denotes the surface area which is in contact with the viscous fluid, $S_{swimmer}$ signifies the entire swimmer surface, and $\mathbf{x}_{swimmer}$ is the position vector of an arbitrary point on swimmer surface. Here, $\boldsymbol{\tau}$ in Eqs. (3.8) and (3.9) signifies the shear stress on the tail surface exerted by the surrounding flow field (Landau and Lifshitz, 2005b), and $\mathbf{n}$ is the local surface normal vector.

Initial conditions for the time-dependent approach are $\mathbf{V} = 0$ and $\boldsymbol{\Omega}_{body} = \mathbf{0}$ at $t = 0$; the constraint equations are solved at each time increment based on the fluid resistance corresponding to the resultant rigid-body velocities of the preceding time step combined with current wave propagation.

The last two rows of the constraint equations, i.e. Eqs. (3.8) and (3.9), are excluded in the CFD-model to eliminate the lateral rigid-body rotations for helical micro swimmers and swimming robots with helical tails. Moreover, the symmetry of induced flow field by the travelling plane wave naturally cancels out three degrees of freedom, i.e. Ω_x, Ω_z and U_y, without further modification of the constraint equations. Hence, all hydrodynamic forces are calculated on the swimmer's frame, i.e. **xyz**-frame. Eliminating lateral rotations of the swimmer in the channel frame, i.e. **xrθ**-frame, greatly simplifies the mesh deformation in $\Omega(t)$ avoiding numerical convergence issues, and also gets rid of extra rotation matrix calculations between frames.

Equations (3.1)-(3.2), in unbounded viscous medium simulations, are cast in dimensionless form for unbounded domain study; with the diameter of the body, D_{body} as the length scale and $2\pi/\omega_{tail}$ as the time-scale, and hence $\omega_{tail}/D_{body}/2\pi$ as the velocity scale. Therefore, the scaling Reynolds number becomes $\mathrm{Re} = \rho\omega_{tail}D_{body}^2/2\pi\mu$. Scaling Reynolds number used in CFD-model is set to 10^{-2}. Complete list of variables used in the base-case CFD simulation is presented in Table 3.1 and all CFD simulations for unbounded viscous medium are conducted with those particular values, unless otherwise noted. Furthermore, in-channel swimming simulations are carried out with actual dimensions and physical properties of silicone oil.

CFD simulations are carried out using the commercial software, COMSOL Multiphysics (COMSOL AB 2010). Second order Lagrangian tetrahedral elements are used in simulations. For each simulation, the tail of the swimmer is discretized with identical

element size resulting in at least 300K degrees-of-freedom depending on the channel size, i.e. diameter.

Linear system of equations is solved with the PARDISO linear solver (Schenk and Gärtner, 2004) and a second order backward difference formula with variable time-stepping for numerical integration with the maximum time step set to 0.025 s for time dependent studies. Computations take an average of twenty hours per simulation on a high-end workstation running on Linux to complete three full periods of tail rotation. However, simulations governed with stationary Navier-Stokes equations are faster since there are no intermediate time steps to compute in order to recalculate the Jacobian matrix of the numerical problem satisfying the numerical tolerances.

Table 3.1: Base-case design parameters used in CFD-model for the unbounded viscous medium study.

Parameter Name	Simulation Value
Spherical body diameter, D_{body}	1
Tail diameter, D_{tail}	0.1
Apparent tail length, L_{tail}	2
Helical wave length, λ	2/3
Helical wave amplitude, B_o	0.1
Helical wave propagation frequency, f_{tail}	1
Fluid density, ρ	1
Scaling Reynolds number, Re	10^{-2}
Dynamic viscosity, $\mu = 1/\mathrm{Re}$	100
Bounding cylindrical-channel length, L_{ch}	10
Bounding cylindrical-channel diameter, D_{ch}	10

4. REDUCED-ORDER MICROHYDRODYNAMIC MODEL

There exist three major approaches used in analytical solutions to the viscous flows and the exerted fluid resistance on the rigid or deforming slender objects submerged in: the slender-body-theory (SBT), which uses special set of functions called Stokeslet embedded in the governing equation to represent the force fields induced by local flows in viscous fluid (Lighthill, 1976; 1995; Liron and Shahar, 1978); the resistive-force-theory (RFT), which further simplifies the problem by using resistive force coefficients (RFC) to implement a linear relationship between local surface velocity of a slender body and corresponding fluid resistance acting on it (Gray and Hancock, 1955, Brennen and Winet, 1977; Johnson and Brokaw, 1979); and the asymptotic solutions of Stokes based flows induced by the planar wave propagation in unbounded viscous medium by perturbation methods (Taylor, 1951), and by the helical wave propagation in bounded viscous mediums solved with the help of a set of harmonic functions representing the induced flow fields (Felderhof, 2010). The latter two approaches are used to predict the forward swimming velocities in kinematic fashion, although Taylor further discussed the hydrodynamic stresses exerted on a tail carrying out planar wave propagations.

These methods and coefficients discussed above are applicable for highly viscous flows, i.e. creeping flows, where all acceleration effect inside the fluid are comparatively small on the order of magnitude, thus can be neglected altogether (Batchelor, 2005). However, there exist some corrections to this approach on the fluid resistance acting on moving rigid particles for transition Reynolds number flows, oscillatory motions and far field effects (Odar and Hamilton, 1964; Happel and Brenner, 1965; Lovalenti and Brady., 1993a; 1993b; Landau and Lifshitz, 2005b). Here, the focus is strictly on the creeping flow conditions.

4.1. Resistive Force Theory (RFT) Models

Microhydrodynamic models with resistive force coefficients are employed to predict time-dependent velocity of the swimmer robots, and results are validated with experimental observations (Tabak *et al*., 2011; Tabak and Yesilyurt, 2012a; 2012b) and results obtained via CFD-models (Tabak and Yesilyurt, 2010a; 2010b). The microhydrodynamic model, which is also simply referred to as hydrodynamic model in the following text for convenience, emerges as a flexible tool in which a variety of physical stimuli, e.g. external magnetic torque, can be implemented and coupled to the hydrodynamic problem.

Here, the building blocks of the hydrodynamic model are discussed in detail. Figure 4.1 depicts the frames of references on swimmers with tails carrying out either planar or helical wave propagations. Local Frenet-Serret frames differ by the position on the tail: the tangential direction, **t**, points the local tangent on both wave propagation methods; the normal direction points the symmetry axis in helical swimmers and sideways on swimmers with planar waves; finally, the binormal direction points the negative **s**-direction in helical swimmers, whereas is perpendicular to the surface with planar waves.

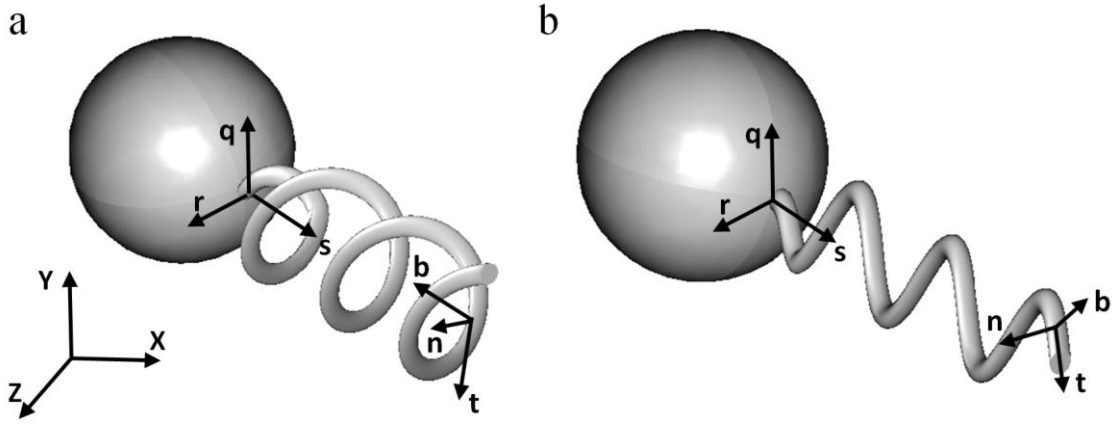

Figure 4.1: Swimmer frames: local Frenet-Serret frames, **tnb**, swimmer frames, **sqr**, and lab frame **xyz**. It is assumed that lab frame and swimmer frame are not coinciding in a perfectly parallel manner, unless otherwise is assumed.

The **sqr**-frame coincide with the center of mass, which is assumed to be at the revolute joint between body and tail in unbounded medium simulations as already depicted in Fig. 4.1, and the **s**-direction coincides with the long axis of the swimmer. The lab frame, in which the observing eye resides, is stationary. Moreover, the Cartesian lab frame is interchangeable with cylindrical coordinates if required.

Time-dependent trajectory of the micro-swimmer robot is obtained from the equation of motion, which balances forces on the robot's body and the tail:

$$\begin{bmatrix}\mathbf{F}\\ \mathbf{T}\end{bmatrix}_{body} + \begin{bmatrix}\mathbf{F}\\ \mathbf{T}\end{bmatrix}_{tail} + \begin{bmatrix}\mathbf{F}\\ \mathbf{T}\end{bmatrix}_{external} = 0, \tag{4.1}$$

where **F** and **T** are force and torque vectors, and subscripts *body* and *tail* refer to the body and the tail of the swimming robotic device. For simplicity, it is assumed that the body of the swimmer is a blunt object such as a spheroid, and the tail is subject to a motion that generates propulsion force in viscous flows, such as the rotation of a helix, or traveling-plane waves on a slender rod as commonly observed among micro swimming organisms (Brennen and Winet, 1977).

The resistive-force-theory approach employs force coefficients in order to predict the fluid resistance acting on a highly localized position on the deforming surface of a slender body due its velocity along an arbitrary **i**-axis as follows (also see Fig. 4.2):

$$\mathrm{d}F_i = -c_i U_i \mathrm{d}\ell, \tag{4.2}$$

where $\mathrm{d}\ell$ is the infinitesimal length along the slender rod as depicted in Fig. 4.2. This approach is one of the key elements to the hydrodynamic model presented in this text.

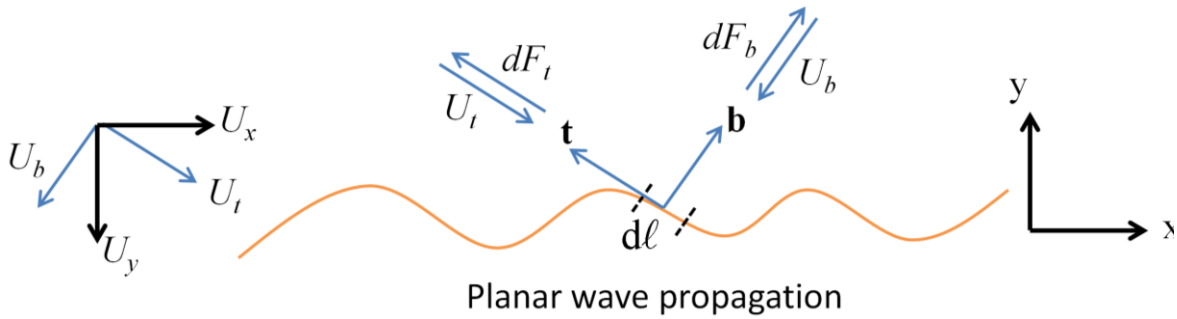

Figure 4.2: Local surface tangent and binormal directions with relative flow velocities and corresponding fluid resistance acting on a travelling plane wave propagating tail.

Based on Eq. (4.2), for creeping flows, at low Reynolds numbers, equations of motion can be cast in a linear system of equations relating the generalized force and velocity vectors by means of the 6-by-6 resistance matrix, **B**, as follows:

$$\begin{bmatrix} \mathbf{F} \\ \mathbf{T} \end{bmatrix} = -\mathbf{B} \begin{bmatrix} \mathbf{V} \\ \boldsymbol{\Omega} \end{bmatrix}, \tag{4.3}$$

Once the linear relationship between the motion and the resultant fluid resistance acting on a rigid-body is modeled as presented by Eq. (4.3), the next step is to implement resistance matrices for the parts, i.e. body and tail, and finally for the entire swimmer subject to the actuation method.

Time-dependent resistance matrix of the tail, $\mathbf{B}_{tail}$, is obtained from the integration of the product of velocity components, which are projected onto the local Frenet-Serret coordinates (see Appendix 5), and local force coefficients, which are projected once again onto the lab coordinates in the following fashion:

$$\mathbf{B}_{tail} = \int_0^{\ell_{tail}} \begin{bmatrix} (\mathbf{RCR}')_{3\times3} & (-\mathbf{RCR}'\mathbf{S}_{tail})_{3\times3} \\ (\mathbf{S}_{tail}\mathbf{RCR}')_{3\times3} & (-\mathbf{S}_{tail}\mathbf{RCR}'\mathbf{S}_{tail})_{3\times3} \end{bmatrix} \mathrm{d}\ell\,, \tag{4.4}$$

where ℓ_{tail} is the actual length of the tail, i.e. measured along the deformed slender rod. The 3-by-3 square matrix to the upper left corner of the resistance matrix of tail

corresponds to the fluid resistance due to sole rigid-body translations or surface deformations. The matrix **R** denotes the rotation from local Frenet-Serret frames to the common swimmer frame and is specified as:

$$\mathbf{R} = [\mathbf{t}(s,t) \quad \mathbf{n}(s,t) \quad \mathbf{b}(s,t)], \tag{4.5}$$

where the vector **t** denotes the local tangent, the vector **n** denotes local normal and the vector **b** denotes local binormal (see Appendix 5 for details). The matrix **C** contains the local resistive force coefficients, $c_{\{t,n,b\}}$ in diagonal form, which are discussed in section 4.1.3 in detail:

$$\mathbf{C} = \begin{bmatrix} c_t & 0 & 0 \\ 0 & c_n & 0 \\ 0 & 0 & c_b \end{bmatrix}. \tag{4.6}$$

The 3-by-3 matrix to the upper right corner of the resistance matrix, $\mathbf{B}_{tail}$, is responsible for coupling the rigid-body rotations of the swimmer to the translational resistance acting on the tail. The matrix $\mathbf{S}_{tail}$ is the skew-symmetric matrix representing the local cross-products transforming angular velocity vector into linear velocity vector, based on the fact that $\mathbf{\Omega} \times \mathbf{P} = -\mathbf{P} \times \mathbf{\Omega}$, and the negative sign is already taken account for in Eq. (4.4):

$$\mathbf{S}_{tail} = \begin{bmatrix} 0 & -P_z & P_y \\ P_z & 0 & -P_x/\alpha \\ -P_y & P_x/\alpha & 0 \end{bmatrix}, \tag{4.7}$$

where the vector **P** denotes the local position of an arbitrary position on the tail surface, e.g. given for a left-handed helical tail with respect to the center of mass, $[s_{com}\ q_{com}\ r_{com}]'$, of the swimmer as:

$$\mathbf{P} = \begin{bmatrix} \alpha s - s_{com} \\ B(s,t)\cos(\omega_{tail} t - k\alpha s) - q_{com} \\ B(s,t)\sin(\omega_{tail} t - k\alpha s) - r_{com} \end{bmatrix} \tag{4.8}$$

and the local amplitude $B(s,t)$ on the helical tail is given as:

$$B(s,t) = B_o \min(1, s/0.1)\min(1, 0.25/t)\,. \tag{4.9}$$

Here, the first min function in the local amplitude, $B(s,t)$, is responsible for the converging end forming the joint between body and tail. The second min function is the time ramp to attain maximum amplitude throughout the tail. To model a planar wave propagating tail, one would simply set the second or third rows of vector **P** to zero.

The 3-by-3 matrix to the lower left corner of the resistance matrix, $\mathbf{B}_{tail}$, is responsible for coupling the rigid-body translations of the swimmer to the rotational resistance acting on the tail. Thus, an upstream along **s**-direction would eventually rotate the helical tail freely if it is untethered and not actuated. Finally, the 3-by-3 matrix to the lower right corner of the resistance matrix, $\mathbf{B}_{tail}$, corresponds to the fluid resistance, i.e. viscous torque, due to mere rigid-body rotations of the swimmer and its tail.

It is important to note that, the normal component of the resistive force coefficients has no effect on viscous force and torque acting on the swimmer's tail; however, rigid-body translations and rotations in lateral directions are directly affected by the resistive force coefficient in normal direction, c_n, (see Appendix 4 for further details).

The resistance matrix of the swimmer's body, $\mathbf{B}_{body}$, is implemented in a similar fashion to the resistance matrix of its tail, but with a simpler procedure. The resistance matrix is given as:

$$\mathbf{B}_{body} = \begin{bmatrix} \mathbf{D}_T & -\mathbf{D}_T\mathbf{S}_{body} \\ \mathbf{S}_{body}\mathbf{D}_T & \mathbf{D}_R \end{bmatrix}, \tag{4.10}$$

where the resistive force coefficient matrices $\mathbf{D}_T$ and $\mathbf{D}_R$ are given as:

$$\mathbf{D}_T = \begin{bmatrix} D_{T,s} & 0 & 0 \\ 0 & D_{T,q} & 0 \\ 0 & 0 & D_{T,r} \end{bmatrix}, \tag{4.11}$$

and

$$\mathbf{D}_R = \begin{bmatrix} D_{R,s} & 0 & 0 \\ 0 & D_{R,q} & 0 \\ 0 & 0 & D_{R,r} \end{bmatrix}. \tag{4.12}$$

The 3-by-3 skew-symmetric matrix $\mathbf{S}_{body}$ is written for the center of mass of the body, thus the 3-by-3 upper right and 3-by-3 lower left matrices, which are responsible for coupling rigid-body rotations to fluid resistance and coupling rigid-body translations to viscous torque respectively. However, those matrices are equal to zero if the body has a symmetry axis which coincides with the long axis of the tail.

The resistance matrix of the entire swimmer is obtained by superimposing the resistance matrices of body and tail, which are calculated separately. Furthermore, the effective resistance matrix of the swimmer depends on the actuation method, e.g. the resistance matrix of a magnetically actuated swimmer would be different than that of a bacteria-like swimmer.

A single link swimmer, i.e. magnetically driven helical swimmers, has a rigid joint between their body and tail (Tabak *et al*., 2011; Zhang *et al*., 2009; 2010). The entire swimmer is rotated by an external magnetic field, which in turn, leads to six-degrees of freedom to solve for. Thus the effective resistance matrix of the swimmer becomes:

$$\mathbf{B}_{swimmer} = \mathbf{B}_{body} + \mathbf{B}_{tail}. \tag{4.13}$$

A bio-inspired bacteria like swimmer, on the other hand, has a revolute joint allowing body and tail to rotate with different rates in opposite directions (Tabak and Yesilyurt, 2012a; 2012b). This leads to total seven degrees of freedom; however, the rotation of the

helical tail is utilized for the thrust generation. Hence, the number of total degrees of freedom to be solved is reduced to six. Furthermore, the effective resistance matrix of the swimmer is written as:

$$\mathbf{B}^{*}_{swimmer} = \mathbf{B}_{body} + \mathbf{B}^{*}_{tail} . \tag{4.14}$$

where $\mathbf{B}^{*}_{tail}$ is obtained by setting the entire fourth row of the tail resistance matrix, $\mathbf{B}_{tail}$, to zero. Hence the rotation rate of the tail is excluded from the general solution given the fact that the actuation frequency, ω_{tail}, is already known.

4.1.1. Resistance Coefficients for Rigid Bodies of Well-Known Geometries

There are several resistance coefficients for known geometries, i.e. spheres and spheroids, (Perrin, 1934; Berg, 1993; White, 2006); however, Perrin (1934) provided the most complete set for prolate and oblate spheroids known:

$$D_{T,s} = 16\pi\mu \frac{r^2_{body,s} - r^2_{body,\{q,r\}}}{(2r^2_{body,s} - r^2_{body,\{q,r\}})S - 2r_{body,s}}, \tag{4.15}$$

$$D_{T,\{q,r\}} = 32\pi\mu \frac{r^2_{body,s} - r^2_{body,\{q,r\}}}{(2r^2_{body,s} - 3r^2_{body,\{q,r\}})S + 2r_{body,s}} \tag{4.16}$$

for rigid-body translations; and

$$D_{R,s} = \frac{32}{3}\pi\mu \frac{(r^2_{body,s} - r^2_{body,\{q,r\}})r^2_{body,\{q,r\}}}{2r_{body,s} - r^2_{body,\{q,r\}}S}, \tag{4.17}$$

$$D_{R,\{q,r\}} = \frac{32}{3}\pi\mu \frac{r_{body,s}^4 - r_{body,\{q,r\}}^4}{(2r_{body,s}^2 - r_{body,\{q,r\}}^2)S - 2r_{body,s}} \tag{4.18}$$

for rigid-body rotations, with the geometric function S in Eqs. (4.15)-(4.18) as given by:

$$S = \begin{cases} \dfrac{2}{(r_{body,s}^2 - r_{body,\{q,r\}}^2)^{0.5}} \log \dfrac{r_{body,s} + (r_{body,s}^2 - r_{body,\{q,r\}}^2)^{0.5}}{r_{body,\{q,r\}}}, & \Leftarrow r_{body,s} > r_{body,\{q,r\}} \\ \dfrac{2}{(r_{body,\{q,r\}}^2 - r_{body,s}^2)^{0.5}} \tan^{-1} \dfrac{(r_{body,\{q,r\}}^2 - r_{body,s}^2)^{0.5}}{r_{body,s}}, & \Leftarrow r_{body,s} < r_{body,\{q,r\}} \end{cases}, \tag{4.19}$$

4.1.2. Hydrodynamic Effects on the Body Resistance

However, either a perfect sphere or of a complex shape, the effective resistance acting on the swimming robot's body changes drastically with presence of nearby solid boundaries, to which a deliberate correction is required in order to achieve accurate resistance force predictions. Happel and Brenner (1965) elaborated on two distinctive resistance corrections for spherical bodies moving confined to the cylindrical channels; preferably undergoing rigid-body translations parallel to the channel's symmetry axis. The first correction is intended for the upstream, i.e. channel flow, and given as:

$$F_x = -6\pi\mu R_{body} \left\{ U_{body,x} - U_{ch,x} \left[\left(1 - \frac{(R_{ch} - \mathrm{d}_{body})^2}{R_{ch}^2} \right) \left(1 + \frac{R_{body}}{R_{ch}} f_{ecc} \right) - \frac{2}{3} \frac{R_{body}^2}{R_{ch}^2} \right] \right\} \tag{4.20}$$

where $U_{ch,x}$ signifies the channel flow, $U_{body,x}$ is the velocity of the spherical body, and d_{body} is the shortest distance between center of the body to the cylindrical channel wall. Happel and Brenner (1965) provided a look-up table for the eccentricity function, f_{ecc}, as a function of $(R_{ch} - \mathrm{d}_{body})/R_{ch}$, from which the following curve fit is obtained (also see Fig. 4.3):

$$f_{ecc} = 0.0001529e^{11.28(R_{ch}-d_{body})/R_{ch}} - 0.1363((R_{ch}-d_{body})/R_{ch})^{0.6786} + 2.113. \quad (4.21)$$

Here, the average channel flow, $U_{ch,x}$, induced by a translating body confined to a constant cross-section cylindrical tube with closed ends can be predicted as $U_{ch,x} = U_{body,x} \cdot A_{body}/(A_{ch}-A_{body})$ for all practical purposes where A_{ch} is the cross sectional area of the channel and A_{body} is the effective area opposing the fluid in front during forward translation.

The second correction presented by Happel and Brenner (1965) is based on the eccentricity of the spherical body confined to the cylindrical channels of infinite lengths combined with the ratio of the radius of the spherical body to the radius of the channel it is confined to. This correction does not deal with upstream velocity field but regards the direct hydrodynamic interaction between body and channel walls as:

$$F_x = -6\pi\mu R_{body} U_{body} f_{ecc} \frac{R_{body}}{R_{ch}}. \quad (4.22)$$

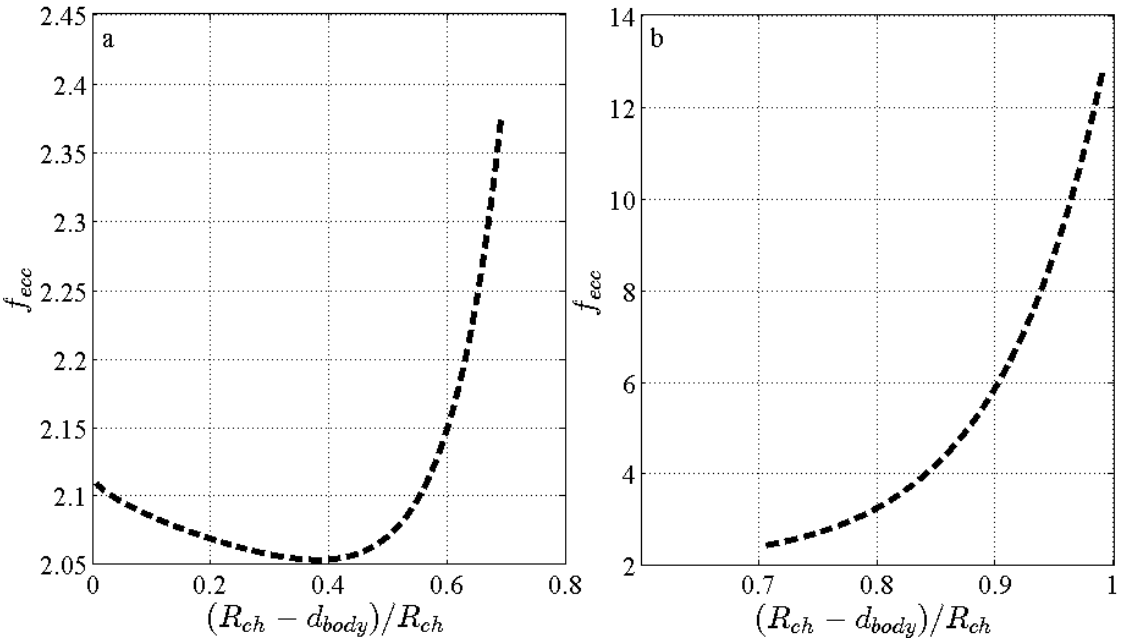

Figure 4.3: Eccentricity function, f_{ecc}.

Further discussion on the effect of local proximity to solid boundaries can be found in (Happel and Brenner, 1965).

Moreover, Tabak *et al.* (2011) presented an approach to handle the presence of channel boundaries by stiffening the resistance matrix elements in accordance with the minimum local proximity. The resistance matrix elements are modified to attain numerical stiffness as the swimmer moves closer to a solid boundary in order to simulate the bouncing-off effect without actually coming into contact.

In order to simulate the bouncing-off effect, an artificial concentric channel with a radius smaller than that of the actual one is implemented numerically. The channel correction is conditionally turned on when the swimming robot penetrates this artificial channel (see Fig. 4.4) and the elements of the resistance matrices are altered as follows:

$$\mathbf{B}_{ij} = \begin{cases} \dfrac{k_{wall}}{(\mathrm{d}_{ch} - \delta)/\mathrm{d}_{ch}} \mathbf{B}_{ij}, & \Leftarrow \delta \neq 0;\ \mathrm{i} \neq \{1,4\} \\ \mathbf{B}_{ij}, & \Leftarrow \delta = 0 \end{cases} \tag{4.23}$$

where δ is the penetration depth of the swimming robot, d_{ch} is the distance between artificial and actual channels, and k_{wall} is the stiffness constant of the artificial channel.

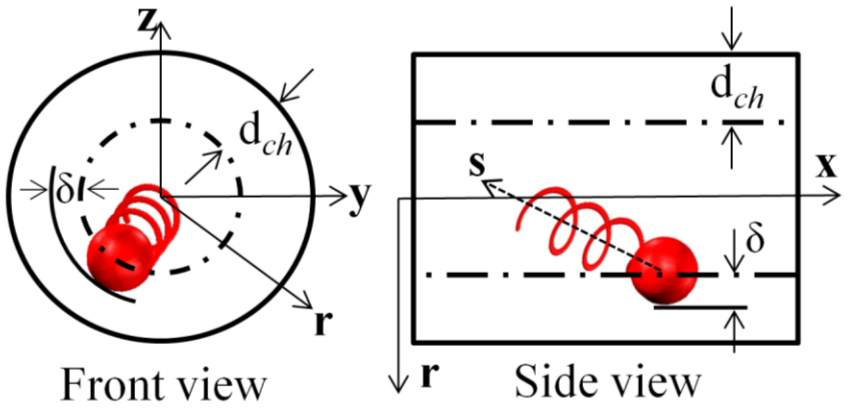

Figure 4.4: The artificial inner channel, demonstrated with dotted line, and the actual channel. Resistance matrices are modified when swimming robot penetrates the artificial channel.

Moreover, the complex flow field induced by the helical swimmer is known to result in hydrodynamic interaction between its body and tail (Keller and Rubinow, 1976; De la Torre and Bloomfield, 1977; Phan-Thien, 1987; Watari and Larson, 2010). One may reinterpret the resistance matrix of the body to incorporate the hydrodynamic interactions with non-zero off-diagonal terms, which would not exist for an otherwise isolated axisymmetric body (Happel and Brenner, 1965). The hypothesized translational resistance matrix, in general form, is:

$$\mathbf{D}_{T,modified} = \begin{bmatrix} D_{T,ss} & D_{T,sq} & D_{T,sr} \\ D_{T,qs} & D_{T,qq} & D_{T,qr} \\ D_{T,rs} & D_{T,rq} & D_{T,rr} \end{bmatrix} \tag{4.24}$$

It will be evident in the next chapter that, indeed, the hydrodynamic interaction (HI) between body and tail requires special consideration, and the resolution relies with modified diagonal elements and non-zero off-diagonal terms in the body resistance matrix, $\mathbf{D}_T$.

4.1.3. Resistive Force Coefficients for a Wave Propagating Slender Rod

The next step is to find out appropriate force coefficients, but accurate calculation of the force coefficients is extremely difficult. Here, a list of coefficient sets provided in literature in order to predict local fluid resistances in unbounded and bounded, i.e. in-channel or near plane wall, viscous mediums.

Several coefficient sets are presented in literature for unbounded viscous medium assumption, and they solely incorporate the effect of wave geometry. Sir Lighthill's (1976) suboptimal local force coefficient set based on SBT analysis is:

$$c_n = c_b = \frac{4\pi\mu}{\ln(0.18\lambda/\alpha r_{tail}) + 0.5}, \tag{4.25}$$

and

$$c_t = \frac{2\pi\mu}{\ln(0.18\lambda/\alpha r_{tail})}. \tag{4.26}$$

The local force coefficient set presented by Gray and Hancock (1977) is:

$$c_n = c_b = \frac{4\pi\mu}{\ln(2\lambda/r_{tail})+0.5}, \tag{4.27}$$

and

$$c_t = \frac{2\pi\mu}{\ln(2\lambda/r_{tail})-0.5}. \tag{4.28}$$

The local force coefficient set presented by Johnson and Brokaw (1979) is:

$$c_n = c_b = \frac{4\pi\mu}{\ln(2\lambda/r_{tail})-0.5}, \tag{4.29}$$

and

$$c_t = \frac{4\pi\mu/1.8}{\ln(2\lambda/r_{tail})-0.5}. \tag{4.30}$$

Resistive force coefficients presented in this section account for the local distance of the center of the tail, d_{tail}, to the channel walls. One fairly detailed conditional coefficient set is presented by Brennen and Winet (1977) as follows:

$$c_b = \begin{cases} \dfrac{4\pi\mu}{\ln(\lambda/r_{tail})+0.193-3\lambda/8\mathrm{d}_{tail}}, & \Leftarrow \dfrac{\lambda}{2\mathrm{d}_{tail}} \le 1 \\ \dfrac{4\pi\mu}{\ln(2\mathrm{d}_{tail}/r_{tail})}, & \Leftarrow \dfrac{\lambda}{2\mathrm{d}_{tail}} > 1 \end{cases}, \tag{4.31}$$

$$c_n = \begin{cases} \dfrac{4\pi\mu}{\ln(\lambda / r_{tail}) + 0.193 - 3\lambda / 4d_{tail}}, & \Leftarrow \dfrac{\lambda}{2d_{tail}} \le 1 \\ \dfrac{4\pi\mu}{\ln(2d_{tail} / r_{tail}) - 1}, & \Leftarrow \dfrac{\lambda}{2d_{tail}} > 1 \end{cases}, \tag{4.32}$$

and

$$c_t = \begin{cases} \dfrac{2\pi\mu}{\ln(\lambda / r_{tail}) - 0.807 - 3\lambda / 16d_{tail}}, & \Leftarrow \dfrac{\lambda}{2d_{tail}} \le 1 \\ \dfrac{2\pi\mu}{\ln(2d_{tail} / r_{tail})}, & \Leftarrow \dfrac{\lambda}{2d_{tail}} > 1 \end{cases}, \tag{4.33}$$

which, considering the distorted symmetry of the induced flow field around the tail due to the presence of a boundary, introduces dissimilar local resistive force coefficients in normal and binormal directions as presented in Eqs. (4.31)-(4.32).

Lauga *et al.* (2006) presented a simpler resistance coefficient set formulated as a subset that of the coefficient set presented by Brennen and Winet (1977):

$$c_n = c_b = \frac{4\pi\mu}{\ln(2d_{tail} / r_{tail})}, \tag{4.34}$$

and

$$c_t = \frac{2\pi\mu}{\ln(2d_{tail} / r_{tail})}. \tag{4.35}$$

4.1.4. Calculating Resistive Force Coefficients with CFD Analysis

In addition to the force coefficients presented in literature, it is possible to calculate resistive force coefficients from CFD simulations. The force and torque values computed

can be employed along with the resultant velocity values, in either time-dependent or time averaged fashion. A simple form, i.e. employing time-averaged values of only velocity and force components in **s**-axis of the swimmer, i.e. $\overline{U}_s$, $\overline{F}_{t,s}$ and $\overline{T}_{t,s}$, without lateral velocities, is represented by Eq. (4.36): the equation is obtained by carrying out the integration in Eq. (4.4) in symbolic form explicitly followed by rearranging as:

$$\begin{bmatrix} \overline{F}_{t,s} \\ \overline{T}_{t,s} \end{bmatrix} = -\alpha L_{tail} \left\{ \begin{bmatrix} B_o^2 k^2 & 1 \\ B_o^2 k & -B_o^2 k \end{bmatrix} \overline{U}_s + \begin{bmatrix} k & -k \\ 1 & B_o^2 k^2 \end{bmatrix} B_o^2 \omega_{tail} \right\} \begin{bmatrix} c_b \\ c_t \end{bmatrix}. \tag{4.36}$$

Thus, the corresponding resistive force coefficient can be obtained by simplifying and rearranging Eq. (4.4) for time-averaged swimming confined to the long axis of the robot. A more general form can be obtained by including all velocity components of rigid-body translation and rotation vectors of the swimmer. Furthermore, Eq. (4.36) can be rewritten in time-dependent fashion to calculate the force coefficients to incorporate any possible transient effects; however, accelerations in viscous flows are beyond the scope of this study.

This method is used for CFD simulations carried out for swimmers moving in unbounded viscous medium for validation of hydrodynamic model. Moreover, the obvious advantage of this method is that all flow fields, interactions and end-effects on the tail are accounted for.

In addition to constant resistive force coefficient pair calculated from a CFD analysis carried out with a single helical tail, a custom coefficient set can be implemented with a novel geometric representation of a rotating helical tail. The helical tail is assumed to be composed of series of tori and rods, i.e. each wave is projected on a single torus and single rod as depicted in Fig. 4.5. The local hydrodynamic forces, which are calculated in the directions of surface tangent, normal and binormal directions, acting on the torus and the rod undergoing rigid-body translation and rotations are utilized in a series of curve fit analyses to formulize the custom force coefficient set. Details of the CFD analysis, curve fit study, and the resultant force coefficients are presented in Appendix 2.

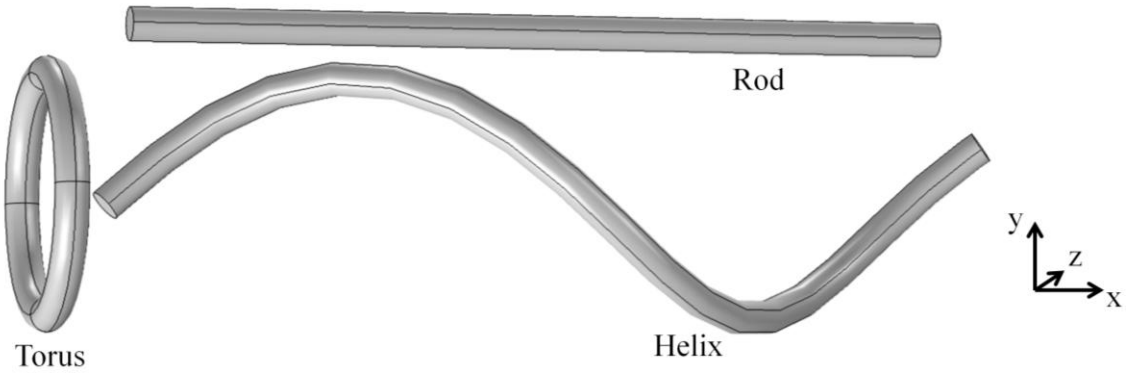

Figure 4.5: Representing a single helical wave with a torus and a rod.

4.1.5. Actuation System Implementation and Solving The Equation of Motion

Finally, the actuation systems are coupled to the hydrodynamic model in order to include the external stimuli acting on the swimmer, either through DC-motor dynamics for the bacteria like robotic prototype or by the effective magnetic torque acting on the body.

4.1.5.1. On-board powered swimmer

The external torque in equation of motion (see Eq. (4.1)) is obtained by means of coupled mechanical and electrical properties of the actuation system, i.e. DC-motor dedicated to rotate the helical tail. All electromechanical properties except rotor friction are experimentally measured: effective battery voltage V(t) and total electrical resistance R(t) are dependent on instantaneous motor current I(t).

Motor current is determined by the following differential equation:

$$\mathrm{L}\frac{\mathrm{dI}(t)}{\mathrm{d}t}+\mathrm{R}(t)\mathrm{I}(t)=\mathrm{V}(t)-\mathrm{K_b}\omega_\mathrm{m} \tag{4.37}$$

where L is the motor inductance, ω_m is the total instantaneous rotational velocity of the DC-motor, and $\mathrm{K_b}$ is the back-EMF constant of the DC-motor (Spong and Vidyasagar, 1989).

Linear relation constant B_{eff} between effective rotational friction, which is dominated by the interaction between prototype robotic swimmer and the channel wall, and the instantaneous rotational velocity of the motor, is computed online by the following equation (Spong and Vidyasagar, 1989):

$$(\mathrm{B}_{eff} + \mathrm{K_b K_m} / \mathrm{R}(t))\omega_{\mathrm{m}} = \mathrm{V}(t)\mathrm{K_m} / \mathrm{R}(t) - T_h(t) \tag{4.38}$$

where $\mathrm{K_m}$ is the torque constant, and $T_h(t)$ is the instantaneous hydrodynamic load on the rotor. It is noted that moments of inertia of swimmer or motor are not included. Once B_{eff} is resolved, the friction torque in equation of motion (see Eq. (4.1)) is given by:

$$\mathbf{T}_{external,\,friction} = \left[-\mathrm{B}_{eff}\omega_{\mathrm{m}} \;\; 0 \;\; 0\right]', \tag{4.39}$$

and the resultant swimming velocity vectors are solved by:

$$\begin{bmatrix}\mathbf{V}\\ \boldsymbol{\Omega}\end{bmatrix}_{swimmer} = -(\mathbf{B}^{*}_{swimmer})^{-1}\left(\mathbf{B}_{tail}\begin{bmatrix}\mathbf{0}_{3\times 3}\\ \omega_{tail}\\ 0\\ 0\end{bmatrix} - \begin{bmatrix}\mathbf{0}\\ \mathbf{T}_{external,\,friction}\end{bmatrix}\right) \tag{4.40}$$

where the inverse of the effective resistance matrix is handled with a special method utilized by Fujimoto (2007) (also, see Appendix 5 for further details).

4.1.5.2. Magnetically driven swimmer

External torque vector in equation of motion (see Eq. (4.1)) is due to the magnetic field, which is generated by Helmholtz coil pairs, applied along the **x**-axis in lab frame. Magnitude of the magnetic field, **H,** along the axis of a single coil is proportional to the current passing through that coil, and given by (Jiles, 1998):

$$\|\mathbf{H}\| = \frac{N\mathrm{I}_{coil} R_{coil}^2}{2(R_{coil}^2 + l^2)^{1.5}} \tag{4.41}$$

where N is the number of turns, I_{coil} is the magnitude of the current, R_{coil} is radius of the Helmholtz coil pairs, l is the distance of the magnetic swimmer from each coil.

The resultant torque felt by the magnetic head of the swimmer is given by:

$$\mathbf{T}_{external,magnetic} = \mathcal{R}^{'} \mu V \|\mathbf{M}\| \|\mathbf{H}\| n_x \sin(\gamma) \tag{4.42}$$

where V is the volume of the magnetic body, μ is the magnetic permeability, and **M** is the magnetization of the magnetic head. The direction of the resultant torque is denoted by the normal vector n_x. The projection of the magnetic field from the lab frame to swimmer frame is handled by the transpose of the rotation matrix, $\mathcal{R}$, implemented based on quaternion rotations (Baraff, 2001) (also, see Appendix 5 for further details). Angle between the external magnetic field and the body is denoted by γ and computed as the integral of the difference between the angular velocities of body and the rotational magnetic field:

$$\gamma = \int_{t_0}^{t_1} (2\pi f_{magnetic} - \Omega_s)\, \mathrm{d}t \tag{4.43}$$

where $f_{magnetic}$ is the actuation frequency of the magnetic field, and Ω_s is the resultant swimmer rotation along **s**-axis, which is initially 0 and updated at each simulation time step beforehand the equation of motion is solved. In the case when the swimmer rotates with the frequency of the magnetic field the angle γ remains constant; however, when the strength of the field is not enough to overcome the fluid's resistance it varies with time. The resultant swimming velocity vectors are solved by:

$$\begin{bmatrix} \mathbf{V} \\ \mathbf{\Omega} \end{bmatrix}_{swimmer} = \mathbf{B}_{swimmer}^{-1} \left(\begin{bmatrix} \mathbf{0} \\ \mathbf{T}_{external,magnetic} \end{bmatrix} \right) \tag{4.44}$$

where the inverse of the effective resistance matrix is handled with a special method utilized by Fujimoto (2007) (see Appendix 5).

Continuous steady torque is sustained by means of the rotating magnetic field as long as the swimmer rotates with the field. When the swimmer loses its synch with the magnetic field, effective torque drops and the swimmer can no longer rotate at the same rate with the field, thus, the propulsion becomes erratic. The maximum frequency that the swimmer can follow without loss of propulsion is called step-out frequency (Tabak *et al*., 2011).

4.1.6. Projecting the Rigid-Body Kinematics onto the Lab Frame

The swimmer velocity and position vector in lab frame, i.e. **xyz**-frame, is calculated with the help of quaternion rotations (see Appendix 5). Resultant velocity vector is given by:

$$\begin{bmatrix} \mathbf{V_{xyz}} \\ \mathbf{\Omega_{sqr}} \end{bmatrix} = \begin{bmatrix} \mathcal{R} & \mathbf{0} \\ \mathbf{0} & \mathbf{I} \end{bmatrix} \begin{bmatrix} \mathbf{V_{sqr}} \\ \mathbf{\Omega_{sqr}} \end{bmatrix} \tag{4.45}$$

where **I** is 3-by-3 identity matrix, and $\mathcal{R}$ is the rotation matrix from swimmer frame to the lab frame. The position of the center of mass of the swimming robot, $\mathbf{X}_{com}$, in swimmer's frame of reference is obtained by:

$$\mathbf{X}_{com} = \int_0^{\tau} \mathbf{V_{xyz}} \, \mathrm{d}t \tag{4.46}$$

and position of an arbitrary location, e.g. on the tail surface, is expressed in the lab frame as follows:

$$\mathbf{P_{xyz}} = \mathbf{X}_{com} + \mathcal{R}\mathbf{P} \, . \tag{4.47}$$

4.2. Slender-Body-Theory (SBT) Models

Slender-body-theory is based on modeling the flow field around a point in space as a hydrodynamic singularity, e.g. point force, which loses its strength in radial direction due to viscous dissipation (Chwang and Wu, 1975; Lighthill, 1996b). The mathematical functions used to represent these singularities are called Stokeslet, (Lighthill, 1976; Brennen and Winet, 1977; Johnson and Brokaw, 1979). Stokeslet functions can be cast to predict the swim velocity of a rotating helical body and the flow field induced by it (Lighthill, 1976; 1995).

Sir Lighthill proposed two distinct solutions to the fluid resistance acting on a helical swimmer based on Stokeslet solutions. In his first analysis, Lighthill (1976) derived resistance coefficients from the distribution of Stokeslets and point forces on an infinite helix in an unbounded fluid. A number of simplifying assumptions are used in the derivation of resistance coefficients. The local normal, c_n, and tangential, c_t, components of the resistive force coefficients are obtained from the Stokeslet representation of the velocity on the tail as follows:

$$c_t = \frac{2\pi\mu}{-\ln\varepsilon - 0.5 + \alpha^2 A_1 + (1-\alpha^2)A_2(\alpha)}, \tag{4.48}$$

and

$$c_n = \frac{4\pi\mu}{-\ln\varepsilon + (2\alpha^2 - 1)A_1(\alpha) + 2(1-\alpha^2)A_2(\alpha)}. \tag{4.49}$$

Here α is the ratio between apparent and actual lengths of the tail; ε is given by a relationship based on tail's radius, r_{tail}, α, and wavelength, λ : $\varepsilon = 5.2 r_{tail}\alpha/\lambda$. A_1 and A_2 are periodic integrals of functions of assumed local flow fields and specified in (Lighthill,

1976) (also see Appendix 8). This new set can also be utilized in resistive-force-theory based hydrodynamic model.

In his second analysis, Lighthill (1976) proposed a more generalized representation, referred as c_x approach within this text, and formulated the fluid resistance along the symmetry axis of a helical swimmer without dealing with local fluid resistances. Furthermore, the forward velocity is formulated with correction for the presence of a towed body, which also allowed prediction of resultant body rotation rate. Final equations are given as:

$$U_x = \lambda C_U (1-\alpha^2)\left[-1-\ln(\varepsilon)+\mathrm{A}_1(\alpha)\right]\chi\omega_{tail}/2\pi\,, \tag{4.50}$$

$$\Omega_x = 4\pi\mu B_o^2 \omega_{tail}\chi C_\Omega \mathrm{L}_{tail}/D_{R,x}\,, \tag{4.51}$$

where ω_{tail} is the tail actuation frequency, $D_{R,x}$ is the rotational drag coefficient of the swimming robot's body in the **x**-axis. C_U and C_Ω are translation and rotation rate correction functions for the swimmer's body, respectively, and χ is the dimensionless torque acting on helical tail. Further details of equations can be found in (Lighthill, 1976). Also, refer to Appendix 8 for detailed derivations.

4.3. Asymptotic Solutions of Stokesian Representation of Bounded Flows

Felderhof (2010) formulated the forward velocity of a helical body which is rotating with an actuation frequency of ω and confined to a cylindrical channel concentrically. Author's analysis is based on the analytical procedure presented by Happel and Brenner (1965) for mobility in cylindrical channels of the form:

$$\mathbf{V} = \nabla\Psi + \nabla\times(\Omega n_x) + r\frac{\partial}{\partial r}(\nabla\Pi) + \frac{\partial\Pi}{\partial r}n_x \tag{4.52}$$

in cylindrical frame, **xrθ**, with harmonic functions (Felderhof, 2010) specified as:

$$\Psi(x,r,\theta,t) = A_{c1}\mathrm{I}_1(kr) + A_{c2}\mathrm{K}_1(kr)\ \sin(kx-\omega t+\theta)\,, \tag{4.53}$$

$$\Omega(x,r,\theta,t) = A_{c3}\mathrm{I}_1(kr) + A_{c4}\mathrm{K}_1(kr)\ \cos(kx-\omega t+\theta)\,, \tag{4.54}$$

$$\Pi(x,r,\theta,t) = A_{c5}\mathrm{I}_1(kr) + A_{c6}\mathrm{K}_1(kr)\ \sin(kx-\omega t+\theta)\,, \tag{4.55}$$

where $A_{c\{1,2,3,4,5,6\}}$ are the coefficients of modified Bessel functions of the first kind, K_1, and second kind, I_1, and are solved with the boundary conditions of no-slip on the surfaces of rotating helical body and cylindrical channel (Felderhof, 2010). Furthermore, in this text, a hydrodynamic interaction coefficient, Υ_x, is included in the final solution to take the effect of a towed blunt body in the forward velocity calculations. Detailed derivation of coefficient matrix and forward velocity is presented in Appendix 8.

5. ANALYSIS OF THE INDUCED FLOW FIELD WITH THE CFD-MODEL

This section presents the base-case rigid-body kinematics of swimmers particularly with planar and helical wave propagations, and focuses on the flow field induced by the helical wave propagation extensively. The numerical studies conclude that the hydrodynamic interaction between body and helical tail is of great importance but a comprehensive quantitative analysis based on the wave and tail geometry is not presented in literature to date. The numerical investigations presented in literature do not include the time-dependent relationship between the velocity and corresponding hydrodynamic force acting on the swimmer's body (Johnson, 1980; Phan-Thien, 1987).

The focus of interest here is the flow field results, which are computed by the CFD-models used to examine the 4 degree-of-freedom motion, of a bacteria-like, i.e. helical, swimmer. The helical swimmer is comprised of a rotating rigid tail and a spherical body with a revolute joint in between. Swimmer is fully submerged in a viscous fluid, which is bounded by a large stationary cylindrical channel. Channel diameter is ten times that of the sphere diameter in order to simulate infinite medium. The time-dependent swimming velocity vector is computed under the condition of zero-net-force-swimming. Resultant flow field surrounding the swimmer is governed by the time-dependent Navier-Stokes equations subject to continuity, i.e. conservation of mass.

Distinct counter rotating forward and backward flows emerge surrounding the swimmer. Based on hydrodynamic interaction between these flow fields, fluid resistance on swimmer's body and tail are coupled in time-domain. It is observed that the resistance on the body differs from analytical predictions under the influence of the rotating tail, and a modified resistance approach, which greatly depends on the wave geometry, is needed.

Furthermore, the hydrodynamic interaction leads to a phase-shift between instantaneous lateral velocity of the swimmer and the corresponding fluid resistance

exerted on its body. Given the complicated shape of the tail, conventional diagonal resistance matrix approach for axisymmetric rigid particles moving in viscous flows is not appropriate to account for such effects acting on the surface of swimmer's body. In this study, hydrodynamic interaction (HI) coefficients are introduced on the diagonal and off-diagonal terms of the resistance matrix of the body to compensate the complex flow field interactions in analytical calculations. Moreover, inspection is carried out on the relationship between HI-coefficients and tail geometry with parameterized wave length and amplitude, and observed that hydrodynamic interaction (HI) coefficients are more sensitive to the former.

In addition to the hydrodynamic interaction within helical swimmers, similar interaction is detected in the kinematic results of the swimmers with planar wave propagations. The kinematic validation reveals that the rigid-body rotations due to the hydrodynamic torque induced by plane wave propagation induce rotational flow around the body decreasing its effective rotational resistance, as will be described in the next section.

5.1. Kinematic Analysis on the Base-Case Design

This section deals with pure kinematics of the rigid-body motion of an isolated swimmer fully submerged in a viscous fluid. It is numerically observed that the instantaneous lateral velocity is comparable with the forward velocity in magnitude albeit has a zero time-average. Swimmer's trajectory is strictly confined to a plane with strictly planar wave propagations; however, extends to the third dimension with helical wave propagation. In a sense, planar wave propagation is considered as a subsection of helical wave propagation in the sense of rigid-body kinematics.

5.1.1. Helical Wave Propagation Results

Figure 5.1 shows the swimming velocity vector of the robot with base-case parameters, i.e. B_o = 0.1 and λ=2/3, and demonstrates the trajectory of the micro robot in the channel frame. Forward velocity V_x (see Fig. 5.1a) and body rotation rate Ω_x (see Fig. 5.1c) reach to a virtually steady value as the initial ramp is satisfied and wave amplitude reaches to maximum. Lateral velocities, on the other hand, depict steady periodic behavior by sinusoidal waves with zero time-average. The π/2 phase between V_y and V_z observed in Fig. 5.1b suggests a three dimensional time-dependent trajectory, $\hat{S}(t)$, for the swimmers with rotating helical tails, as already suggested by Keller and Rubinow (1976), Frymier and Ford (1997), Corkidi *et al*. (2008), and Hsu and Dillon (2009).

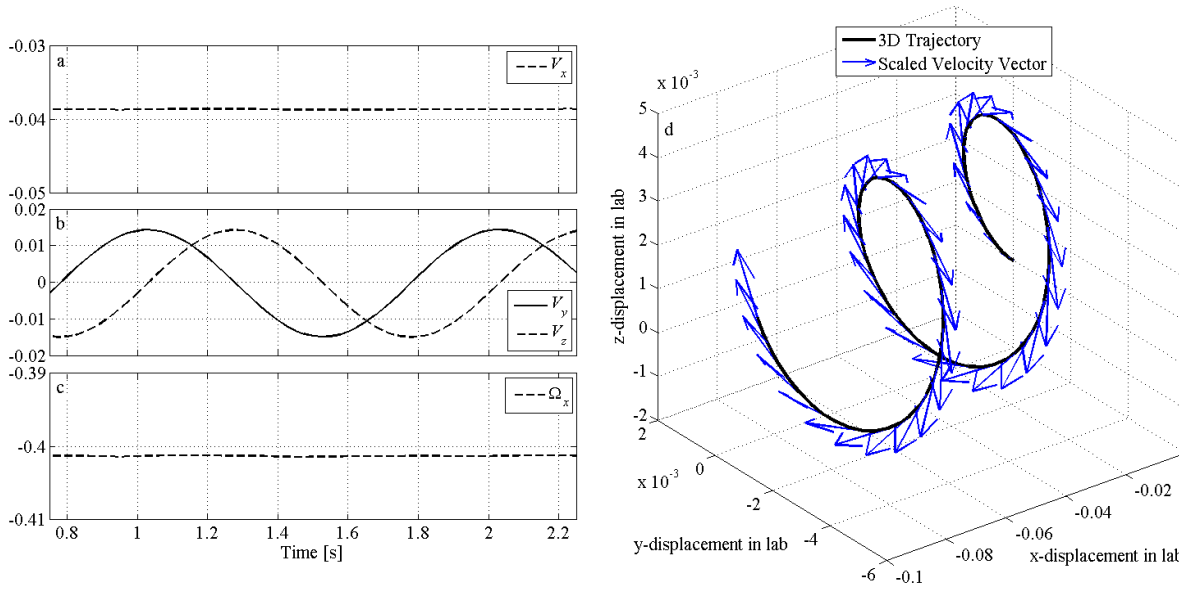

Figure 5.1: Time dependent velocity vector and rigid body translation of the helical swimmer's center of mass: Forward velocity of the micro robot (a); lateral velocities of the micro robot (b); body rotation rate (c); helical trajectory of the swimmer in channel frame **xyz** (d). Tangent velocity vectors are scaled by 0.5 and depict the velocity of the swimmer's center of mass at each **xyz**-position inside the bounding channel.

Figure 5.1d shows the three dimensional trajectory of the swimming micro robot's center of mass with scaled velocity vectors tangent to swimmer's path in the channel frame, **xyz**. It is noted that elimination of lateral rotations of the swimmer leads to swimmer frame, **sqr**, and lab frame, **xyz**, coinciding for the duration of simulations, as discussed earlier.

5.1.2. Planar Wave Propagation Results

Planar wave propagation is a special case of helical wave propagation. Figure 5.2 presents the rigid-body velocity vector of the swimmer with planar wave propagating tail. The magnitude of the forward velocity is half that of the helical swimmer (see Fig. 5.2a), and one of the lateral degrees of freedom is cancelled due to the symmetry of the induced flow field induced by the planar wave propagation (Tabak and Yesilyurt, 2007a; 2010a; 2010b) (see Fig. 5.2b). Swimmer's body does not rotate around the long axis because no **x**-rotation is induced; however, the entire swimmer rotates along the **z**-axis with Ω_z where there is no deformation on the tail (see Fig. 5.2c).

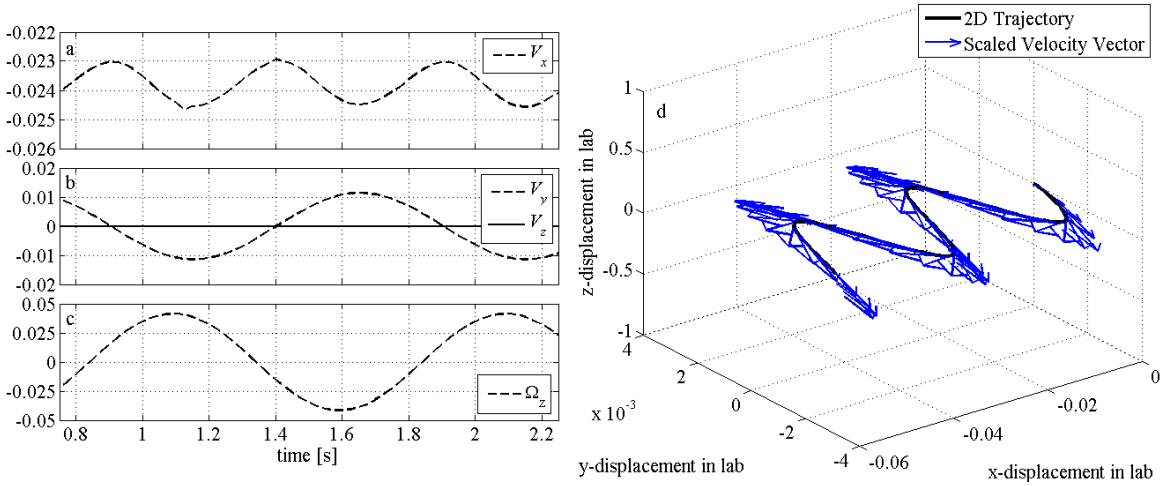

Figure 5.2: Time dependent velocity vector and rigid body translation of the planar wave propagating swimmer's center of mass: Forward velocity of the micro robot (a); **l**ateral velocities of the micro robot (b); body rotation rate (c); 2D trajectory of the swimmer in channel frame **xyz** (d). Tangent velocity vectors are scaled by 0.5 and depict the velocity of the swimmer's center of mass at each **xyz**-position inside the bounding channel.

Provided that the rigid-body rotations are confined to **xy**-plane, the swimmer's trajectory is two dimensional (see Fig. 5.2d). However, this result is contradictory to the 3D traction results of the sperm swimming presented by Corkidi *et al*. (2008) provided that the tail deformation in the CFD simulation is imposed with respect to a rigid joint between body and tail of the swimmer. Trajectory of swimmer's center of mass is represented by the black line and the position dependent velocity vectors are represented by blue arrows in Fig. 5.2d.

5.2. Analysis of the Flow Fields Induced by Helical Wave Propagations

Figure 5.3a demonstrates a layer of the **x**-component of flow field circulating around the swimmer. Forward flow field with a magnitude of 0.02 in negative **x**-direction (light isosurface) is induced by the no-slip boundary condition imposed on swimmer boundaries following rigid-body translations of the swimmer, whereas backward flow field with a magnitude of 0.09 in positive **x**-direction (dark isosurface) is generated by the rotating tail's pump-effect, which will be explained in detail in the following section.

The total 3D flow field induced by the helical swimmer is depicted in Fig. 5.3b by dense streamlines captured at t = 1.975 s: given the no-slip boundary conditions imposed on swimmer surfaces, i.e. the rigid-body rotations of swimmer's body and tail, the surrounding fluid is forced to swirl.

Streamlines presented in Fig. 5.3b depict how the flow field, which is relative to the swimmer, is perturbed by the rotation of swimmer's body and tail: streamlines follow the symmetry axis of the channel from the inlet where they start, virtually parallel to the **xy**-plane till twisted by the swimmer. The effect of rigid-body rotations are contained in a three dimensional space narrow in diameter around the swimmer where hydrodynamic interaction between body and tail actually takes place. However, the complexity of the three dimensional streamlines indicate the necessity for two dimensional flow field analyses. Furthermore, the direction of the streamlines at the back of the swimmer is subject to the instantaneous lateral velocity, e.g. in the positive **y**-direction at t = 1.975 s.

Figure 5.3c demonstrates with normalized 3D arrows, in a more simplified approach, that the rotation of body and tail induce counter rotating, i.e. tangential, flow fields around the swimmer, away from the revolute joint between the body and tail. The normalized arrows depicted in Fig. 5.3c indicate that the distinct flow fields induced by body and tail would run into each other around the revolute joint, thus leading to the complex flow field presented in Figure 5.3b, hence hydrodynamic interaction.

5.2.1. Effect of Body Geometry on the Induced Flow Fields

According to CFD simulations, the fluid resistance on swimmer's body is affected greatly by the flow field which is induced by the pump-effect of the rotating tail. Figure 5.4 depicts the effect of tail rotation in detail revealing the hydrodynamic interaction (HI) between swimming robot's body and its rotating tail. In order to single out the influence of tail rotation, bodies with and without rotating tails are studied by means of resultant flow fields.

First, a time-dependent velocity vector is imposed on the surface of an isolated spherical body submerged in an unbounded viscous medium. The velocity vector is identical to that obtained from the base-case CFD-model which is represented in Fig. 5.1. Resultant streamline profile represents the flow field on **yz**-plane around the moving and rotating sphere, at t = 1.275 s (see Fig. 5.4a). Depicted flow field is symmetrical with respect to **x**-axis since the instantaneous **y**-velocity, V_y, is zero at t = 1.275 s.

Next, a non-rotating helical tail is placed on the right hand side of the sphere as presented in Fig. 5.4b. Boundary conditions on the non-rotating helical tail are set identical to that of the spherical body except for the rigid body rotation, thus the entire swimmer is being dragged through the viscous fluid. The streamlines depicting the flow field around the sphere becomes less dense signifying decreased viscous drag. Moreover, the viscous friction at the back of the body is partially distributed over the helical tail, and, although the total fluid resistance is increased, the resistance on the sphere is slightly decreased (see Table 5.2).

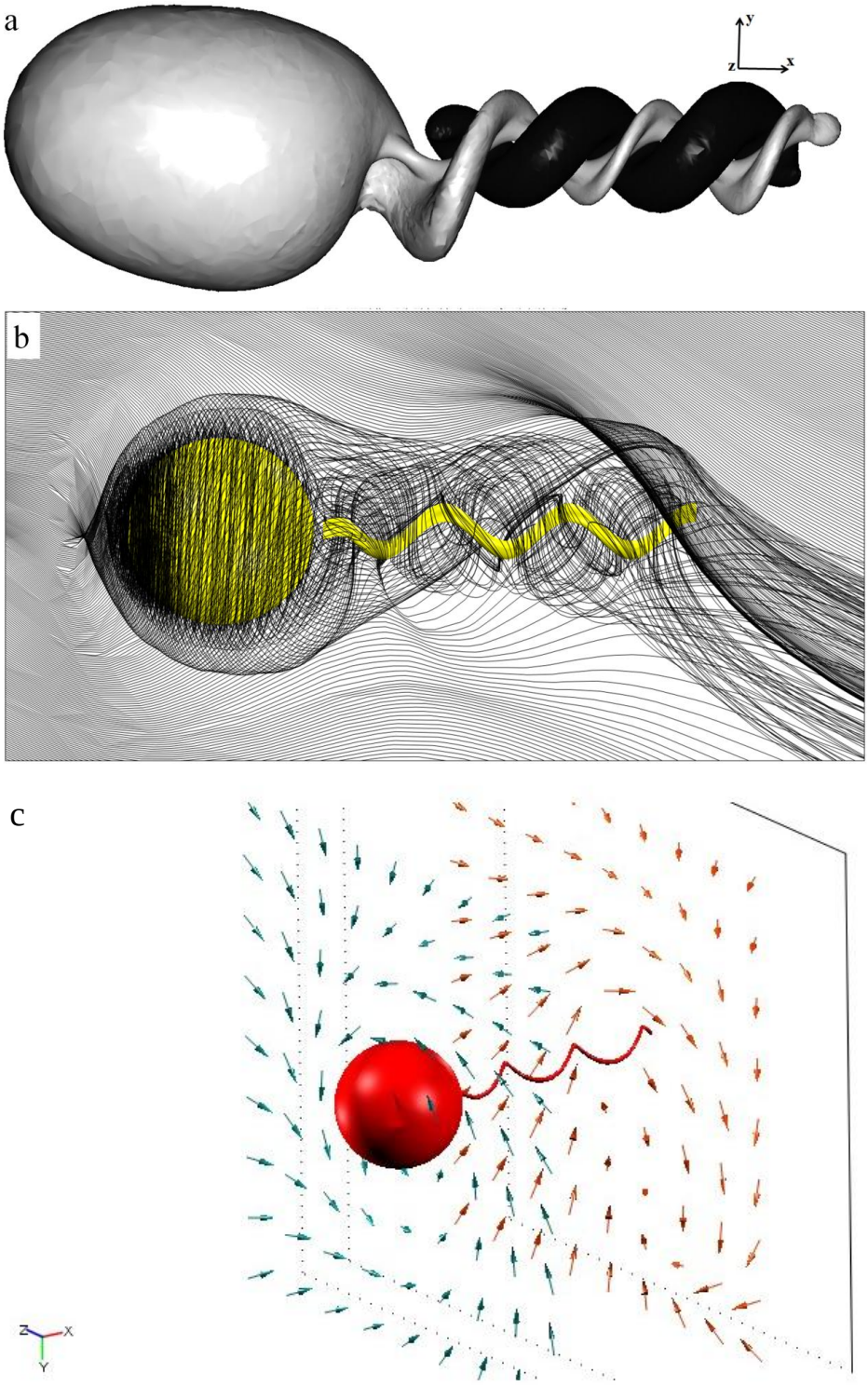

Figure 5.3: Flow field induced by the helical swimmer: the **x**-component of the induced flow field, fully enclosing the two link swimmer (a); 3-dimensional flow field around the swimmer (b); tangential flow fields induced by the body and helical tail (c). Figures demonstrate the instant t = 1.975 s.

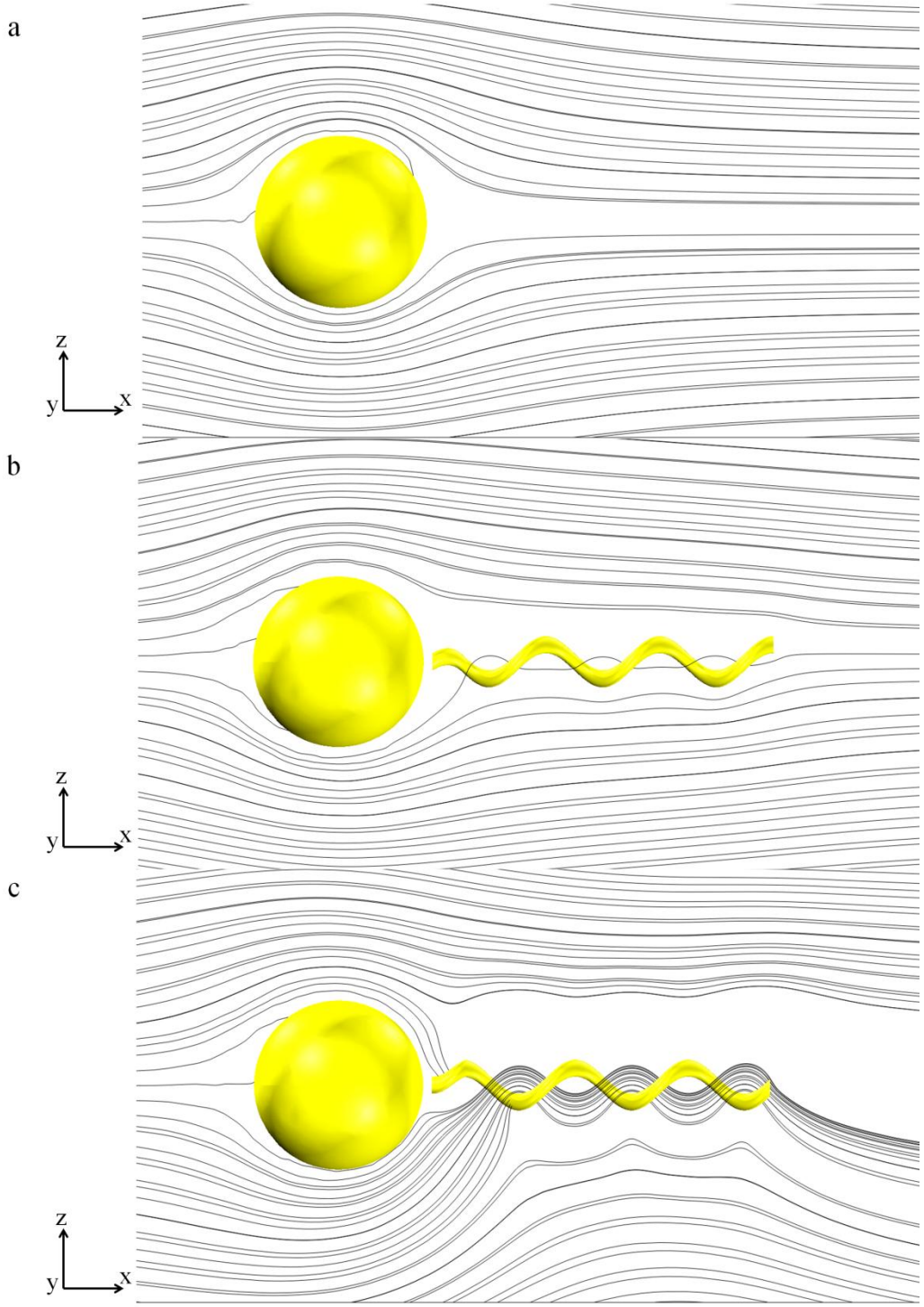

Figure 5.4: Effect of tail rotation on the flow field: depicted by thin black streamlines on **xy**-plane with the swimming velocities presented in Figure 5.1 imposed as boundary conditions; isolated spherical body (a); spherical body with non-rotating helical tail (b); spherical body and helical tail, which rotate with Ω_x and ω_{tail}, respectively (c). Streamline profiles are captured at t = 1.275 s while instantaneous **y**-velocity of the swimmer is zero.

However, when the helical tail is allowed to rotate with an angular velocity of ω_{tail} on its long axis, the streamline density around the body increases considerably (see Fig. 5.4c). This phenomenon is, in effect, a substantial increase in the velocity gradient due to normal stress build up at the back of the spherical body amplifying the net fluid resistance in the **x**-direction (see Table 5.2). The rotational flow field driven by the pump-effect is also evident through the streamlines running down the **x**-axis of the helical tail: streamlines behind the body are forced to follow the long axis of the helical tail and purged at the back of the swimmer.

The relation between the geometry of the swimmer's body and the induced flow field is further studied with two axisymmetric bodies. First, a prolate spheroid having a long semi-axis 2.15 times as long as short semi-axis of it is inspected. The CFD-model is solved for three cases: isolated spheroid (see Fig. 5.5a), spheroid with non-rotating helical tail (see Fig. 5.5b), and spheroid with helical tail, which is rotating with the angular velocity of ω_{tail} (see Fig. 5.5c). Second, the prolate spheroid is replaced with a body of streamlined-profile with respect to pointed-ends on both sides, which was suggested by Bourot (1974) and to have less viscous resistance in contrast with a perfect sphere of same volume (also see Hinojosa and Martel (2005)). Similar to the study carried out for prolate spheroid, CFD simulations are conducted for isolated streamlined body (see Fig. 5.5d), streamlined body with non-rotating tail (see Fig. 5.5e), and streamlined body with rotating tail (see Fig. 5.5f). In all cases, the short-axis of the studied body is equal to the radius of the perfect sphere presented in Fig. 5.4. Furthermore, detailed information on the geometry of the latter body can be found in (Bourot, 1974).

The boundary conditions on both geometries are exactly the same as that imposed on the spherical body. The mesh quality, i.e. maximum element size, is also identical that of the simulations conducted with spherical body.

The average forward and maximum lateral resistance force values for bodies without a helical tail are directly calculated with the CFD-model as presented in Table 5.3, and later used to single out the effect of rotating and non-rotating helical tails, respectively, by carrying out CFD simulations with boundary conditions presented with Eq. (5.3)-(5.5). The thin black streamlines surrounding the bodies without helical tail, which are calculated at time t = 1.275, are presented in Figs. 5.5a,d depicting the flow field on **xz**-plane;

streamlines separate from the surface of the body towards the end due to the boundary conditions.

It is observed in Figs. 5.5b,e , which illustrate the streamlines around the body with an attached non-rotating rigid tail, that under the influence of the tail the streamline density further decreases near the revolute joint at the back of the body. Hence, the forward and lateral drag values slightly decrease while rotational resistance remains unchanged (see Table 5.3).

Figures 5.5c,f , however, clearly demonstrate that the rotation of the tail disturbs the flow field around the body compressing the streamlines towards the body regardless of its shape and profile. Increasing spatial density in streamlines points out the additional shear acting on the body on the direction opposite to the propulsion, while decreasing the lateral drag of the body by assisting its instantaneous lateral translation (see Table 5.3).

5.3. End-Effects on Helical Tail

The resistive force theory approach is viable to calculate the drag force per unit length on a deformed slender body, which is carrying out creeping motion while fully submerged in a viscous fluid. Thus, in the following study, corresponding local force distribution on the swimmer's rotating helical tail is resolved by projecting the **xyz**-forces computed by CFD-model in channel frame onto the local Frenet-Serret coordinates signified as **tnb** (see Fig. 5.6 and Appendix 5) with local tangential, **t**, normal, **n**, and binormal, **b**, vectors (Hanson and Ma, 1994; Hanson and Ma, 1995) and given by:

$$\boldsymbol{\sigma}_{\mathbf{tnb}} = \begin{bmatrix} \mathbf{t} & \mathbf{n} & \mathbf{b} \end{bmatrix}^{-1} \boldsymbol{\sigma}\big|_{\mathbf{x},tail}, \tag{5.1}$$

where $\boldsymbol{\sigma}$ signifies the total stress on the tail surface exerted by the surrounding flow field (Landau and Lifshitz, 2005b), whereas total local velocity vector is calculated with the help of Eq. (5.2) as:

$$\mathbf{U_{tnb}} = \begin{bmatrix} \mathbf{t} & \mathbf{n} & \mathbf{b} \end{bmatrix}^{-1} \mathbf{U_{x,tail}}\,, \tag{5.2}$$

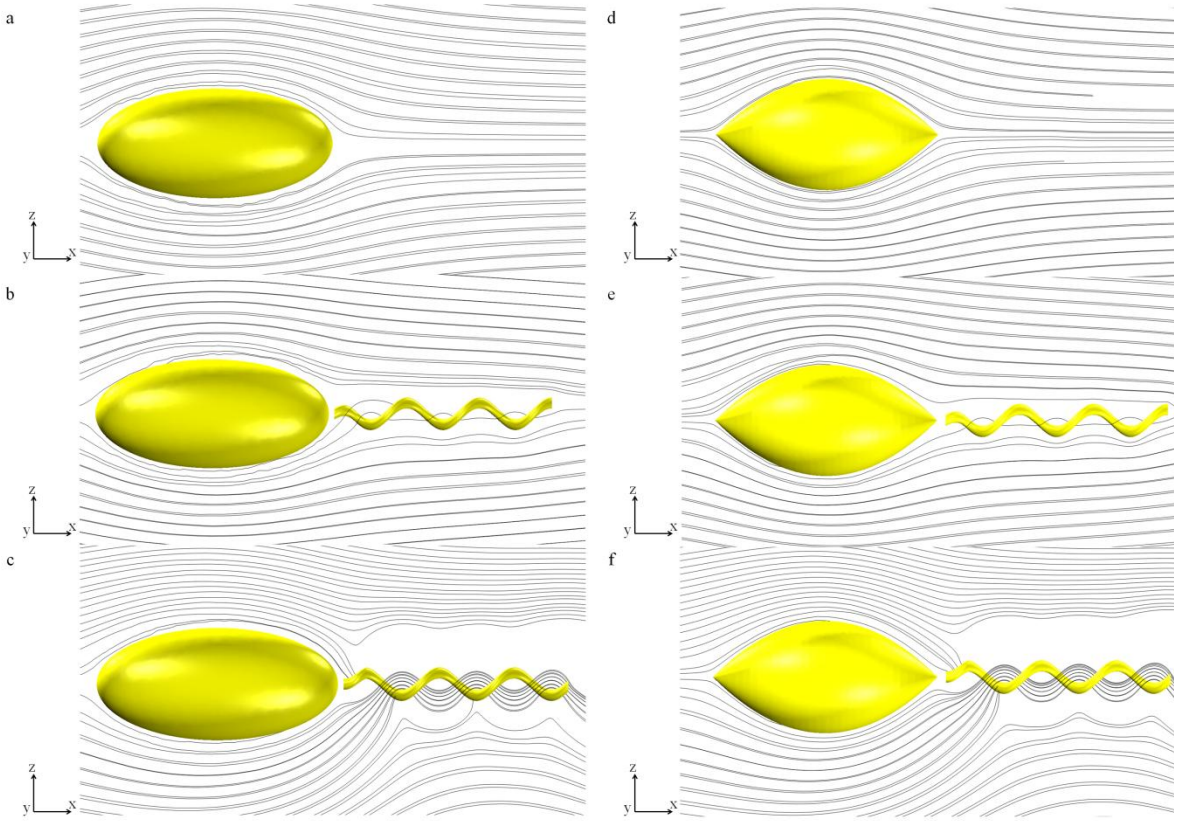

Figure 5.5: Effect of tail rotation on the flow field, with different body geometries: around a prolate-spheroid (a-c) and the body with streamlined profile as suggested by Bourot (1974) (d-f) depicted by thin black streamlines on **xy**-plane: single body (a-d); body with non-rotating helical tail (b-e); body and helical tail, which rotate with Ω_x and ω_{tail}, respectively (c-f).

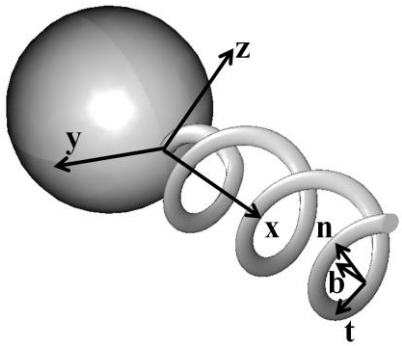

Figure 5.6: Local Frenet-Serret frames (**tnb**) on helical tail and swimmer frame (**xyz**). Normal direction is perpendicular to the long axis, i.e. **x**-axis, of the helix, tangent direction has no **x**-component except for the converging end, and the binormal direction coincides with **x**-axis.

Simple resistive force calculations based on the linear relationship $F_j = c_j U_j$ with $j = \{t,n,b\}$ (Gray and Hancock, 1955) are carried out in order to predict the force distribution per unit length on the helix to single out the additional hydrodynamic effects rendered by full Navier-Stokes solutions in CFD-model. Local tangential, normal and binormal fluid resistance forces exerted per unit length of the helical tail at $t = 1.975$ s are presented in Fig. 5.7. The linear relationship constants are determined via solving the inverse problem of 'suitable coefficient to predict the local flow resistance': the force coefficient, c_t, between local tangential velocity and local tangential fluid resistance is 530 (see Fig. 5.7a), whereas constants c_n and c_b are determined to be 730 by visual inspection as depicted in Figs. 5.7b-c.

The effect of converging end is predicted fairly well; however, body-tail interaction is evident on binormal resistance force plots as given in Fig. 5.7c. Furthermore, the local jump in the normal drag force depicted in Fig. 5.7b arises due to the discontinuity caused by the local ramp function embedded in the local wave amplitude function. On the other hand, end-effects on the trailing-edge are not fully resolved by resistive-force-theory approach as observed in Fig. 5.7, which suggests that the fluid resistance near the free end is partially dependent on the local surface velocity, and that the flow field coming out at the back of the swimmer is also introducing additional drag near the free end of the helix.

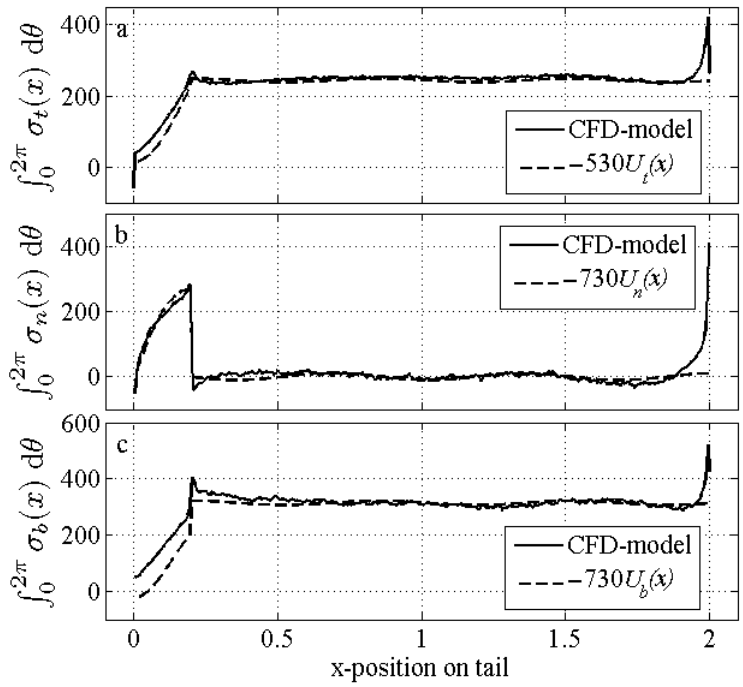

Figure 5.7: Local force distributions per length on the helical tail: CFD-based local tangential force distribution compared with $-c_t U_t(x)$ (a), CFD-based local normal force distribution compared with $-c_n U_n(x)$ (b); CFD-based local binormal force distribution compared with $-c_b U_b(x)$ (c), at t = 1.975 s.

In effect, resistive-force-theory approach predicts the lateral drag force at the middle section of the finite-length tail where fluid resistance occurs solely due to surface velocity as also portrayed through **y**-force and **z**-force distribution in Fig. 5.8. However, presence of a spherical body affects local lateral force distribution on the converging end within its 5 per cent in length as depicted in Fig. 5.8.

Furthermore, end-effects are evident near the free-end of the helix. Results also imply that if the tail was infinite in length than the net lateral force would vanish leading to zero lateral motion, thus, resistive-force-theory would be sufficient as earlier discussed by Johnson (1980). It is noted that the linear relation coefficients used to predict the local force values per unit length in lateral directions as presented in Fig. 5.8 are determined as $c_y = c_z = 650$ by solving the inverse problem.

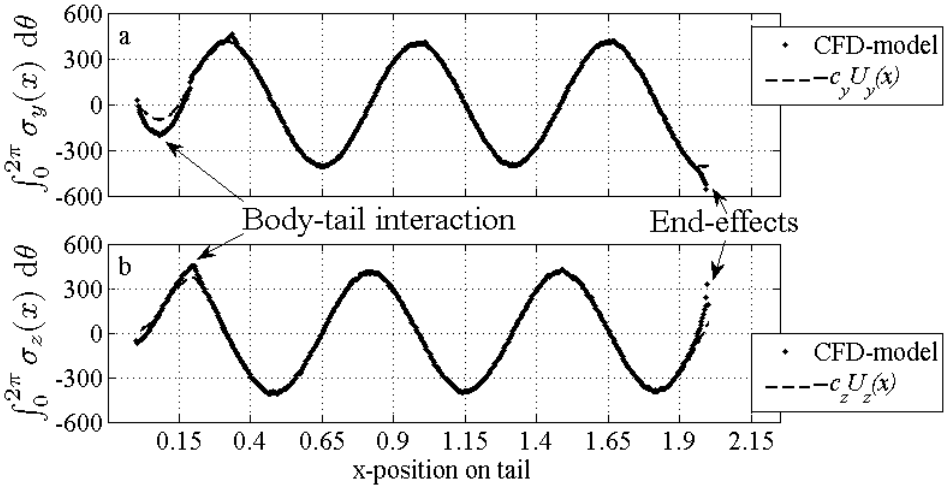

Figure 5.8: CFD-based lateral viscous resistance vector on tail: effective **y**-drag distribution per unit length compared with $-c_y U_y(x)$ (a); effective **z**-drag distribution per unit length compared with $-c_z U_z(x)$ (b), on helix shaped rotating tail at t = 1.975.

Local fluid resistive force coefficients insofar presented in literature are analytically derived for infinite length filaments based on Stokesian flow conditions and strongly depend on the wave geometry (Lighthill 1976; Gray and Hancock 1977). Table 5.1 presents a comparison on local resistive force coefficients based on the CFD-model presented here and the ones calculated from literature. It is noted that, binormal resistive force coefficients are equal to the normal resistive force coefficients; a condition subject to the symmetry of the local flow field around the helical tail, which is no longer applicable with presence of a nearby solid boundary (Brennen and Winet, 1977).

Table 5.1: Resistive force coefficient (RFC) comparison

RFC source	$\{c_t, c_n, c_b\}$
Gray and Hancock (1977)	{226,332,332}
Johnson and Brokaw (1979)	{251,452,452}
Lighthill (SBT-based set) (1976)	{538,781,781}
Lighthill (sub-optimal set) (1976)	{522,737,737}
CFD-based coefficient set (Figure 5.8)	{530,730,730}

5.4. The Pump-Effect of Helical Wave Propagation

A rotating but otherwise anchored helical tail submerged in viscous fluids would act as a pump (Raz and Avron, 2007; Tabak and Yesilyurt, 2008; Koz and Yesilyurt, 2008). However, if the anchoring force is released, the momentum exerted on the surrounding viscous domain via tail rotation is transformed into net thrust partially. A rotating rigid helix would translate forward with the negative of the wave propagation velocity if completely embedded in a solid. However, given the fact that the wave propagation velocity is simply bigger than the forward propulsion velocity, rotating tail would propel itself while keep pushing the flow on the opposite direction. Thus the mechanical energy transferred into the surrounding fluid is dissipated simultaneously by the hydrodynamic drag on the entire surface of moving swimmer and by the back-flow driven by the pump-effect of the tail in the direction of wave propagation (also see Fig. 5.3a).

Swimming robot moves mainly with the hydrodynamic force acting in the normal directions of the rotating helical tail's surface (Gray and Hancock, 1955). The fluid is pushed by the rotating boundary; however, the velocity of the back-flow decreases drastically away from the surface of the helical tail due to excessive shear loss. Hence, the swimmer is not pushed by the inertial effects of the backflow; however, the induced pressure force constitutes the half of the binormal force acting on the helical tail (see Figs. 5.7c and 5.9d). Furthermore, rotation of the backflow is due to the tangential component of the fluid resistance acting on the helical tail. In effect, the pump-effect is a direct result of the rotation of helical tail and, also, is responsible for the discrepancy between analytical and numerical fluid resistance calculations in forward and lateral directions carried out for the towed body.

Body and helical tail of the swimming robot undergo rigid-body rotations separately, inducing consecutive rotational flow fields due to the no-slip condition of the entire swimmer surface. These distinct counter rotating forward and backward flow fields emerge interacting with one another. Based on the hydrodynamic interaction between these flow

fields and the amplified normal stress in the long axis of the tail, fluid resistance on swimmer's body and tail are coupled. Hence, the effective fluid resistance acting on the swimmer's body is associated with the surrounding flow field, which is perturbed by the rotating tail. It is observed that the resistance on the body differs from analytical predictions under the influence of the rotating tail, and the modified resistance values greatly depend on the wave geometry.

Pressure field induced by the swimmer's rotating helical tail is depicted in Fig. 5.9: high and low pressure zones are wrapped around the tail with a matching helical profile as illustrated in Fig. 5.9a; however, it is observed that these pressure fields do not encapsulate swimmer's body but come to a sudden halt right at the back of it. Isosurfaces portrayed in Fig. 5.9a show that the pressure zones symmetrically circle the helix. Figures 5.9b-d demonstrate the pressure force distribution per unit length, which is computed by integrating the dimensionless static pressure on the tail surface over its circumference with respect to its surface normal components n_j in local Frenet-Serret coordinates.

It is also demonstrated that the induced pressure, p, has no contribution to the fluid resistance along the local tangential direction on the tail surface (see Fig. 5.9b), while a pressure build up, thus the amplified normal stress along the **x**-axis is numerically confirmed in the binormal direction (see Figs. 5.9c-d). Moreover, end-effects induce additional pressure force per unit length along the binormal and normal directions near free tip of the helix as depicted in Figs. 5.9c-d, while normal pressure distribution has a local jump owing to the discontinuity of spatial ramp marking the converging end. It is noted that half of the fluid resistance on the local normal and binormal directions are due to pressure force as presented in Figs. 5.7b-c and Figs. 5.9c-d.

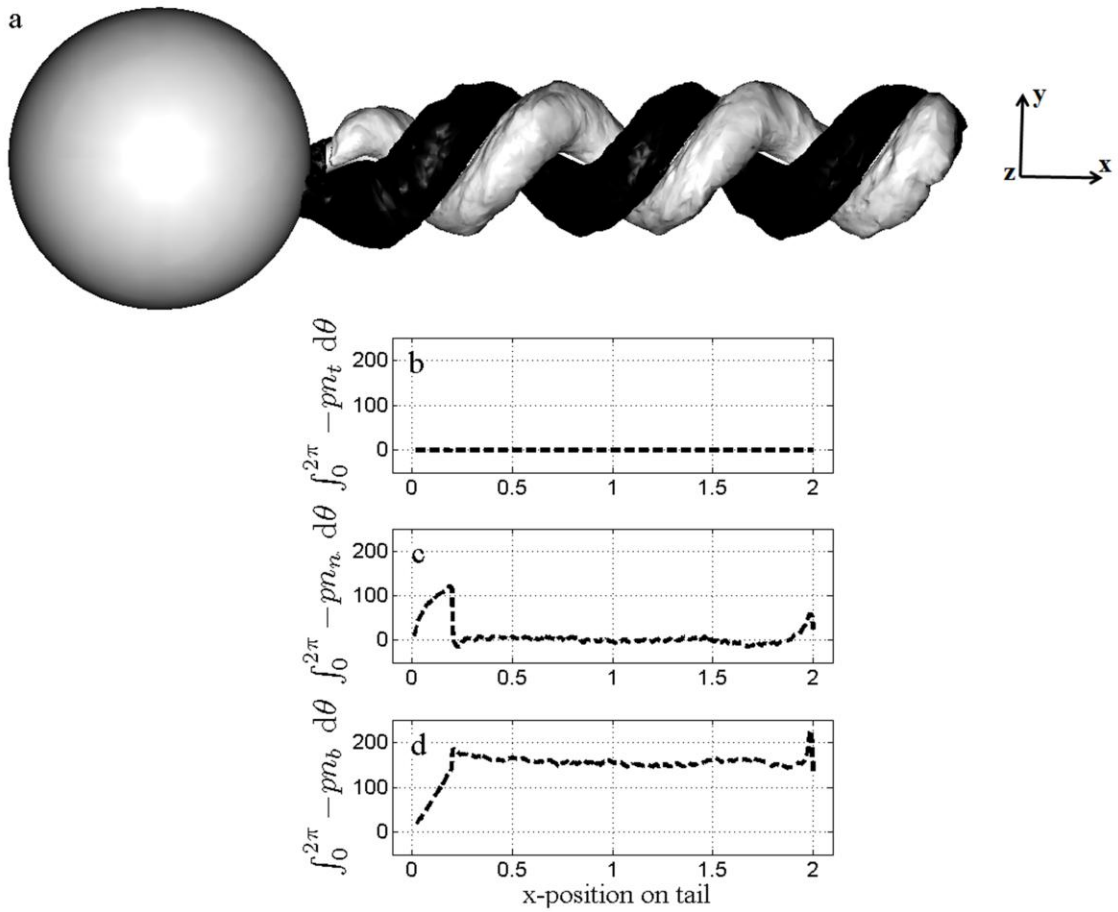

Figure 5.9: Pressure field and pressure force distribution along the tail: Pressure field with dark isosurface signifying high pressure field 100 in magnitude (gauge), and light isosurface signifying low pressure field -100 in magnitude (gauge) (a); pressure force distribution per unit length presented in tangential (b), normal (c), and binormal (d) directions, resolved at t = 1.975 s.

5.4.1. Vortex Formation

The flow field around the swimmer is induced due to the rigid-body rotations of the tail and the body. The fluid around the body (see Fig. 5.10a) is forced to rotate due to no-slip boundary conditions. Resultant tangential flow diminishes in radial direction due to viscous loss. Similarly, a tangential flow is wrapped around the helical tail. Flow field around the clockwise rotating swimmer body has a magnitude of 0.0125 (see the light isosurface in Fig. 5.10a). The counterclockwise rotating tail invokes an enclosing flow field

with a matching helical profile 0.25 in magnitude (see the dark isosurface in Fig. 5.10a); flow field around the tail is stronger because of the fact that the rotation rate of the swimmer's body is smaller than the rotation rate of the tail.

Furthermore, the rotation of the helical tail induces a rotating axial flow, which is trapped next to the long axis of the tail in radial direction. Given the wave velocity, $\lambda\omega_{tail}/2\pi \cong 0.6$, is bigger compared to the forward swim, $V_x \cong 0.04$, the rotating tail actually pushes the viscous fluid in the direction of wave propagation as already depicted in Fig. 5.3a. This highly localized stream running down the long axis of the tail (see Fig. 5.10a) is also a rotational flow field due to the no slip boundary conditions imposed on the tail. In comparison with the abruptly diminishing **x**-component, the tangential component of the flow field dies out behind the helical tail given that the influence of the rigid-body rotation dissipates slower with viscous effects (see Fig. 5.10a).

Gradient of the local flow field has the highest value along the circumference of the forced vortex and the tangential flow component completely diminishes at the center where **x**-velocity attains its largest value, therefore leading to the clockwise rotation of the stream presented in Fig. 5.10a. Figure 5.10b illustrates the flow-field induced by the rotating tail as slices of normalized arrows at six different locations along **x**-axis on deformed tail. Each slice is evenly spaced and depicts the flow field in a local circular zone with a non-rotational center on the **yz**-plane. Further inspection of these non-rotational centers reveals that the circulating jet coincides with a forced vortex, which is forming as a mirror image to the cross-section of the helical tail with respect to its long axis as demonstrated in Fig. 5.10b.

The forced vortex formation observed in CFD solutions confirms the flow field results presented by Lighthill's (1996) based on Stokeslet analysis on a helical tail, in which he also concluded that the torque exerted on the fluid leads to vortex formation located close to the tail and perpendicular to its long axis. Lighthill demonstrated that the induced field should change its direction of flow on the plane perpendicular to the long axis near the center of the helical tail. Furthermore, he argued that the induced force field, which is signified by Stokeslets, manifests localized flow fields in the direction of wave propagation. However, Lighthill's analysis focused on an infinite length tail without a body being towed.

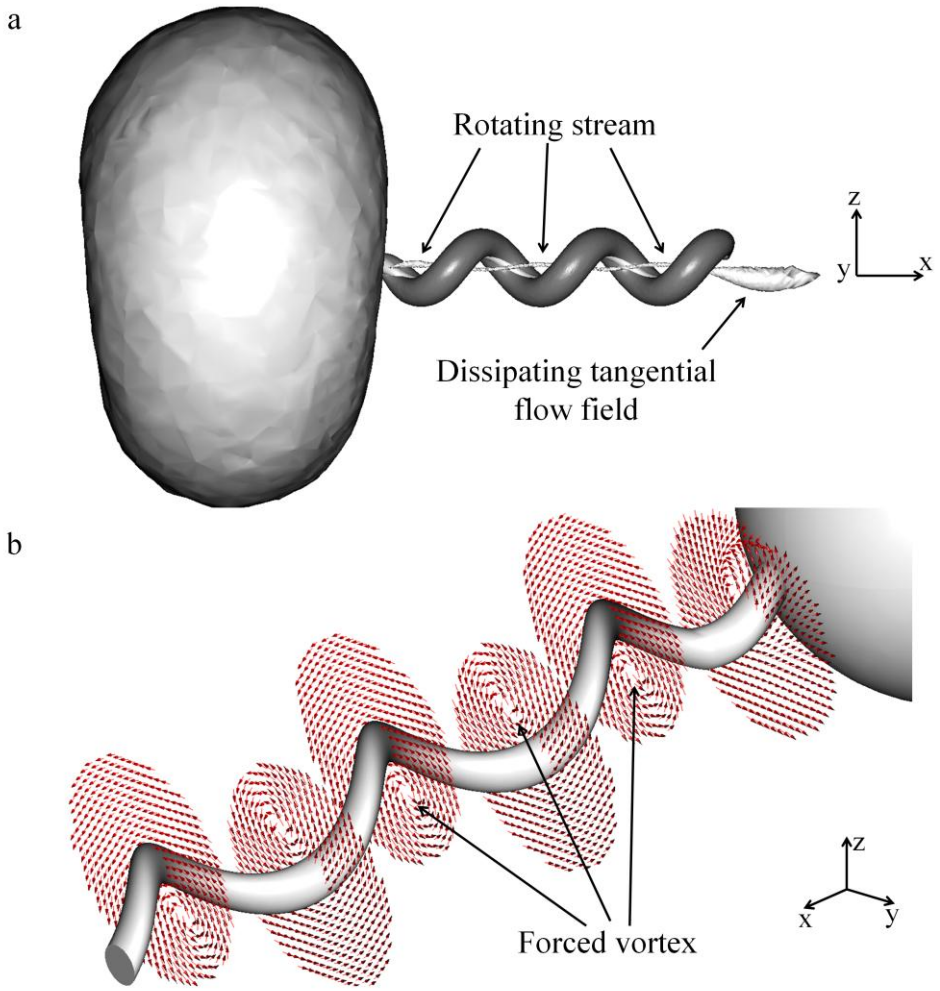

Figure 5.10: Induced tangential velocity fields around the swimmer: Tangential component of the velocity field fully enclosing the swimmer's body, while two separate rotational fields emerge around the tail (a); velocity fields on **yz**-plane with visible forced-vortex patterns located at x= {0.25:0.33:2.25} with respect to center of mass located at the revolute joint (b). Normalized arrows signify local flow field with forced vortex at the center. Both figures demonstrate the instant at t = 1.275 s.

The rotational flow field demonstrated in Fig. 5.10a dies out behind the helical tail and its magnitude is demonstrated in Fig. 5.11 in terms of the **x**-vorticity strength, $|\omega_x|$, at the back of the rotating helical tail with respect to parameterized wave geometry, i.e. total number of waves, N_λ, and wave amplitude, B_o, solved with identical meshing of $\Omega(t)$ and with the same boundary conditions used in the base CFD simulation. Total number of

waves on helical tail, and helical wave amplitudes studied are N_λ = { 2, 2.1, 2.25, 2.5, 2.75, 3, 3.1, 3.25, 3.5, 3.6, 3.75 } and B_o= { 0.0125, 0.025, 0.05, 0.075, 0.1, 0.125, 0.15 }, respectively. Figure 5.11a shows that the magnitude of **x**-vorticity increases linearly with increasing wave number N_λ whereas in Fig. 5.11b it is observed that **x**-vorticity has a nonlinear relationship with wave amplitude. In general, strength of the rotational field increases as the helical tail converges to a rotating hollow cylinder with increasing, N_λ, (see Fig. 5.11a) and as the tangential velocity of the free end of the rotating helix, i.e. $\omega_{tail}B_o$, increases (see Fig. 5.11b). It is noted that latter effect is proved to be dominant on the induced flow field at the back of the tail.

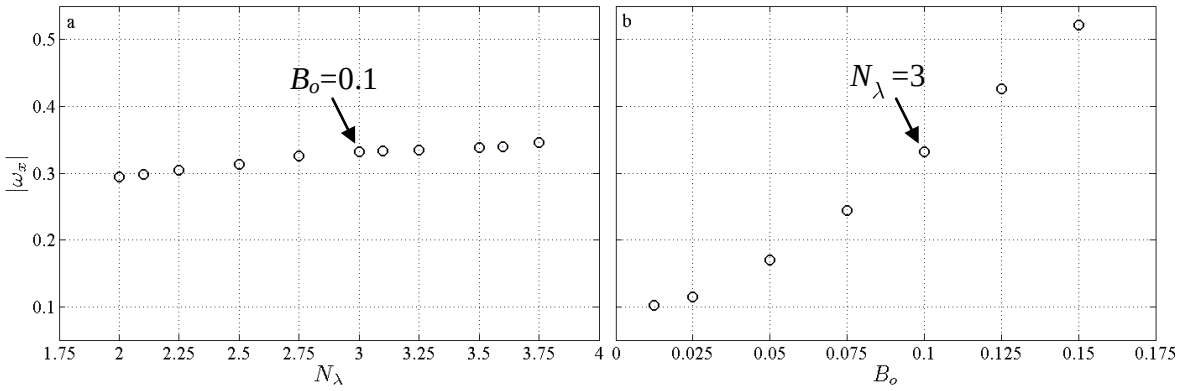

Figure 5.11: Variations in the strength of the **x**-component of the vorticity with respect to parameterized wave geometry: N_λ dependence of the strength of the **x**-vorticity (a); B_o dependence of the strength of the **x**-vorticity (b). Vorticity values are obtained at (x,y,z) = (2.35,0,0) with respect to center of mass located at the revolute joint, i.e. on the ejected rotating flow field illustrated in Figure 5.10a.

5.4.2. Hydrodynamic Interaction between Body and Tail

Results indicate that the body-drag is affected greatly by the pump-effect which perturbs the surrounding flow field induced by the rotating helical tail and the swimming action of the micro robot. Figure 5.12 depicts the effect of tail rotation revealing the hydrodynamic interaction (HI) between swimming robot's body and its rotating tail with the help of surrounding flow field's strength with the viscous domain of influence. First, the

time dependent velocity vector **V**, which is obtained from the CFD-model and given by Fig. 5.1, is imposed on the surface of the spherical body without a tail attached to it, i.e. $\mathbf{U}_{\mathbf{x},body} = \mathbf{u}_{\mathbf{x},body} = \mathbf{V}$ (also see Eq. (3.7)). Resultant streamline profile resolved at t = 1.975 s exhibits a spherical object moving inside a viscous domain (see Fig. 5.12a) and **x**-component of the consequential flow field completely encapsulates the body with a profile of spheroid (see Fig. 5.12a).

Furthermore, the flow field extends in positive **x**-direction with an attached but non-rotating helical tail (see Fig. 5.12b) and the corresponding body-drag is reasonably smaller than that of the single body (see Table 5.2) due to separation effect observed in Fig. 5.12b. The shape of the flow field depicted in Fig. 5.12b is irregular due to instantaneous non-zero lateral velocity. It is noted that boundary conditions on the helical tail represented in Fig. 5.12b are set as $\mathbf{U}_{\mathbf{x},tail} = \mathbf{u}_{\mathbf{x},tail} = \mathbf{V}$, similar to Eq. (3.8) without the tail rotation.

However, an additional flow field arises compressed against the spherical body with presence of a rotating helical tail (see Fig. 5.12c), on which the boundary conditions are given as $\mathbf{U}_{\mathbf{x},tail} = \mathbf{u}_{\mathbf{x},tail} = \mathbf{V} + \omega_{tail} \times \mathbf{P}$, which is the same as Eq. (3.8).

The spatial compression observed in Fig. 5.12c is, in effect, a substantial increase in the velocity gradient leading to higher opposing viscous friction in the vicinity due to the pump-effect, thus leading to amplified effective fluid resistance in the **x**-direction (see Table 5.2).

Moreover, presence of the rotating helical tail behind the body reduces its lateral fluid resistance as an additional outcome of the pump-effect. The flow driven by the pump-effect contributes to the instantaneous lateral thrust of the swimming robot. Non-zero lateral forces occur owing to the geometric impurity introduced by the ramp function in local amplitude function simultaneously combined with the local body-tail interaction on the tail (De la Torre and Bloomfield, 1977; Johnson, 1980). Figure 5.13 demonstrates the streamlines at the back of the spherical body at t = 1.025 while the **y**-velocity V_y is 0.0143 in positive **y**-direction: the flow in the positive **y**-direction at the back imposes additional shear stress on the spherical body, which is already moving with a positive **y**-velocity (see Fig. 5.13).

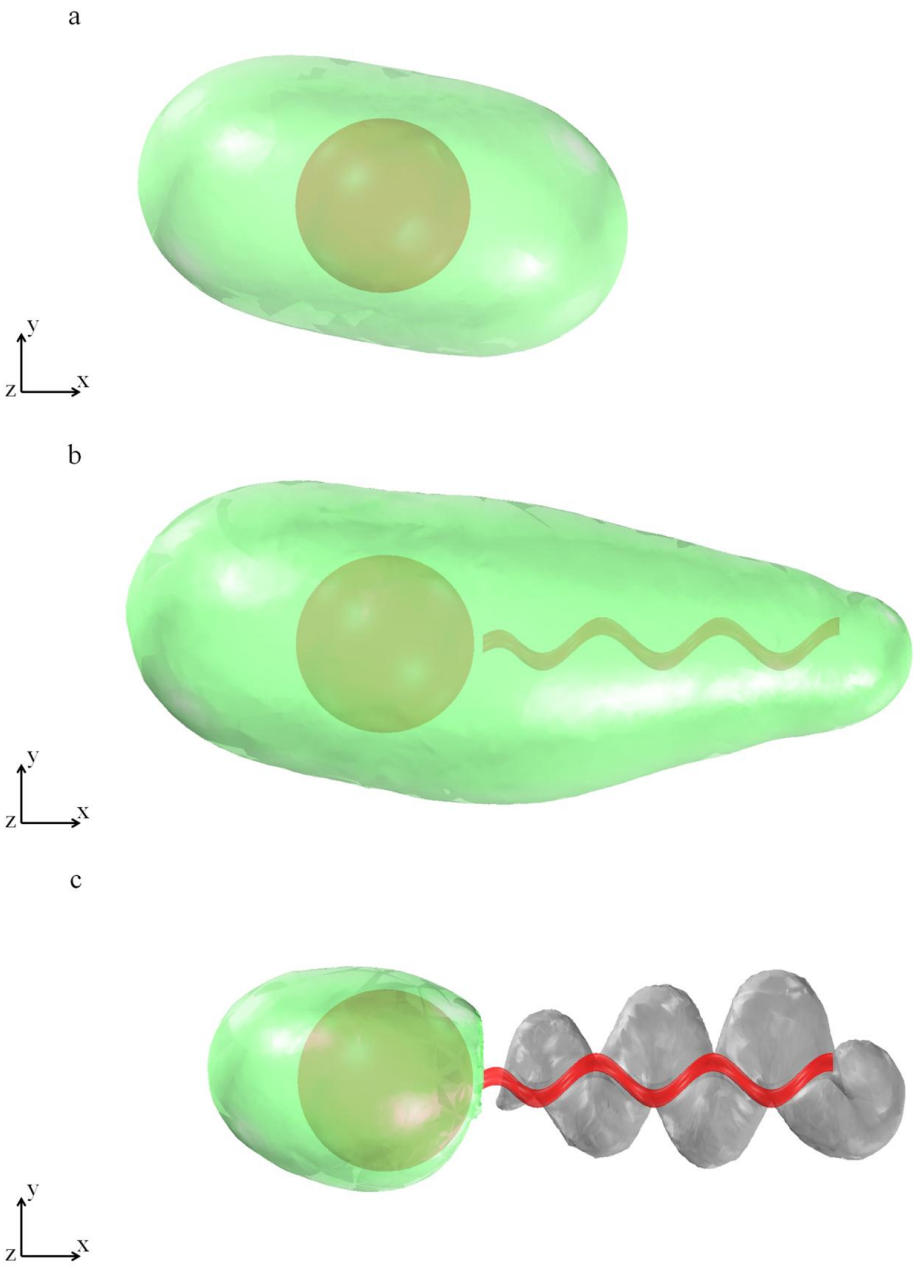

Figure 5.12: Spatial compression effect of tail rotation on the flow field around the body: depicted by three dimensional isosurfaces of flow field's **x**-component (a-c), obtained with the swimming velocities presented in figure 2 imposed as boundary conditions: Isolated spherical body (a); spherical body with non-rotating helical tail (b); spherical body and helical tail, which rotates with ω_{tail} (c). The **x**-component of the rotational flow field around the helix in (c) is 0.036 in magnitude, whereas around the body in (a-b) is 0.02 in magnitude. Isosurfaces are captured at t = 1.975 s.

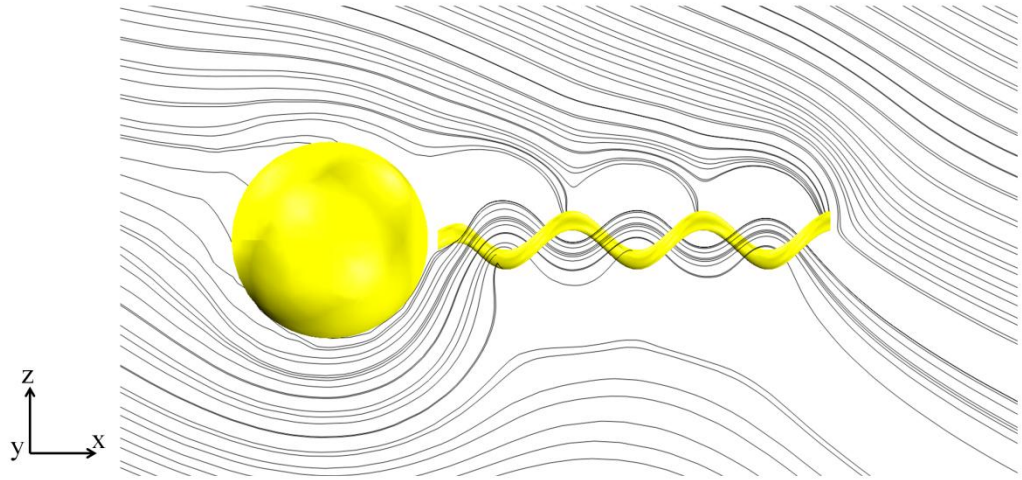

Figure 5.13: Effect of tail rotation on the lateral flow field: depicted by thin black streamlines on **xy**-plane with the swimming velocities presented in Figure 5.1 imposed as boundary conditions: Spherical body and helical tail, which rotates with ω_{tail}. Streamline profiles are captured at t = 1.025 s while instantaneous **y**-velocity of the swimmer is 0.0143 in positive **y**-direction.

5.4.2.1. Normal stress acting on the body

In order to inspect the pump-effect further, the CFD analysis is extended to include comparisons on the normal force components acting on the front and back hemispherical surfaces of the body with respect to parameterized wave length and wave amplitude. Simulations are conducted on the spherical body with the helical tail, which has varying wave numbers and amplitudes of N_λ = { 2, 2.1, 2.25, 2.5, 2.75, 3, 3.1, 3.25, 3.5, 3.6, 3.75 } and B_o = { 0.0125, 0.025, 0.05, 0.075, 0.1, 0.125, 0.15 }, respectively.

Effect of parameterized wave geometry is presented in comparison with an isolated spherical body undergoing rigid-body translations and rotations identical to that of the base-case CFD-model results. Figure 5.14a demonstrates that the increased normal stress due to pump-effect has small sensitivity to wave numbers, N_λ, ranging between 1.75 to 4. The time-averaged **x**-force $F_{x,avg}$ on the hemispherical surface at the back is at least twice as big as the **x**-force exerted at the front, and 2.53 times bigger than that exerted on both

hemispherical surfaces of an isolated sphere with computed force-free swimming velocity vector of the base case design imposed as velocity boundary conditions. Furthermore, the nonlinear relation between N_λ and maximum instantaneous lateral force, $F_{\{y,z\},max}$, is demonstrated in Fig. 5.14b: with wave numbers including half waves, i.e. N_λ = {1.5, 2.5, 3.5,…}, the lateral fluid resistance on the spherical body rises to local maxima, with N_λ = 2.5 and as large as 4.24 times that exerted on the hemispherical surfaces of an isolated sphere, and dips to local minima with full waves, i.e. N_λ = {1, 2, 3,…}. However, the fluid resistance at the front surface attains its minimum with wave numbers equal to N_λ = {1.1, 2.1, 3.1,…}, and climbs to local maxima with N_λ = {1.6, 2.6, 3.6,…}. Additionally, the time-averaged hydrodynamic **x**-torque, $T_{x,avg}$, exerted on the surface of the spherical body due to body rotation, Ω_x, has a fairly symmetrical distribution at front and back hemispherical surfaces, close to that exerted on the isolated sphere presented in Fig. 5.14c, i.e. amplified with 1.15. This result implies that the rotational flow fields induced by the rotating helical tail do exert but fairly insignificant hydrodynamic torque on the swimmer's body as opposed to the amplification due to additional normal and shear stress.

Figure 5.14d depicts the time-averaged **x**-force, $F_{x,avg}$, acting on the hemispherical surfaces with varying wave amplitude, B_o. The fluid resistance on both hemispherical surfaces increase linearly with increasing amplitude; however, the amplification at the back is higher, e.g. wave amplitude of B_o = 0.1 causes forward resistance almost three times that exerted on the hemispherical surfaces of an isolated spherical body. Varying amplitude has a similar effect on lateral force, $F_{\{y,z\},max}$: the amplification at the back is slightly higher; however, smaller than the increase in $F_{x,avg}$, i.e. wave amplitude of B_o = 0.1 causes lateral translation to increase 1.5 times that of the isolated sphere moving with velocity vector calculated by the base case CFD-model (see Fig. 5.14e). Akin to the wave number results, the amplification in the time-averaged hydrodynamic torque $T_{x,avg}$ acting against the rotation, Ω_x, is fairly close at the front and back of the body; however, have a nonlinear relationship with varying wave amplitude (see Fig. 5.14f).

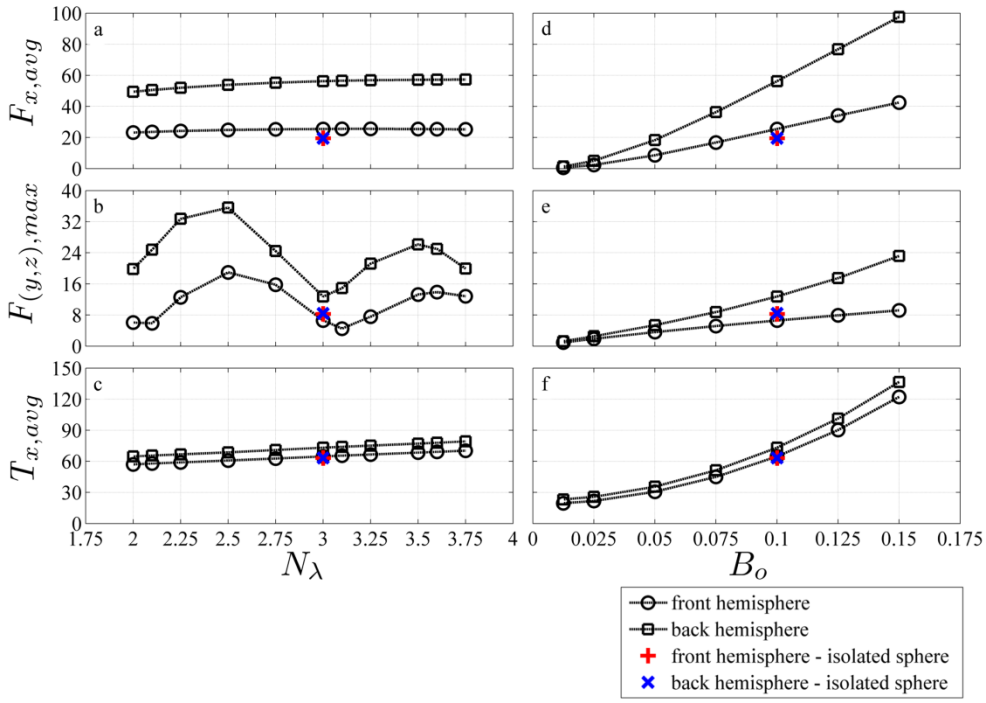

Figure 5.14: Relation between the helical wave geometry and the total fluid force exerted on fore and back hemisphere of swimmer's spherical body; on the **x**-force with respect to N_λ (a); on the lateral forces with respect to N_λ (b); on the **x**-torque with respect to N_λ (c); on the **x**-force with respect to B_o (d); on the lateral forces with respect to B_o (e); on **x**-torque with respect to B_o (f).

To conclude, it is observed that the fluid resistance on **x**-axis has greater sensitivity to varying wave amplitude, whereas the effect of total number of waves on the helical tail is more important for lateral fluid forces acting on the body. As the wave amplitude increases the additional normal stress acting at the back of the body due to the pump-effect increases; however, changing the wave length has a minor effect. On the other hand, as the total number of waves on the tail varies, the magnitude of the lateral shear on the body attains local minima and maxima with it. Furthermore, the additional shear effect on the lateral translation increases with increasing amplitude because of the increased velocity of the back-flow. Finally, one may deduce from the relatively small amplification on the rotational fluid resistance that pure rotation of the flow field has a less significant effect on overall body resistance. However, the latter observation will be proven incorrect in the next section.

5.4.2.2. Hydrodynamic interaction in body resistance calculations

Effective body-drag forces are modified with corresponding HI-coefficients based on the following comparative analysis based on CFD results with analytical drag formulae, and corresponding results are presented in Table 5.2 and Table 5.3; for spherical body, prolate spheroid and streamlined body, respectively, which are presented in Figs. 5.4 and 5.5. The amplitudes of the hydrodynamic interaction, i.e. Υ_T for rigid-body translation and Υ_R for rigid-body rotation of the swimmer's body, are calculated based on the ratio of fluid stress integral obtained by CFD-model solutions to the viscous sphere drag formulae presented in literature as follows:

$$\Upsilon_{T,j} = \begin{cases} F_{j,\text{avg}} / D_{T,j} V_{j,\text{avg}} & \Leftarrow j = x \\ F_{j,\max} / D_{T,j} V_{j,\max} & \Leftarrow j = y,z \end{cases}, \tag{5.3}$$

and

$$\Upsilon_{R,j} = T_{j,\text{avg}} / D_{R,j} \Omega_{j,\text{avg}}, \tag{5.4}$$

where F_j is the normal fluid force on an arbitrary **j**-axis obtained by integrating total hydrodynamic stresses over entire body surface in that direction, subscripts avg and max signify the time-averaged and maximum values, respectively. Similarly, $T_{j,\text{avg}}$ denotes the time-averaged viscous torque exerted on the swimmer's body along its axis of revolution. Here, $D_{T,j}$ and $D_{R,j}$ are given as $6\pi\mu R_{body}$ and $8\pi\mu R_{body}^3$, respectively, for an isolated perfect sphere in an unbounded fluid regardless of the axis of translation and rotation (Happel and Brenner, 1965).

Nonetheless, a simple amplitude ratio given by the above equations is inadequate to predict the instantaneous lateral fluid resistance on the spherical body due to its time-dependent interaction with the rotating helical tail via induced flow field around the

swimmer. Figure 5.15 demonstrates that there exists a constant phase-shift between lateral drag forces calculated with literature-based $D_{T,\{y,z\}}$ formulae and the ones resolved by the CFD-model, which found by integrating the total fluid force along lateral directions over entire surface of the spherical body. The phase-shift, in fact, is between the lateral swimming velocities and lateral drag forces.

The conventional diagonal drag-force matrix, which is signifying the linear relationship between the velocity vector and corresponding fluid resistance for an axisymmetric particle undergoing rigid-body translations while solely rotating around its symmetry axis is:

$$\begin{bmatrix} (\mathbf{F}_{body})_{3\times1} \\ T_{body,x} \end{bmatrix} = \begin{bmatrix} D_{T,x} & & & \\ & D_{T,y} & & \\ & & D_{T,z} & \\ & & & D_{R,x} \end{bmatrix} \begin{bmatrix} \mathbf{V} \\ \Omega_x \end{bmatrix}, \tag{5.5}$$

In this study, the resistance matrix in Eq. (5.5) is modified in order to compensate for the HI-effect in time-domain, and non-zero off-diagonal terms are introduced to couple the lateral forces with lateral velocities of the swimmer as follows:

$$\begin{bmatrix} (\mathbf{F}_{body}(\phi))_{3\times1} \\ T_{body,x} \end{bmatrix} = \begin{bmatrix} D_{T,x}\Upsilon_{T,x} & 0 & 0 & 0 \\ 0 & D_{T,y}\Upsilon_{T,y}\cos(\phi) & D_{T,y}\Upsilon_{T,y}\sin(\phi) & 0 \\ 0 & -D_{T,z}\Upsilon_{T,z}\sin(\phi) & D_{T,z}\Upsilon_{T,z}\cos(\phi) & 0 \\ 0 & 0 & 0 & D_{R,x}\Upsilon_{R,x} \end{bmatrix} \begin{bmatrix} \mathbf{V} \\ \Omega_x \end{bmatrix}, \tag{5.6}$$

where the phase-angle , ϕ , for the spherical body is obtained from Fig. 5.15 by solving the inverse problem of phase-shift. The forward motion in Eq. (5.6) does not require phase-angle correction because the amplified normal-force at the back of the body is a steady effect due to continuous rotation of the helical tail. Similarly, the hydrodynamic torque acting on the body is a constant reaction to continuous body and tail rotations in opposite directions.

Furthermore, the direction of amplification in **yz**-plane is time dependent as depicted in Fig. 5.15. Hence the phase angle, although not a function of time itself, stands for the

time-dependent hydrodynamic interaction between swimmer's body and tail and the time-dependent lateral fluid resistance on the body, which is actually analogous to the complex impedance in RLC circuits.

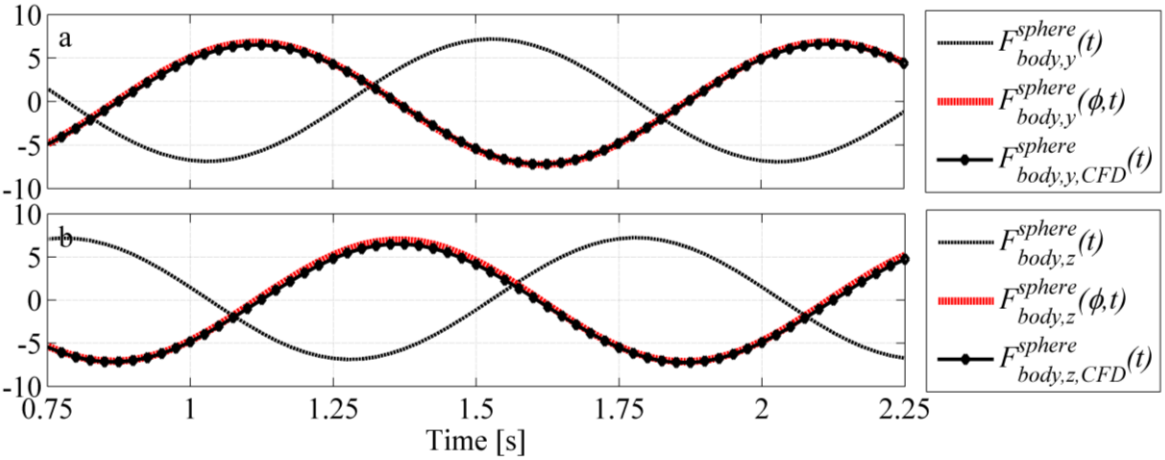

Figure 5.15: Comparison on the performance of unmodified and modified resistance matrices with CFD results: **y**-drag exerted on body (a); **z**-drag exerted on the body (b). Constant phase shift between lateral velocities and lateral forces demand a modified resistance approach: conventional drag matrix in Eq. (5.8) cannot predict instantaneous viscous force exerted on the swimmer's body; however, revised drag matrix in Eq. (5.9) provides significantly improved results.

Table 5.2: Hydrodynamic interaction (HI) coefficients for the spherical body.

Scenario	Fluid-Drag
Single sphere (Fig 5.4a)	$\{\Upsilon^{sphere}_{T,x}=1.06,\ \Upsilon^{sphere}_{T,\{y,z\}}=0.92,\ \Upsilon^{sphere}_{R,x}=1.00,\ \phi^{sphere}=0\}$ [a]
Sphere with non-rotating helical tail (Fig 5.4b)	$\{\Upsilon^{sphere}_{T,x}=0.93,\ \Upsilon^{sphere}_{T,\{y,z\}}=0.85,\ \Upsilon^{sphere}_{R,x}=1.00,\ \phi^{sphere}=0\}$ [a]
Sphere with rotating helical tail (Fig 5.4c)	$\{\Upsilon^{sphere}_{T,x}=2.24,\ \Upsilon^{sphere}_{T,\{y,z\}}=0.51,\ \Upsilon^{sphere}_{R,x}=1.09,\ \phi^{sphere}=1.17\pi\}$ [a]

[a] Subject to domain meshing and numerical solution tolerance of 10^{-3}.

Table 5.3: Force calculations for elongated and streamlined bodies.

Scenario	Fluid-Drag
Single prolate spheroid (Fig 5.5a)	$\{F_{x,\text{avg}}^{spheroid} = 47.1,\ F_{\{y,z\},\max}^{spheroid} = 25,\ T_{x,\text{avg}}^{spheroid} = 215.5\}$ [a]
Single streamlined body (Fig 5.5d)	$\{F_{x,\text{avg}}^{Bourot,1974} = 42.6,\ F_{\{y,z\},\max}^{Bourot,1974} = 20.3,\ T_{x,\text{avg}}^{Bourot,1974} = 167.9\}$ [b]
Prolate spheroid with non-rotating tail (Fig 5.5b)	$\{F_{x,\text{avg}}^{spheroid} / F_{x,\text{avg},no\ tail}^{spheroid} = 0.97,\ F_{\{y,z\},\max}^{spheroid} / F_{\{y,z\},\max,no\ tail}^{spheroid} = 0.99,\ T_{x,\text{avg}}^{spheroid} / T_{x,\text{avg},no\ tail}^{spheroid} = 1.00\}$ [c]
Streamlined body with non-rotating tail (Fig 5.5e)	$\{F_{x,\text{avg}}^{Bourot,1974} / F_{x,\text{avg},no\ tail}^{Bourot,1974} = 0.88,\ F_{\{y,z\},\max}^{Bourot,1974} / F_{\{y,z\},\max,no\ tail}^{Bourot,1974} = 0.95,\ T_{x,\text{avg}}^{Bourot,1974} / T_{x,\text{avg},no\ tail}^{Bourot,1974} = 1.00\}$ [d]
Prolate spheroid with rotating tail (Fig 5.5c)	$\{F_{x,\text{avg}}^{spheroid} / F_{x,\text{avg},no\ tail}^{spheroid} = 1.89,\ F_{\{y,z\},\max}^{spheroid} / F_{\{y,z\},\max,no\ tail}^{spheroid} = 0.43,\ T_{x,\text{avg}}^{spheroid} / T_{x,\text{avg},no\ tail}^{spheroid} = 1.04\}$ [e]
Streamlined body with rotating tail (Fig 5.5f)	$\{F_{x,\text{avg}}^{Bourot,1974} / F_{x,\text{avg},no\ tail}^{Bourot,1974} = 1.69,\ F_{\{y,z\},\max}^{Bourot,1974} / F_{\{y,z\},\max,no\ tail}^{Bourot,1974} = 0.49,\ T_{x,\text{avg}}^{Bourot,1974} / T_{x,\text{avg},no\ tail}^{Bourot,1974} = 1.02\}$ [f]

[a,b] Subject to meshing and numerical solution tolerance of 10^{-3}.
[c,e] Determined with respect to the force solutions presented in ([1]).
[d,f] Determined with respect to the force solutions presented in ([2]).

Numerical results show that the effective fluid resistance $F_{x,avg}$ due to forward velocity V_x varies linearly with N_λ (see Fig. 5.16a). Moreover, the HI-coefficient for forward swim, $\Upsilon_{T,x}$, should converge to a limiting value as the rotating helical tail converges to a rotating hollow cylinder with increasing N_λ, after which the all thrust and pump-effect will diminish completely. The amplitude of the lateral HI-coefficient $\Upsilon_{T,\{y,z\}}$ reaches local maxima with N_λ = {1.25, 2.25, 3.25,…} and dips to local minima with N_λ = {1, 2, 3,…} (see Fig. 5.16b). The main reason for this behavior is incomplete waves: with full waves, the $V_{\{y,z\}}$ components of the swimming velocity are small, thus the body does

interact with the induced flow field minimally. On the other hand, incomplete waves induce lateral thrust and swimmer body moves sideways leading to further interaction with the surrounding flow field. A similar local minima and maxima relation is observed between $\Upsilon_{R,x}$ and N_λ. However, the variations are negligible and the overall relation can be practically deemed as linear; however, inversely proportional to varying N_λ as presented in Fig. 5.16c.

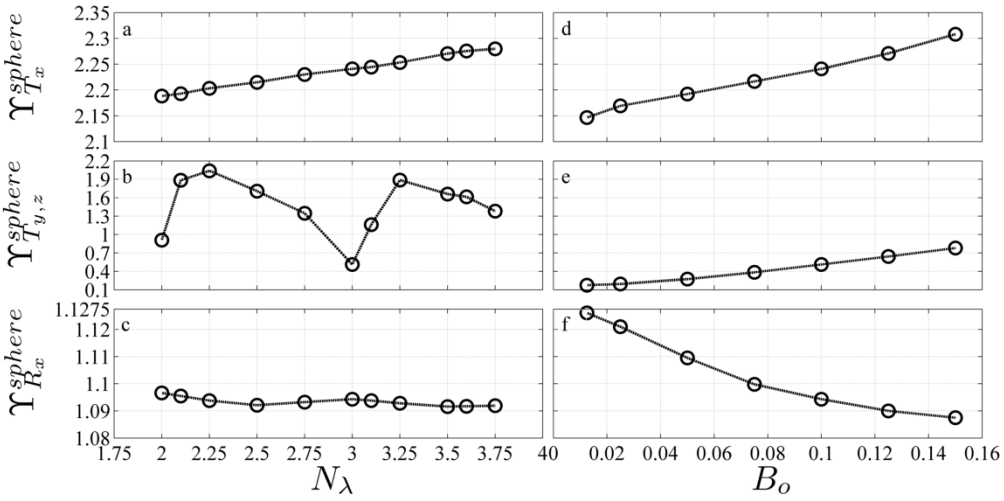

Figure 5.16: Relation between the hydrodynamic interaction coefficients (amplitude of the HI) and the helical wave geometry: on the forward translation with respect to N_λ (a); on the lateral translation with respect to N_λ (b); on **x**-rotation with respect to N_λ (c); on the forward translation with respect to B_o (d); on the lateral translation with respect to B_o (e); on **x**-rotation with respect to B_o (f).

The relationship between $\Upsilon_{T,x}$ and wave amplitude is linear meaning that the normal stress acting on the hemispherical surface at the back of the body increases with increasing B_o, akin to increasing N_λ (see Fig. 5.16d). The amplitude of lateral HI-coefficient, $\Upsilon_{T,\{y,z\}}$, varies linearly with wave amplitude; however, the amplification effect is low (see Fig. 5.16e). Lastly, the relationship between $\Upsilon_{R,x}$ and amplitude is inversely proportional: as the wave amplitude increases, the rotational field induced by the helical tail widens following the tail geometry, but dissipates towards its long axis where the revolute joint is placed. Hence, the body is less affected by the tangential component of the flow field as B_o

increases with $\Upsilon_{R,x}$ converging to 1. It is observed that the amplitude of HI-coefficients more sensitive to total number of waves, except for hydrodynamic torque (see Fig. 5.16f).

The base-case CFD simulation computes a 1.17π phase-shift for the helical tail with N_λ = 3 and B_o = 0.1. Phase-angle dips to local minima with presence of wave with lengths shorter than half-wave on the tail, i.e. including quarter of a wavelength such as N_λ = {1.25, 2.25, 3.25,…} to be exact. Local minima of the phase-angle, ϕ, coincides with the local maxima of $\Upsilon_{T,\{y,z\}}$ in Fig. 5.16b. Phase-shift reaches to local maxima with the presence of half waves such as N_λ = {1.5, 2.5, 3.5,…} where coincide with local maxima of $F_{\{y,z\},\max}$ on the hemispherical surface to the back (see Fig. 5.14b).

It is deduced that the change in phase-shift affects the amplitude of the lateral HI-coefficient with varying N_λ due to the instantaneous lateral translation overlapping with the instantaneous downstream due to the pump-effect of rotating tail. Given that lateral translation velocity $V_{\{y,z\}}$, is no longer in tandem in the same direction with the additional flow induced by the helical tail's rotation, the total lateral fluid resistance increases at N_λ = {1.25, 2.25, 3.25,…} (see Fig. 5.17a). Similarly, the effective lateral fluid resistance decreases when the instantaneous lateral translational velocity and the stream driven by the pump-effect counteract minimally with N_λ = {1, 2, 3, 4…} (see Figs. 5.16b and 5.17b).

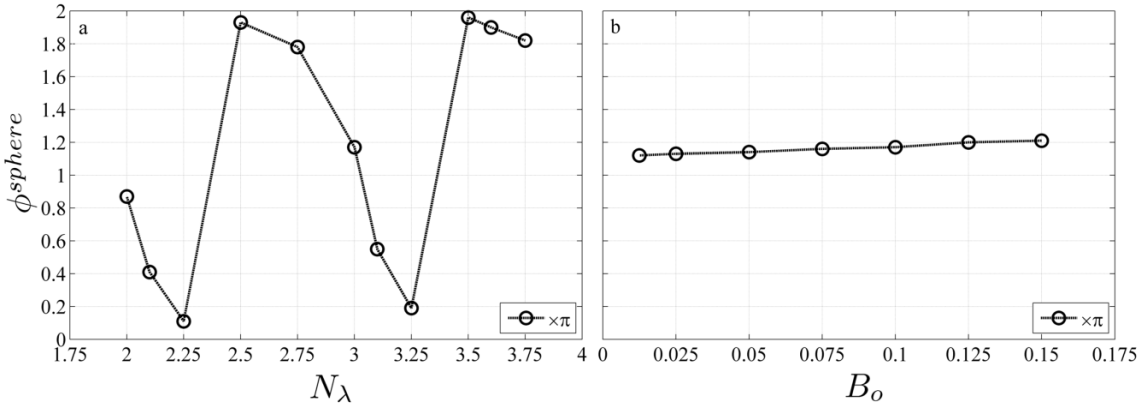

Figure 5.17: Effect of wave geometry on hydrodynamic interaction coefficients (phase of the HI) and the helical wave geometry: on the drag of the spherical body with an attached rotating helical tail; with respect to total number of waves on helical tail, N_λ (a); with respect to wave amplitude, B_o (b).

Additionally, the phase-angle, ϕ, varies linearly with the wave amplitude, B_o, as presented in Fig. 5.17b. The sensitivity of the phase-angle to the helical wave amplitude is considerably small; hence the change in phase-shift is monotonic with respect to B_o. Figure 5.17b also implies that the phase-angle has a minimum greater than 0 for a rotating helical tail with N_λ = 3 regardless of the wave amplitude B_o, except for B_o = 0.

5.5. Conclusions

CFD simulations are carried out in order to study the four degrees of freedom mobility of an untethered micro swimmer. The micro swimmer is composed of a spherical body with a helical tail and fully submerged in a viscous domain governed by full time-dependent Navier-Stokes equations subject to continuity. Mesh deformation due to tail rotation and rigid-body swimmer translation, with respect to bounding stationary channel walls, inlet, and outlet, is handled by arbitrary-Lagrangian-Eulerian method. Rigid body translations and body rotation rate of the swimmer are computed by means of force-free and torque-free swimming constraints imposed on the swimmer surface. Velocity vector required to satisfy force-free and torque-free swimming action is obtained by setting the hydrodynamic force and torque integrations over entire swimmer surface to be equal to 0 at each time step during CFD simulations.

Three distinctive physical phenomena related to the pump-effect are observed in detail: Vortex formation on the long axis of the swimmer, which is presented with flow field plots, additional normal stress on the swimmer's body is quantified with comparisons on the hemispherical surface at the front and back of a spherical body, and amplitude and the phase-angle of the hydrodynamic interaction (HI) coefficients are introduced and quantified with respect to parameterized wave geometry. A series of numerical experiments with the CFD-model are carried out in order to study the effect of body geometry and wave

geometry on the additional flow fields driven by the pump-effect. It is concluded that the wave geometry has a superior impact on the pump-effect.

The vortex formation arises under the influence of rigid-body rotation of the helical tail: tail exerts a continuous torque on the flow it is rotating around. Furthermore a stream of backflow is induced by the same rotation. Since the propulsion velocity is smaller than the wave propagation velocity, a backflow is induced with respect to swimmer's center of mass (Lighthill, 1996). This backflow rotates with the tail and is pushed out at the back of the swimmer where it dissipates due to excessive viscous dissipation.

Qualitative studies are carried out on the effect of body geometry on the induced flow field with a perfect sphere, a prolate spheroid and a streamlined body suggested by Bourot (1974), separately under identical boundary conditions imposed on the their surface. Both elongated bodies have short-semi axes identical to that of the sphere's radius. It is observed that, presence of a non-rotating helical tail decreases the resistance to the forward and lateral translations in comparison with isolated prolate-spheroid and streamlined body, while the rotational resistance remaining constant. However, as the tail rotates the streamline density increase towards the body. This phenomenon leads to extra hydrodynamic resistance acting on the swimmer's body in forward and lateral directions. Furthermore, analysis is expanded to include quantitative study of the hydrodynamic force and torque values acting on the hemispherical surfaces at the front and back of the spherical body with rotating helical tail in comparison with force and torque values acting on an isolated sphere. It is confirmed that the rotating helical tail induces extra normal stress at the back of the spherical body.

The hydrodynamic interaction between the swimmer's body and rotating helical tail is quantified with the CFD-model. It is established that the diagonal drag matrix, which is conventionally used in order to calculate the viscous resistance on an axisymmetric body is not adequate to predict the instantaneous lateral fluid resistance exerted with the presence of a second rotating body of helical geometry. Therefore, a modified resistance matrix is introduced with non-zero off-diagonal elements in order to predict the lateral resistance acting on the swimmer's body accurately. Furthermore, two hydrodynamic interaction (HI) coefficients, i.e. resistance amplitude and phase-angle of cross interaction in lateral directions, are hypnotized and numerically confirmed. The amplitude is obtained simply by

the ratio of CFD-based fluid resistance acting on swimmer's body to the analytical fluid-drag predictions. On the other hand, the phase-angle is calculated solving the inverse problem of phase-shift between instantaneous lateral force and velocity vectors.

Finally, a quantitative study is carried out on the relationship between HI-coefficients and the wave geometry, i.e. geometry of the rotating helical tail. Amplitude of the forward HI-coefficient, $\Upsilon_{T,x}$, increase linearly with increasing total number of waves, N_λ, and with increasing wave amplitude B_o. Amplitude of the lateral HI-coefficient, $\Upsilon_{T,\{y,z\}}$, has a nonlinear relationship with total number of wave length on the helical tail, N_λ: $\Upsilon_{T,\{y,z\}}$ attains local maxima with N_λ = {1.25, 2.25, 3.25,…}, and dips to local minima with N_λ = {1, 2, 3,…}. However, $\Upsilon_{T,\{y,z\}}$ increases linear-monotonically with increasing wave amplitude B_o. The amplitude of rotational HI-coefficient, $\Upsilon_{T,x}$, varies nearly linearly, i.e. nonlinearly with a very low sensitivity, with varying N_λ; however, increases with a nonlinear dependence on increasing B_o. It is observed that total number of waves, N_λ, play an important role in translational fluid resistance, whereas the hydrodynamic torque acting against rigid-body rotations is more sensitive to wave amplitude.

The phase-angle of the lateral HI-coefficients, ϕ, has a nonlinear relationship with total number of waves: ϕ reaches local maxima with N_λ = {1.5, 2.5, 3.5,…}, and dips to local minima with N_λ = {1.25, 2.25, 3.25,…}. On the other hand, there is a linear relationship between $\Upsilon_{T,\{y,z\}}$ and B_o with an especially low sensitivity to the change in wave amplitude. Furthermore, it has been established that change in the phase angle, ϕ, affects the change in $\Upsilon_{T,\{y,z\}}$ by means of increase or decrease in effective instantaneous lateral resistance to the translation on the swimmer's body. It is established that the phase-angle is greatly affected by N_λ; however, is mildly sensitive to the wave amplitude.

6. VALIDATION OF THE REDUCED-ORDER HYDRODYNAMIC MODEL

In the surrogate model presented here, hydrodynamic forces on the tail are obtained from local resistive force coefficients which are either calculated from analytical formulas available in literature, such as from Lighthill's slender body theory, or obtained from the integration of the stress tensor in the flow field computed by the CFD simulation experiment for a representative design with fixed values of the design variables such as amplitude and wavelength of the helical waves.

Body resistance coefficients are known for isolated objects such as spheroids in unbounded fluid media: for example the resistance coefficient is $F_i / U_i = -6\pi\mu R_{body}$ for the hydrodynamic force F_i acting on an isolated spherical object of radius r moving with velocity U_i in an unbounded fluid of viscosity μ in the i direction; and the resistance is the same for all directions. In the presence of an actuated tail attached to the spherical body, hydrodynamic interaction (HI) coefficients, Υ_i , are used. HI-coefficients scale the resistance coefficient in an arbitrary **i**-direction individually, namely $F_i / U_i = -\Upsilon_i (6\pi\mu R_{body})$. Hydrodynamic interaction coefficients are different for each direction due to rotation of the helical tail, which breaks the symmetry of the flow over the spherical body, and are calculated from the solution of the inverse problem for a fixed representative design.

The hydrodynamic model is validated with measurements of Goto *et al.* (2001) for a group of species of micro organisms with varying body and tail dimensions, and with three-dimensional time-dependent CFD simulation experiments for swimmers with designs other than the one used to obtain resistance coefficients. Furthermore, a validated hydrodynamic model allows to construct efficient geometric designs for desired operations with given physical constraints such as consumable energy available to the system, as well as

determining physical properties which are hard to measure physically such as resistive force coefficients of a complex geometry in micro or nanoscales.

6.1. Validation with Goto's Observations on Natural Swimmers

Goto *et al.* (2001) presented measured forward velocity and body rotation rates for various specimens of *Vibrio Alginolyticus*, whose dimensions and tail rotation rates vary individually. Since the authors could not measure the frequency of the tail's rotation, they used the body rotation rate as a constraint to obtain the tail's frequency from boundary-element model (BEM) solution of the flow around the swimmer. Table 6.1 shows geometric parameters of individual organisms; for all cases radius of the tail is 16 nm, wavelength of the helical waves is 1.37 μm and the amplitude (helical radius) is 0.1487 μm.

Table 6.1: Geometric parameters of V. *Alginolyticus* specimens; observed by Goto *et al*. (2001).

Specimen	Frequency (Hz)	Tail Length (μm)	Body **s**-semi-axis, $R_{body,s}$ (μm)	Body **q** and **r**-semi-axes $R_{body,\{q,r\}}$ (μm)
A	187.70	4.89	1.885	0.415
B	123.20	4.90	1.320	0.380
C	73.95	5.24	1.380	0.405
D	244.70	5.19	1.975	0.400
E	126.20	5.03	1.785	0.405
F	220.10	5.07	2.260	0.380
G	477.10	4.87	2.280	0.410

Time-averaged forward velocity and the body-rotation rate of swimmers are calculated from the hydrodynamic model and compared with the measurements of Goto *et*

al. (2001) in Fig. 6.1. Based on the dimensions of swimmers given in Table 6.1, the resistance coefficients of the body in the **s**-direction, $D_{T,s}$ and $D_{R,s}$, which are used in the resistance matrix of the swimmer's body, are determined for oblique spheroids as follows (Berg, 1993):

$$D_{T,s} = \Upsilon_{T,s} 4\pi\mu R_{body,s} \Big/ \left(\log\left(\frac{2R_{body,s}}{R_{body,\{q,r\}}} \right) - 0.5 \right), \tag{6.1}$$

for forward velocity and

$$D_{R,s} = \Upsilon_{R,s} (16/3)\pi\mu R_{body,s} R^2_{body,\{q,r\}}, \tag{6.2}$$

for rigid-body rotation along the symmetry axis. Here, $R_{body,\{s,q,r\}}$ are the radii of the body in the **s, q** and **r**-directions respectively, and $\Upsilon_{T,R}$ are the coefficients, which are used to specify the discrepancy of the body drags from the ideal case for isolated spheroids in infinite media. As shown in Fig. 6.1, there is a significant discrepancy between the measurements and the model results when resistance coefficients of bodies are taken as the ones for isolated objects in infinite medium, i.e. for: $\Upsilon_{\{T,R\},\{s,q,r\}} = 1$the maximum error is 87% in the average forward velocity for specimen G, and 47.2% in the body-rotation rate for specimen B.

From specimen C, the interaction coefficients are found to be $\Upsilon_{T,s} = 2.37$ and $\Upsilon_{R,s} = 1.49$ from the solution of the inverse problem. As shown in Fig. 6.1, the agreement between the hydrodynamic model and measurements is very good for updated resistance coefficients of the body: maximum error is 8.2% in the average forward velocity for specimen G, and 6.5% in the body rotation rate for specimen F. Correction factors, 2.37 and 1.49 for $D_{T,s}$ and $D_{R,s}$ respectively, indicate that actual body resistance coefficients must be larger than the ones for isolated spheroid objects in infinite medium. Despite that specimens have different body and tail dimensions and tail rotation rates (see Table 6.1), corrections obtained from a single specimen work very reasonably well for other specimens

who are not too different as well. Thus, once the resistance coefficients of the body are obtained accurately, hydrodynamic model would perform sufficiently well in subsequent design and control studies.

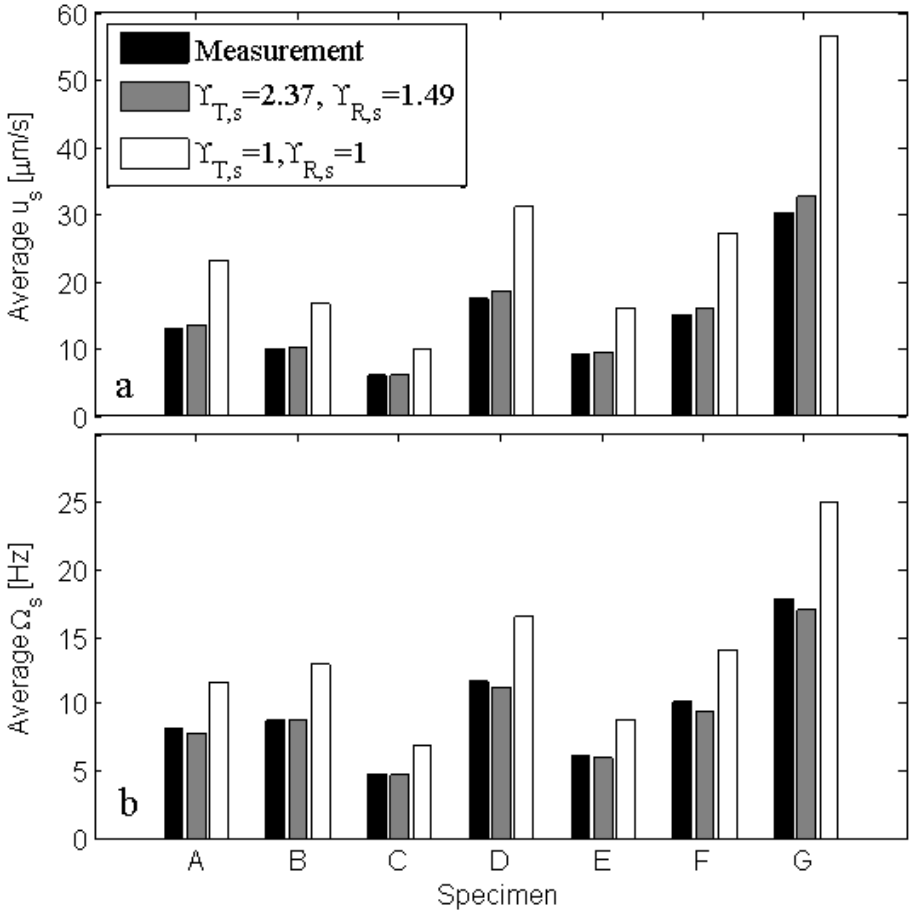

Figure 6.1: Comparisons on natural swimmers and hydrodynamic model results: the time-averaged forward velocity (a); and angular velocity of the body (b), which are between the measurements reported by Goto *et al*. (2001) and the model for unmodified and corrected body drags, are presented.

It is reasonable to expect that hydrodynamic interactions between the body and the tail would have an effect on the resistance force coefficients of the tail as well. In effect, the linearity of the equation of motion, which consists of the force-free swimming condition and the resistance relationship between the forces and velocities, allows that hydrodynamic interactions can be included in the resistance matrix of only one component, either the body or the tail. Furthermore, results of previous numerical studies show that the total drag force

on the tail is not affected by the choice of body as much as the total drag force on the whole swimmer is affected (Ramia *et al*., 1993).

6.2. Estimation of Hydrodynamic Interaction Coefficients and Resistive Force Coefficients from the CFD-model

Two sets of resistive force coefficients are used for tails in the hydrodynamic model: the first set is by Lighthill (1976), i.e. SBT-based $c_{t,n}$ coefficients; and the second set is obtained from the CFD simulation for a stationary swimmer with a rotating helical tail. The helical radius (amplitude) of the tail is set to 0.1 and the wavelength to 2/3 as the base-case design (see Table 3.1).

The resistive force coefficients, c_n and c_t computed from the base-case CFD simulation are easily calculated as 995.5 and 775.2, respectively, with the help of Eq. (4.36). Arguably, the constant pair of force coefficients, which are obtained from the CFD simulation, incorporates realistic flow conditions such as the finite length and radius of the tail and the trailing-edge force due to the motion of the tip of the tail, which are not taken into account in the derivation of the resistance coefficients from the slender body theory (Lighthill, 1976). Furthermore, the resistive force coefficients found from CFD-model differs from the resistive force coefficients presented in Fig. 5.7, provided that the end-effects and body-tail interactions modifying the local resistance close to body are taken into account in the latter calculations.

SBT-based resistive force coefficients presented by Lighthill (1976) vary with the parameter α, which is the ratio of the chord length of the tail to its apparent length and varies with the amplitude and wavelength. Fig. 6.2a shows the variation of the c_n / c_t ratio with respect to number of waves, and Fig. 6.2b shows the variation of the ratio with respect to amplitude for helical tails and traveling plane waves. The constant c_n / c_t ratio for the pair, which is obtained from the CFD simulation for the base case, is also shown on the plots in Fig. 6.2. For traveling-plane-wave tails, wavelength-averaged value of α, the ratio of the chord length to apparent length, is used as it varies locally due to the converging end

unlike the ratio for the helical tail, which remains constant independent of the local position on the tail.

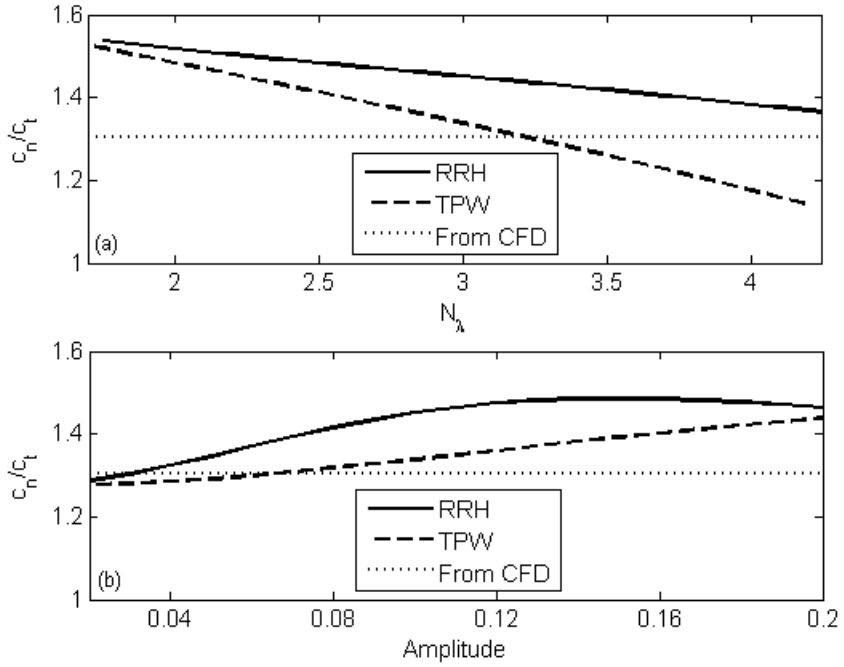

Figure 6.2: The ratio of the utilized resistive force coefficients; obtained from Lighthill's slender-body-theory (1976), as a function of the number of waves (a), and amplitude (b) for rotating rigid helical (RRH) tails and traveling plane waves (TPW).

Resistance coefficients for the body are obtained from the well-known drag coefficients of spherical objects multiplied by translational and rotational hydrodynamic interaction coefficients in the k^{th} direction, $\Upsilon_{T,k}$ and $\Upsilon_{R,k}$ respectively, and used as diagonal factors in the body resistance instead of modified resistance matrix due to the fact that time-dependent swimming behavior is not inspected with this chapter: $\Upsilon^{Helical\ Tail,SBT}_{\{T,s;T,q;R,s\}}$

Interaction coefficients account for the hydrodynamic effect of the tail's motion on the body's resistance coefficients, which are the diagonal elements of the resistance matrix of the body. Off-diagonal elements of the body resistance matrices can be used to account for more general interactions between the directions of body's motion, for example the well-known Magnus effect, which is recently observed for micro particles at very low Reynolds numbers (Cipparone *et al.*, 2011), can be described as the force in the **q**-direction due to the motion of the body in the **s**-direction and the rotation in the **r**-direction, in

swimmer's frame of reference. Moreover, strictly-diagonal form of the body resistance matrix, which is considered here, can be viewed as the result of the diagonalization of a general form that includes all hydrodynamic interactions.

For helical propulsion, it is assumed that in addition to the interaction coefficient in the swimming direction, $\Upsilon_{T,s}^{Helical\ Tail}$, only a single translational resistance for the body in lateral directions, i.e. $\Upsilon_{T,q}^{Helical\ Tail} = \Upsilon_{T,r}^{Helical\ Tail}$, is necessary; and only one coefficient is necessary for the rotation in the swimming direction, $\Upsilon_{R,s}^{Helical\ Tail}$, as body rotations in other directions are not calculated in the model for helical tails for simplicity.

Interaction coefficients for the spherical body of the free swimmer that corresponds to the base-case representative design are calculated directly from the ratio of forces and velocities obtained from the CFD simulation. Time-dependent forward velocity of the swimmer is nearly constant varying within 0.6% of its average value, -0.038. The net hydrodynamic drag force in the swimming direction on the spherical body of swimmer is obtained as 81.7, which corresponds to 2.28 times the well-known drag force on spherical objects. Therefore the interaction coefficient in the swimming direction is obtained as, $\Upsilon_{T,s}^{Helical\ Tail,CFD} = 2.28$. Similarly, the angular velocity of the swimmer is almost constant varying within 0.2% of its time-averaged value, which is obtained as -0.4; the torque exerted on the spherical body is 1.09 times its well-known value for spherical objects and sets the value interaction coefficient for rotations in the swimming direction as $\Upsilon_{R,s}^{Helical\ Tail,CFD} = 1.09$.

Lateral velocities and forces are both sinusoidal in time with zero mean and amplitude of 0.015 and 7.235 respectively. The phase between the wave forms of lateral velocities and forces is equal to $\pi/2$.The ratio of the amplitudes of the lateral forces and the lateral velocities is 0.51 times the spherical drag; however, for lateral directions, interaction coefficient from the solution of the inverse problem are obtained as $\Upsilon_{T,q}^{Helical\ Tail,CFD} = \Upsilon_{T,r}^{Helical\ Tail,CFD} = 1.24$.

Actual values of interaction coefficients vary with the choice of resistive force coefficients used for the tail, since the effect of hydrodynamic interactions between the body and the tail is evaluated by the interaction coefficients applied only to body

resistances. Therefore, for the resistive force coefficients obtained from Liqhthill's slender-body-theory (1976), a new set of interaction coefficients are necessary. In this case, the inverse problem is solved for already calculated velocities to obtain interaction coefficients for the body resistance matrices, which are calculated as $\Upsilon_{T,s}^{Helical\ Tail,SBT} = 3.35$, $\Upsilon_{T,q}^{Helical\ Tail,SBT} = \Upsilon_{T,r}^{Helical\ Tail,SBT} = 1.1$, and $\Upsilon_{R,s}^{Helical\ Tail,SBT} = 0.85$.

Flagellar propulsion with traveling plane waves (TPW), in essence, can be considered as a special case of the helical propulsion since the deformation of the tail in the **r**-direction is set to zero. Therefore, it is assumed that resistive force coefficients obtained for the swimmer with the rotating helical tail should perform reasonably well here. In this case, interaction coefficients for body resistances are required for the forward motion of the swimmer in the **s**-direction, $\Upsilon_{T,s}^{Planar\ Wave}$, lateral motion of the swimmer in the **q**-direction, $\Upsilon_{T,q}^{Planar\ Wave}$, and the rotation of the body in the **r**-direction, $\Upsilon_{T,r}^{Planar\ Wave}$. The interaction coefficient in the swimming direction is calculated from the ratio of the time-averaged force and the time-averaged velocity in that direction, which are obtained from the CFD simulation of the free swimmer with the traveling-plane-wave tail whose amplitude and wavelength are set to the base-case values, 0.1 and 2/3 respectively; the calculated value of the interaction coefficient is obtained as, $\Upsilon_{T,s}^{Planar\ Wave,CFD} = 2.21$. This value is very close to the one obtained for the swimmer with the helical tail.

Similarly, from the ratio of the amplitudes of the lateral force and the lateral velocity, which are zero in average, the lateral interaction coefficient is obtained as: $\Upsilon_{T,q}^{Planar\ Wave,CFD} = 3.14$. Lastly, the interaction coefficient for the rotational resistance of the body in the **r**-direction perpendicular to the plane of propagating wave is obtained from the amplitude ratio of the torque and the angular velocity in that direction as $\Upsilon_{R,r}^{Planar\ Wave,CFD} = 0.45$.

Interaction coefficients are also calculated from the solution of the inverse problem for both sets of resistive force coefficients, from the CFD simulation for the stationary swimmer with a helical tail and from Lighthill's SBT-bsed $c_{t,n}$ coefficients; and the results are presented in Table 6.2. It is somewhat surprising to see that the interaction coefficient for the **r**-rotation of the swimmer is negative. It is suspected that the result is an artifact of using only the diagonal components of the body resistance matrix. In effect, the **r**-rotation

of the swimmer is strongly linked with the **q**-translation of the swimmer, i.e. lateral rigid-body translation and rotation of the swimmer, due to the strong coupling between the **r**-torque on the swimmer and the **q**-force on the tail and the fact that the center of mass of the swimmer coincides with the center of the spherical body. In essence, having a very large interaction coefficient in the **q-** translation and a negative one for the **r**-rotation could be the result of more complex interactions between the two modes of the motion. Furthermore, these observations indicate the necessity of phase angle approach to the problem of time dependent velocity and fluid resistance of the planar wave propagating tail, in a similar fashion to the analysis conducted for rotating helical tail.

Table 6.2: Interaction coefficients for the body resistance matrices of the spherical body

Propulsion type	Tail resistance coefficient	Body drag factor
RRH (Helical Wave)	Lighthill's SBT-based $c_{t,n}$ formulae	$\Upsilon^{Helical\ Tail,SBT}_{\{T,s;T,q;R,s\}} = \{3.35; 1.1; 0.85\}$
RRH (Helical Wave)	CFD-based $c_{t,n}$ = {995.5, 775.2}	$\Upsilon^{Helical\ Tail,CFD}_{\{T,s;T,q;R,s\}} = \{2.24; 1.25; 1.09\}$
TPW (Planar Wave)	Lighthill's SBT-based $c_{t,n}$ formulae	$\Upsilon^{Plane\ \mathrm{Wave},SBT}_{\{T,s;T,q;R,s\}} = \{1.95; 6.75; -2.5\}$
TPW (Planar Wave)	CFD based $c_{t,n}$ = {995.5, 775.2}	$\Upsilon^{Plane\ \mathrm{Wave},CFD}_{\{T,s;T,q;R,s\}} = \{1.65; 8; -3\}$

6.3. Parametric Validation with Computational Fluid Dynamics (CFD) Simulations

The hydrodynamic model is validated with additional CFD simulations for different amplitudes and wavelengths than the ones used in the representative design for the estimation of interaction coefficients for the body and resistance coefficients for the tail presented in the section "5.4.2.2. Hydrodynamic interaction in body resistance calculations" in detail. The study can be extended to other parameters such as the body radius, tail length, body type etc. Here, only wavelength and amplitude are considered for clarity and conciseness as design variables of flagellar propulsion. Moreover, frequency, diameter of the body and fluid properties are lumped into the scaling Reynolds number used in

simulations. Thus, for small Reynolds numbers, the velocity of the robot scales linearly with the frequency of tail rotations and its body size.

For swimmers with helical tails, hydrodynamic model results are compared with CFD simulation results in Fig. 6.3. Average forward velocity (see Fig. 6.3a), amplitude of the lateral velocity (see Fig. 6.3b) and the body rotation rate (see Fig. 6.3c) are plotted against the amplitude, which is the radius of the helix. According to hydrodynamic model results with resistive force coefficients from Lighthill's slender-body-theory based analysis (1976), magnitude of the time-averaged forward velocity increases with the amplitude with a rate that slows down at higher values. The model results with CFD-based force coefficients also show that the average velocity increases with the amplitude; in this case, a slightly better agreement with actual simulation results is observed than the case with SBT-based force coefficients. The agreement between the hydrodynamic surrogate model and simulation results is better at small values of the amplitude than large ones (see Fig. 6.3a), thus, indicating that as the helical radius increases and the flow induced by the tail gets stronger than the case used for the estimation of interaction coefficients the accuracy of the surrogate model deteriorates. Percentage errors from the plots are listed in Table 6.3 for all cases.

Time-dependent lateral motion of the swimmer is periodic with zero mean-value. However, the amplitude of the lateral velocity increases with the amplitude of the helical waves almost linearly; the agreement is slightly better for the force coefficients from the slender body theory than the force coefficients obtained from the CFD simulation for the stationary swimmer (see Fig. 6.3b). Similarly, in Fig. 6.3c, model results with analytically obtained force coefficients from the slender body theory agree with simulation results for large wave amplitudes better than the results with constant force coefficients (11.8% error vs. 42.7%); agreement is poorer for both sets of coefficients at small amplitudes.

Average forward velocity, amplitude of the lateral velocity and the average body rotation rate are plotted against the number of waves in Figs. 6.3d,f , respectively. The forward velocity predicted by the hydrodynamic model indicates that the wavelength does not have a significant effect, and agrees well with CFD simulation results for both sets of parameters (see Fig. 6.3d), i.e. 6.9% for constant c_n and c_t, and 9.3% for c_n and c_t from the slender-body-theory (SBT). The amplitude of the lateral velocity peaks at half integer

values of the number of waves, i.e. for N_λ = 1.5, 2.5, 3.5, etc, and falls at full integer values. When the helical waves are in full-periods, forces in the lateral directions are minimal, and emerge only due to the bias introduced by the shape function embedded in position dependent amplitude function used to implement wave deformations. However, when the helical waves do not have full turns, the symmetry is broken and hydrodynamic forces in lateral directions emerge and the effect is maximized when the incomplete wave is half.

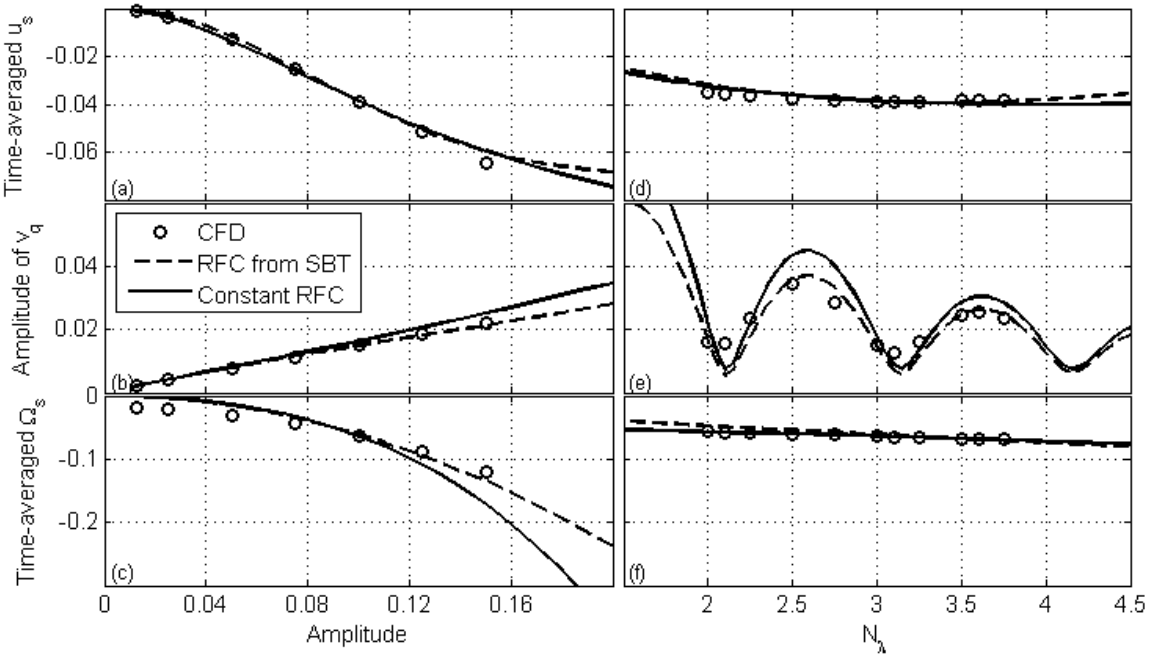

Figure 6.3: Helical wave validations: time-averaged forward (a,d), amplitude of the lateral (b,e), and rotation of the body (c,f) against the amplitude (a-c) and number of waves (d-f) for helical tails: circles are CFD results, solid lines are for hydrodynamics model with resistive force coefficients obtained from the CFD simulation for a stationary swimmer, and dashed lines are for hydrodynamic model results with resistive force coefficients obtained from Lighthill's slender-body-theory (SBT) based approach (1976).

Moreover, the intensity of the lateral motion diminishes as the number of waves increases indicating that the effect of the incomplete wave is diluted as the total number of waves on the tail increases. Overall, the hydrodynamic model predicts the lateral motion well especially with analytical resistive force coefficients compared to resistive force coefficients computed from the CFD simulation for the stationary swimmer (see Fig. 6.3e).

Lastly, the rotation rate of the body does not vary with the number of waves on the tail significantly, and predicted reasonably well with the hydrodynamic model as shown in Fig. 6.3f.

For swimmers with traveling-plane-wave tails, hydrodynamic model results are compared with CFD simulation results in Fig. 6.4 for both sets of parameters: resistive force coefficients from the slender body theory (RFC from SBT) and corresponding hydrodynamic interaction coefficients of the body, and resistive force coefficients determined from the CFD simulation for stationary swimmer with the helical tail (constant RFC) and corresponding interaction coefficients.

Time-averaged forward velocity, amplitude of the lateral velocity and the amplitude of the angular velocity of the body in the **r**-direction increase with the amplitude, and are predicted very well with the hydrodynamic model for both sets of parameters (see Figs. 6.4a-c). Time-averaged forward velocity of the swimmer is plotted against the number of waves on the tail in Fig. 6.4d. For small number of waves, hydrodynamic model results agree well with CFD simulation results for both sets of coefficients. However, time-averaged velocity calculated by the model with force coefficients from the slender body theory decreases with increasing number of waves for large values. Model results with constant force coefficients agree very well with CFD simulation results for large number of waves as well.

The lateral velocity of the swimmer in the **q**-direction is periodic in time with zero-average value. Amplitude of the lateral velocity varies with the number of waves on the tail similarly to helical tails with the exception that peaks are observed at number of waves equal to full integers and bottoms at half-integers as shown in Fig. 6.4e. In part this is because of the effect of the amplitude-shape function, which introduces a bias near the body and breaks the balance of forces towards the tip of the tail (see Fig. 6.5): for half integer waves on the tail **q-**direction forces are symmetric and net force is small, on the other hand for full integer waves the motion of the tip of the tail is not balanced by the motion of the tail near the body. Hydrodynamic model results agree very well qualitatively with the CFD results despite a slide shift in the results for number of waves larger than 3.5. Moreover, the hydrodynamic model with resistive force coefficients from the slender body theory predicts that the overall trend of the amplitude of the lateral velocity decreases

slowly with respect number of waves on the tail, although results of the model with constant force coefficients show a decreasing trend as the number of waves increases and agrees well with the CFD simulation results (see Fig. 6.4e). Lastly, the amplitude of **r**-rotations of the body follows a trend with peaks near the half integer waves and falls at slightly larger values than the full integer number of waves on the tail (see Fig. 6.4f). Although the overall trend agrees well with the CFD simulation results, the range of the falls and peaks are not as large in CFD simulation results as in the hydrodynamic model results.

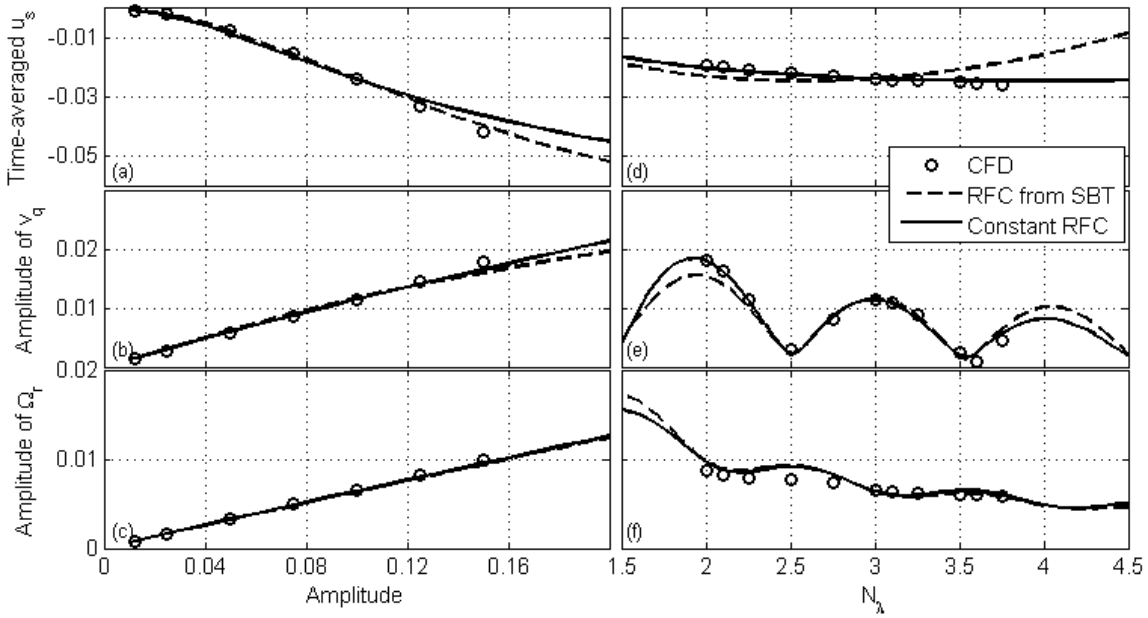

Figure 6.4: Planar wave validations: time-averaged forward velocity (a), amplitude of the lateral velocity (b), and amplitude of body rotation around the **r**-axis (c) are plotted against the amplitude of waves for TPW tails (a-c) and number of waves (d-f). Circles are CFD results, solid lines are for hydrodynamics model with resistive force coefficients obtained from the CFD simulation for a stationary swimmer with a helical tail, and dashed lines are for hydrodynamic model results with resistive force coefficients obtained from Lighthill's slender body theory (SBT) based approach (1976).

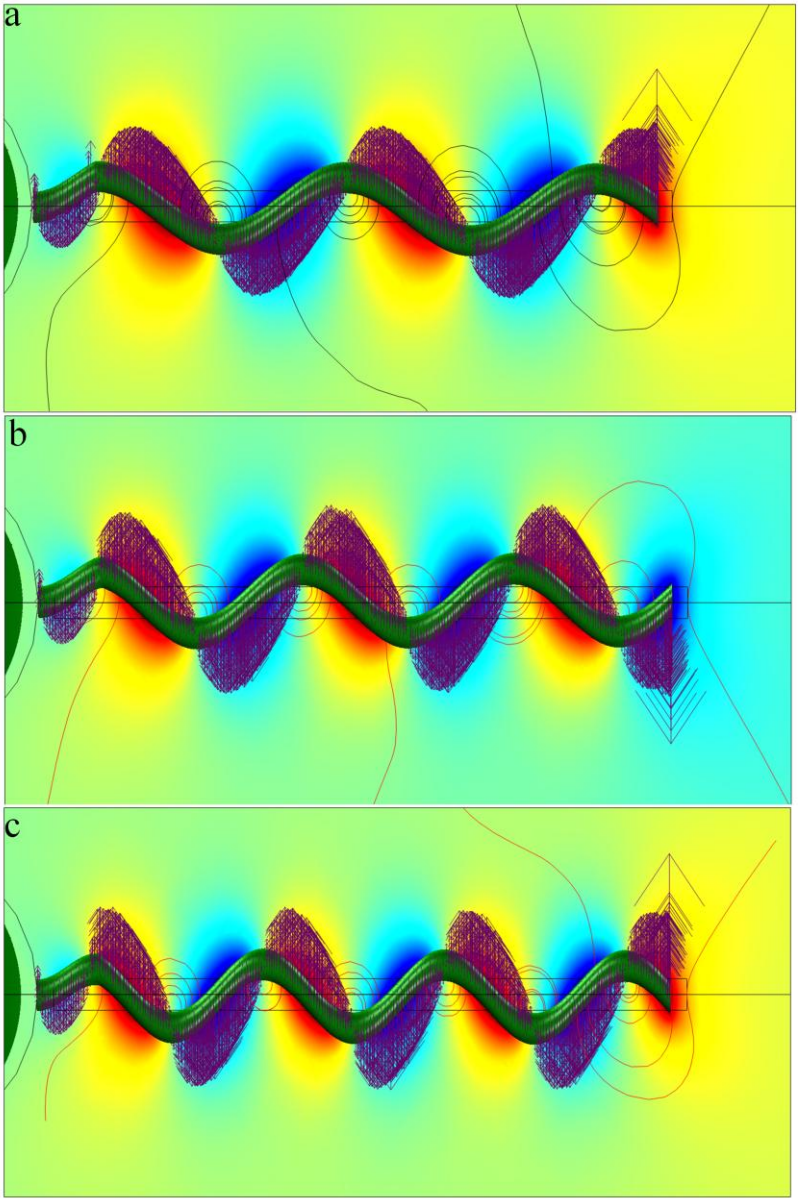

Figure 6.5: Flow and force field around the sinusoidal plane wave propagating tail: proportional dense arrows represent the fluid resistance along **y**-direction; streamlines denote the velocity field; background color map demonstrates the local **y**-velocity. The lateral force acting on the tail cancels out with the presence of half waves (a,c); however, the canceling out effect vanishes due to the converging end towards the body with full waves (b).

Summary of the performance of the hydrodynamic surrogate model is presented in Table 6.3. Overall, the surrogate model agrees very well with CFD simulation results for both sets of resistive force coefficients (RFC) used in the model and for both actuation types.

Table 6.3: Errors in predictions of the hydrodynamic model, (absolute error; range of calculated velocity values)

		Number of Waves		Amplitude	
		CFD-based constant c_n, c_t	Analytical c_n, c_t	CFD-based constant c_n, c_t	Analytical c_n, c_t
Helical tail	$\bar{u}_s$	0.0025, [-0.0327, -0.0393]	0.0033, [-0.0319, -0.03939]	0.0047, [-0.0011, -0.0596]	0.0046, [-0.0008, -0.0597]
	$V_{q,\max}$	0.0085, [0.0073, 0.0435]	0.0102, [0.0052, 0.0356]	0.003, [0.002, 0.0251]	0.00074, [0.002, 0.0212]
	$\bar{\Omega}_s$	0.0011, [-0.0574, -0.0694]	0.00843, [-0.0708, -0.4783]	0.0516, [-0.0009, -0.1722]	0.00143, [-0.0009, -0.1349]
Traveling plane waves	$\bar{u}_s$	0.0011, [-0.020, -0.024]	0.0031; [-0.0186, -0.0226]	0.0056; [-0.0006, -0.0364]	0.0023; [-0.0005, -0.0397]
	$V_{q,\max}$	0.0013; [0.0023, 0.018]	0.0022; [0.0015, 0.0203]	0.0012; [0.0015, 0.0165]	0.0017; [0.0016, 0.0160]
	$\Omega_{r,\max}$	0.0014; [0.0059, 0.0096]	0.0010; [0.0058, 0.0095]	4.1×10^{-4}; [8.2, 95.1] $\times10^{-4}$	5.5×10^{-4}; [8.1, 93.8]$\times10^{-4}$

6.4. Conclusions

Forward and lateral translational and rotation of bio-inspired micro swimmers that consist of a body and an actuated tail are predicted with a hydrodynamic surrogate model, which is based on a number of parameters used in the resistive relationship between the force and velocity vectors on the tail and the body. The hydrodynamic model runs essentially in real-time to predict the full trajectory of swimmers unlike the three-dimensional CFD-model that completes the solution of the Navier-Stokes equations in hours if not a day.

For the actuated tail of the swimmer, which is considered as either a rotating helix or traveling-plane-wave deformations on a flexible rod, two sets of resistive force coefficients are used: one set is from the slender body theory of Lighthill (1976), and the second set is directly calculated from a single CFD simulation for a stationary swimmer with a helical tail for which the amplitude and wavelength are set to 0.1 and 2/3, respectively in non-dimensional units. For each form of flagellar actuation and the set of force coefficients, hydrodynamic interaction coefficients are estimated for the body of the swimmer from the solution of the inverse problem for the base case values of the amplitude and the wavelength. Then the hydrodynamic model is validated directly against CFD-model results for swimmers with helical and traveling-plane-wave tails for which the amplitude is varied between .01 and .15 and the wavelength is varied between 0.5 and 1. For all cases, the surrogate hydrodynamic model results agree reasonably well with CFD-model results.

Furthermore, experimentally measured time-averaged forward velocity and body rotation rates for micro organisms that are presented in literature are compared with the results of the hydrodynamic model with resistive force coefficients obtained from the slender body theory. Once the hydrodynamic interaction coefficients of the body are determined from the inverse problem for a fixed specimen, predicted forward velocities and body rotation rates agree very well with the measurements for other species with different body and tail dimensions.

6.4.1. Applications of Validated Hydrodynamic Model: Search for Optimum Geometric Designs

Design of an artificial micro swimmer can be carried out with the validated hydrodynamic surrogate model that can replace the computationally exhaustive three dimensional CFD-model simulations. For instance, the energy consumption of the robot with B_o = 0.1 and λ = 2/3 can be minimized with the maximization of its efficiency, which is signified as:

$$\eta = \frac{\Pi_{body}}{\Pi_{tail}}, \tag{6.3}$$

where $\Pi_{body} = F_x U_x$ is the average rate of work done to move the body of the robot with the velocity of U_x against the drag force on the body, F_x, and Π_{tail} is the rate of work done to actuate the tail of the robot and calculate from $\Pi_{tail} = T_x \omega_{tail}$ for helical tails, where T_x is the torque needed to rotate the tail with the angular velocity, ω_{tail}. For travelling plane waves, the rate of actuation work is calculated from the integration of the product of the local force and the local net velocity in the lateral direction over the entire tail length.

Average forward velocity (see Figs. 6.6a-b) and the hydrodynamic efficiency of swimmers (see Figs. 6.6c-d) are calculated with the hydrodynamic model for amplitudes varying between 0.01 and 0.5 and for number of waves between 0.5 and 5. According to Figs. 6.6a-b, there is a similarity between the forward velocity of swimmers with helical tails and traveling plane waves, former with the maximum velocity of 0.21 for $B_o = 0.5$ and $N_\lambda = 1$, and the latter with the maximum velocity of 0.12 for the same amplitude and $N_\lambda = 0.8$. Therefore, in order to design a swimmer with the fastest velocity, one has to build a tail with a single helical turn with the largest amplitude. Moreover, swimmers with helical tails are considerably faster than the ones with traveling plane waves.

From Figs. 6.6c-d, the efficiency of the swimmers with helical tails is considerably larger than the efficiency of the swimmers with traveling plane waves; the maximum efficiency for the helical tails is obtained as 2.5%, and as 0.29% for traveling plane waves. Furthermore, the hydrodynamic efficiency values for helical swimmers, which are on the order of 10^{-1}, agree with the efficiency study carried out by Purcell (1997).

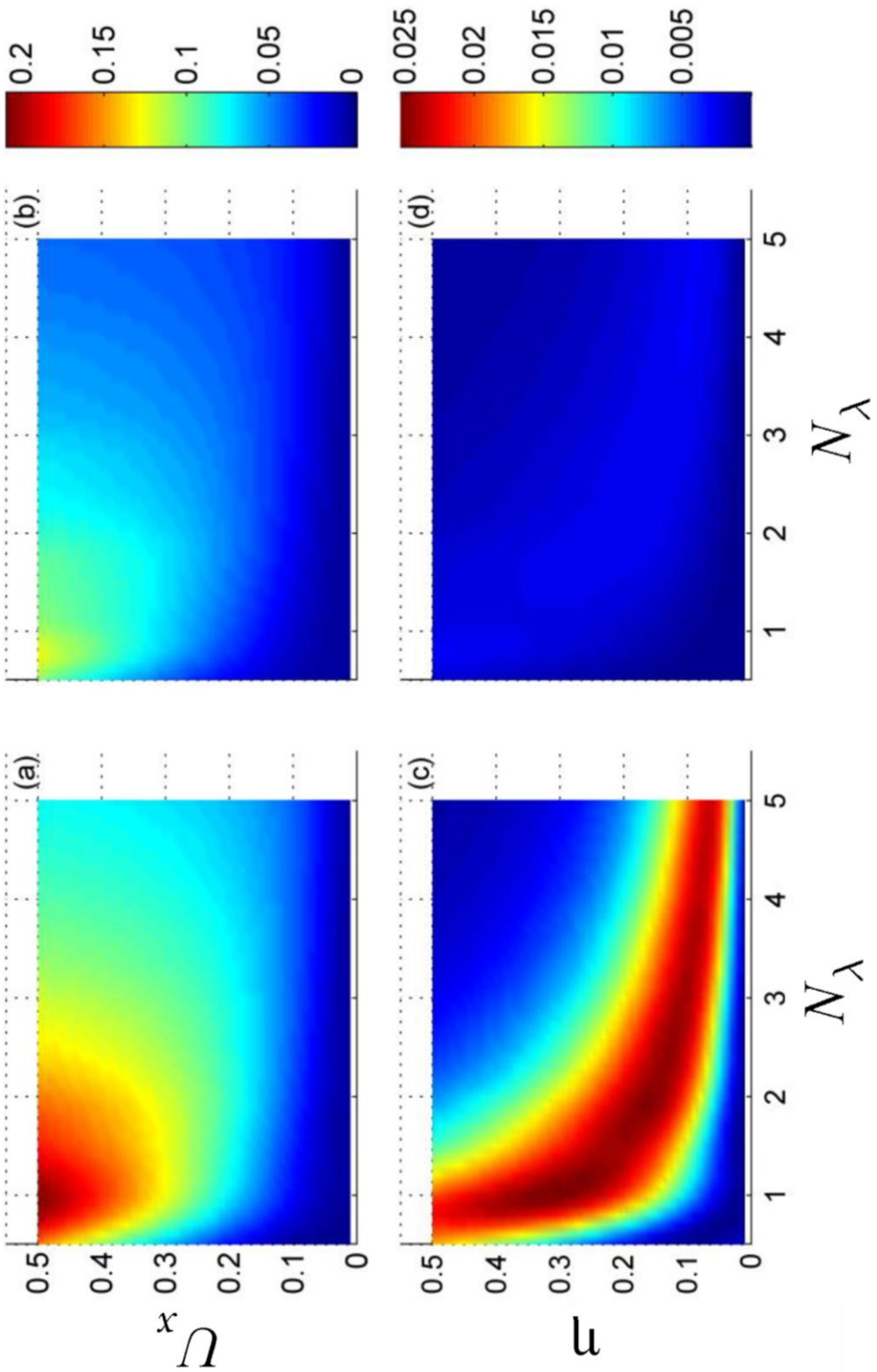

Figure 6.6: Hydrodynamic efficiency and forward velocity values for bio-inspired robots with helical and planar wave propagation tails of base case design parameters.

7. IN-CHANNEL SWIMMING RESULTS

This section presents the results of experimental studies on untethered on-board powered helical swimmer. All experiments are conducted in channels filled with viscous fluid, i.e. silicone oil. There are two kind of swimming orientations; namely vertical and horizontal swimming. Results obtained by vertical experiments are utilized to validate the CFD-model provided that contact friction and lubrication effects are absent. However, the horizontal channel experiments with varying channel diameters constitute the bulk of the experimental work on in-channel swimming. Moreover, experimental results are predicted and compared with the hydrodynamic model.

Images captured by the CCD-camera are inspected frame-by-frame in order to resolve the body rotation rate, Ω_{body}, and tail rotation rate, ω_{tail}, along with swimmer's forward velocity U_x only, given that the robot's weight is bigger in magnitude than the buoyancy force acting on it. Hence, infinitesimal lateral rigid body translations or rotations are neglected. Furthermore, based on the Nyquist-rate, the sampling rate of the CCD-camera is found sufficient to resolve the rotation rates of the swimmer's body and tail in the lab frame where the camera is positioned.

Results are obtained by averaging out five distinct measurements and visible error bars are calculated with 95% confidence interval (see Appendix 6 for further detail on helical tails and observed velocity values). Observed rotation rate of the tail is input in SBT and RFT-based hydrodynamic models as the actuation frequency of the tail, ω_{tail}, in order to study the performance of the reduced-order hydrodynamic model. It is noted that the actuation frequencies are not controlled; the observed tail and body rotation rates are actually due to the motor torque balancing the effective hydrodynamic shear torque and friction on the entire swimming bio-inspired robot.

RFT model calculations are carried out with all rows of the resistance matrices set to zero except the first and the fourth row of robot's total resistance matrix to ensure the calculation of the trajectory for two degrees of freedom, forward translation and body rotation. Helical tail is discretized by at least 100 intervals per wavelength.

Furthermore, given that the replaced fluid would flow around the body in the direction of wave propagation, fluid resistance acting on the swimming robot's body is modified with the correction presented by Happel and Brenner (1965) in order to account for the effect of upstream. This correction is carried out for the simulations, which employ tangential and normal resistive force coefficients, representing the experiments with channels having closed ends; with either vertical or horizontal orientation. The proximity of the swimmer's body to channel wall is assumed to be 1 μm. However, the channel diameter effect for pure eccentricity (see Fig. 7.1) is not corrected for validation of in-channel experiments, given the fact that eccentricity function leads to much higher correction factors than that of the HI-coefficients used in this analysis.

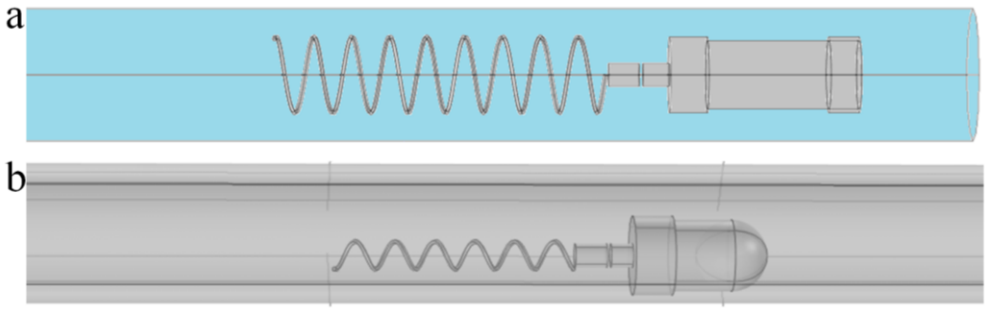

Figure 7.1: Swimmer position with respect to cylindrical channel: Concentric swimmer (a); eccentric swimmer (b).

Time-integration of the model with resistive-force-theory (RFT) based approach is carried out by Adams-Bashforth-Moulton PECE solver (Shampire and Gordon, 1985). It is noted that each simulation took approximately two to three seconds with a 64-bit high-end Linux-based workstation. Time-averaged RFT and experiment-based results presented here are obtained via averaging out the final two periods whereas results obtained by SBT-based approach are already time-averaged do not require further processing.

Lastly, the reader will find in Appendix 1 a brief discussion about the experimental work on the piezoelectric actuation based planar wave propagation with early experimental

results, which is accompanied with a discussion on the reasons why that actuation method is not further studied.

7.1. Horizontal vs. Vertical In-Channel Swimming Experiments

In horizontal in-channel swimming experiments, the bio-inspired robot is moving near the wall with an indeterminate instantaneous proximity due to the combined effect of gravitational pull, buoyancy and hydrodynamic lift; however, in vertical in-channel swimming experiments the weight of the body is reduced such that the geometry of the wet surface remained unchanged and the overall density of the robotic prototype is equal to that of the silicone oil. Six tails, of which all actual length and weight of the wires used are exactly the same, with different apparent lengths are used in the comparative study of horizontal versus vertical in-channel swimming experiments (see Appendix 6 and Fig. 7.2)

Vertical channel experiments are carried out with robots having a cork glued at the tip of its body. The cork does not only assures average density to be equal to that of the silicon oil, but also exerts a torque due to buoyancy, which forces the robot translate parallel to gravitational pull. As the robot translates forward within the channel, its body replaces fluid in front which in turn induces a local back flow around. Provided that the channel is long enough, bio-inspired robot tends to move away from the channel wall, i.e. at the center along the symmetry axis, due to the combined effect of buoyancy torque, back flow induced by replaced fluid, and the constant rotation of the body.

When the symmetry axis of the channel is aligned perpendicular to the gravitational pull, with extra weight in the body, the robot sits at the bottom. The tail rotation provides enough thrust to push the body forward which separates from the surface, and furthermore acquires extra traction due to the close proximity to channel walls, thus the forward swimming velocity increases in comparison with the vertical channel experiments even with reduced tail rotation rates (see Fig. 7.2). In fact, the forward velocities of horizontal in-channel swimming experiments being either comparable to or bigger that the forward velocities observed for vertical in-channel experiments implies the amplification effect of local lubrication on the rotating helical tail on the forward thrust.

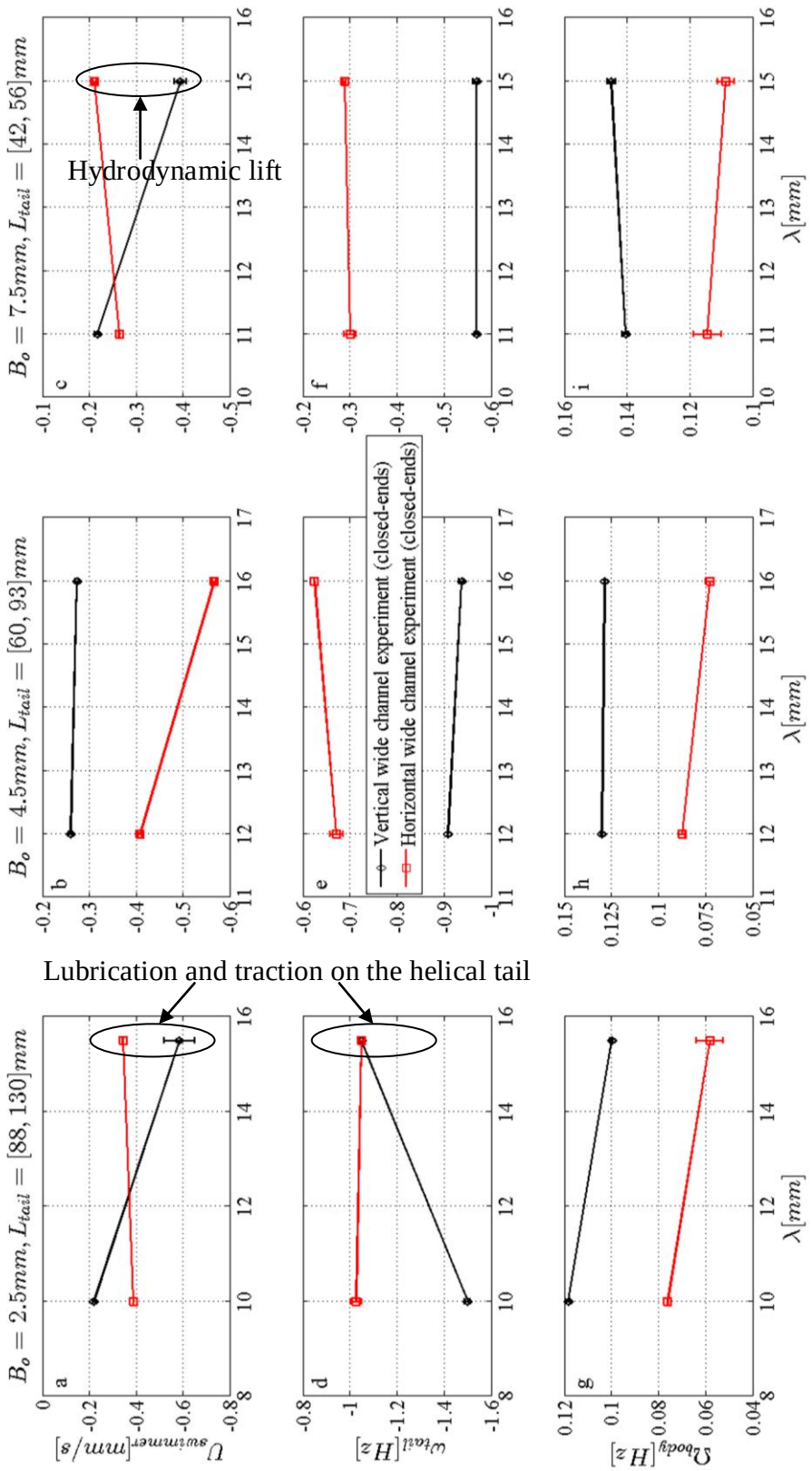

Figure 7.2: Vertical experiments vs. horizontal experiments in closed-ended wide channels.

One of the two exceptions, where the forward velocities are comparable, is the case where the total length of the robot is bigger than half length of the swimmer (see Fig. 7.2a). In fact, robot did not have enough distance to free itself from the channel walls, thus the wall effect, traction due to local lubrication, acting on the robotic prototype's tail results in faster swimming velocity than that of the horizontal experiment. Moreover the extra shear torque acting on the tail prevented the motor to rotate with a much faster angular velocity (see Fig 7.2d). The other instance is one with the largest wave amplitude (see Fig. 7.2.c): in this instance, while swimming in horizontal channel, the body is lifted further away from the channel wall towards the center where the effective body resistance is higher in comparison (Happel and Brenner, 1965) leading to smaller forward velocity values.

7.2. Vertical Experiment Results vs. Reduced-Order Hydrodynamic Model

Here, registered velocity values from the vertical swimming experiments are predicted with RFT-based hydrodynamic model using the resistive force coefficient sets presented in literature or obtained by torus-rod analogy, SBT methods presented by Lighthill (1976), and the asymptotic solutions of Stokes flow in channels presented by Felderhof (2010).

The body resistance coefficients of prolate spheroids (Perrin, 1934), although not suitable in this particular case, in motion are adjusted with Υ_x values, which are obtained by inverse velocity kinematics, for rigid-body translation and rotation of the cylindrical body. This procedure is carried out for only once for every coefficient set. The hydrodynamic interaction (HI) coefficients, which signify the combined interactions between body, tail and the channel, are listed in Table 7.1. Interaction coefficients compensate for geometric effects, body tail interactions and robot channel interaction altogether. It is observed that the agreement between the hydrodynamic model results and experimental results fades with changing tail geometry.

Here, the performance of selected resistive force coefficient sets, SBT-approach and asymptotic analysis are compared with the vertical channel experiment results (See Figs.

7.3-7.5). It is observed that resistive force coefficients implemented for bounded viscous mediums are slightly favorable. It is also observed that the forward velocity of the robotic prototype and the body rotation rate increases with increasing B_o/R_{body} ratio. The results are inconclusive to study the effect of varying wave length on the velocity values given that an incremental increase in total number of waves, combined with varying tail length, may result in slight decrease or increase in the forward swimming velocity and body rotation rate.

It is presented in Fig. 7.3 that resistive force coefficient sets, which are presented for unbounded viscous mediums, provide reasonably well predictions on the forward swimming velocity with large wave amplitudes (see Figs. 7.3b-c). On the other hand, they have a better performance on the body rotation rates with smaller wave amplitudes (see Figs. 7.3d-e).

It is observed in Fig 7.4 that the resistive force coefficient sets given for bounded viscous mediums predict the forward velocity and body rotation rates with a reasonable agreement for small wave amplitudes (see Figs. 7.4a-b,d-e). However, as the wave amplitude increases the hydrodynamic model calculations deviate with considerable error (see Figs. 7.4c,f). It is noted that the RFC set based on torus-rot representation of the helical waves predicts the velocity values with comparable success for small wave amplitudes; however, the error for large wave amplitudes is greater than that presented by the RFC sets found in literature (see Figs. 7.4c,f).

Finally, Fig. 7.5 depicts the velocity calculations with SBT-based approach presented by Lighthill (1976) and the asymptotical solution presented by Felderhof (2010). It is observed that asymptotic solution of the forward velocity of a rotating helical tail and SBT-based approach do not agree with the experimental results of forward velocity with respect to varying wave amplitude (see Figs. 7.5a,c). On the other hand, the body rotation rates predicted with SBT method agrees well with experimental results for small wave amplitudes (see Fig. 7.5d-e), but with large wave numbers predictions fail drastically.

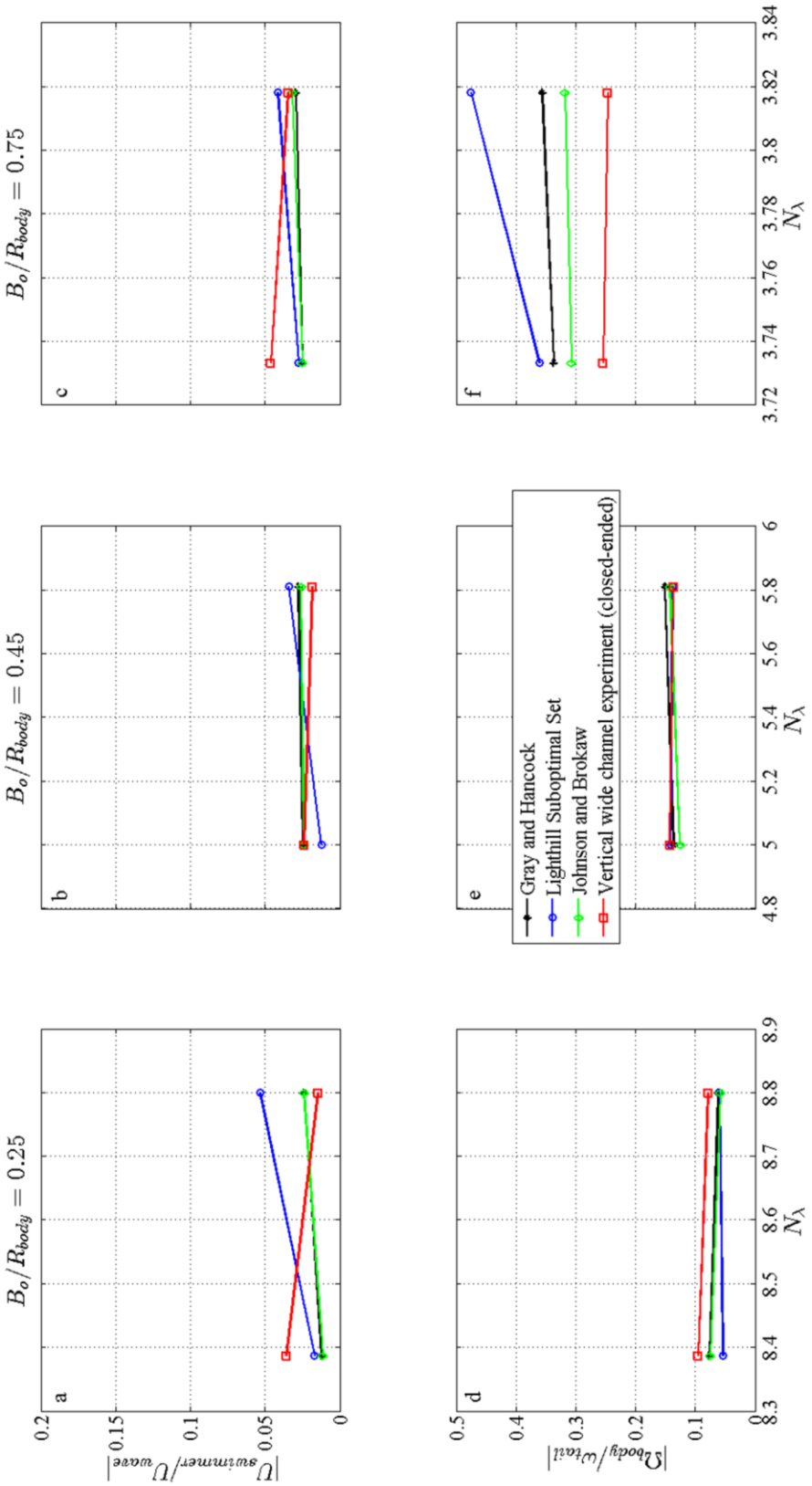

Figure 7.3: Closed-ended vertical wide channel results predicted with unbounded-medium resistive force coefficients.

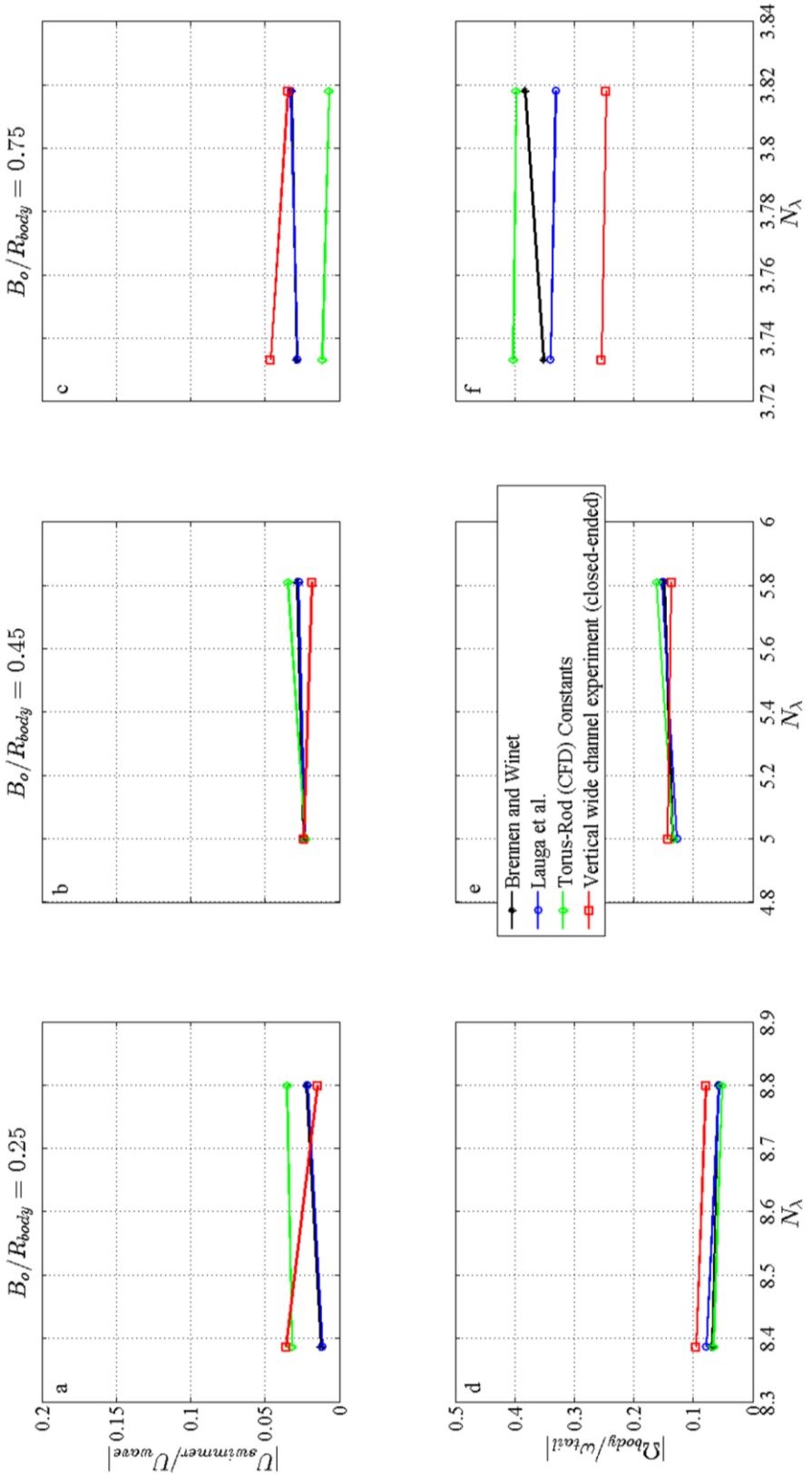

Figure 7.4: Closed-ended vertical wide channel results predicted with bounded-medium resistive force coefficients.

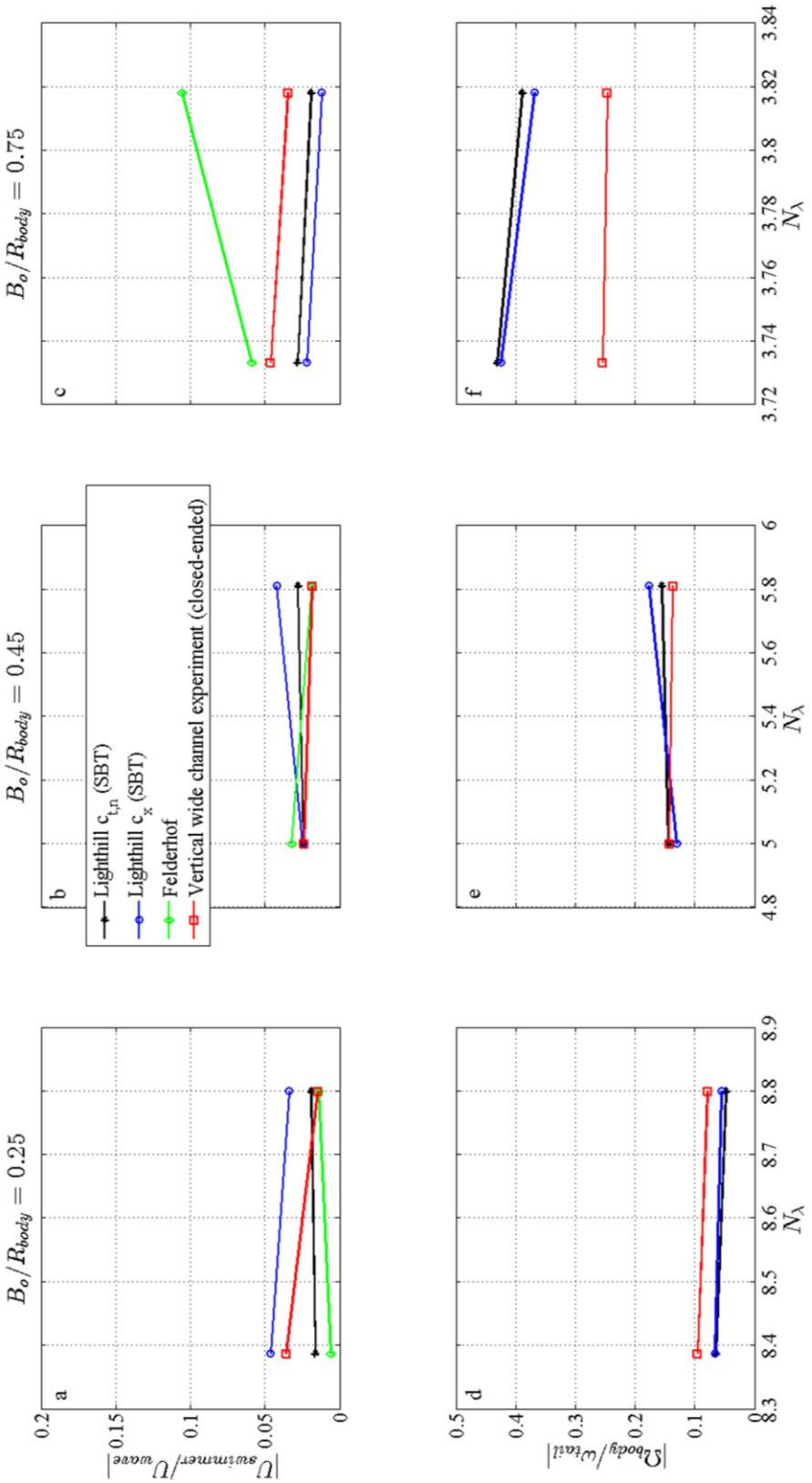

Figure 7.5: Closed-ended vertical wide channel results predicted with SBT-based-approach and Stokes flow based asymptotic solutions.

Table 7.1: Vertical channel (wide, closed-ended) interaction coefficients; under the assumptions of bio-inspired robots moving in unbounded and bounded fluid.

RFC set	Fluid-Drag
Gray and Hancock (1955)	$\{\Upsilon_{T,x}^{body}=16,\ \Upsilon_{R,x}^{body}=1.4\}$
Lighthill (suboptimal set, 1976)	$\{\Upsilon_{T,x}^{body}=4.5,\ \Upsilon_{R,x}^{body}=3.4\}$
Johnson and Brokaw (1979)	$\{\Upsilon_{T,x}^{body}=21,\ \Upsilon_{R,x}^{body}=1.4\}$
Brennen and Winet (1977)	$\{\Upsilon_{T,x}^{body}=18.5,\ \Upsilon_{R,x}^{body}=1.85\}$
Lauga *et al.* (2006)	$\{\Upsilon_{T,x}^{body}=27,\ \Upsilon_{R,x}^{body}=1.4\}$
Torus-Rod Coefficients	$\{\Upsilon_{T,x}^{body}=15,\ \Upsilon_{R,x}^{body}=2.5\}$
Lighthill SBT-based $c_{t,n}$ (1976)	$\{\Upsilon_{T,x}^{body}=8.5,\ \Upsilon_{R,x}^{body}=0.625\}$
Lighthill, c_x, unbounded SBT (1976)	$\{\Upsilon_{T,x}^{body}=4.75,\ \Upsilon_{R,x}^{body}=2.5\}$
Felderhof, bounded Stokes flow (2010)	$\Upsilon_x=105$

7.3. Vertical Experiment Results vs. Computational Fluid Dynamics (CFD) Model

7.3.1. Effect of Wave Geometry on Vertical Swimming with Constant Wire Length

CFD simulations governed by stationary Navier-Stokes equations subject to continuity are validated by the velocity results obtained by the vertical channel experiments. Simulations are carried out with channel and robot dimensions with the scale of 1:1, and actual physical properties, i.e. density and dynamic viscosity, are used for the fluidic domain.

Figure 7.6 demonstrates in dimensionless fashion that the CFD-model is a valid representation for bio-inspired robots in channels; unless the proximity between the two is small enough to induce lubrication effects and, possibly, surface contact (see Fig. 7.6a). The average error between forward velocities is within the range of 12.5%, whereas the average error between the body rotation rates is within the range of 40% (see Fig 7.6.e). Furthermore, the sensitivity to varying amplitude and wave length are predicted accurately.

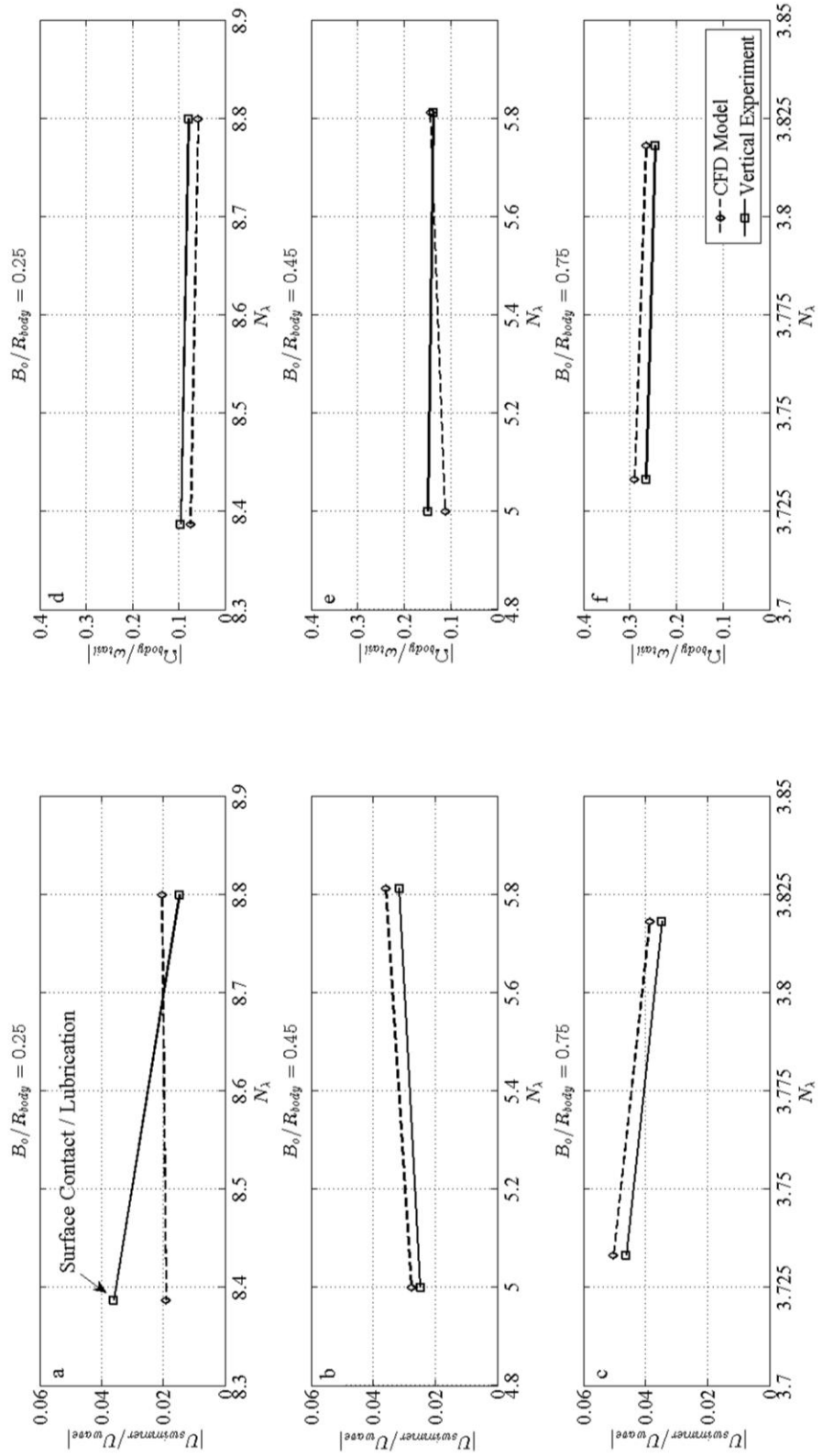

Figure 7.6: Closed-ended vertical wide channel results: experiments vs. CFD.

7.3.2. Effect of Channel Diameter on Vertical Swimming with Constant Wire Length

The geometry of the robot's body in vertical channel experiments prohibits known procedures, i.e. fluid resistance calculations for blunt objects such as spheroids moving near solid boundaries while confined to cylindrical channels (Happel and Brenner, 1965), to determine the outcome of the channel diameter on the actual fluid resistance exerted for the axial swimming conditions. However, with the help of a verified CFD-model, one can determine the effect of channel radius by conducting series of simulations with parameterized channel geometry.

Such study is presented in Fig. 7.7: CFD model validated with vertical in-channel swimming results is used here to investigate the effect of the channel diameter. As the channel diameter, $2R_{ch}$, reduces, the body acts like a plug and swimmer's forward velocity decreases given that the replaced fluid is to overcome increased shear resistance in order to flow through the gap between the body and the channel. The lower limit of forward velocity is obviously zero, where the incompressible fluid is trapped in front. On the other hand, as the ratio of channel radius to body radius increases, the forward velocity increases up to a maximum value, after which decreases slightly converging to unbounded swimming conditions. It is noted that, when the forward velocity is maximum, combination of the amplified shear on the body and the amplified thrust on the rotating helical tail is at its maximum towards the swimming direction.

The body of the swimmer has the dominant role in comparison with its rotating helical tail, because of its geometry combined with the ratio of $R_{body}/B_o > 1$. In effect, the maximum forward velocity values in Figs. 7.6a-e correspond to maximum shear gain on the tail with minimum shear loss on the body due to presence of cylindrical channel bounding the viscous liquid domain. Furthermore, the body rotation rates (see Figs. 7.6f-j) converge to a limiting value as the channel diameter increases.

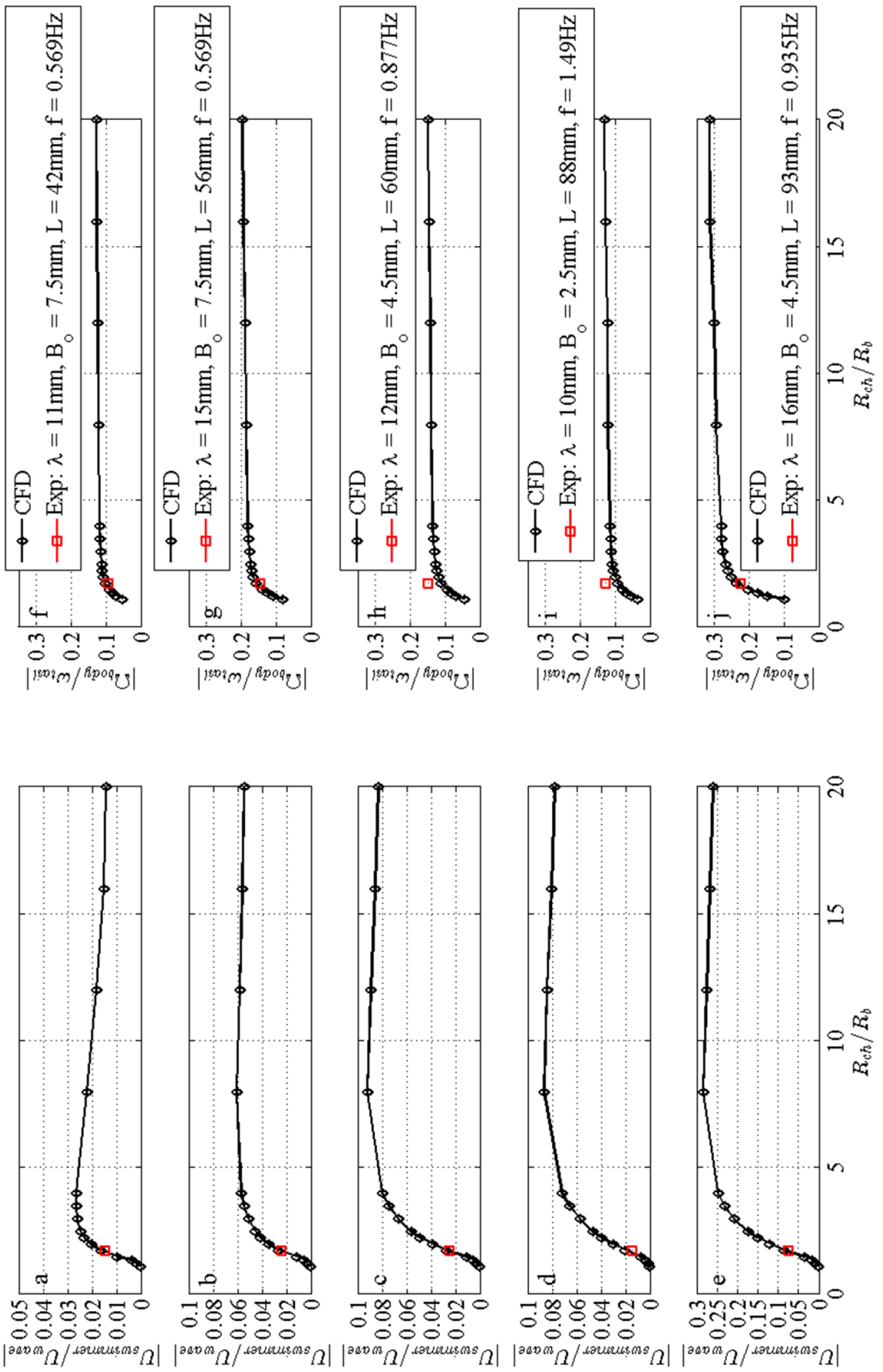

Figure 7.7: Closed-ended vertical wide channel results: effect of channel radius.

7.4. Horizontal Experiment Results vs. Reduced-Order Hydrodynamic Model

Here, registered velocity values from the horizontal swimming experiments in wide-channels with closed ends are predicted with RFT-based hydrodynamic model using different resistive force coefficients, SBT methods presented by Lighthill (1976), and the asymptotic solutions of Felderhof (2010).

The body resistance coefficients of prolate spheroids (Perrin, 1934), akin to the vertical in-channel swimming study, are adjusted with proper Υ_x values for rigid-body translation and rotation of the cylindrical body only once. Interaction coefficients used in the following table also compensate for the geometric effect of the robot's cylindrical body and the combined interactions between body, tail and cylindrical channel. Furthermore, it is observed that further interaction between the robot and the channel wall, i.e. lubrication, traction and friction, resulted in slower forward velocities and body rotation rates. Hence the required interaction coefficients, $\Upsilon_{\{T,R\},x}$, to calibrate the body resistance are significantly smaller in magnitude.

Table 7.2: Horizontal channel (wide, closed-ended) interaction coefficients; under the assumptions of bio-inspired robots moving in unbounded and bounded fluid.

RFC set	Fluid-Drag
Gray and Hancock (1955)	$\{\Upsilon_{T,x}^{body}=6.85,\ \Upsilon_{R,x}^{body}=1.75\}$
Lighthill (suboptimal set, 1976)	$\{\Upsilon_{T,x}^{body}=0.5,\ \Upsilon_{R,x}^{body}=4\}$
Johnson and Brokaw (1979)	$\{\Upsilon_{T,x}^{body}=9,\ \Upsilon_{R,x}^{body}=1.55\}$
Brennen and Winet (1977)	$\{\Upsilon_{T,x}^{body}=8.025,\ \Upsilon_{R,x}^{body}=2.25\}$
Lauga *et al*. (2006)	$\{\Upsilon_{T,x}^{body}=12,\ \Upsilon_{R,x}^{body}=1.6\}$
Torus-Rod Coefficients	$\{\Upsilon_{T,x}^{body}=6,\ \Upsilon_{R,x}^{body}=3\}$
Lighthill SBT-based $c_{t,n}$ (1976)	$\{\Upsilon_{T,x}^{body}=3.75,\ \Upsilon_{R,x}^{body}=1\}$
Lighthill, c_x, unbounded SBT (1976)	$\{\Upsilon_{T,x}^{body}=3,\ \Upsilon_{R,x}^{body}=2.5\}$
Felderhof, bounded Stokes flow (2010)	$\Upsilon_x=50$

Figures 7.8-7.10 represent the performance of different resistive force coefficient sets, SBT analysis, and the asymptotic solutions based on Stokes flow assumptions. Figure 7.8 depicts that unbounded medium RFC sets are inadequate to predict the forward velocity values and body rotation rates coherently. The correlation between the results obtained by the RFC sets presented by Gray and Hancock (1955) and Johnson and Brokaw (1979) is strong for the ratio of B_o/R_{body} = 0.45 (see Fig. 7.8b); however, as the ratio varies the agreement is deteriorated (see Fig. 7.8a,c). Furthermore, the suboptimal RFC set presented by Lighthill (1976) provides reasonable predictions only for large wave amplitudes (see Fig. 7.8c). Moreover, the body rotation rates are predicted with significantly less error for smaller wave amplitudes (see Fig. 7.8d-e), and the error increases with increased wave amplitude (see Fig. 7.8f).

In Fig. 7.9, similar to the unbounded RFC sets, bounded RFC sets only agree with the experimental results, i.e. forward swimming velocities, for a specific ratio of helical wave amplitude to the minor axis of the body of the robotic prototype, i.e. B_o/R_{body} = 0.45 (see Fig. 7.9b). Furthermore, the disagreement between the predictions of the hydrodynamic model using torus-rod representation based RFC set and the horizontal in-channel experiments is bigger in amplitude than those obtained by the other RFC sets (see Fig. 7.9a,c). Lastly, the agreement between the hydrodynamic model and horizontal in-channel experiments is similar to the results obtained by unbounded medium RFC sets; although as the wave amplitude increases the predictions fail, the error with torus-rod representation based RFC set offers the most successful results.

Figure 7.10 presents the comparisons on horizontal in-channel experiments and the predictions of SBT-based approaches and asymptotic calculations. Here it is observed that the SBT methods and asymptotical calculations provide the worst results with exception of $c_{t,n}$ set, which was formulated based on the SBT analysis carried out by Lighthill (1976), for smaller wave amplitudes (see Fig. 7.10a-b). Furthermore, Felderhof's (2010) asymptotical solution also predicts the forward velocity values with reasonable error and successful prediction of sensitivity to varying N_λ values (see Fig. 7.10a). However, for large wave amplitude, i.e. B_o/R_{body} = 0.75, Feldorhof's analysis fails to predict the forward velocity drastically (see Fig. 7.10c). Furthermore, predictions of SBT method in body rotation rates are also similar to the previous results but less dense around the experimental results.

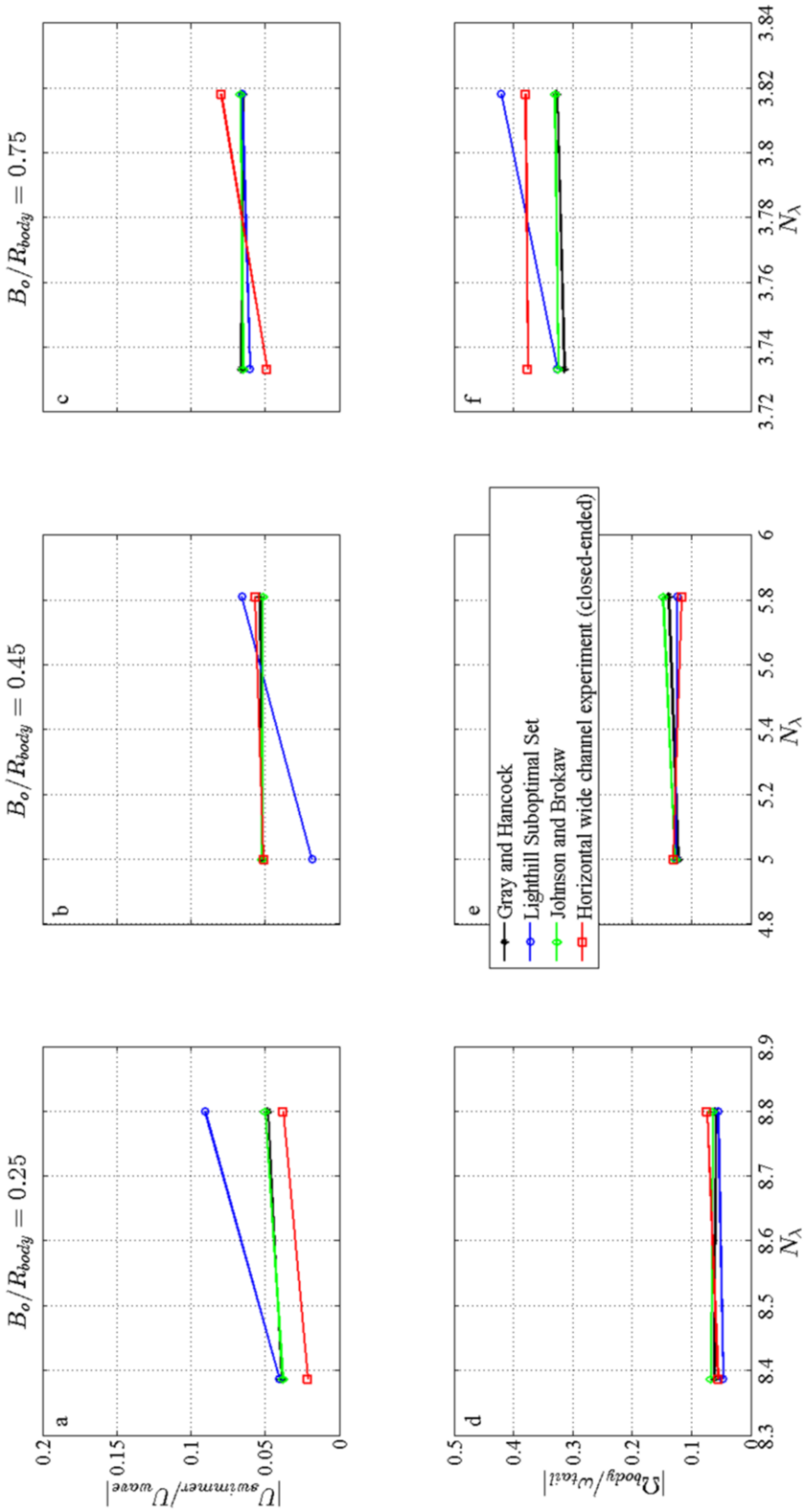

Figure 7.8: Closed-ended horizontal wide channel results predicted with unbounded-medium resistive force coefficients.

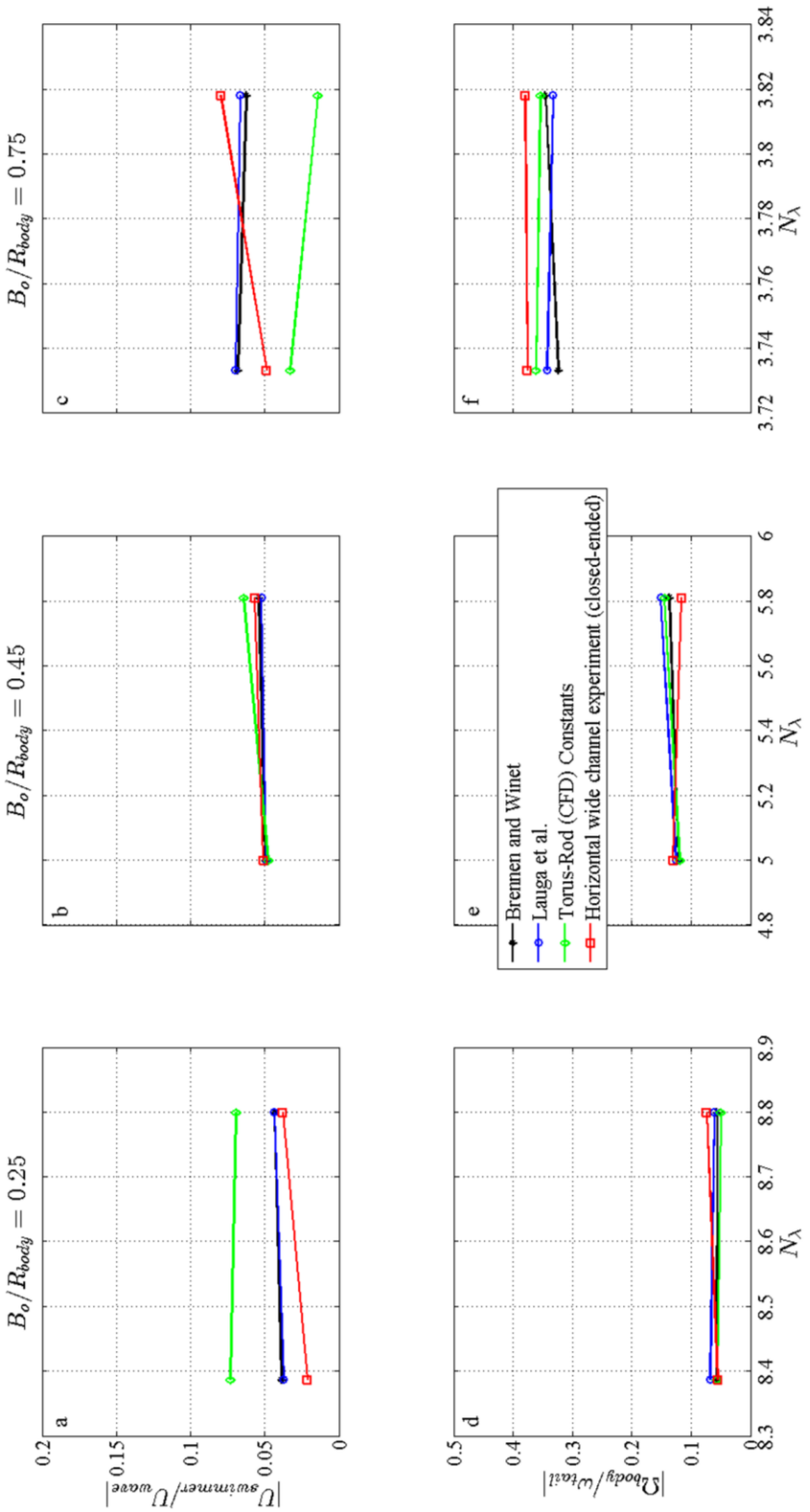

Figure 7.9: Closed-ended horizontal wide channel results predicted with bounded-medium resistive force coefficients.

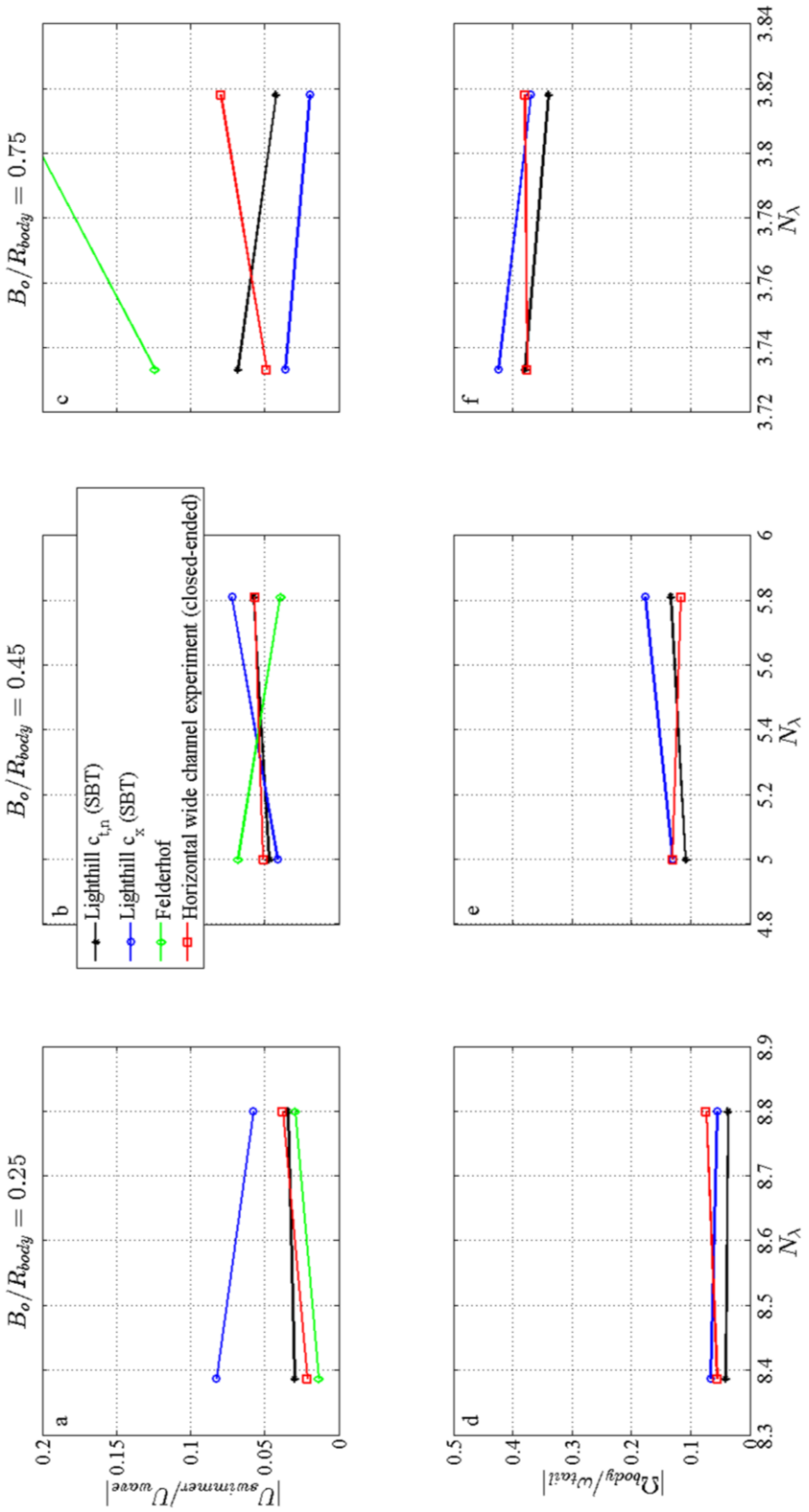

Figure 7.10: Closed-ended vertical wide channel results predicted with SBT-based-approach and Stokes flow based asymptotic solutions.

The interaction coefficients presented in Table 7.1 indicate that the thrust force values calculated by Lighthill's (1976) SBT-based coefficients and suboptimal set are much smaller than that calculated by other coefficient sets and methods. One reason of the high correction factors is the concentric swimming of the robotic prototype, i.e. the interaction between body and channel exerts fairly larger shear force on the body when the swimmer is concentric. Furthermore, the cylindrical shape of the body is underestimated by the resistance coefficients of prolate spheroids (Perrin, 1934).

In comparison with the interaction coefficients presented in Table 7.1, the interaction coefficients presented in Table 7.2 indicate that the hydrodynamic interaction of channel and tail amplified the forward thrust on the rotating helical tail, thus faster propulsion velocities are observed. However, the resultant fluid resistance on the cylindrical body is also expected to increase due to the friction and hydrodynamic wall effects in close proximity. Nevertheless, smaller interaction coefficients applied to the resistance matrix of the body indicates that the hydrodynamic effects acting on the tail are dominant in comparison with the effective forward friction acting on the swimmer's body.

7.5. Horizontal Experiment Results vs. Computational Fluid Dynamics (CFD) Model

CFD simulations governed by the stationary Navier-Stokes equations subject to continuity, in horizontal channel experiments, are rendered inadequate due to the close proximity between the swimming robot and the cylindrical channel wall.

Simulations, similar to the vertical experiment study, are carried out with channel and robot dimensions with the scale of 1:1, and actual physical properties, i.e. density and dynamic viscosity, are used for the viscous fluidic domain. Although the actual distance is not known, the swimming robot's body is placed in 1 mm proximity to the channel wall, and its long axis is positioned parallel to the long axis of the channel.

Figure 7.11 demonstrates in dimensionless fashion that the additional hydrodynamic interaction acting on the rotating helical tail induces increased forward thrust which pushes the bio-inspired robotic prototype forward, i.e. in negative **x**-direction, with a higher velocity than that of the vertical swimming, where the robot swims concentrically with the

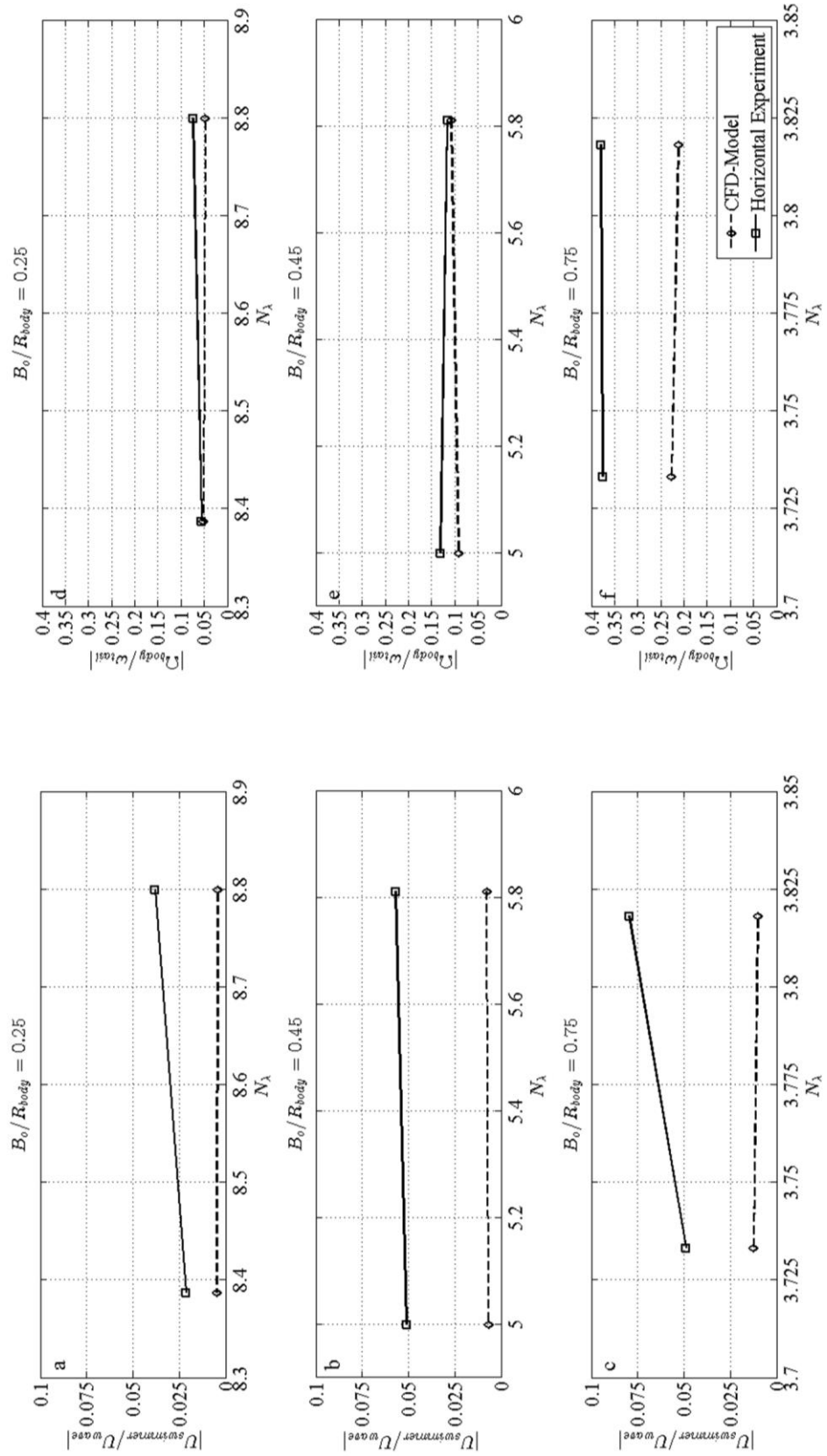

Figure 7.11: Closed-ended horizontal wide channel results: experiments vs. CFD.

channel. It is deduced that further study requires lubrication analysis on the part of tail-channel interaction. Furthermore, the sensitivity to varying wave length and wave amplitude is not predicted accurately in Fig. 7.11; suggesting that the hydrodynamic lift and contact friction on the body differs with respect to the geometry of the helical tail.

7.6. Effects of the Wave Parameters on Swimming in Horizontal Channels with Constant Helix Length

Extensive horizontal in-channel swimming experiments are conducted to study the relationship between swimming velocity vector and wave geometry for swimming bio-inspired robot confined in cylindrical channels of different geometries. The reader will find the geometric properties of the rigid helical tails used in experiments and the observed velocities of the robotic prototype actuating them separately, in Appendix 6.

Figure 7.12 presents the experimental results in dimensional form with error bars with 95% interval. The observed tail and body rotation rates are actually due to the motor torque balancing the effective hydrodynamic shear and friction torque acting on the entire swimming bio-inspired robot during the swimming motion as a direct result of conservation of angular momentum. Body rotation rates are within the same range regardless of wave length and amplitude, i.e. between 0.075 Hz and 0.125 Hz. The motor rotation rates, ω_m, are subject to the rotation rates of the helical tail which are subject to the traction and friction acting on them due to proximity and weight (see Fig. 7.12a-d).

To eliminate the tail rotation rates as a separate factor in the results, they are used to obtain the non dimensional velocity values. Figure 7.13 shows that the forward velocity of the swimming robot slightly differs from narrow channels with open and closed ends; however, significantly slower than that of the swimming robots confined to wide channels. On the other hand, the body rotation rates in Fig. 7.13 suggests that the effective torque acting on the swimming robot is subject to the tail geometry, channel geometry and flow field inside the channel. The last effect is of great importance since the replaced fluid is forced to flow around the body in the direction of wave propagation.

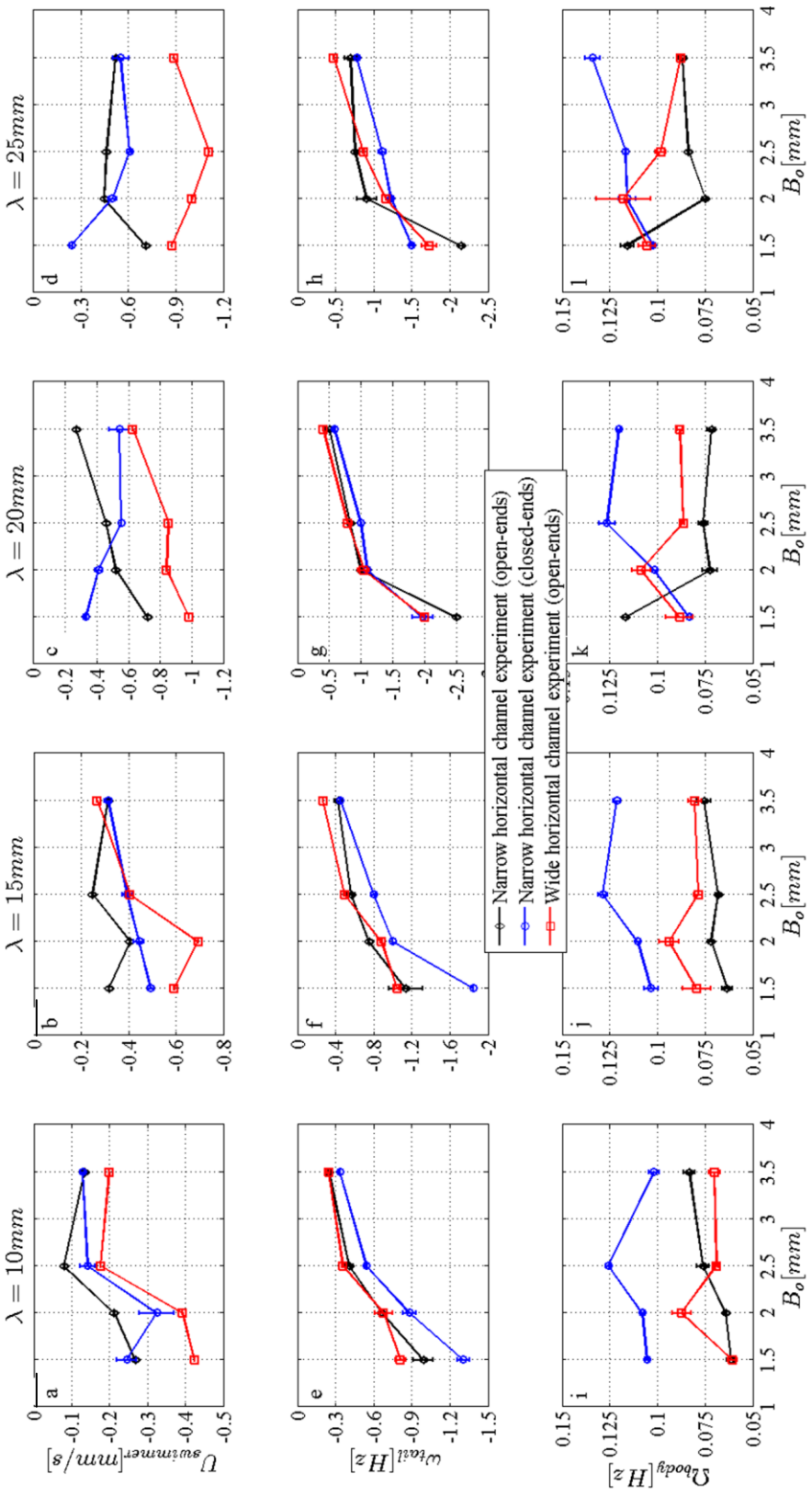

Figure 7.12: Horizontal channel experiment results with constant helix (tail) length, in dimensional form.

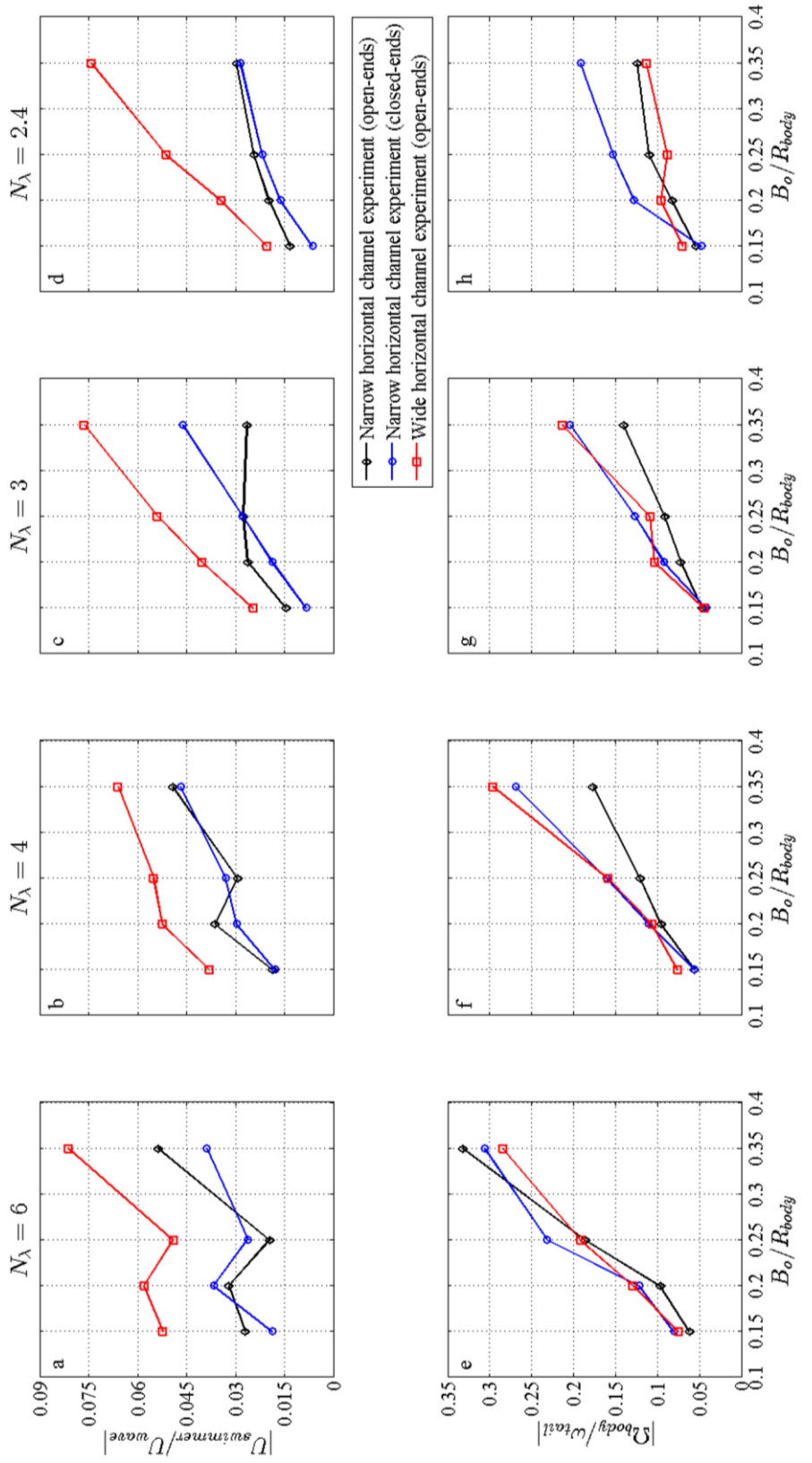

Figure 7.13: Horizontal channel experiment results with constant helix (tail) length, in dimensionless form.

It is observed that the forward velocity and body rotation rates increase with increasing wave amplitude. Also, body rotation rates decrease with increasing wave length. The relationship between forward velocity and wave length demonstrates a more unpredictable trend under the influence of channel geometry.

7.6.1. Experiments vs. Hydrodynamic Model in Wide Channels with Open Ends

Here, recorded velocity values from the horizontal swimming experiments in wide channels with open ends are predicted with RFT-based hydrodynamic model using different resistive force coefficients, force coefficients based on SBT approach articulated by Lighthill (1976), and the asymptotic solutions of Stokes flow in channels presented by Felderhof (2010).

The body resistance coefficients of prolate spheroids (Perrin, 1934), are adjusted with proper Υ_x values for rigid-body translation and rotation of the cylindrical body only once. The body of the swimming robotic prototype is as presented in Figs. 2.1b and 7.1b, i.e. shorter in length and has no cork at the tip (also see Table 2.1 for geometric properties).Given the fact that the body geometry is similar to the prolate spheroids, the interaction coefficients used for resistance matrix calibrations are found to be much smaller in general (see Table 7.3).

Figures 7.14-7.16 present the performance of force coefficients and Stokes flow solutions. The force coefficients for bounded viscous medium provide better solutions; however, as the total number of waves increase, the agreement between experiments and predictions weaken for all coefficient sets. Furthermore the sensitivity of c_x method articulated by Lighthill (1976) is superior to all other coefficient sets and Stokes flow solutions of Felderhof (2010).

Comparisons on the horizontal in-channel swimming experiment results and the predictions obtained with bounded medium RFC sets are presented in Fig. 7.14. It is observed that the hydrodynamic model successfully predicts the forward velocities and body rotation rates of the swimmers with helical tails having small N_λ values, i.e. $N_\lambda \leq 3$ (see Figs. 7.14c-d,g-h); however, as the N_λ values increase the calculations fail in

predictions (Figs. 7.14a-b,e-f). The reason being for this phenomenon is the increasing weight of the helical tail provided that the apparent length is kept constant in this study (also see Table 2.1): friction due to excessive weight decreases forward velocity and body rotations rates and hydrodynamic model calculations

Figure 7.15 presents the performance of bounded medium RFC sets. The forward swimming velocities are predicted reasonably well with smaller N_λ values (see Figs. 7.15c-d). Furthermore, calculated body rotation rates agree well with the observation for N_λ = {2.4, 3, 4} (see Figs. 7.15f-h), which is better than the calculations obtained by unbounded medium RFC sets. Moreover, the predictions fail for small wave lengths as expected (see Figs. 7.15a-b,e). It is also noted that the RFC set based on torus-rod representation provides results comparable to that obtained by RFC set presented by Brennen and Winet (1977).

Figure 7.16 shows the performance of SBT methods and asymptotic solution. It is observed that all methods present reasonable predictions for larger wave lengths, i.e. for smaller N_λ (see Figs. 7.16c-d,g-h). However, the SBT-based c_x formulation presented by Lighthill (1976) performs with superior accuracy compared to all other methods presented so far and predicts the forward velocity and body rotation rate values (see Figs. 7.16a-b,e-f).

Table 7.3: Horizontal channel (wide, open-ended) interaction coefficients; under the assumptions of bio-inspired robots moving in unbounded and bounded fluid.

RFC set	Fluid-Drag
Gray and Hancock (1955)	$\{\Upsilon_{T,x}^{body}=1.925,\ \Upsilon_{R,x}^{body}=1.3\}$
Lighthill (suboptimal set, 1976)	$\{\Upsilon_{T,x}^{body}=0.4,\ \Upsilon_{R,x}^{body}=1.6\}$
Johnson and Brokaw (1979)	$\{\Upsilon_{T,x}^{body}=2.35,\ \Upsilon_{R,x}^{body}=1.275\}$
Brennen and Winet (1977)	$\{\Upsilon_{T,x}^{body}=3.25,\ \Upsilon_{R,x}^{body}=1.4\}$
Lauga *et al.* (2006)	$\{\Upsilon_{T,x}^{body}=3.65,\ \Upsilon_{R,x}^{body}=1.4\}$
Torus-Rod Coefficients	$\{\Upsilon_{T,x}^{body}=7.1,\ \Upsilon_{R,x}^{body}=1.55\}$
Lighthill SBT-based $c_{t,n}$ (1976)	$\{\Upsilon_{T,x}^{body}=1.3,\ \Upsilon_{R,x}^{body}=0.75\}$
Lighthill, c_x, unbounded SBT (1976)	$\{\Upsilon_{T,x}^{body}=2.05,\ \Upsilon_{R,x}^{body}=0.6\}$
Felderhof, bounded Stokes flow (2010)	$\Upsilon_x=8$

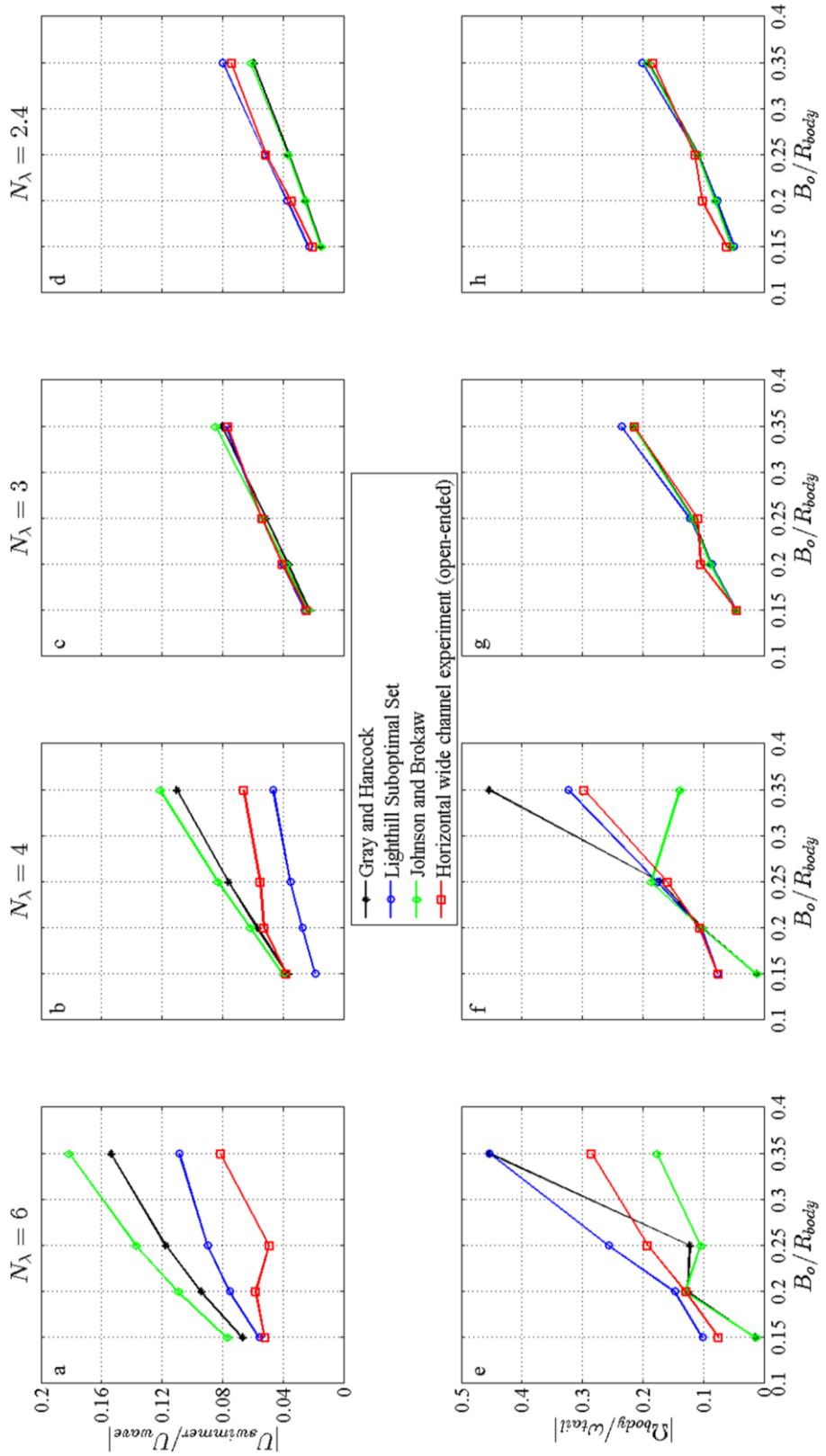

Figure 7.14: Open-ended horizontal wide channel results predicted with unbounded-medium resistive force coefficients.

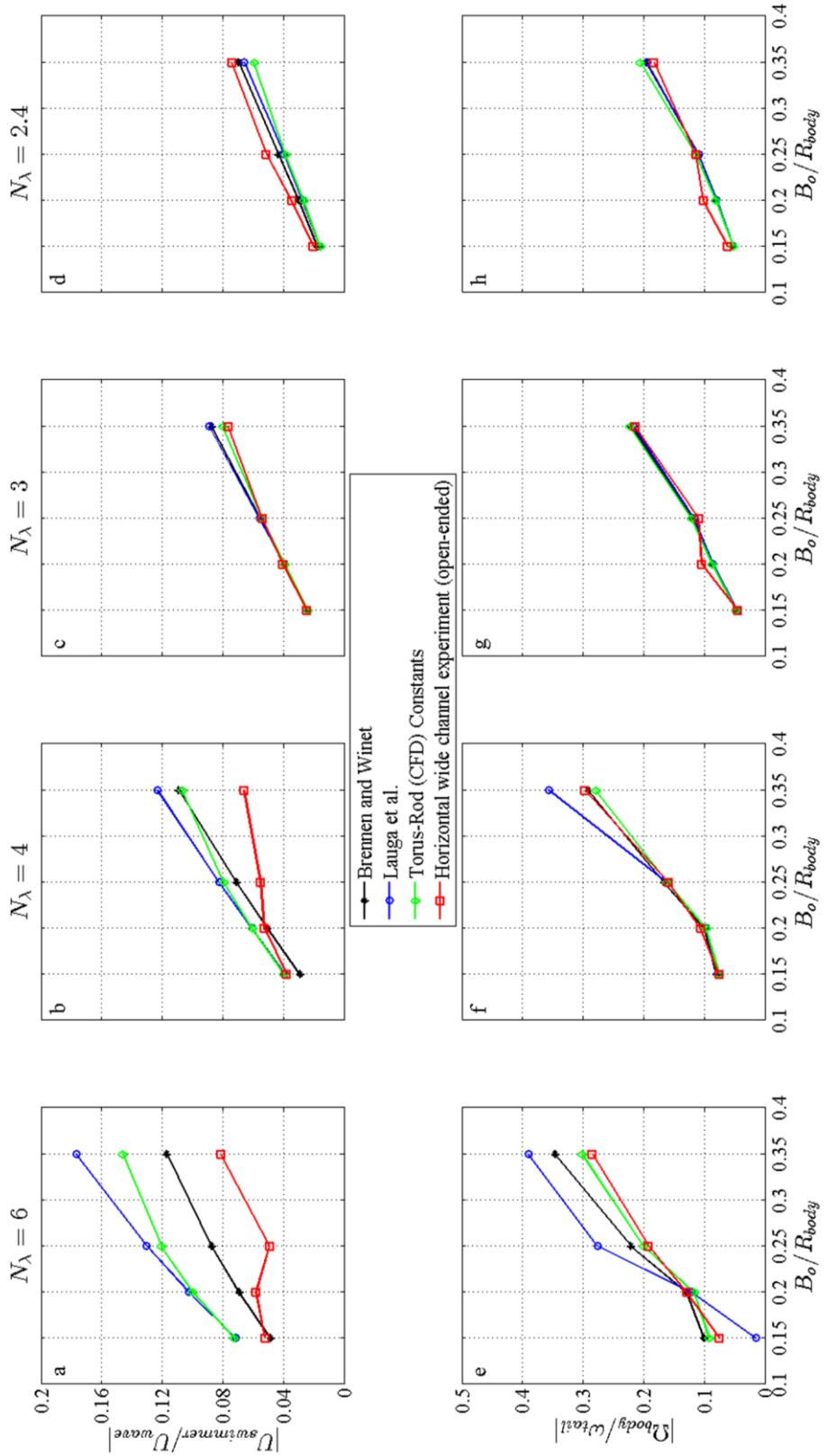

Figure 7.15: Open-ended horizontal wide channel results predicted with bounded-medium resistive force coefficients.

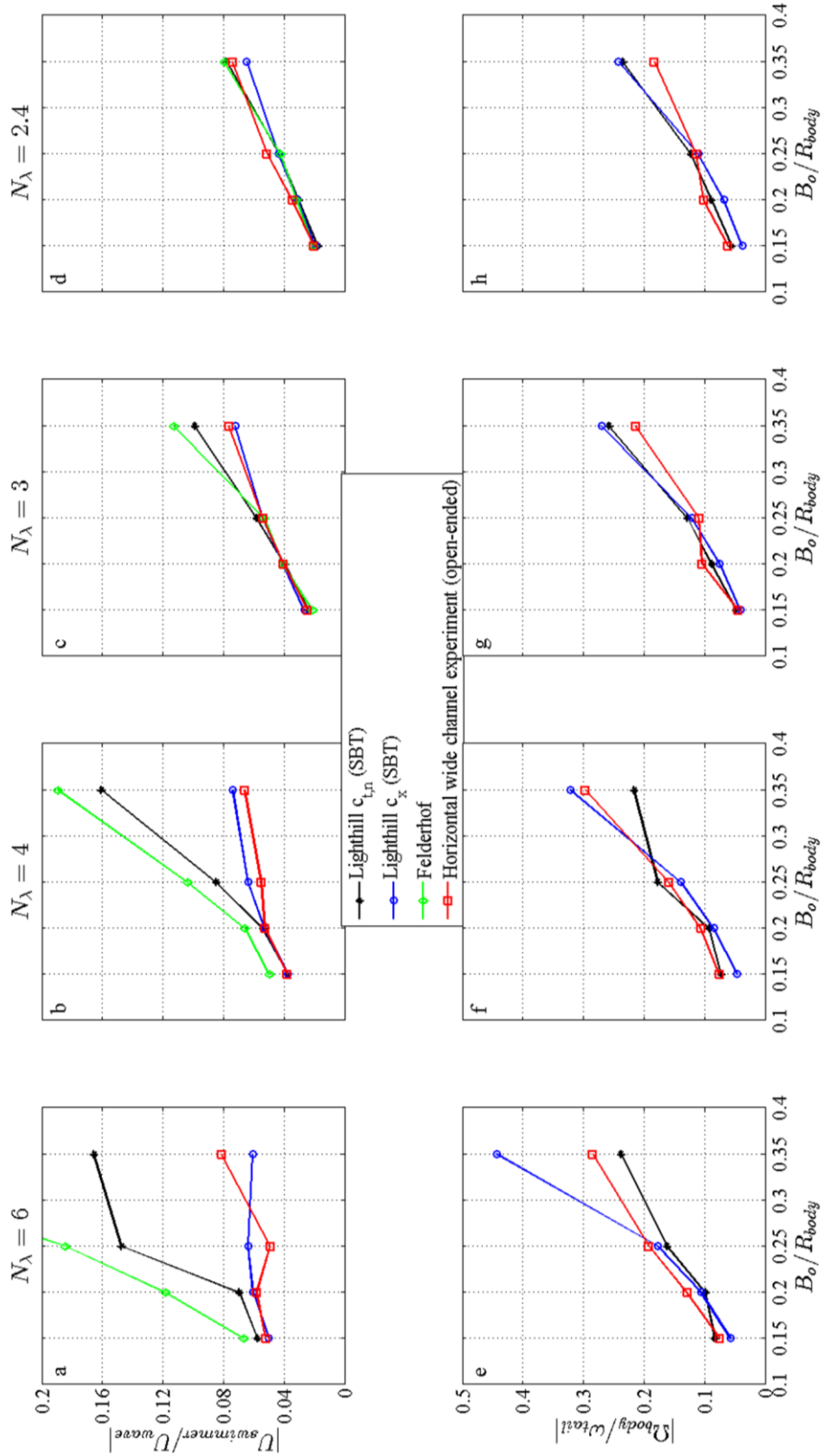

Figure 7.16: Open-ended horizontal wide channel results predicted with SBT-based-approach and Stokes flow based asymptotic solutions.

To conclude, as the total number of waves, N_λ, increases the propulsion velocity decreases consecutively due to increased weight (see Figs. 7.14a-7.16a). Hence, the interaction coefficients utilized in hydrodynamic model could not predict accurate velocity values with any of the resistive force coefficient (RFC) sets. This result further implies that the forward thrust is comparable to the contact friction on the swimmer in magnitude due to its total weight (also see Appendix 6 for tail weights).

7.6.2. Experiments vs. Computational Fluid Dynamics (CFD) Model in Wide Channels with Open Ends

The CFD simulations are carried out for swimming robots in wide channels filled with viscous fluids. Induced flow fields by the two degree-of-freedom swimming, i.e. forward translation and body rotation rate, are governed by stationary Navier-Stokes equations subject to continuity. The actuation frequencies of the helical tails are set as the individual ω_{tail} values obtained from the in-channel experiments carried out with horizontal wide channels with open ends (see Figs. 7.12e-h).

CFD simulations are carried out to single out and emphasize the wall effects on the rotating helical tail. First, swimming robots are placed concentrically with the channel as depicted in Fig. 7.17, than swimmer body is replaced with proximity of 1 mm to the cylindrical channel while still parallel to the long axis of the channel (see the eccentric swimmer results in Fig. 7.17). Both simulation studies predict slower forward velocity and body rotation rate values.

The reason for this discrepancy is the extra hydrodynamic shear acting on the rotating helical tail, which is clearly exerted by the presence of the cylindrical channel, and confirmed by the eccentric swimming robotic prototype results obtained by CFD simulations. The forward velocity increases with increasing eccentricity of the swimming robot. Reduced proximity, i.e. smaller than 1 mm, studies are excluded because of the fact that analyzing lubrication on a simultaneously translating and rotating surface of a curved geometry is beyond the scope of this text.

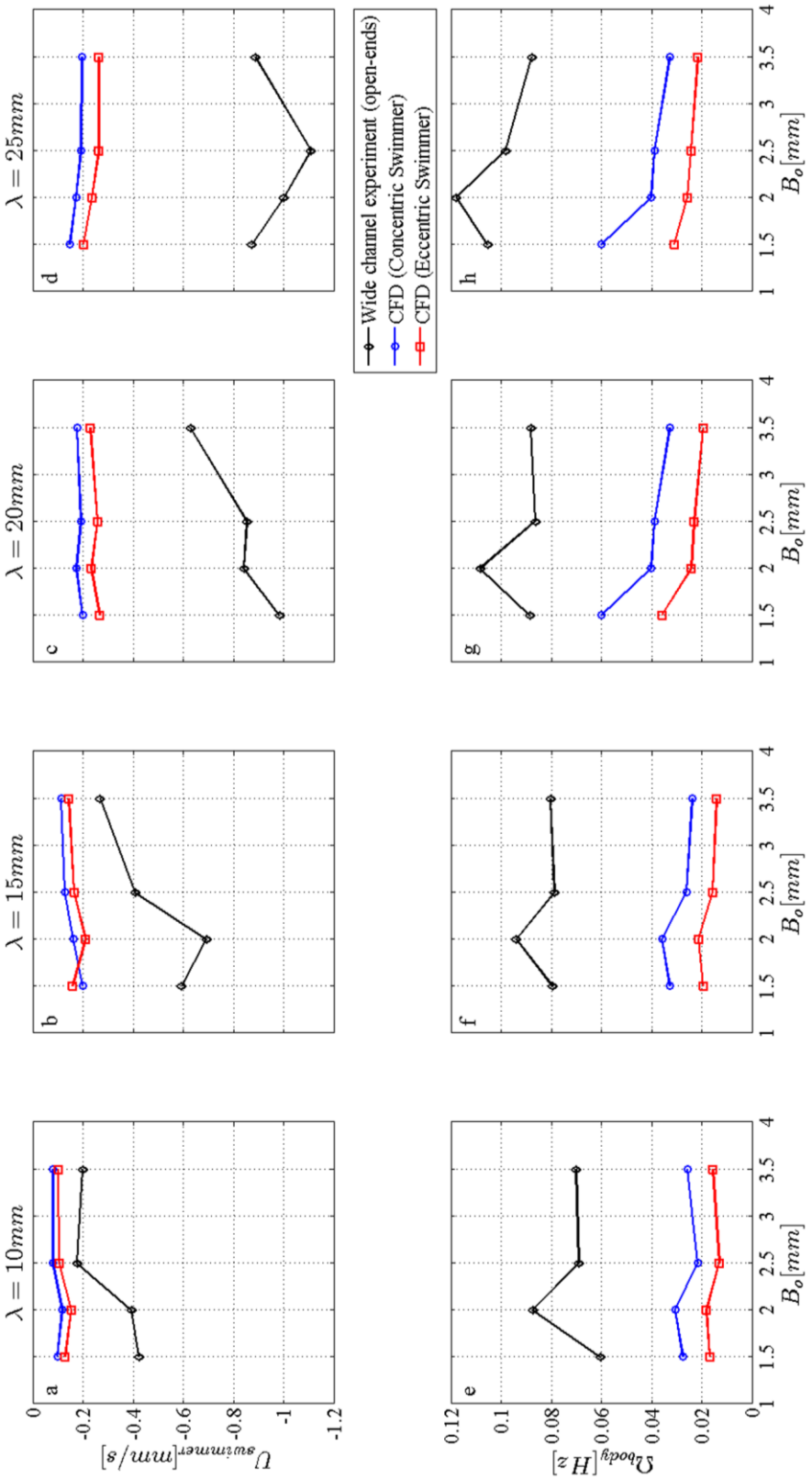

Figure 7.17: Open-ended horizontal wide channel results, Experiments vs. CFD.

7.6.3. Experiments vs. Hydrodynamic Model in Narrow Channels with Open Ends

Here, registered velocity values from the horizontal swimming experiments in narrow channels with open ends are predicted with RFT-based hydrodynamic model using different resistive force coefficients, and SBT methods presented by Lighthill (1976) and the asymptotic solutions of Stokes flow in channels presented by Felderhof (2010).

The body resistance coefficients of prolate spheroids (Perrin, 1934), are adjusted with proper Υ_x values for rigid-body translation and rotation of the cylindrical body only once. As the channel radius decreases the effective fluid resistance acting on the body also increases. Hence, the interaction coefficients for narrow channel experiments with open ends are bigger than that of the wide channel experiments with open ends (see Table 7.4).

Figure 7.18 presents the predictions of hydrodynamic model with unbounded medium RFC sets. The forward velocities are predicted successfully but only for the largest wave lengths (see Fig. 7.18d). As the total number of waves on the helical tail increases, the agreement in forward velocity results totally disappears (see Figs. 7.18a-c). However, body rotation rates are predicted successfully except for the heaviest helical tail, i.e. N_λ = 6 and B_o/R_{body} = 0.35 (see Figs. 7.18e-h).

Figure 7.19 depicts the performance of resistive force coefficients formulated for swimmer moving near solid boundaries. Similar to the performance of the unbounded medium RFC sets, forward velocities of the robots with largest wave lengths, i.e. N_λ = 2.4, are predicted with reasonably small error (see Fig. 7.19d). However, as N_λ increases the hydrodynamic model fails in predicting the forward velocities accurately (see Fig. 7.19a-c). The body rotation rates are predicted with great agreement (see Fig. 7.19e-h), except for N_λ = 6 and B_o/R_{body} = 0.35 (see Figs. 7.18e).

Lastly, Fig. 7.20 shows the performance of SBT approaches and asymptotical solutions. It is observed that the c_x coefficient approach formulated by Lighthill (1976) provides the most satisfying results for swimming velocities when compared to other methods (see Figs. 7.20a-d). As for the body rotation rates, the SBT-based $c_{t,n}$ coefficient

set presented by Lighthill (1976) is proved to be the best choice of RFC set (see Figs. 7.20e-h), except for N_λ = 6 and B_o/R_{body} = 0.35.

As presented in Figs. 7.18-7.20, both the resistive-force-theory and slender-body-theory approaches, as Stokes flow based analysis and the asymptotic solution, generally lack the accuracy to predict the forward velocity values for shorter wave lengths. Furthermore, force coefficient sets for bounded viscous medium provide the best results for body rotation rates. Moreover, the forward velocity results obtained by the c_x approach (Lighthill, 1976) are in good agreement with the experiments.

Furthermore, the observed numerical error in forward velocities depicted in Figs. 7.18a-7.20a with higher N_λ are found to be similar to the error observed in wide channel experiments with open ends suggesting that the friction acting on the swimmer is somewhat comparable with little sensitivity to channel diameter. One may deduce that increased weight results in dominant friction despite the swimmer's ability to push itself

Table 7.4: Horizontal channel (narrow, open-ended) interaction coefficients; under the assumptions of bio-inspired robots moving in unbounded and bounded fluid.

RFC set	Fluid-Drag
Gray and Hancock (1955)	$\{\Upsilon_{T,x}^{body} = 3.2,\ \Upsilon_{R,x}^{body} = 1.65\}$
Lighthill (suboptimal set, 1976)	$\{\Upsilon_{T,x}^{body} = 1.65,\ \Upsilon_{R,x}^{body} = 2.05\}$
Johnson and Brokaw (1979)	$\{\Upsilon_{T,x}^{body} = 4,\ \Upsilon_{R,x}^{body} = 1.625\}$
Brennen and Winet (1977)	$\{\Upsilon_{T,x}^{body} = 5.55,\ \Upsilon_{R,x}^{body} = 1.775\}$
Lauga *et al.* (2006)	$\{\Upsilon_{T,x}^{body} = 6.25,\ \Upsilon_{R,x}^{body} = 1.75\}$
Torus-Rod Coefficients	$\{\Upsilon_{T,x}^{body} = 11.7,\ \Upsilon_{R,x}^{body} = 1.95\}$
Lighthill SBT-based $c_{t,n}$ (1976)	$\{\Upsilon_{T,x}^{body} = 2.7,\ \Upsilon_{R,x}^{body} = 0.925\}$
Lighthill, c_x, unbounded SBT (1976)	$\{\Upsilon_{T,x}^{body} = 3.45,\ \Upsilon_{R,x}^{body} = 0.8\}$
Felderhof, bounded Stokes flow (2010)	$\Upsilon_x = 12.5$

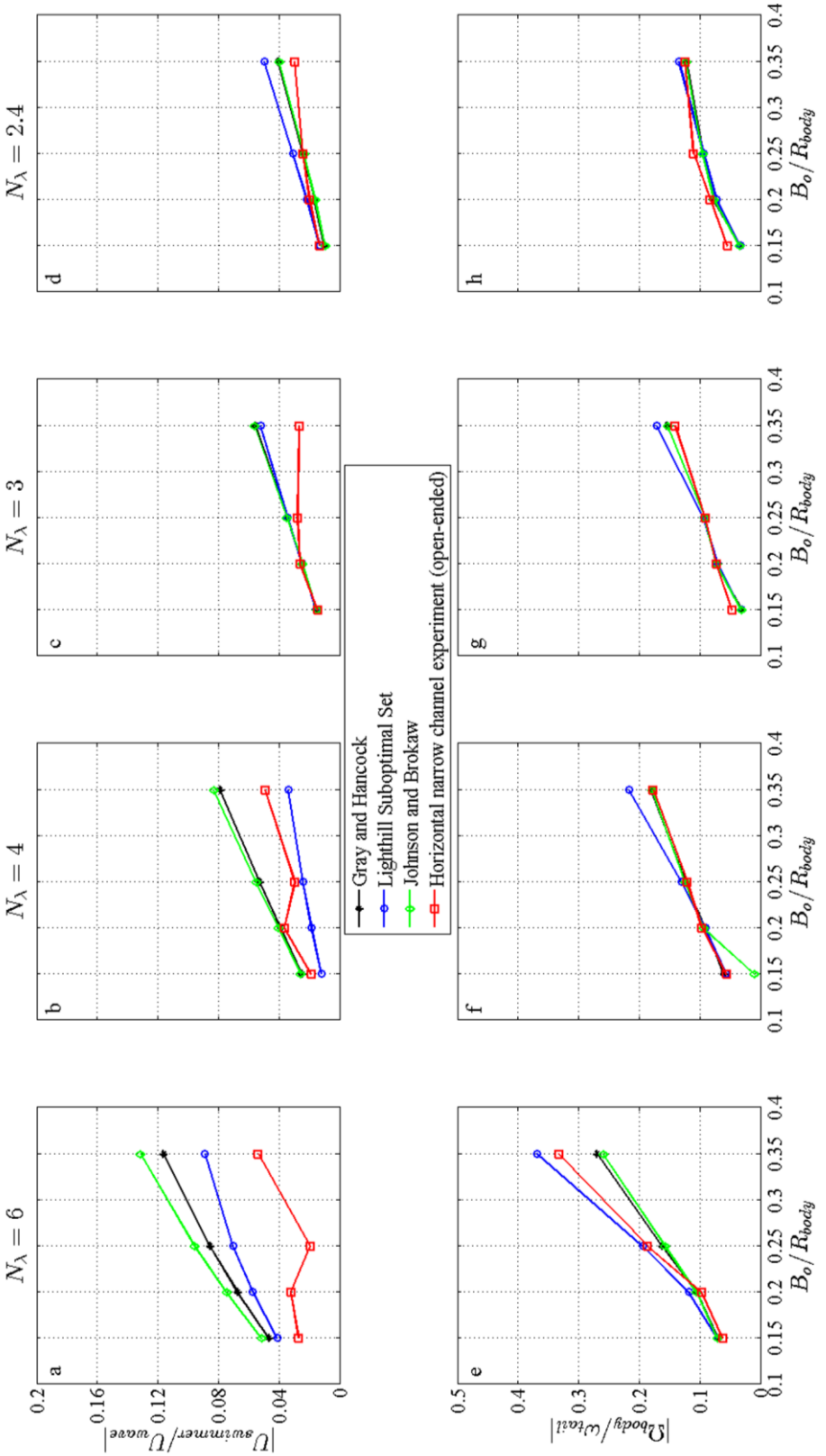

Figure 7.18: Open-ended horizontal narrow channel results predicted with unbounded-medium resistive force coefficients.

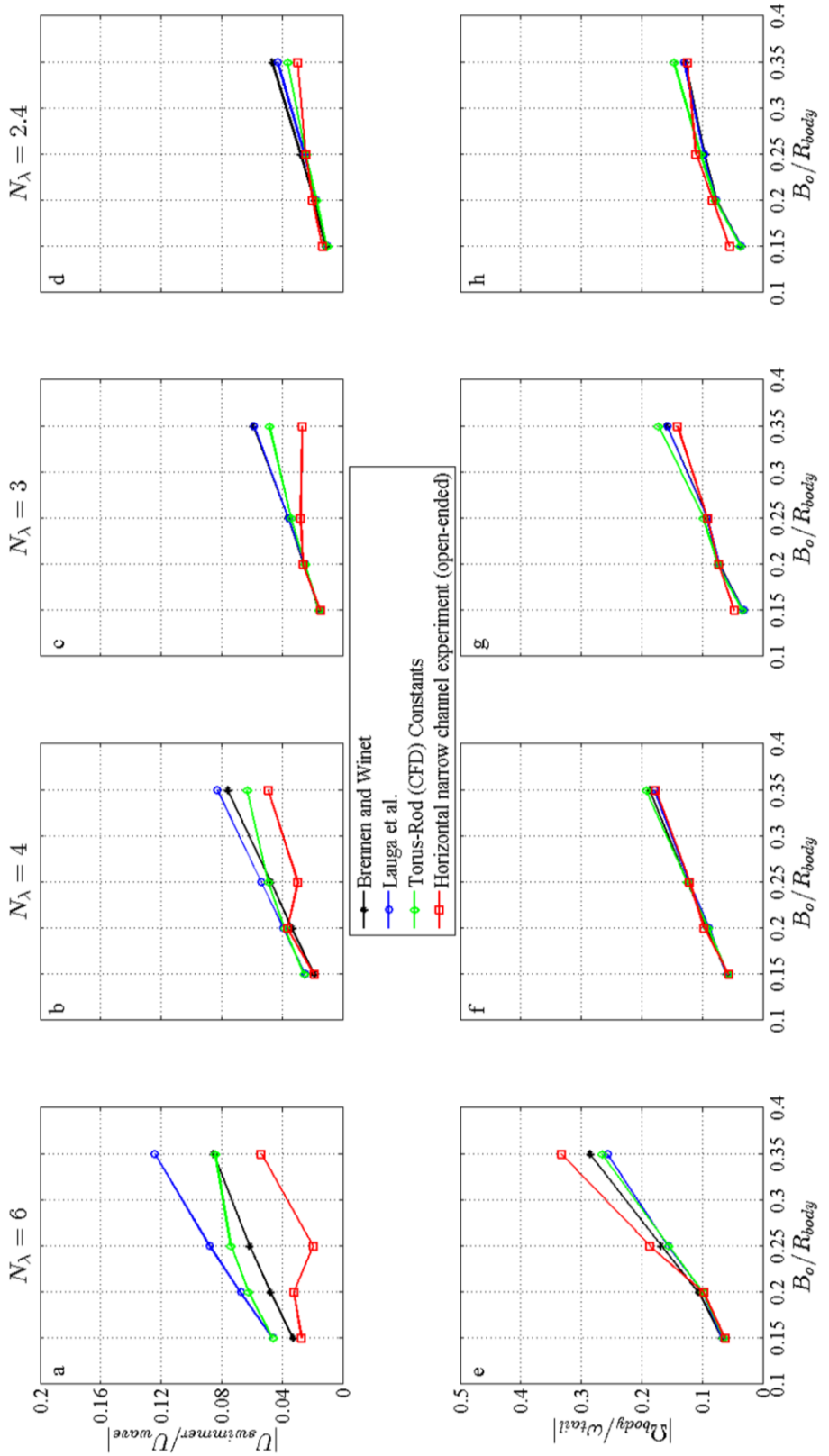

Figure 7.19: Open-ended horizontal narrow channel results predicted with bounded-medium resistive force coefficients.

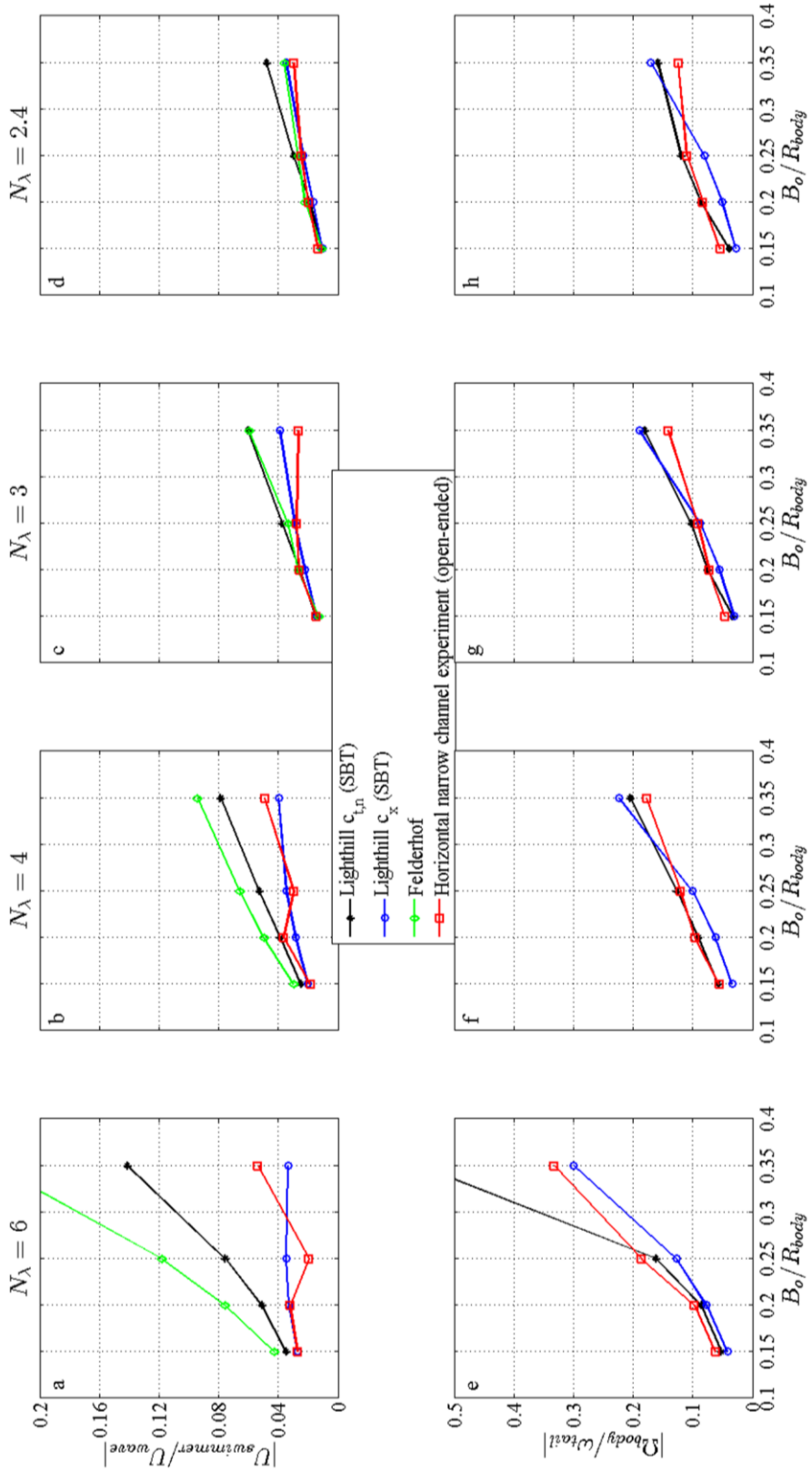

Figure 7.20: Open-ended horizontal narrow channel results predicted with slender-body-theory (SBT) approach and Stokes flow based asymptotic solutions.

7.6.4. Experiments vs. Computational Fluid Dynamics (CFD) Model in Narrow Channels with Open Ends

The CFD simulations are carried out for swimming robots in narrow channels filled with viscous fluids. Induced flow fields by the two degree-of-freedom swimming, i.e. forward translation and body rotation rate, are governed by stationary Navier-Stokes equations subject to continuity. The actuation frequencies of the helical tails are set as the individual ω_{tail} values registered during experiments on horizontal narrow channels with open ends, which were observed in the lab frame (see Figs. 7.12e-h).

First, swimming robots are placed concentrically with the channel, i.e. concentric swimmer in Fig. 7.21, than swimmer body is replaced with proximity of 1 mm to the cylindrical channel while still parallel to the long axis of the channel (see the eccentric swimmer results in Fig. 7.21). Both simulation studies predict slower forward velocity and body rotation rate values.

The reason being for this discrepancy is the hydrodynamic interaction between the walls of the cylindrical channel and the rotating helical tail, i.e. combination of traction decreasing the tail rotation rate and lubrication amplifying the forward thrust, exerted by the presence of the cylindrical channel, which is confirmed by the eccentric swimming robot results. The forward velocity increases with increasing eccentricity of the swimming robot. The relationship between swimming robot's proximity to the cylindrical channel wall concurs with the horizontal wide channel results: the concentric swimmer moves with the slowest forward velocity values, and faster velocity values are obtained with swimmers placed 1 mm away from the cylindrical wall. It is noted that, the swimmer moves near the wall under the influence of gravitational pull and the actual distance in between is not measured.

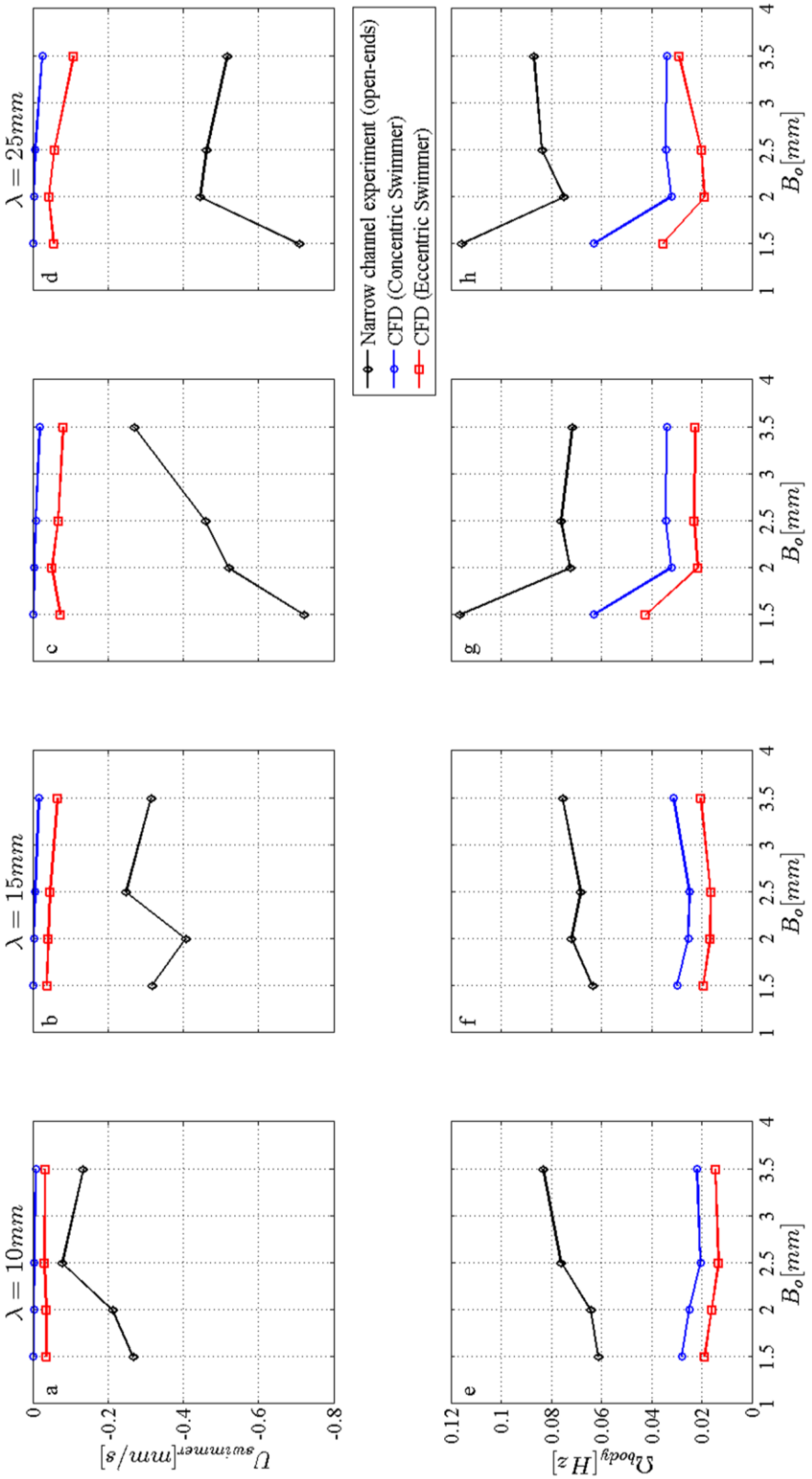

Figure 7.21: Open-ended horizontal narrow channel results, Experiments vs. CFD.

7.6.5. Experiments vs. Hydrodynamic Model in Narrow Channels with Closed Ends

Here, measured velocity values from the horizontal narrow in-channel swimming experiments with closed ends are predicted with RFT-based hydrodynamic model using different resistive force coefficients, SBT methods presented by Lighthill (1976), and the asymptotic solutions of Stokes flow induced in channels articulated by Felderhof (2010).

The body resistance coefficients of prolate spheroids (Perrin, 1934), are adjusted with proper Υ_x values for rigid-body translation and rotation of the cylindrical body only once. As the channel radius decreases the effective fluid resistance acting on the body also increases. Furthermore, the presence of closed-ends imposes extra drag on the robot's body; hence the interaction coefficients are slightly bigger than that of the swimmers confined to the narrow channel with open ends (See Tables 7.4 and 7.5).

Provided that the replaced fluid would flow around the body in the direction of wave propagation, fluid resistance acting on the swimming robot's body needs to incorporate the resistance corrections for channel flows presented by Happel and Brenner (1965). These corrections are used with the hydrodynamic model employing tangential and normal resistive-force-coefficients assuming that the distance between the body surface and channel wall is 1 μm; however, the asymptotic solution to the in-channel Stokes flow field (Felderhof, 2010) does not require such corrections although the correction coefficient Υ_x reflects the extra shear force acting on the swimmer's body.

Figure 7.22 presents the comparative results of in-channel experiments with closed-ends and hydrodynamic model using bounded medium RFC sets. It is observed that the calculations are in good agreement with the recorded forward velocity values for N_λ = {2.4, 3} (see Figs. 7.22c-d). However, as the helical waves shrinks in length, the forward velocity predictions fail (see Figs. 7.22a-b). On the other hand, the body rotation rates are predicted successfully with N_λ = {2.4, 3, 4} with RFC sets presented by Gray and Hancock (1955) and Brenen and Winet (1977) (see Figs. 7.22e-h). However, the

suboptimal set presented by Lighthill (1976) performs the worst with the largest N_λ values (see Fig. 7.22e).

Figure 7.23 depicts the performance of bounded medium RFC sets in predicting rigid-body velocities of the swimming robotic prototypes. It is observed that the most coherent and accurate predictions are obtained by bounded medium RFC sets, except for the heavy swimmers as presented in Fig. 7.23a. The forward velocities of the lighter robotic prototypes and all body rotation rates are predicted with good agreement (see Figs. 7.23b-d,e-h).

Finally, Fig. 7.24 presents the predictions of SBT-based approach and asymptotical solution. It is observed that forward velocities are predicted well with larger wave lengths, i.e. N_λ = {2.4, 3} (see Figs. 7.24c-d), but the predictions worsen with increasing N_λ (see Figs. 7.24a-b). However, similar to the previous results, the predictions of c_x approach (Lighthill, 1976) agrees well with the forward velocities even with heavy robots (see Figs. 7.24a-d). Moreover, the SBT-based $c_{t,n}$ set given by Lighthill (1976) provides the best results in body rotation rate predictions with larger wave lengths, i.e. N_λ = {2.4, 3} (see Figs. 7.24g-h). On the other hand, as the wave length decreases the calculations of c_x approach (Lighthill, 1976) offer comparable predictions except for the largest wave amplitudes (see Figs. 7.24e-f).

Table 7.5: Horizontal channel (Narrow closed-ended) interaction coefficients; under the assumptions of bio-inspired robots moving in unbounded and bounded fluid.

RFC set	Fluid-Drag
Gray and Hancock (1955)	$\{\Upsilon_{T,x}^{body} = 3.25,\ \Upsilon_{R,x}^{body} = 1.1\}$
Lighthill (suboptimal set, 1976)	$\{\Upsilon_{T,x}^{body} = 2,\ \Upsilon_{R,x}^{body} = 1.45\}$
Johnson and Brokaw (1979)	$\{\Upsilon_{T,x}^{body} = 4,\ \Upsilon_{R,x}^{body} = 1.1\}$
Brennen and Winet (1977)	$\{\Upsilon_{T,x}^{body} = 5.7,\ \Upsilon_{R,x}^{body} = 1.25\}$
Lauga *et al.* (2006)	$\{\Upsilon_{T,x}^{body} = 6.25,\ \Upsilon_{R,x}^{body} = 1.245\}$
Torus-Rod Coefficients	$\{\Upsilon_{T,x}^{body} = 11.3,\ \Upsilon_{R,x}^{body} = 1.45\}$
Lighthill SBT-based $c_{t,n}$ (1976)	$\{\Upsilon_{T,x}^{body} = 3.4,\ \Upsilon_{R,x}^{body} = 0.66\}$
Lighthill, c_x, unbounded SBT (1976)	$\{\Upsilon_{T,x}^{body} = 3.9,\ \Upsilon_{R,x}^{body} = 0.61\}$
Felderhof, bounded Stokes flow (2010)	$\Upsilon_x = 18$

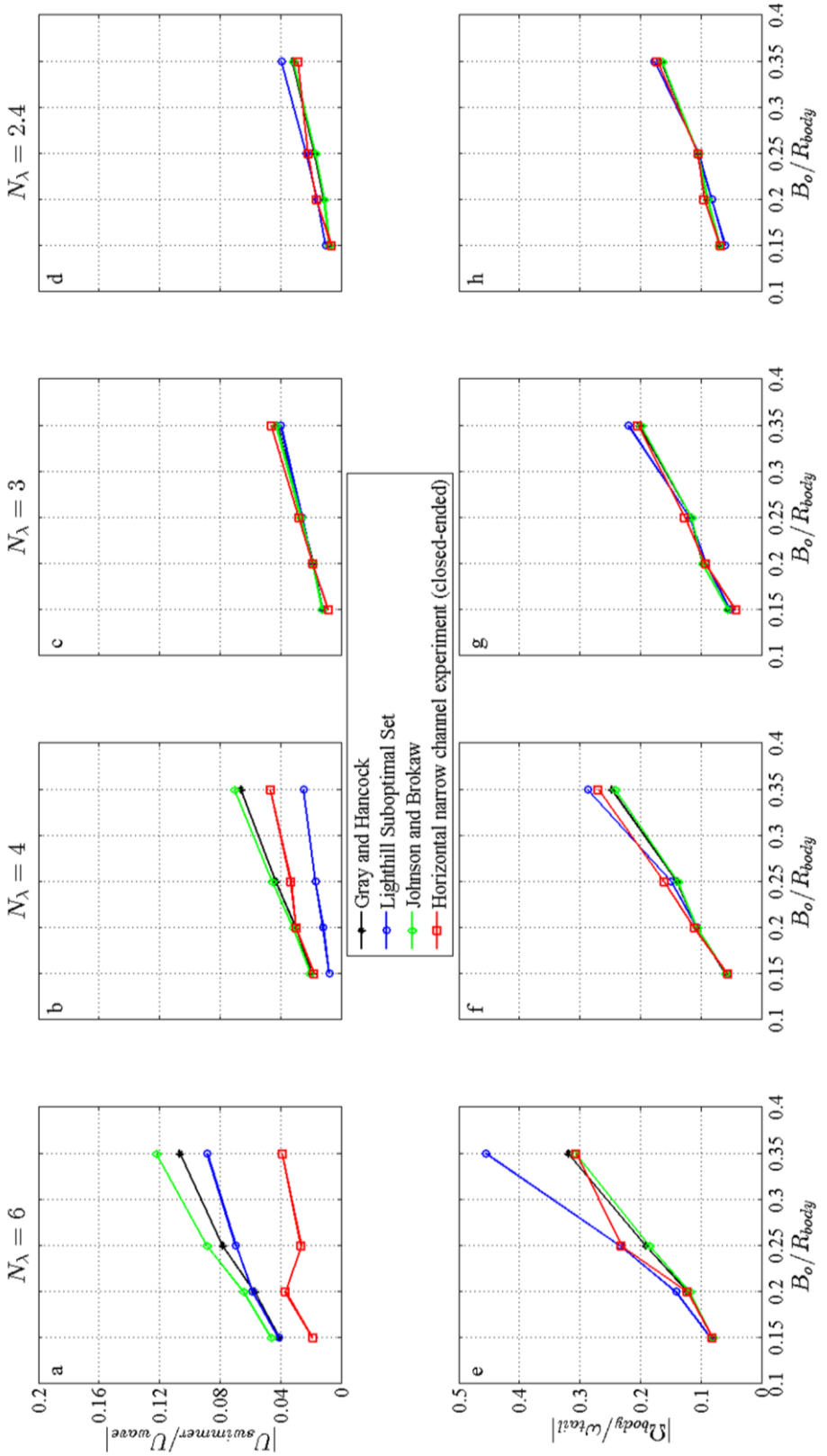

Figure 7.22: Closed-ended horizontal narrow channel results predicted with unbounded-medium resistive force coefficients.

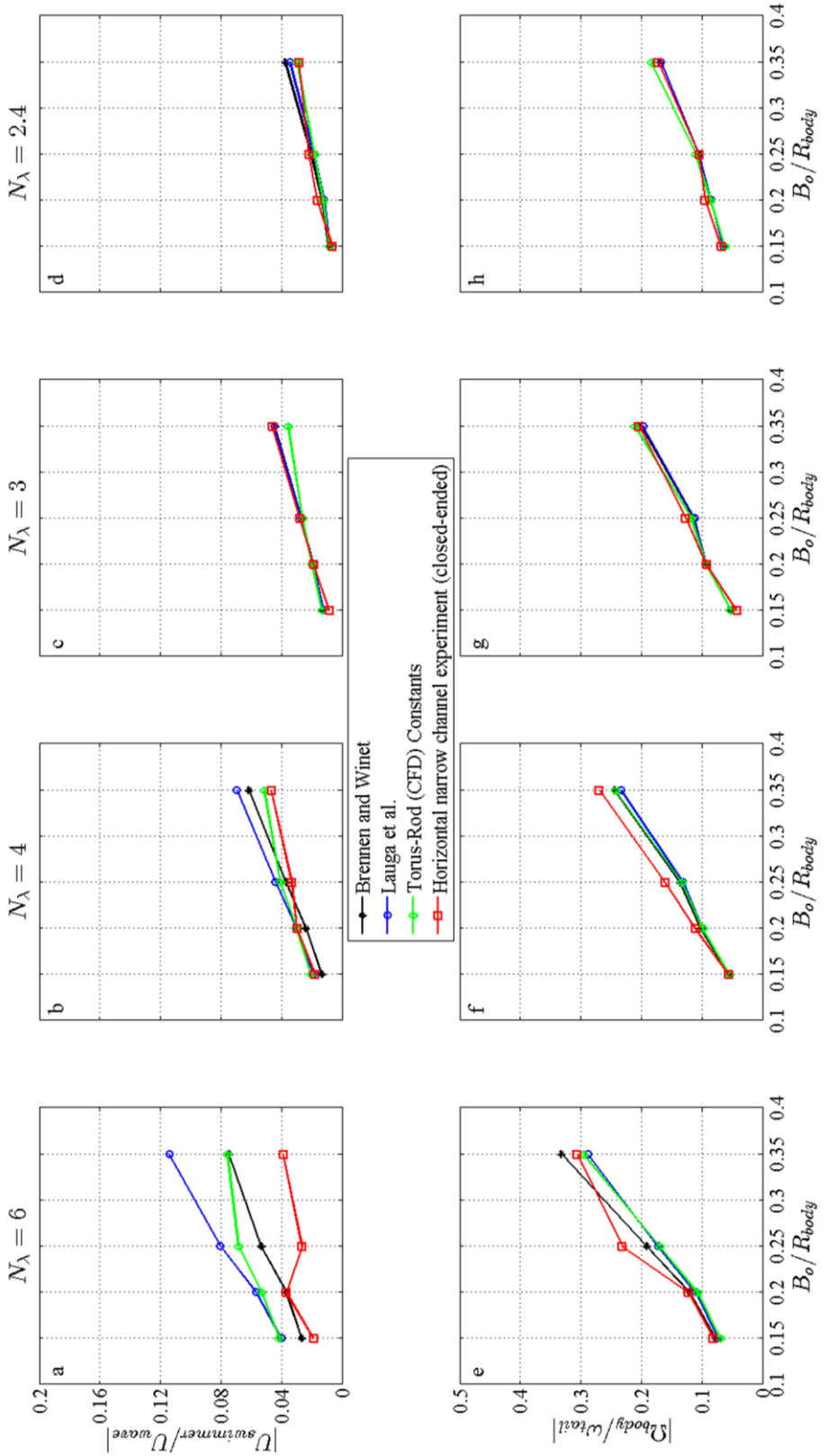

Figure 7.23: Closed-ended horizontal narrow channel results predicted with bounded-medium resistive force coefficients.

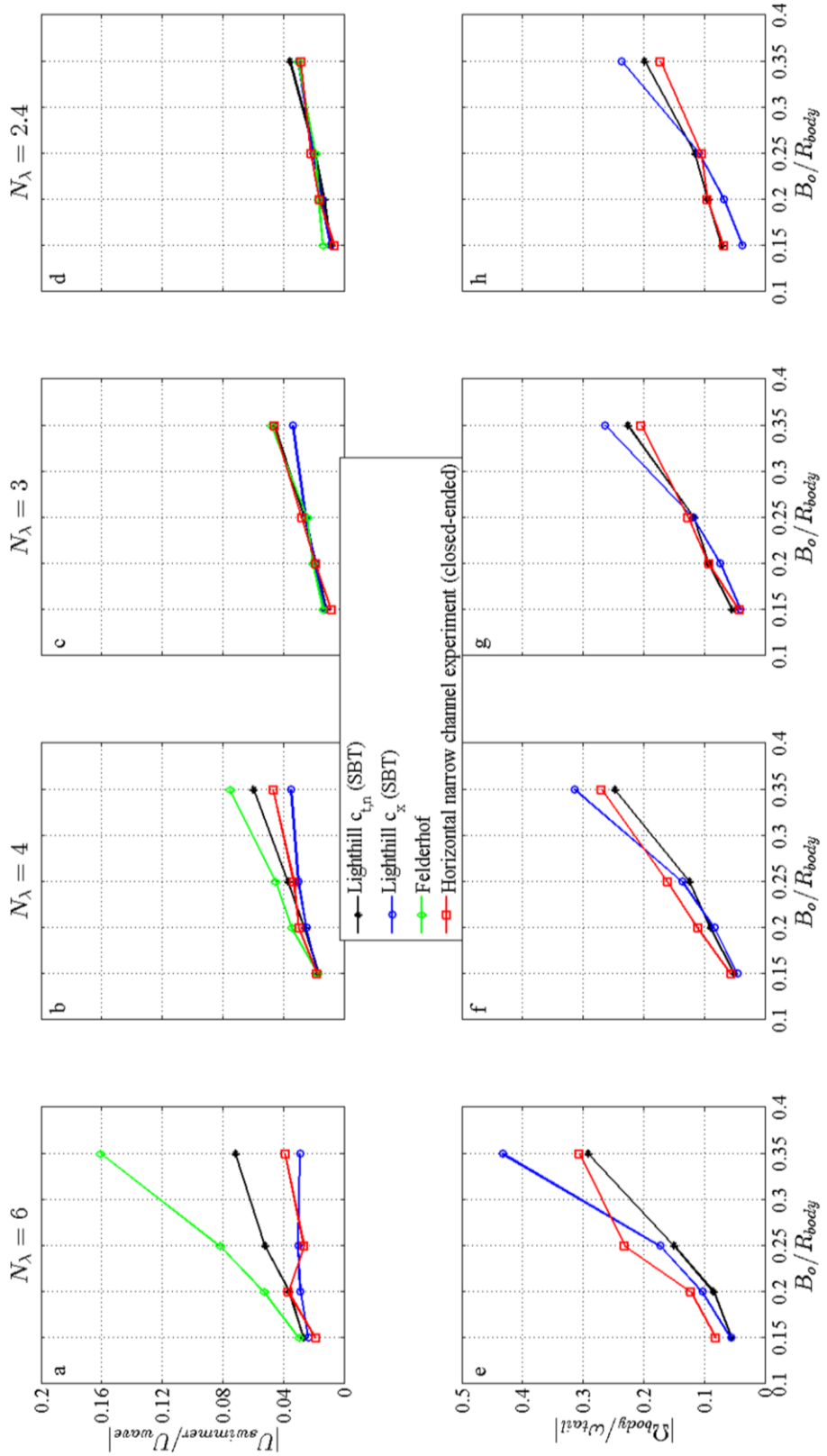

Figure 7.24: Closed-ended horizontal narrow channel results predicted with slender-body-theory (SBT) approach and Stokes flow based asymptotic solutions.

To sum up, bounded medium force coefficients presents better result with varying wave geometry (see Figs. 7.22-7.24). Furthermore, the SBT-based c_x approach presented by Lighthill (1976) predicts the forward velocity components in good agreement with the experiments as depicted in Fig. 7.24. Lastly, the error observed in forward velocities for larger N_λ values are consistent with previous results based on the swimmer's increased weight (see Figs. 7.22a-7.24a).

7.7. Further Discussion on the Comparative Results

CFD-model is validated with the vertical channel experiments where the swimmer is translating along the symmetry axis of the cylindrical channel with closed ends. Observed sensitivity to the parameterized wave geometry in vertical channel experiments further demonstrates the fidelity of the CFD results presented in earlier chapters. On the other hand, the disagreement between horizontal channel experiments and CFD results with bio-inspired robots swimming in horizontal channels shows the importance of the combined effect of lubrication acting on the rotating helical tail and surface friction acting on the body and possibly on the helical tail.

Furthermore, comparisons on the horizontal in-channel swimming studies with different resistive force coefficients demonstrate that, any coefficient set may be used to predict rigid-body kinematics of a specific body-tail assembly. However, the sensitivity of a selected coefficient set to varying wave and channel geometries, and the proximity to the channel wall differ from each other. Furthermore, the SBT-based c_x analysis articulated by Lighthill (1976) and the position dependent resistive force coefficients presented by Brennen and Winet (1977) provide more advantageous results in comparison with other coefficient sets. In addition, the resistive force coefficients presented by Gray and Hancock (1955) perform reasonably well with the channel flow correction articulated by Happel and Brenner (1965). Moreover, the proposed novel torus-rod representation based resistive force coefficient set provide similar results with literature based coefficient sets; however, do not improve the overall performance of the microhydrodynamic model.

Hereon, the important modeling issues emerged throughout this chapter are discussed in further detail by means of comparisons between resistive-force-theory and slender-body-theory methods, and the results obtained by coupled actuation dynamics.

7.7.1. Contact Friction and Lubrication Effect

In this section, the motor rotation rate, ω_m, and the effective external rotational torque acting on the swimmer is studied. As it is presented in Figs. 7.25a-d and Figs. 7.26a-d by the time-averaged forward velocities, U_x, robots travel slower in narrow channels indicating that the effective fluid drag exerted on untethered robots is higher in the narrow channel than in the wide channel, assuming forward thrust is the same if not increased by traction Moreover, the observed rotation rate of the DC-motor, ω_m , are found to be identical in wide and narrow channel experiments as presented in Figs. 7.25e-h and Figs. 7.26e-h. Furthermore, different effective rotational friction constants, B_{eff}, calculated by the RFT-model, which is using the resistive force coefficients of Gray and Hancock (1966), in both channels (see Figs. 7.25i-l and Figs. 7.26i-l) can be attributed to different flow field characteristics.

It is suspected that surface contact occurs intermittently under the influence of the complex flow field induced by the untethered robot around the body and the tail, given the fact that each body-tail assembly has a constant individual mass. Thus smaller B_{eff} suggests longer lift-off time where lubrication effects become more important. It is also observed that B_{eff} is mostly dependent on the amplitude B_o instead of the wave length λ as depicted in Figs. 7.25i-l and Figs. 7.26i-l.

Forward velocities predicted by the SBT-model, i.e. c_x approach as referred in this text, (Lighthill, 1976), are in better agreement with the experimental results than the RFT-model results as demonstrated in Figs. 7.25a-d and Figs. 7.26a-d. Effects of the helical tail parameters are predicted with high accuracy via SBT approach with a few exceptions: In Fig. 7.25d it is observed that both RFT and SBT-model's calculations fail to predict the wave amplitude B_o dependency accurately for λ =25 mm. In general, forward velocity increases converging to a maximum as wave length increases, and also it decreases with increasing wave amplitude B_o, except for the instance of λ =25 mm. The latter behavior

transforms into a more complex pattern as untethered robot is placed inside the narrow channel.

Observations presented in Fig. 7.25e-h and Figs. 7.26e-h illustrate that the hydrodynamic torque required for the rotation of the body increases with the amplitude, B_o, thus total rotation rate, ω_m, values of the DC-motor decreases. On the other hand, similarly to forward velocity results, ω_m increases with the wave length converging to a maximum and saturates thereafter. It is noted that, body rotation rates are on the order of 10^{-2} to 10^{-1}. It is also noted that SBT and RFT-based calculations predict observed body rotation rates within 1 to 50 percent error; large values of error are observed with the RFT-based model.

It is experimentally and numerically confirmed that as the channel shrinks in diameter, the shear drag on the untethered robot increases and reduces its speed. The lowest velocity decrease is observed as 0.0653 mm/s for λ=10 mm and B_o = 3.5 mm, while the largest velocity drop occurs as 0.648 mm/s for λ=25 mm and B_o = 2.5 mm. It is also noted that 17% reduction in channel radius results in 38.9% decrease in the global average velocity of all body-tail assemblies.

Furthermore, it is deduced by the contact friction calculations carried out by actuation system equations incorporated in RFT-model that the bio-inspired robotic prototype is in intermittent contact with the channel surface under the influence of other forces such as the weight and buoyancy as well as the induced flow field within the channel. It is noted that proposed hydrodynamic model has the advantage of predicting effective friction without prior knowledge about the channel surface morphology, e.g. roughness, with a single calibration.

Moreover, in order to single out the effect of friction effects between swimmer and cylindrical channel wall, a new set of experiments are conducted with bio-inspired robots using stripped-wires (see Fig. 7.27). This case study includes 12 different unclothed tails, with exact dimensions to that of the clothed ones, and horizontal wide channel with open ends (see Appendix 6).

Results clearly suggest that as the contact between helical tail and channel increases, the ratio of swimming velocity to wave velocity tends to increase, to which the physical limit is 1 as for the motion of a screw inside a solid medium, e.g. wood.

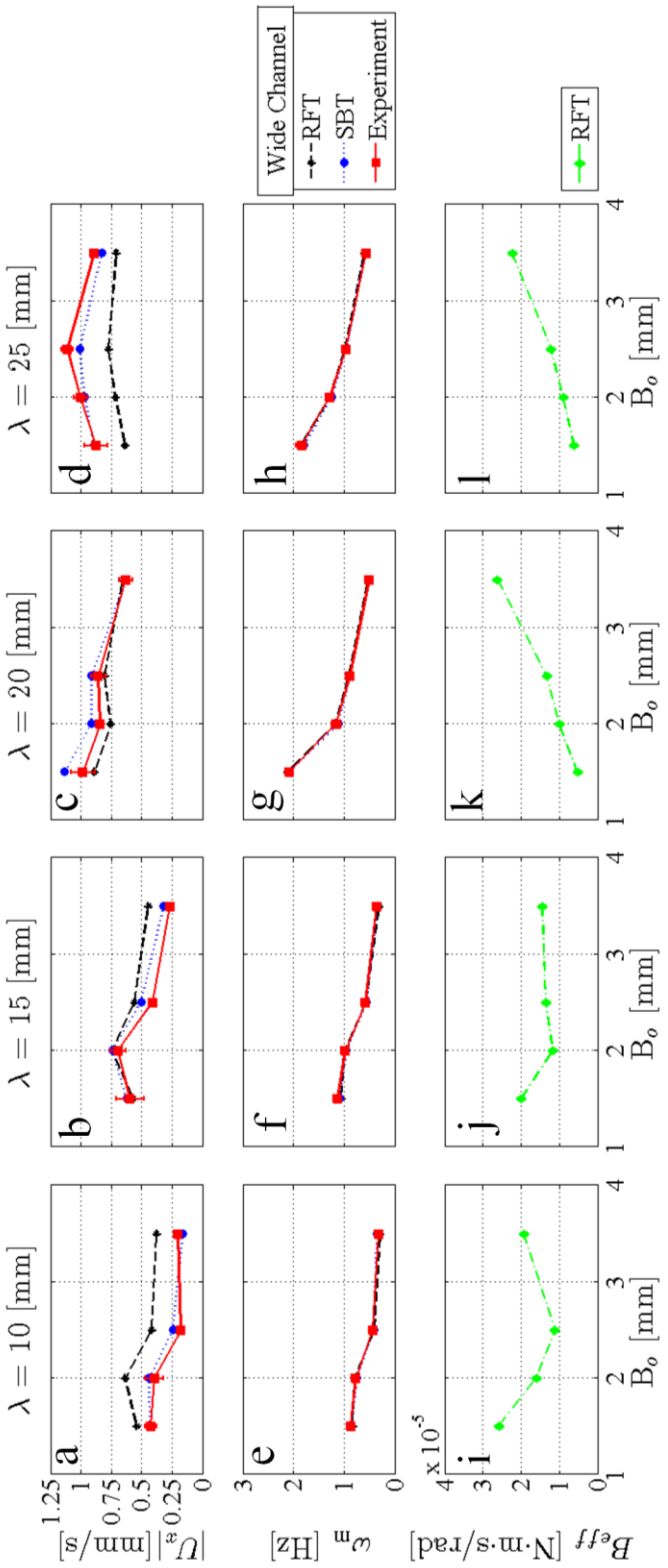

Figure 7.25: Open-ended horizontal wide channel experiment results, RFT vs. SBT: with respect to parameterized wave length and wave amplitude: time-averaged forward velocity (a-d); time-averaged motor rotation rate (e-h); time-averaged effective rotational friction constant (i-l). Re_{max} = 0.0058 with B_o = 2.5 mm and λ = 25 mm.

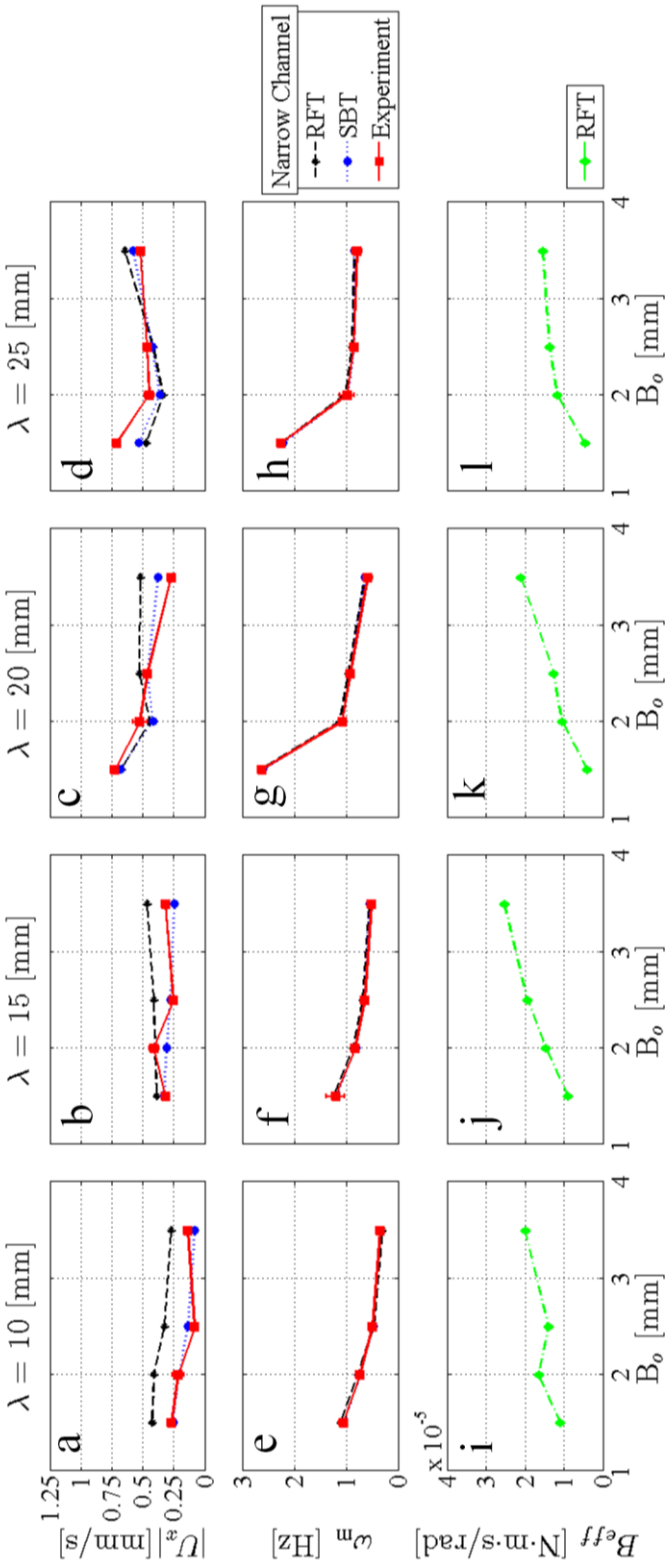

Figure 7.26: Open-ended horizontal narrow channel experiment results, RFT vs. SBT: with respect to parameterized wave length and wave amplitude: time-averaged forward velocity (a-d); time-averaged motor rotation rate (e-h); time-averaged effective rotational friction constant (i-l). Re_{max} = 0.0038 with B_o = 1.5 mm and λ = 20 mm.

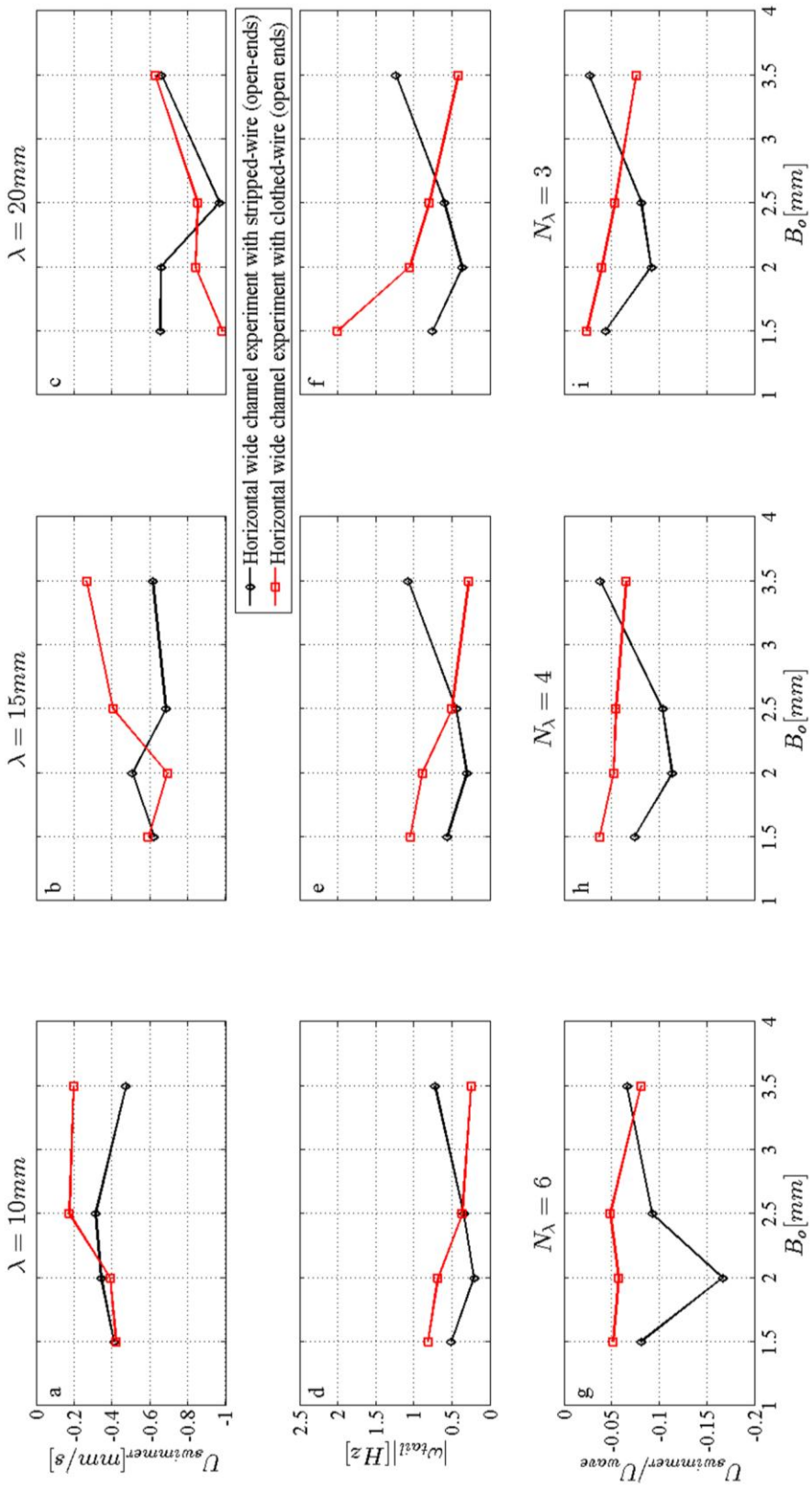

Figure 7.27: Effect of friction and lubrication: Experiments on swimming in open-ended wide horizontal channel.

However, as the wave amplitude increases, the swimmer cannot provide enough lift to separate itself from the surface, given the fact that the total weight increases due to fixed apparent tail length L_{tail}. Thus, combined with the increased contact friction on body and tail, the ratio of forward velocity of the swimmer to the wave velocity drops as presented in Figs. 7.27g-i. Furthermore, Figs. 7.27g-i show that there is a global maximum coinciding with B_o = 2 mm. In fact, it is safe to say that this global maximum is dependent on surface characteristics, effective weight of the swimmer. Hence, further study is required to resolve the interaction of swimmer and channel walls in close proximity.

7.7.2. Predicting the Effect of Channel Diameter on Body Resistance

The wall of cylindrical channel has a nonlinear effect on the fluid resistance exerted on the robot's body during rigid-body translation; however, the analytical studies include well known geometries and special conditions, such as spherical body moving parallel to the symmetry axis of the channel (Happel and Brenner, 1965).

One might use the reflection study presented by Happel and Brenner (1965) just to grasp the relation in between. For instance, with the eccentricity function value given f_{ecc} = 5.905 for $(R_{ch} - d_{body})/R_{ch}$ = 0.9, which corresponds to a proximity of 1.8 mm, used with Eq. (4.22) leads to the analytical prediction that the forward fluid drag of a spherical body having a radius equal to that of the robot's body, which is undergoing rigid-body translation near a cylindrical wall of an infinitely long channel with a radius equal to that of the wide channel and open ends, should increase by a factor of 4.125. This value is twice as big as the interaction coefficient used for Lighthill's SBT-based c_x approach (1976). A similar calculation for the narrow channel swim experiments provides a factor of 4.75, which is 1.38 times the interaction coefficient used for Lighthill's SBT-based c_x approach (1976).

Hence, one may deduce that the analytical approach is feasible with large B_o/R_{ch} ratios. However, as the proximity to the channel wall decreases, the correction factor further increases, which leads to the conclusion that the geometry of the swimming robot has an important effect on extra shear imposed by the presence of the cylindrical wall.

More accurate predictions may be possible with extensive computational studies; similar to one presented by Higdon and Muldowney (1995).

7.8. Further Analysis and Applications of Validated Hydrodynamic Model

7.8.1. Flow Field Induced by the Swimmer in In-Channel Experiments

Flow field induced by the swimming of a bacteria like robot confined to a channel, either due to translation or pump-effect, has interesting characteristics. The body replaces incremental amount of fluid in front at each forward step; however, the thrust force is not large enough to push the entire fluid column in front with the bio-inspired robot's swimming velocity. In other words, the momentum exerted by the rotating tail dissipates around the swimmer and the induced channel flow is rather insignificant. Similarly, the flow pushed backwards due to the pump-effect does not induce a stream running down the channel but leads to an extra flow field around the swimmer, which has a local velocity vector parallel to swimming velocity vector in the opposite direction.

Figure 7.28 demonstrates the displacement of air bubbles trapped in local flows arisen due to the pump effect and moving actually faster than the robot itself. Ten sequential snap-shots of exactly 1 s intervals demonstrate the in-channel swimming action. The air bubble in the viscous fluid are intentionally placed. The bubble of interest is marked by a green arrow. The net displacement of the swimming robot is approximately 3 units in forward direction, i.e. in terms of little squares visible in the sequential pictures, whereas the displacement of the air bubble is approximately 5 units in forward direction and one unit in lateral direction. Helical tail pushes the viscous fluid in the opposite direction of the swimming velocity. However, the flow changes its direction once purged at the back.

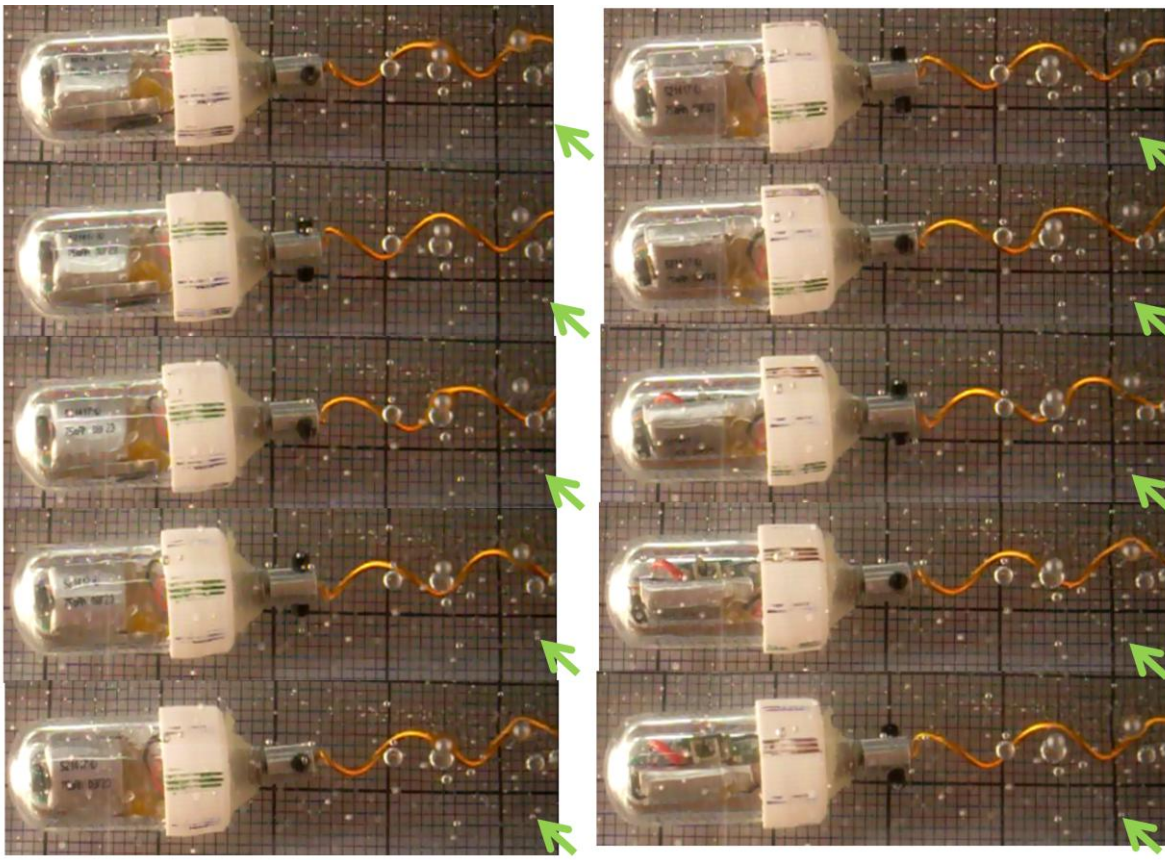

Figure 7.28: Observed flow fields around the swimmer: bubble displacement near the tail.

Stationary CFD-simulations provide similar results on the flow field around the swimmer's rotating tail. Figure 7.29 represents the **x**-component of the induced flow field in **yz**-plane located at $x_{tail} = L_{tail}/5$ away from the revolute joint (see Fig. 7.29a), and the **x**-velocity on a straight line on that plane (see the red line in Fig. 7.29b). The channel diameter is 17.5 mm, the wave amplitude is 3.5 mm and the wave length is 25 mm. The helical tail intersects the straight line with $\omega_{tail}t = \{0, 210\}$ as presented in Fig. 7.29b. It is also clearly portrayed that the **x**-component of the induced flow field has local values larger than that of the prototype robot's swimming velocity, as larger as six times in magnitude in both direction (also see Fig. 7.29b), which indicates that the back-flow induced by the pump-effect may attain large velocity values locally. These results obtained by physical and numerical experiments provide confirmation for Watari and Larson (2010) on the discussion about the instantaneous local velocities attaining larger values than the swimming velocity of the robot.

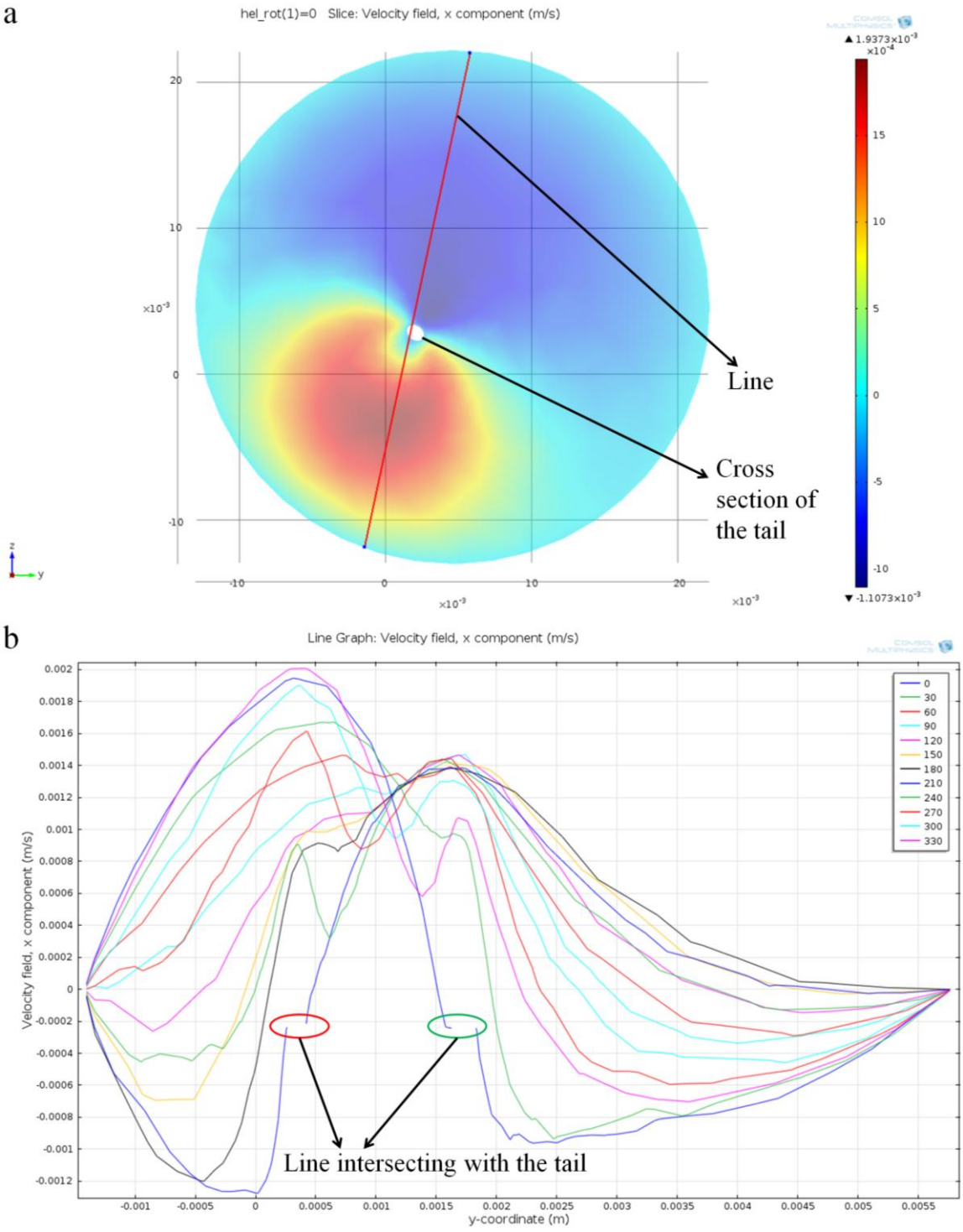

Figure 7.29: Calculated flow fields around the swimmer: CFD-solution of the induced flow field for the swimmer presented in Fig. 7.28.

7.8.2. Model Based Motion Control Studies

Here, the presented hydrodynamic model coupled with actuation system model for the experimented bio inspired bacteria-like robot is kept strictly first order. However, the magnetic actuation would introduce second order effects such as step-out phenomena. Furthermore, the selected approach for incorporating the wall effects on the swimmer robot's body may also introduce instantaneous stiffness to the resistance matrix. Such model can be solved by stiff or non-stiff solvers depending on the overall stiffness of the problem. However, details of a magnetic actuation system is beyond the scope of this text, and it is encouraged to model all effects in first order fashion with disturbance observer to eliminate all second order effects for achieving effortless control operations.

The bacteria-like robot studied here is an under actuated system given that the only possible system input is the motor current; however, the resultant rigid-body motion has six degree-of-freedom, but the dominant motion is the forward swimming. Complete control of the swimmer requires at least three active tails; however, for sake of simplicity, only forward velocity is considered in this simulation study given that the robot is confined to a relatively narrow channel.

The hydrodynamic model coupled with actuation system dynamics can predict the instantaneous motor current. Fig. 7.30 presents the time-averaged motor currents predicted with hydrodynamic model using the resistive force coefficients presented by Brennen and Winet (1977); based on the wide channel experiments (Tabak and Yesilyurt, 2012b). The motor current increases with decreasing wave length and increasing wave amplitude which is consistent with decreasing effective rotation rate of the DC-motor, ω_m, as demonstrated in Figs. 7.30a-d (also see Figs. 7.12e-h). Decrease in rotation rate leads to increasing current because of decreasing back-EMF effect. It is noted that the motor current is 130 mA under no load.

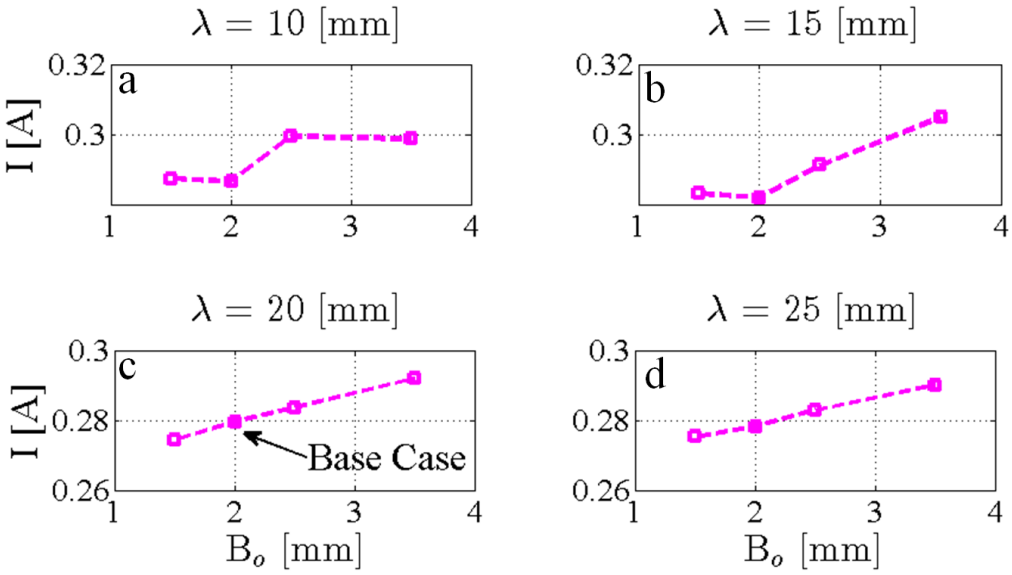

Figure 7.30: Predicted time-averaged motor currents for wide horizontal channel experiments.

PI-control is integrated in the hydrodynamic model in order to simulate the forward swimming of untethered bio-inspired robot under a designed upstream velocity condition, i.e. modeled as a step function as specified in Eq. (7.1). The position control scheme is based on predicting the state of the system at the next time step beforehand (see Fig. 7.31). Robot is given a position reference to follow, and the upstream velocity has initial and time-dependent components acting as disturbance.

$$W_{\mathbf{X}} = W_0 + W\begin{cases} 0 \Leftarrow t < t_0 \,\&\, t > t_1 \\ 1 \Leftarrow t_1 \geq t \geq t_0 \end{cases}, \tag{7.1}$$

where t_0 and t_1 are the instances for rising edge and falling edge upstream conditions, respectively (see Fig. 7.32).

Generated control output is used as the actuation frequency of the tail which is embedded in the rotation matrix between local Frenet-Serret frames and swimmer's own frame of reference. The control output is given by:

$$\omega_{\mathrm{m}} = \mathrm{K_p} e + \mathrm{K_i} \begin{cases} \int e \, \mathrm{d}t & \Leftarrow \mathrm{I}(t) < \beta \mathrm{I_{lim}} \\ 0 & \Leftarrow \mathrm{I}(t) \geq \beta \mathrm{I_{lim}} \end{cases} \tag{7.2}$$

where e is the time-dependent position error, $\mathrm{K_p}$ is the proportional gain, $\mathrm{K_i}$ is the integrator gain, $\mathrm{I_{lim}}$ is the maximum possible current without destroying the driver circuit shown in, and β is a safety factor, e.g. 0.99. The model receives the controller input and calculates the required instantaneous motor current to sustain the desired forward velocity. Thus the effective control input is the motor current, although PI-control algorithm predicts the necessary tail rotation rate.

Additionally, a rudimentary anti-windup method is implemented in order to prevent numerical overflow due to integrator gain: as the motor current is saturated or position error goes to zero, negative of recent error integration is sent back to the ODE solver thus resetting the entire integral back to its initial value, i.e. zero. Derivative gain is excluded given that the model is first order, i.e. in order to avoid introducing additional numerical stiffness to the model.

The following scenario is studied in order to demonstrate the behavior of the model and PI-control algorithm as a model-based control scheme to predict required motor current with saturation. A case study is carried out with λ = 20 mm and B_o = 2 mm with the limit current of 500 mA. The swimmer's center of mass is initially at rest at x = 0 mm and an arbitrary final destination is set as -27 mm down the channel's long axis. Upstream velocity is designated with an initial value of W_0= 0 mm/s and step increase of W= 25 mm/s with the rising edge occurring at t = 4 s and falling edge ensuing at t = 8 s.

In Figs. 7.32 - 7.34, it is demonstrated that the motor current climbs up to 300 mA immediately and saturates at 500 mA when proportional gain $\mathrm{K_p}$ is set to 12 for given position error, and drops to zero as the position error goes to zero. However, proportional control renders inadequate output to follow the reference while untethered bio-inspired robot is under the influence of upstream flow, mainly because of the rate of increase in the controller output, ω_{m}, and the current saturation after the maximum safe limit (see Fig. 7.33). Consistent with experimental results, motor current is well above zero unless position error drops to zero, which is in part subject to numerical error.

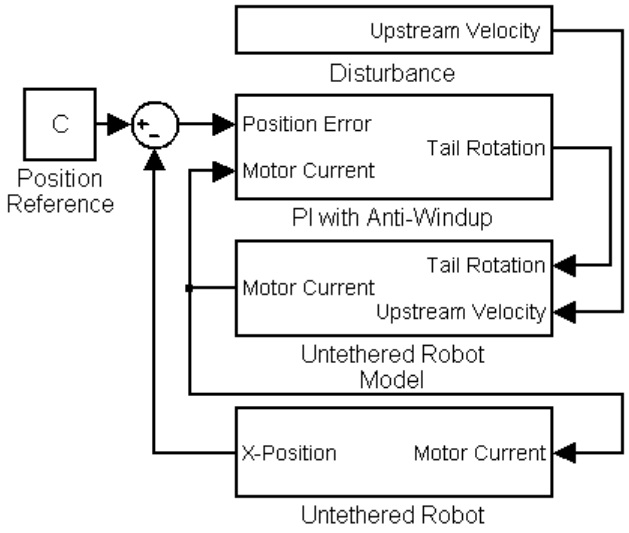

Figure 7.31: The simulated model-based control scheme with the hydrodynamic model, which is coupled with the actuation system dynamics.

As the proportional gain is reduced below K_p = 12, convergence of the system decreases and motor current falls below the maximum limit (see Fig. 7.33) down to 300 mA and drops to zero simultaneously with diminishing position error. Then, integral gain is set to K_i = 12 with K_p = 10 in order to overcome the effect of upstream velocity with a fast convergence rate which results in 4 mm overshoot around t = 0.9 s, which dissipates gradually (see Fig. 7.32). However, corresponding current demand does not dissipate as fast due to the integration history and first order nature of the model (see Fig. 7.33). Typically, higher integrator gain causes higher overshoot but offer a better performance in managing upstream conditions as demonstrated in Fig. 7.33.

Predicted robot velocity values are depicted in Fig. 7.34, and figures are consistent with the position error and motor current plots. It is observed that simulated instantaneous velocity of the untethered bio-inspired robot may reach up to velocities on the order of 100 mm/s.

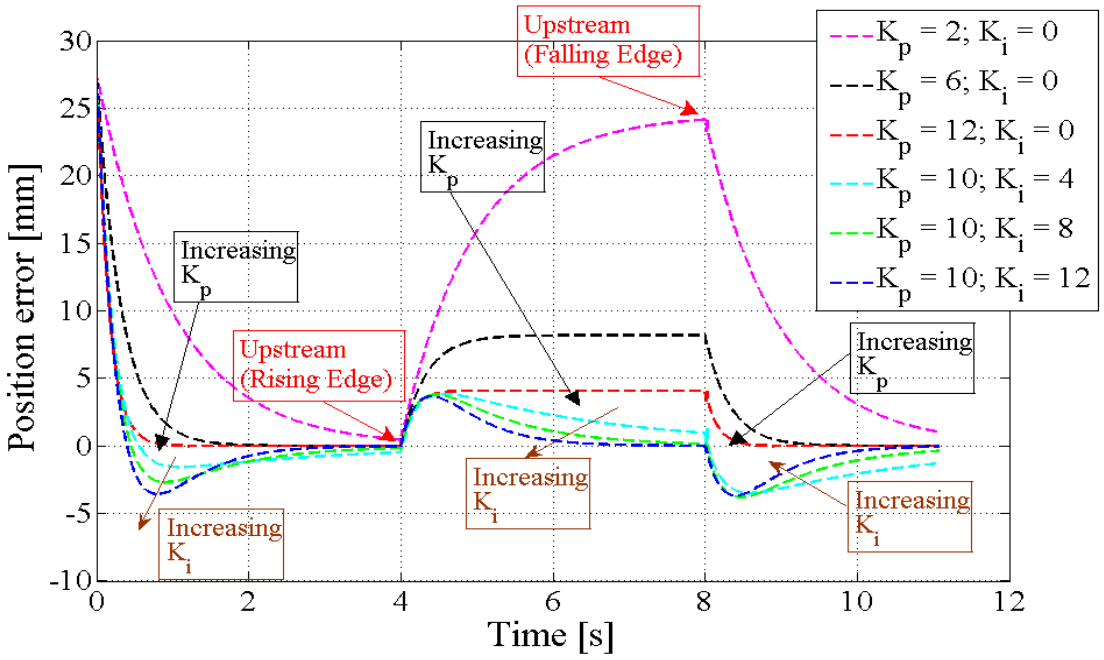

Figure 7.32: Position error of the swimmer robot: the proportional gain performs adequately without a disturbance; however, integral gain is required to overcome the

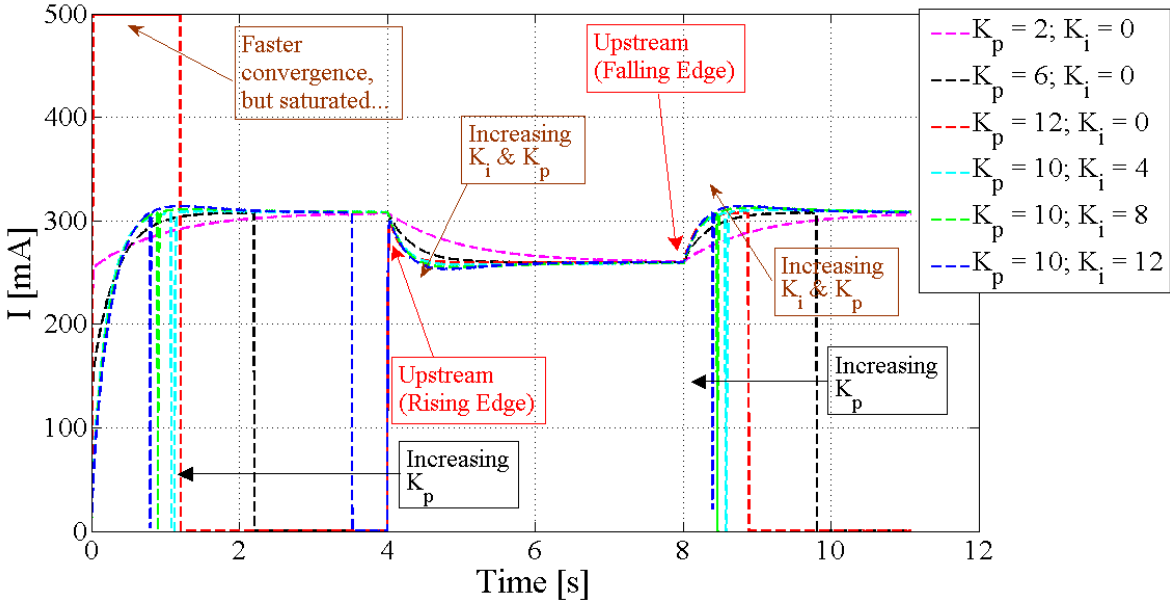

Figure 7.33: Motor current demanded by the swimmer robot. Motor current may saturate without integrator gain, even an upstream velocity is not existent to act as disturbance.

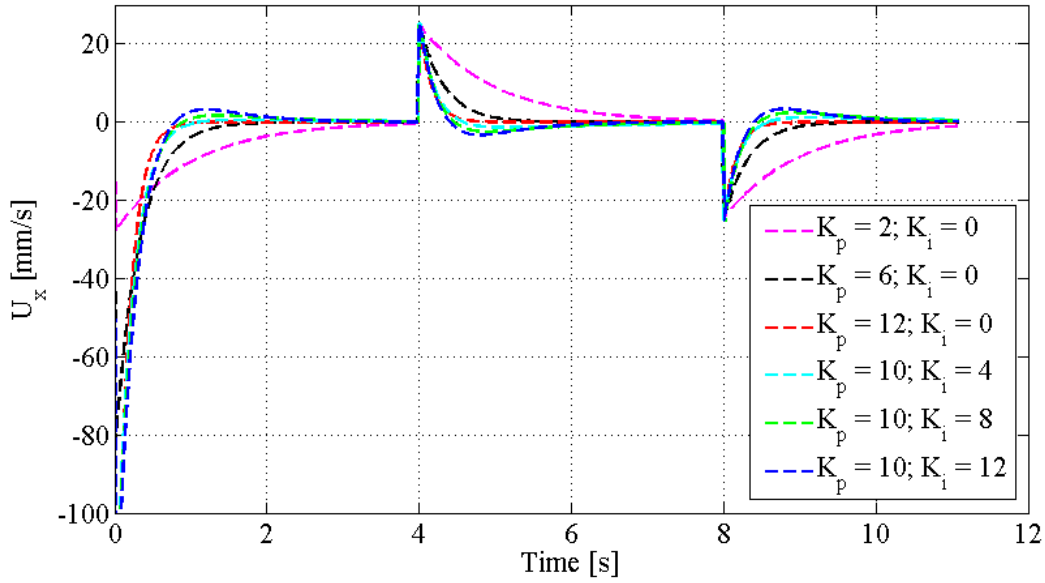

Figure 7.34: Predicted forward velocity of the robot.

Next, control simulations are carried out to study the effect of a pulsating upstream flow with varying proportional and integrator gains. The upstream is modeled as follows:

$$W_{\mathbf{X}} = W \sin(\omega_{upstream} t)\,. \tag{7.3}$$

Sinusoidal (pulsating) upstream with an amplitude, *W*, three times the observed forward velocity of base-case design. Simulating flow conditions inside organic tissue such as blood vessels. It is observed in Figs. 7.35 - 7.36 that the integral gain is required to handle the upstream velocity. Furthermore, although it provides far superior results, PI-controller is not fully adequate to eliminate the position error given that the model is strictly first order. Hence, a disturbance observer designed for first order systems is required for high precision operations (Huba, 2012a; 2012b). Such observer would simply filter out higher order effects and preserve the first order nature of the proposed hydrodynamic model.

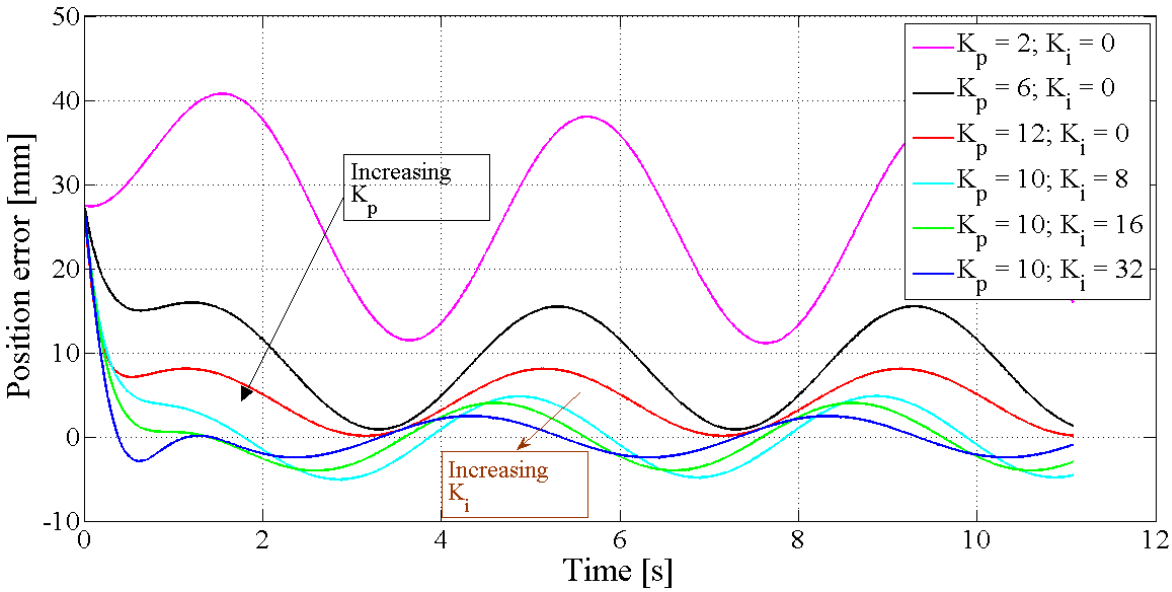

Figure 7.35: Predicted position error of the bacteria-like swimmer robot under the influence of sinusoidal upstream velocity.

Results show that the proposed hydrodynamic model is suitable for control studies: the proportional gain is established adequate for position control purposes due to first order nature of the RFT model; however, it is also demonstrated that integrator gain with anti-windup is necessary in order to determine the required rotation rate of the motor and to drive maximum possible current to minimize position error under the influence of time-dependent upstream velocities acting as disturbance. Furthermore, it is deduced that appropriate disturbance observers are required to achieve high precision operations.

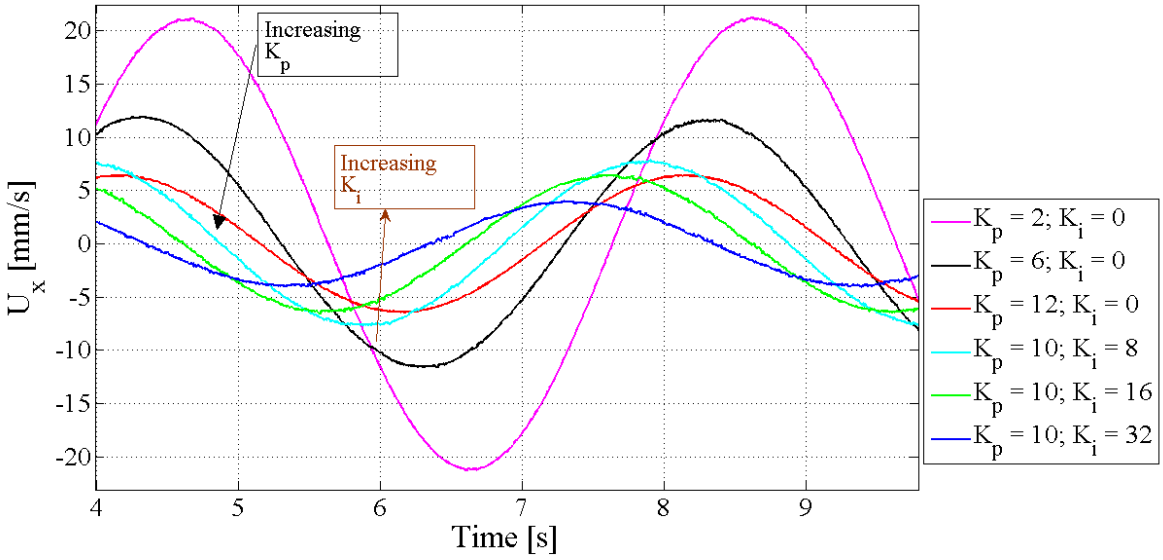

Figure 7.36: Predicted forward velocity of the bacteria-like swimmer robot under the influence of the sinusoidal upstream velocity.

It is noted that gravitational pull has a stabilizing effect on the studied untethered bio-inspired robot mobility, i.e. eliminating lateral rotations and translations which simplifies the analysis and increases the coherence between simulations and experiments. It is also noted that the calculated current is applied on the DC-motor which rotates the helical tail clockwise or counterclockwise depending on the error. Resultant thrust pushes the swimmer forward or backward, while the driving circuitry is protected with integrator anti-windup and current saturation fail-safes. More detailed discussion on anti-windup strategies can be found in (Edwards and Postlethwaite, 1996; 1998).

8. FUTURE WORK

Important subject matters emerged during numerical and physical experiments that would require further investigation and validation. Here, a brief discussion on the lubrication issue is presented based on the experimental results and handling hard surface contact, followed by discussions on efficient geometric designs, searching for unobserved geometric properties of a swimmer or its choice of wave propagation method with limited experimental data, and a simple model-based position control scheme.

The proposed hydrodynamic model is capable of providing high fidelity results within a limited design space much faster than CFD or SBT-based time-dependent models. Given the fact that the hydrodynamic model is first-order in nature, one may even use simple forward-Euler integration in time-domain to predict the velocity vector of a desired geometric design, which is not included in this text. These features present the hydrodynamic model as a flexible and reliable tool; however, the following issues must be addressed before conducting demanding operations.

8.1. Lubrication Analysis

Experimental results indicate that the interaction between rotating helical tail and cylindrical channel walls requires lubrication analysis on extremely fine mesh in the CFD models. The weight of the swimming robot has an advantage of eliminating rigid-body translations and rotations in lateral directions inside a bounding channel with $R_{ch}/R_{body} < 2$. However, intensified traction effect on the helical tail cannot be computed by CFD-models correctly without lubrication analysis. The hydrodynamic model would benefit from an

analytical model of lubrication effects on the tail derived with the help of extensive numerical investigations. The hydrodynamics of helical tails translating and rotating in close proximity to plane or cylindrical walls should be studied coupled with general CFD analysis presented in this text. It is viable to formulate resistive force coefficients for lubrication effects on a rotating machine part (Zeidan *et al.*, 1996), and a similar coefficient set can be derived for rotating and translating body and helical tail of a swimming robot.

A related analysis was carried out by Higdon and Muldowney (1995), in which authors employed lubrication analysis to provide validation of the numerical results. The analytical results were obtained for a rigid spherical particle moving towards the a cylindrical solid boundary and a rigid helical particle moving simultaneously in axial and tangential direction with zero net torque acting on it (Higdon Muldowney, 1995).

Analytical solution of the Reynolds equation (see Eq. (8.1)) in cylindrical coordinates should provide an alternative solution for the lubrication effects on a rotating rigid and flexible helical tails. Helical tails employed in the in-channel experiments presented in this text have a rather combined motion of rigid-body rotation around their long axis while translating along the symmetry axis of the cylindrical channel. Provided that there is an attack angle between the helix and symmetry axis of the channel, the motion of the helical tail can be modeled as the sliding-rolling motion of a toroidal rigid surface over a wall with an ellipsoidal curvature. The general form of Reynolds equation between two surfaces, S_1 and S_2, in close proximity of d in cylindrical coordinates is given as (Stolarski, 1990):

$$\frac{1}{6}\left[\frac{1}{r}\frac{\partial}{\partial r}\left(r\frac{\mathrm{d}^3}{\mu}\frac{\partial p}{\partial r}\right)+\frac{1}{r^2}\frac{\partial}{\partial\theta}\left(\frac{\mathrm{d}^3}{\mu}\frac{\partial p}{\partial\theta}\right)\right]=(U_{r,S_1}-U_{r,S_2})\frac{\partial \mathrm{d}}{\partial r}-2(U_{x,S_1}-U_{x,S_2}) \\ +(U_{\theta,S_1}-U_{\theta,S_2})\frac{1}{r}\frac{\partial \mathrm{d}}{\partial\theta}+\frac{\mathrm{d}}{r}\{\frac{\partial}{\partial r}[r(U_{r,S_1}+U_{r,S_2})]+\frac{\partial}{\partial\theta}(U_{\theta,S_1}+U_{\theta,S_2})\} \quad . \tag{8.1}$$

CFD simulations fully coupled with lubrication analysis are required to numerically solve the swimming of a bio-inspired robotic device in close proximity to cylindrical walls, after which the analytical solution of Eq. (8.1), or a fit study akin to that carried out in torus-rod analysis which provided successful results (see Appendix 2). The results should be confirmed with analytical solutions and be embedded in the hydrodynamic model.

8.2. Collusions with Surrounding Boundaries and Contact Friction Analysis

Consider an artificial swimmer, much like the robotic prototype studied within this text; however, with the dimensions of an *E. coli* (Chattopadhyay and Wu, 2009). Considering the materials in use for MEMS and IC manufacturing, it is conceivable to imagine the swimming robot would have an average density much higher than the surrounding fluid or the mass distribution may not be homogeneous throughout its entire structure. Thus, provided that the neutral buoyancy condition is not satisfied, the swimming robot would eventually come into contact with the bounding walls. A hydrodynamic model is required to handle such occurrences in order to predict the time-dependent velocity vector and trajectory of such a robotic device accurately.

Indeed, the stiffness and friction acting on the point of contact, either on the body or tail, can be incorporated in the hydrodynamic model provided that the position and penetration depth of the robotic device is accurately registered with appropriate sensors or visualizing methods.

Here, for sake of simplicity, the swimming helical robot is assumed to perform in cylindrical channel, which is positioned such that its symmetry axis is perpendicular to the gravitational pull. Assuming that there is no prior information about the surface morphology and local material stiffness of the bounding walls, one may formulate the stiffness and damping effect of the contact in radial direction as follows:

$$F_{r,contact} = -\frac{k_{wall}}{\mathrm{m}_{swimmer}}\delta_r n_r + \frac{b_{wall}}{\mathrm{m}_{swimmer}}U_r n_r \quad \Leftarrow \quad \delta_r \neq 0\,. \tag{8.2}$$

Here, $\mathrm{m}_{swimmer}$ is the total effective mass of the swimmer due to buoyancy and gravity, δ_r is the penetration depth in radial direction, U_r is the instantaneous radial velocity, n_r is the surface normal at the point of contact, which is pointing inwards. The damping constant

of the wall, b_{wall}, may include a conditional switch and sign change to handle sticking and non-sticking wall conditions. The stiffness of the wall, k_{wall} , can be predicted as:

$$k_{wall}\delta_r n_r = (\mathbf{F}_{propulsion} + \mathbf{F}_{fluid\ \text{resistance}} + \mathbf{F}_{gravity} + ...)\cdot n_r \quad \Leftarrow \quad \delta_r \neq 0 \ \& \ U_r \geq 0\,, \qquad (8.3)$$

where the actual goal is to update the instantaneous stiffness of the bounding walls with the help of calculated forces, surface normal and measured penetration depth (see Fig. 8.1). Furthermore, one may calculate the instantaneous damping constant of the wall with a suitable damping condition in order to simulate continuous contact (Ogata, 1997).

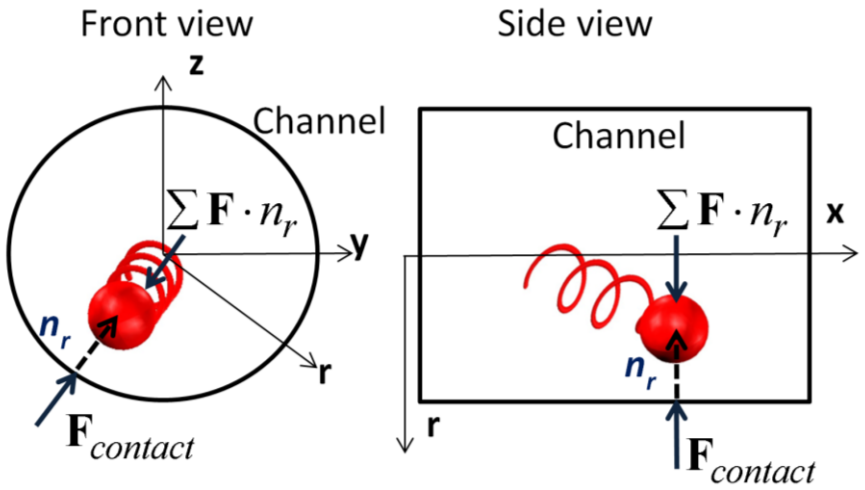

Figure 8.1: The surface normal at the point of contact and the contact force on a heavy robotic swimmer confined in a cylindrical channel.

Figure 8.2 demonstrates the combined effect of gravity and non-sticking wall contact on a heavy helical swimmer's trajectory: the swimmer is placed in a concentric orientation initially. As soon as the simulation starts, gravity pulls the swimmer towards the channel wall and eventually swimmer hits the surface, which has a predefined penetration depth of 10^{-6} m. However, swimmer does not follow a straight line and climbs the wall in clockwise direction up to a height at which gravity pulls it away from the wall such that it starts another descent (see Fig. 8.2a). The propulsive effect from the rotating rigid helix continues to push the swimmer forward regardless of the contact (Fig 8.2b). However, Eq. (8.3) may require further tuning to predict the wall stiffness correctly; hence experimental and

numerical studies are needed to collate data to elaborate further on the wall stiffness and damping constants.

Here, it is also important to acknowledge that during the surface contact, a friction force and torque will emerge against the instantaneous velocity vector, which will eventually exhibit the effect of translational and rotational friction action on the swimmer. There exist several methods to model surface friction (Olsson *et al.*, 1998), one of which may be adapted into the hydrodynamic model to expand the in-channel swimming studies.

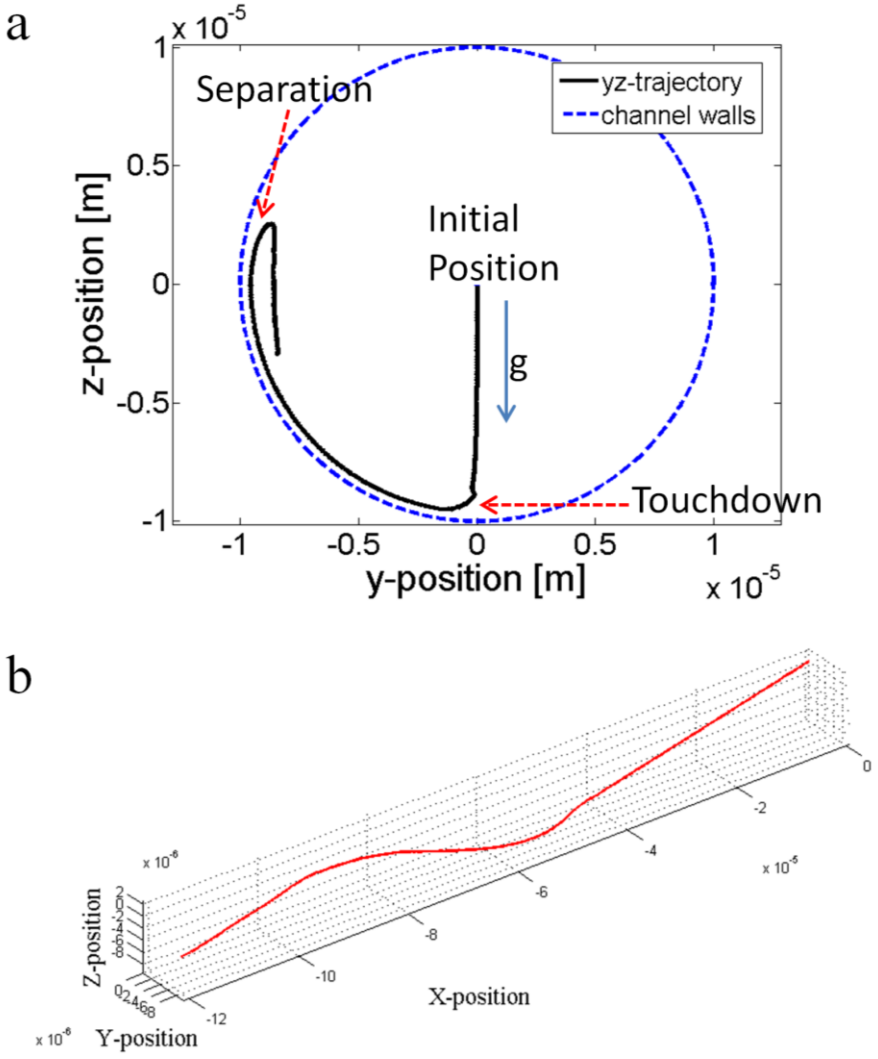

Figure 8.2: Trajectory of a heavy helical swimmer confined to a cylindrical channel: **yz**-trajectory on **rθ**-plane (a); and 3D trajectory (b).

8.3. Inverse Engineering with Limited Observations

In addition to geometric design, hydrodynamic model can also be used to estimate physical properties of natural swimmers. Similar to the procedure of obtaining the interaction coefficients through the solution of the inverse problem discussed above, geometric properties and wave propagation parameters of a natural swimmer can be determined from the hydrodynamic model. For example, given the swimming trajectory of a particular spermatozoon specimen, e.g. the bull sperm cells studied by Friedrich *et al*. (2010), the corresponding wave shape and pattern can be obtained from the solution of the inverse problem. Moreover, Gurarie *et al*. (2011) demonstrated that stochastic model can be used for the prediction of the full three-dimensional trajectory of the swimmer based on two-dimensional observations; hydrodynamic models can be used to improve the predictability of complex trajectories.

8.4. Computation of Force Coefficients by Interpreting the Tail Geometry as Separate Rigid-Bodies.

The Rod-Torus analogy, which is employed in this text to predict the resistive force coefficients in bounded medium, may be expanded to include the off-diagonal elements in the resistive force coefficient matrix, **C**. Experimental studies showed that the propulsive velocity of the robotic prototype is sensitive to the surface morphology, thus the local proximity of the helical tail. Further study may reveal cross coupling elements in rigid-body translation, such as the lift induced by the lubrication effects on a slender body moving parallel to solid boundaries with close proximity or the Magnus effect of rotating bodies (Cipparrone *et al*., 2011), which would be presented by an off-diagonal element in **C**. Moreover, the study can be expanded to include the hydrodynamic interaction between two

tori (Thaokar, 2008) to include the interactions between consecutive waves inside a confined viscous medium.

8.5. Further Experimental Studies

Given the fact that, a therapeutic micro robot is expected to perform in living tissue, in-channel experiments must also be conducted in flexible channels filled with viscous fluids. Furthermore, the experiments, presented in this text, utilize rigid helical tails; however, a new experimental set with flexible tails with parameterized actuation frequency, ω_{tail}, will broaden the analysis into the field of elasto-hydrodynamics (EHD) when combined with the lubrication study.

Furthermore, the simulated position control studies presented in the previous chapter should be validated with actual experiments by position control with suitable sensors integrated in a closed control loop. Figure 8.3 demonstrates an experimental setup for such study. The position of the swimmer can be registered by Hall-effect sensors or with the help of visual servoing. Furthermore, the position of the swimmer can be controlled with respect to a moving submerged obstacle.

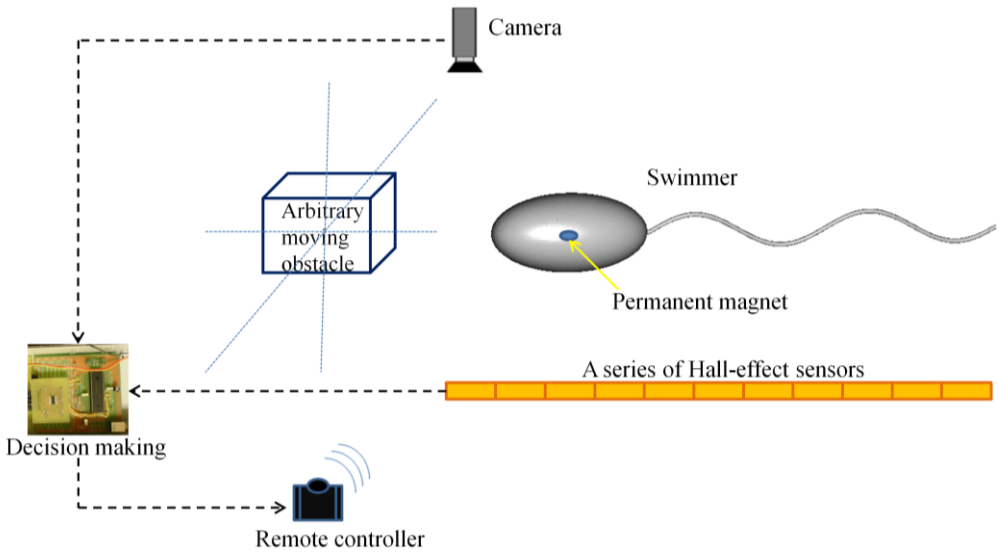

Figure 8.3: Experimental design for position control studies.

In addition to control studies in stationary fluids, upstream velocity conditions may be implemented by viscous pumps and different flow characteristics in time-domain such as sinusoidal functions and impulses can be simulated in physical experiments.

Experimental analysis should also be expanded to include helical tails with heterogeneous wave amplitudes and wave lengths to inspect the effect of changing wave geometry on the same helical tail. Furthermore, in order to inspect the flow field induced by the helical tail and translation of robotic prototype, forward and backward swimming must be studied with macro-PIV as the robots move confined in channels.

9. SUMMARY AND CONCLUSIONS

The motivation of this work is to study the hydrodynamics and rigid-body kinematics of the bio-inspired swimming robots, which are operating fully submerged in confined viscous flows. Main goals are to understand the relationship between channel walls and robot motility, and to understand the interactions between swimming robot's body and tail. The main approach is to conduct physical and numerical experiments, by which a fast and reliable reduced order hydrodynamic model is implemented, improved and validated for specific applications such as design and control of propulsion systems for bacteria-like micro robotic tools.

In this study a bio-inspired swimming robotic prototype was built. The robotic prototype was comprised of two links: body and rigid helical tail. The body was equipped with an on-board power supply and a PWM control circuit with IR receiver. The rigid helical tail was replaceable.

The robotic prototype was utilized in in-channel swimming experiments with cylindrical channels of constant cross-section, which were filled with silicone oil. Two major sets of experiments were conducted. The experiments with vertical channels studied the swimming action without the effect of gravity, surface friction and lubrication. The experiments with horizontal channels studied the effect of channel geometry, i.e. varying diameter and having either open or closed ends.

In vertical studies the neutral buoyancy was obtained by a cork attached at the tip of the swimmer's body. The total mass of the swimmer was constant, thus the actual length of the wire, from which the helical tail was manufactured, was constant. The effect of wave length and amplitude was studied at the expense of varying tail length. All vertical channel experiments were carried out with channels having closed ends, thus the fluid replaced by

the translating body induced a flow of equal volumetric rate around the body in the direction of wave propagation.

In horizontal studies, the weight of the robot was dominant in comparison with the buoyancy force; hence the swimmer sat on the bottom of the channel. The effects of wave length and wave amplitude were studied with constant helical tail length, i.e. at the expense of varying swimmer mass. Furthermore, the channel itself was submerged in a silicone oil bath, which allows open ends.

Experimental results demonstrate that the close proximity to channel walls induce a traction effect on the rotating helical tail which in turn leads to amplified thrust force which overcomes the friction effects on the body. However, as the swimmer was pulled further towards the wall because of the increased total weight, the friction effects overcome the amplified thrust. Hence, the forward velocity reduces. To be able to inspect the effect of traction further, a comparative study was carried out with tails manufactured out of wires covered with soft cloth and with stripped tails. Observations confirms that as the lubrication effects were amplified between the smooth glass surface and stripped smooth copper tail the forward velocity increases.

Furthermore, the cylindrical channel geometry combined with gravitational pull, the rigid-body motions in lateral directions. Similarly, the restoring torque exerted by the cork on the swimmer, the swimmer translates parallel to the symmetry axis, i.e. long axis, of the cylindrical channel.

The uneven distribution of weight between body and tail prevents true neutral buoyancy. The size of the payload, i.e. body, depends on the size of available DC-motor, battery pack and control circuit. The swimmer's body should be as small as possible in order to reduce the fluid resistance; however, the on-board actuation system must be powerful enough to sustain continuous thrust to push the swimmer forward. Hence, there lies a pay off between size and ability to overcome the viscous shear, and the weight of the tail was used to confine the swimming motion in a single direction generally. Consecutively, the swimmer's frame of reference and lab frame was coincident. Furthermore, the overall size of the swimmer prevents swimming velocities as fast as a bacteria does achieve, e.g. distance travelled on the order of total length per unit time, because of the fact that the $Re < 0.1$ condition must be satisfied.

The experimental studies with varying channel geometry showed that the swimming velocity was greatly susceptible to the geometry and proximity of walls confining the flow field. Furthermore, it was also established that the flow field induced inside the swimmer, the upstream due to body translation, affects the overall swimming behavior. To sum up the experimental contributions of this study; the effect of proximity to cylindrical channel walls on confined swimmer's propulsion velocity is studied in vertical and horizontal orientations with respect to gravitational pull, the effect of channel diameter on in-channel propulsion velocity of swimmers is inspected in horizontal channels, and the effect of wave geometry on in-channel propulsion velocity is inspected with parameterized wave amplitude, wave length and tail length.

Next, a CFD-model was implemented to simulate swimmers with helical and planar wave propagating tails. The viscous fluid surrounding the swimmer was bounded by a cylindrical channel, and the induced flow field was governed by Navier-Stokes equations subject to continuity, in either time-dependent or stationary fashion. Time-dependent approach requires dynamic mesh deformations around the swimmer whereas the stationary solution works with stationary meshing of the fluidic domain. The solution time for a robotic swimming simulation in time-domain requires at least a few hours, and even up to a week, to complete full three periods of tail rotation; whereas the stationary simulations require less than an hour.

CFD-model was validated by vertical channel experiments where the swimmer and channel walls do not interact through lubrication or friction. Furthermore, the sensitivity to varying wave and tail geometry predicted in good agreement. In addition to wave geometry study, the effect of channel diameter was studied with CFD mode. Results show that the body of the swimmer has a profound effect on the forward velocity when the ratio of body diameter to helix diameter was larger than unity. Also, the body acts like an obstacle to the replaced fluid in front; hence, the propulsion velocity increases to a maximum where the combined shear and traction on the swimmer was at its minimum. The forward swimming velocity slightly decreases converging to unbounded medium swimming with increasing ratio of the channel radius to the body radius.

Horizontal channel simulations were carried out with swimming robots in eccentric position with respect to the channel's long axis. The proximity of the body was assumed to

be 1 mm in radial direction, which; however, was not enough to determine the forward velocity with reasonable accuracy. This result indicates that the overall proximity of the swimmer was much smaller than 1 mm, thus the CFD-models without lubrication analysis were not capable of simulating actual conditions of swimming in extremely close proximity to solid boundaries.

Furthermore, the hydrodynamic interaction between the body and the tail of the swimmer, which rotate in different directions, were studied in detail. It was observed that the hydrodynamic interaction takes place in close proximity to the surface of the swimmer and the viscous dissipation fades hydrodynamic effects quickly away from it. The flow fields induced by the rotating tail were studied in detail and it was deduced that the pump effect induced increases the hydrodynamic normal stress at the back of the swimmer's body where tail was attached with a revolute joint. The effective forward fluid resistance values, which were calculated by the CFD-model, acting on the body confirms this conclusion. In effect, the streamline density at the back of the body increases resulting in increased flow resistance; however, the change in resistance to the fore was minute in comparison. It was noted that, as the tail rotation terminated, the pump effect diminished and scarce streamline density was observed.

Furthermore, numerical examinations reveal that the lateral resistance of the swimmer's body has a nonlinear relationship with varying tail geometry. The pump effect, i.e. the streamlines forced to travel through the center of the helical tail, imposes extra shear force on the body with a phase angle subject to varying tail geometry. In effect, the lateral resistance drops when the lateral flow field at the back of the body contributes to the instantaneous velocity of the rigid-body translation of the swimmer in lateral direction. On the other hand, as the flow at the back of the flow field has a velocity vector in the opposite direction instantaneous swimming velocity in lateral direction, than the effective lateral resistance of the body increases. The phase angle was utilized to implement a modified resistance matrix with non-zero off-diagonal elements, i.e. a novel interpretation of diagonal resistance matrix to a rotating rigid body under the influence of another rotating rigid-body aligned in close proximity. Moreover, modified resistance matrix calculations predict the hydrodynamic forces acting on the swimmer's body with substantial accuracy. It

was also noted that, when the pump-effect is considered, body geometry was of less importance in comparison with the varying tail geometry.

To sum up the major contributions of the finite-element studies with the flow field induced by the swimmer; the proposed CFD-model is validated with vertical swimming experiments. Then, the effect of channel diameter on propulsion velocity of concentric swimmers is inspected with parameterized channel geometry. The hydrodynamic interaction between body and tail, which are rotating in opposite directions, of a bacteria-like swimmer is qualitatively and quantitatively explained with the help of varying body and tail geometry. Additionally, a novel set of resistive force coefficients are implemented based on representing each individual wave with a torus and rod of same minor-axis including the local proximity of each infinitesimal section of the wave along the axis of the rod to the bounding cylindrical channel wall. The new set is successfully tested against the experimental results and other coefficient sets presented in literature.

Finally, a reduced order hydrodynamic model was implemented based on resistive-force-theory (RFT). All acceleration terms in the flow field and the rigid-body accelerations of the robotic prototype were eliminated from the equation of motion. The premise was to show that an otherwise nonlinear high order stiff system could be represented by a linear system of first-order non-stiff equations.

Reduced-order hydrodynamic model was verified with the experimental results obtained by the in-channel swimming studies and the numerical results obtained by CFD simulations. Validation with CFD studies were carried out for varying wave geometry i.e. parameterized wave amplitude and wave length. Two different resistive force coefficient sets, one of which was a set of formulae based on slender-body-theory (SBT) analysis and the other was a constant force coefficient set obtained directly from the hydrodynamic forces acting on the base-case design based on resistive-force-theory (RFT) approach, were used. The sensitivity and performance of selected and predicted force coefficient sets were studied. It was deduced that, although predictions include numerical error to a certain degree, which was subject to wave geometry, it was possible to predict the kinematics of such swimmer in a certain design space.

The kinematic validations with experimental results were based on utilizing a single interaction coefficient for a single swimmer or group of body-tail assemblies. Different

resistive force coefficients were inspected in comparison with the classification of flow field analysis. One group includes resistive force coefficients (RFC) of unbounded flow field assumption and the second one includes the RFC sets of bounded flow field assumption. The third group includes the slender-body-theory (SBT) based analysis of helical tails with and without bodies and asymptotic solutions of Stokes-based flow field induced in cylindrical channels. It was observed that, SBT analysis and bounded flow field force coefficients provide reasonably better predictions except for robotic prototypes with heavy helical tails, where the effect of friction was clearly observable.

Furthermore, a custom resistive force coefficient set was successfully tested with in-channel swimming experiments. The helical tail was represented by a torus of major radius equal to that of the radius of the helical tail, and a rod. Minor radius of the torus and the radius of the rod are equal to the radius of the slender tail. The proposed formulae incorporate the wave amplitude, local proximity to cylindrical channel wall, and the radius of the cylindrical wall. The required force computations on the torus and rod geometries were carried out by parameterized CFD simulations. The custom set was found to be almost as useful as the other force coefficients presented in literature to take the presence of a solid boundary into account.

It was presented with case studies that, the proposed hydrodynamic model can be utilized in real-time model-based position control studies. The actuation system dynamics can be embedded in the hydrodynamic model by fully coupling the force and torque values. A non-stiff solver will provide fast and reliable results. For instance, it is possible to predict the instantaneous motor current of swimming robotic prototype, which is subject to a limiting value, with a simple PID controller scheme based on the position error. Then, the required motor rotation rate can also be calculated with instantaneous hydrodynamic load and effective friction coupled in the equation of motion of the DC-motor.

Furthermore, a set of CFD simulations would require high-end computational power and extensive computational time to provide design space sweep for effective geometric designs. Furthermore, the mesh quality on the body and tail of the swimmer should be exactly same in order to prevent numerical error to contaminate the results unevenly. However, investigation on a large amount of body-tail assemblies with same mesh quality without intensive convergence problems is a demanding task. On the other hand, the

proposed hydrodynamic model constitutes a reliable and fast tool for such a detailed survey. For instance, it was demonstrated that the swimmer comprised of a perfect sphere and a rotating helical tail presents a more efficient solution in comparison with a swimmer comprised the same body geometry attached to a planar wave propagating tail.

Furthermore, the hydrodynamic model can be used as an auxiliary tool in observations of natural swimmers. For instance, missing information on the dimensions or wave geometry of bacteria can be predicted by solving the inverse problem with the help of proposed hydrodynamic model. Moreover, in the light of experimental results, it was also noted that the hydrodynamic model will benefit a detailed examination on lubrication and friction effects on the swimming robotic prototype, given that the ultimate goal of this study is to model an artificial micro swimmer performing in closed cavities and vessels in human body.

Major contributions of the studies carried out with resistive-force-theory (RFT) based hydrodynamic model can be listed as: validation with the help of experiments and CFD-model results carried out with parameterized wave geometries, implementation of modified resistance matrix based on the hydrodynamic interactions (HI) between body and tail in order to achieve accurate predictions of hydrodynamic forces acting on the swimmer in time-dependent fashion, i.e. akin to complex impedance of an RLC circuit, and the utilization of the proposed hydrodynamic model as a surrogate-model in order to search for efficient swimmer geometries and as a high-fidelity numerical tool for model-based position control.

APPENDIX 1: Experimental Studies on Piezoelectric Actuation

Piezoelectric actuation experiments focused on inducing plane wave propagation on a cm-scale strip. The required power is supplied through a high gain power amplifier which is supplied by an AC-AC transformer followed by a rectifier circuit as depicted in Fig. A1.1. High gain non-inverting power amplifiers are controlled by an analog signal generator board, which receives the analog signals from a digital-to-analog converter and amplify with non-inverting amplifier. Digital-to-analog converter receives sinusoidal control signal information through a USB connection. Digital signals are generated within DOS command prompt with the help of a private executable file. The overall system is capable of driving the piezo-ceramic stacks with 500 Vpp (DC) at a frequency of 33 Hz. Minimum possible phase angle between the piezo-ceramic stacks is 15 degrees.

Although experiments were successful in demonstrating the plane wave propagation in a piezo-ceramic based actuation method, further experimental study was terminated due to the lack of adequate thrust generated by small displacement of the piezo-ceramic stacks, and the presence of power leads introducing weight and extra fluid drag. This section briefly presents the experimental procedure with circuit designs, manufacturing process, experimental setup and datasheets to important components.

The desired wave deformation is simulated with COMSOL (COMSOL AB, 2010) as depicted in Fig. A1.2: piezo-ceramic bender stacks are embedded in a nylon strip and driven in phase.

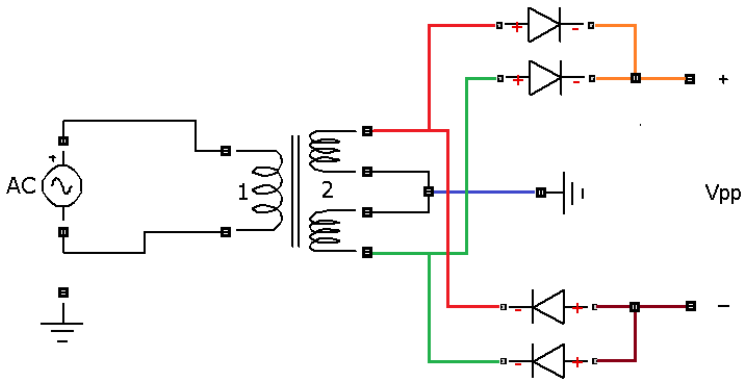

Figure A1.1: Transformer and rectifier circuit; to obtain 420 V_{pp} with 220 V_{AC}.

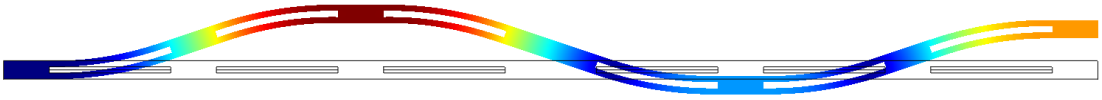

Figure A1.2: PZT-5A4E Piezo-ceramic bender stacks driven in phase invoking the planar wave propagation. Simulation carried out by COMSOL.

The signal generator board was designed to feed the drive voltages to the actuator elements of the swimmer. As individual sections of the swimmer need to be driven by signals that are appropriately phased, a multichannel generator was designed. Figure A1.3 depicts the overall electronics required to drive the tail. While the multichannel signal generator produces sinusoidal signals with necessary phases, a high-voltage amplifier section boosts signal levels to appropriate levels required by the piezoelectric actuators.

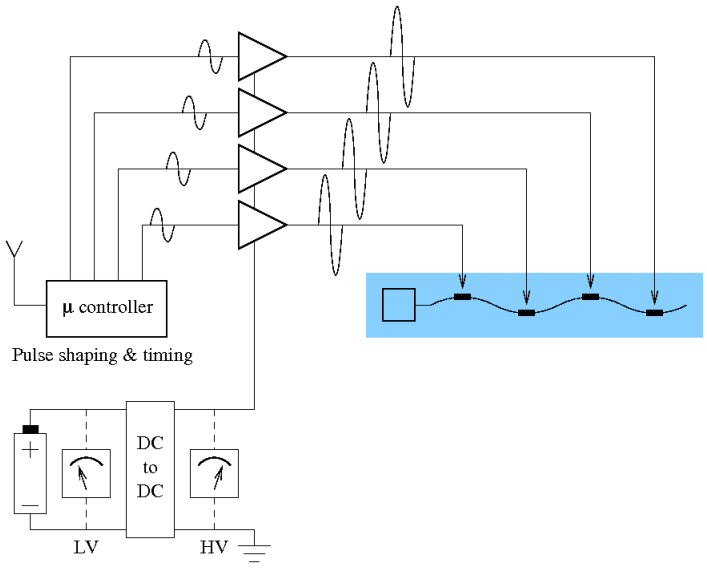

Figure A1.3: Functional block diagram of the signal generator.

The multichannel signal generator circuit is composed of a Microchip PIC4550 microcontroller, which is responsible for the timing and generation of digital samples of the sinusoidal waveform and communications with a host PC, an Analog Devices AD5346 8-bit 8-channel synchronous load digital-to-analog converter (DAC). The DAC outputs are fed into op-amp based buffer amplifiers, which are also used to manually adjust the signal amplitude for each channel. The board design and implemented analog signal generator are presented in Figs. A1.4-A1.8

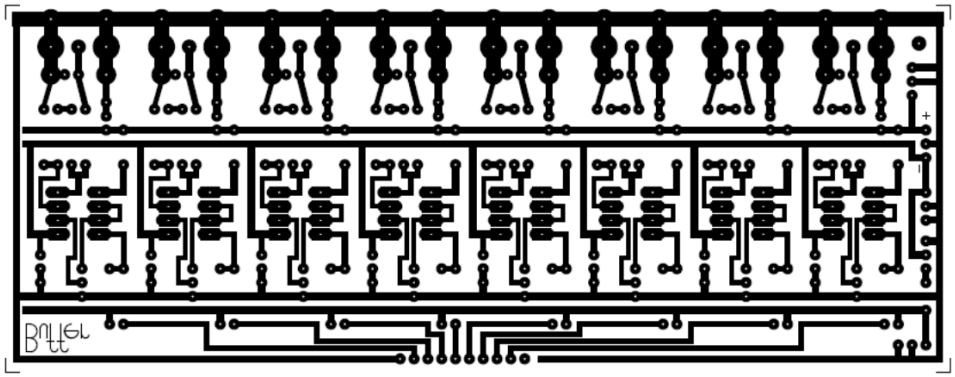

Figure A1.4: Analog signal generator board design: 8 channel operational buffer amplifier circuitry.

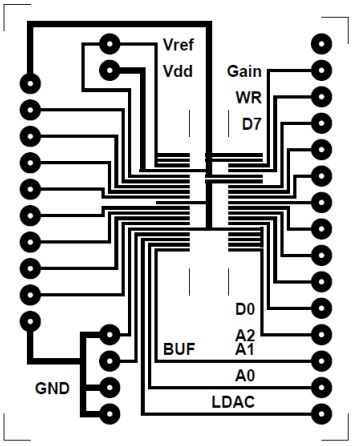

Figure A1.5: Analog signal generator board design: the Digital-to-analog converter circuitry.

Figure A1.6 shows the 8 channel signal generator together with the microcontroller board driving the 8 channel DAC. Signal outputs are tied to high-voltage op-amp boards to produce drive signals of appropriate amplitude.

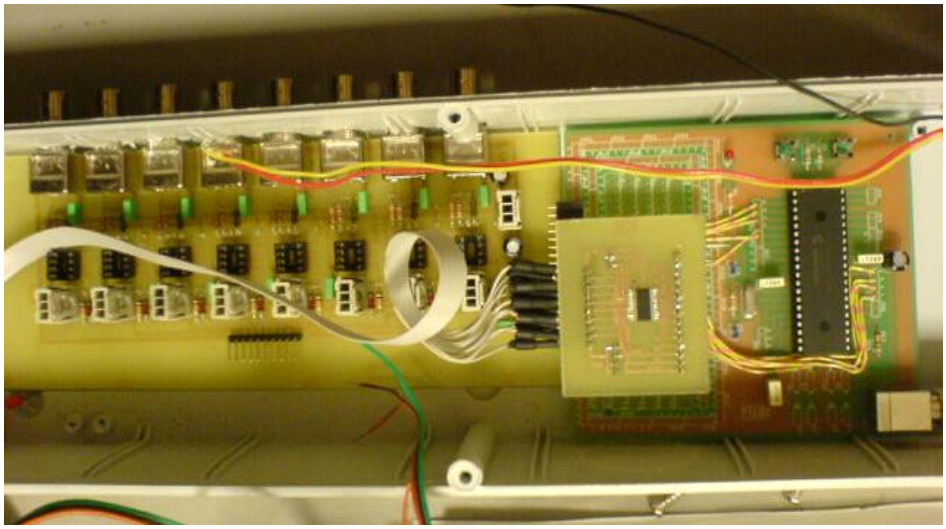

Figure A1.6: Picture of the assembled 8 channel analog signal generator: Buffer circuit, DAC and PIC4550 microcontroller.

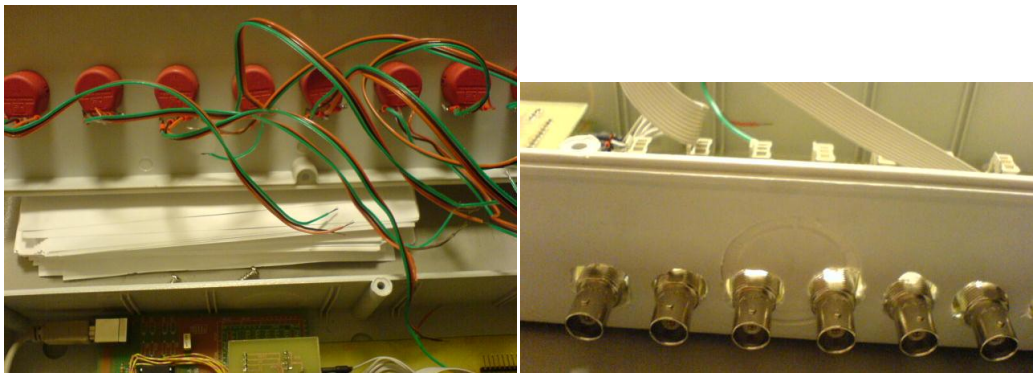

Figure A1.7: Picture of the assembled 8 channel analog signal generator: Manuel tuning elements and analog signal outputs.

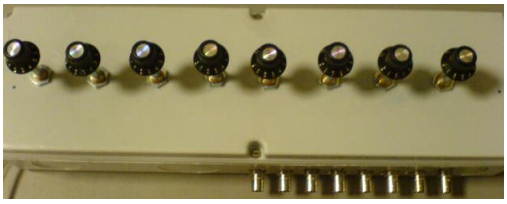

Figure A1.8: Picture of the assembled 8 channel analog signal control box and tuning knobs.

High-voltage amplifier section is designed to boost the data coming through designated control signal channels. Each amplifier board is composed of one control signal input, one power feed and one power output and a linear-power-amplifier with auxiliary elements. Control signal is filtered via a group of JFET (BF245B) as a protection. Similarly, power feed is filtered by a group of 217 V_{DC} Zener diodes to limit the high voltage feed. Circuit design was carried out in a commercial software environment Eagle, as depicted in Fig. A1.9.

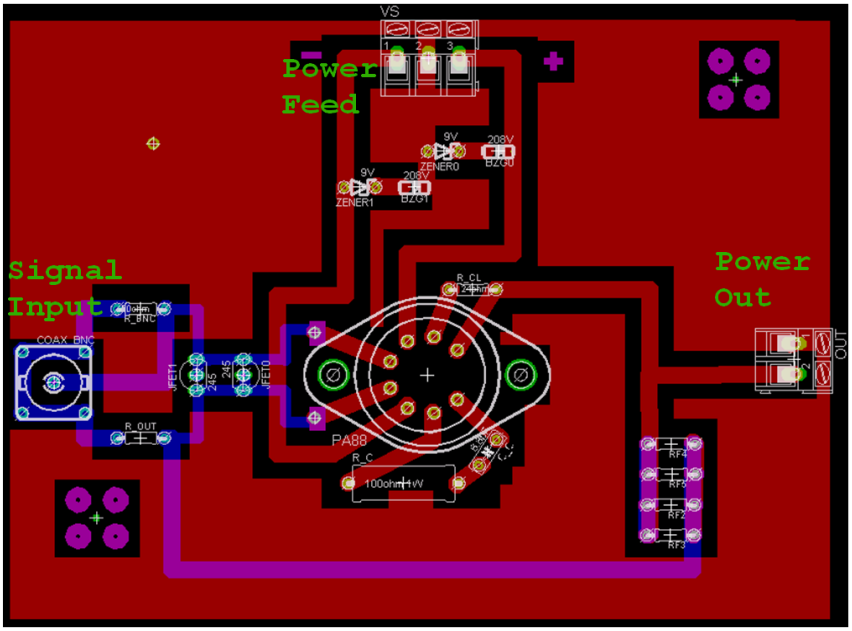

Figure A1.9: High-voltage-amplifier board design.

The linear-power-amplifier of the choice is the Cirrus Logic (Apex Microtechnology Corp., 2006) PA88 model power amplifier with 10 V_{pp} input, 420 V_{pp} output and 33 ms slew rate, i.e. shortest time interval to change the current direction. This feature allows the control signal to have a maximum frequency of 30 Hz. Power feed is connected to a $220V_{AC}$-$420V_{DC}$ transformer/converter unit. Linear-power-amplifier is equipped with an appropriate heat sink assembled on its bottom surface to prevent overheating, and silicone insulation at its leads to prevent any short circuit. The power amplifier is placed inside an actively cooled protective box. The amplifier circuit and protective box are depicted in Figs. A1.10-A1.11.

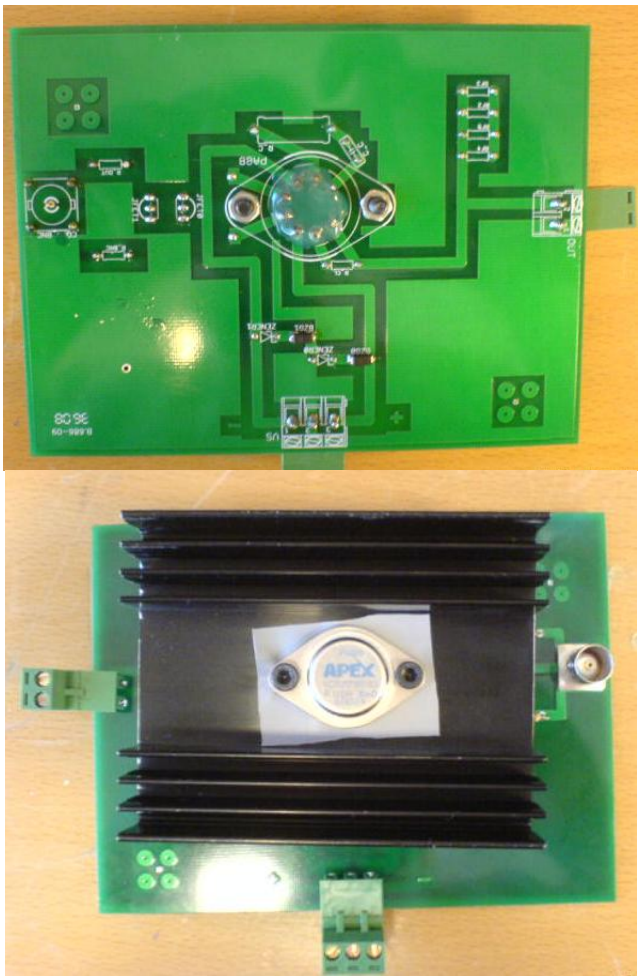

Figure A1.10: Picture of high-voltage-amplifier board (single channel).

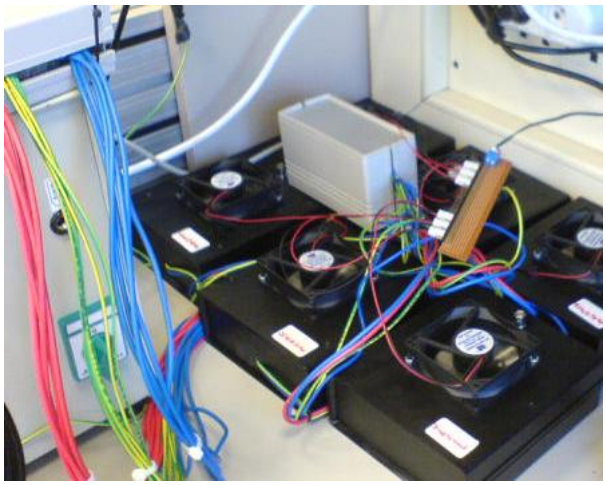

Figure A1.11: Picture of protective boxes with high-voltage-amplifier board installed (6 channels in total).

The circuitry is used to derive 6 cm PZT-5A4E piezo-bender-stacks (Piezo Systems, Inc., 2007) in order to conduct tests. Displacement at the tip of the piezo-ceramic stack is registered by a laser displacement sensor (Keyence LK 031) which was connected to Measurement Computing USB-1616FS analog to digital DAQ unit. Results of frequency and amplitude tests are presented in Figs. A1.12 and A1.13. Generated electrical signal has the form:

$$0.5V_{pp}\sin(\omega_{piezo}t+\varphi_n), \tag{A1.1}$$

where ω_{piezo} is the actuation frequency, φ_n is the phase of the n^{th} piezo-ceramic stack and V_{pp} is the peak-to-peak voltage applied on the piezo-ceramic stack.

Next, a piezo-actuator strip with three piezo-ceramic bender stacks is manufactured. The piezo-strip shown in Fig. A1.14 consists of three piezo-ceramic stacks, all 5A4E, with common ground and separate in-phase power lines. All voltage leads and common ground are cut out of conductive aluminum duct tape and isolated from each other. It is also ensured that each lead is only in contact with one piezo-ceramic stack. The manufacturing procedure of the experimental strip is depicted in Fig. A1.15.

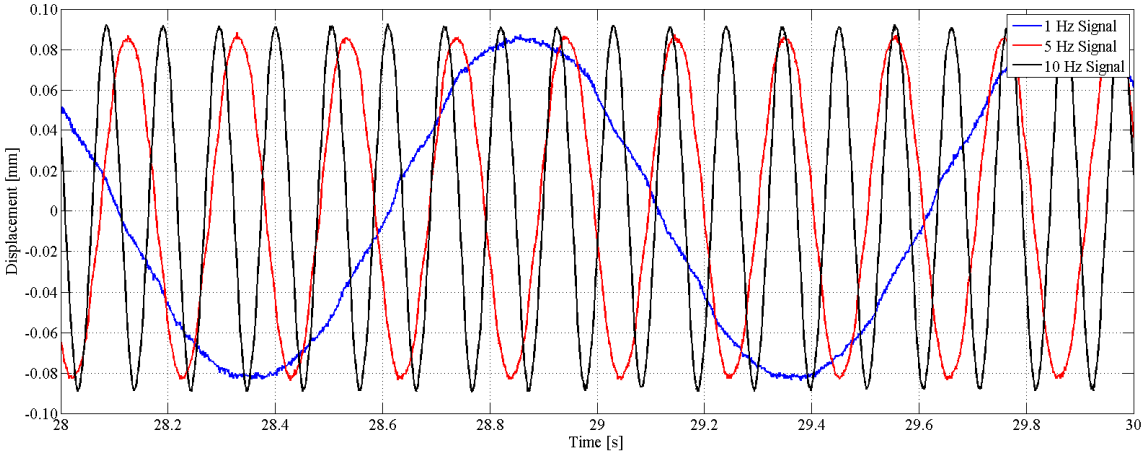

Figure A1.12: Frequency tests; i.e. 1 Hz, 5 Hz and 10 Hz, with V_{pp} = 100 V_{DC}

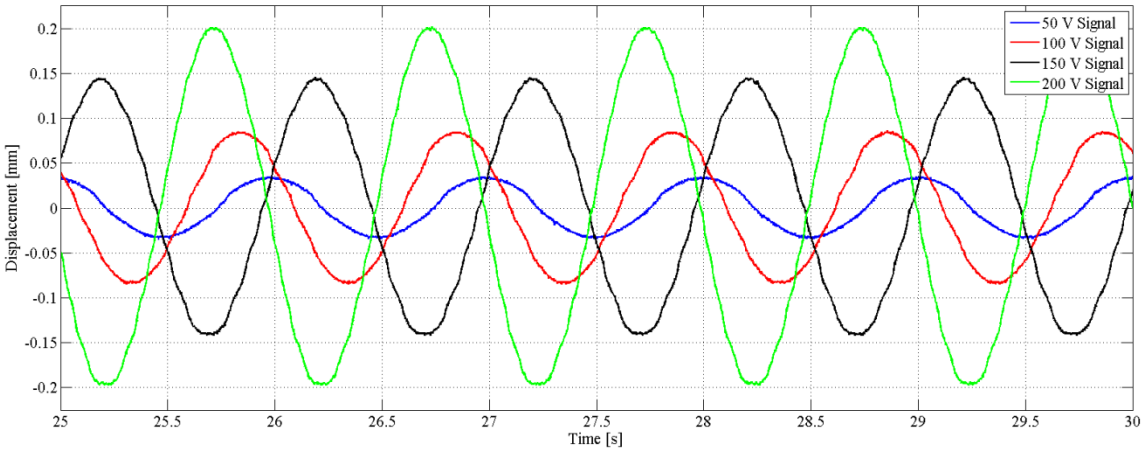

Figure A1.13: Amplitude tests; with signal frequency of 1 Hz. The phase between the signals are due to non-matching time index of the separate experiments.

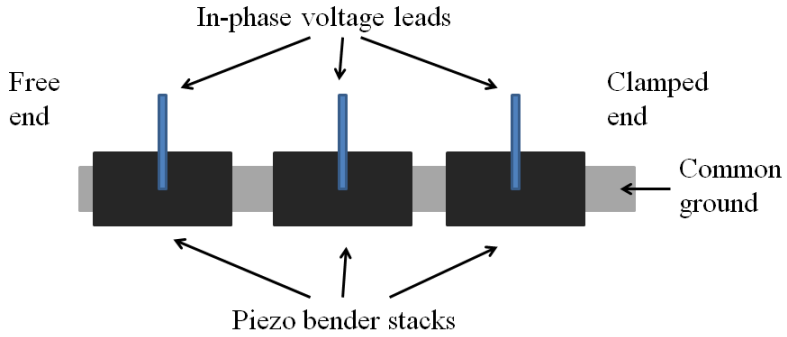

Figure A1.14: Piezo-strip model (not to scale). Dimensions of each piezo-ceramic stack are 12.7 mm x 31.8 mm, with half a centimeter gap between them.

The strip is clamped on one side and hanged in the direction of gravitational pull. The displacement of each section is registered by the laser displacement sensor. The setup is presented in Fig. A1.16. Figure A1.17 shows measurements taken during a case study with 120 degrees phase between the controlling signals of the piezo-ceramic bender-stacks. It is noted that noise, i.e. chatter in displacement curves, are distinguishable but do not corrupt the sensor output significantly.

Figure A1.15: Experimental piezo-strip: All bender piezo-ceramic stacks are placed on a common ground, separate power leads are included and secured, and piezo-ceramic stacks are rigidly linked together with hot silicon, which is an electric insulator.

Figure A1.16: Experimental (displacement sensing) setup: Orientations and positions of the piezo-strip and laser displacement sensor.

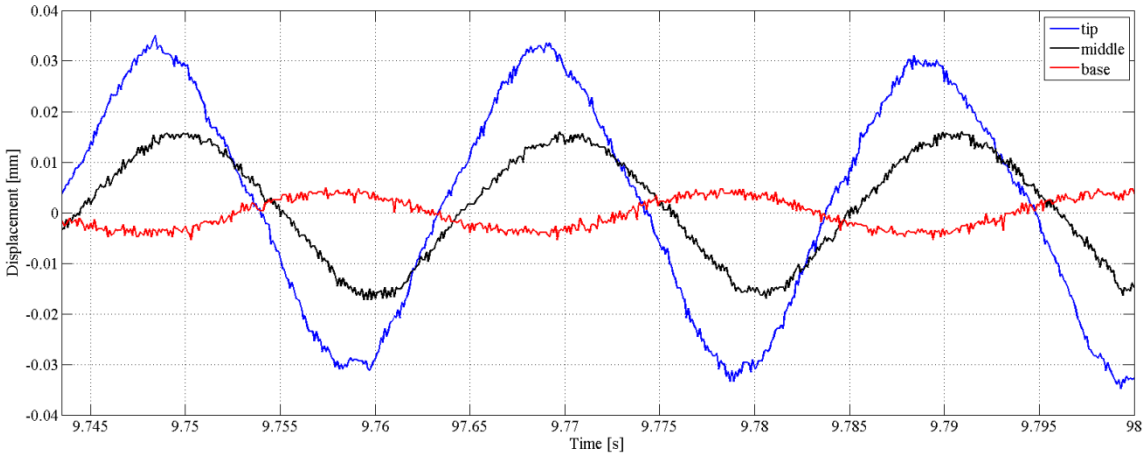

Figure A1.17: Experimentation results obtained by laser displacement sensor for the structure: showed in Figure A1.15 with driving frequency of 5 Hz, and voltage of 25 V_{pp}.

Data sheet of PA88 is supplied by Apex Mircotechnology Corporation (2006):

HIGH VOLTAGE POWER OPERATIONAL AMPLIFIERS

PA88 • PA88A

HTTP://WWW.APEXMICROTECH.COM (800) 546-APEX (800) 546-2739

FEATURES

- HIGH VOLTAGE — 450V (±225V)
- LOW QUIESCENT CURRENT — 2mA
- HIGH OUTPUT CURRENT — 100mA
- PROGRAMMABLE CURRENT LIMIT
- LOW BIAS CURRENT — FET Input

PATENTED

8-PIN TO-3
PACKAGE STYLE CE

APPLICATIONS

- PIEZOELECTRIC POSITIONING
- HIGH VOLTAGE INSTRUMENTATION
- ELECTROSTATIC TRANSDUCERS
- PROGRAMMABLE POWER SUPPLIES UP TO 440V

DESCRIPTION

The PA88 is a high voltage, low quiescent current MOSFET operational amplifier designed for output currents up to 100mA. Output voltages can swing up to ±215V with a dual supply and up to +440 volts with a single supply. The safe operating area (SOA) has no second breakdown limitations and can be observed with all types of loads by choosing an appropriate current limiting resistor. High accuracy is achieved with a cascode input circuit configuration. All internal biasing is referenced to a bootstrapped zener-MOSFET current source. As a result, the PA88 features an unprecedented supply range and excellent supply rejection. The MOSFET output stage is biased on for linear operation. External compensation provides user flexibility.

This hybrid circuit utilizes beryllia (BeO) substrates, thick film resistors, ceramic capacitors and semiconductor chips to maximize reliability, minimize size and give top performance. Ultrasonically bonded aluminum wires provide reliable interconnections at all operating temperatures. The 8-pin TO-3 package is hermetically sealed and electrically isolated. The use of compressible thermal isolation washers and/or improper mounting torque will void the product warranty. Please see "General Operating Considerations".

TYPICAL APPLICATION

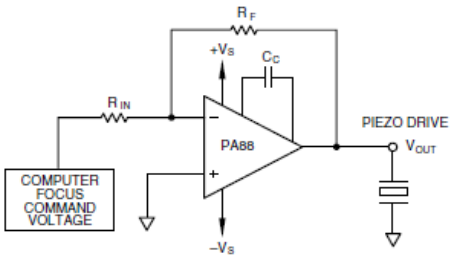

LOW POWER, PIEZOELECTRIC POSITIONING

Piezo positioning may be applied to the focusing of segmented mirror systems. The composite mirror may be composed of hundreds of elements, each requiring focusing under computer control. In such complex systems the PA88's advantage of low quiescent power consumption reduces the costs of power supplies and cooling, while providing the interface between the computer and the high voltage drive to the piezo positioners.

EQUIVALENT SCHEMATIC

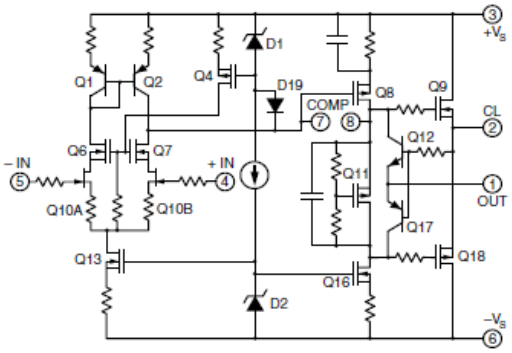

EXTERNAL CONNECTIONS

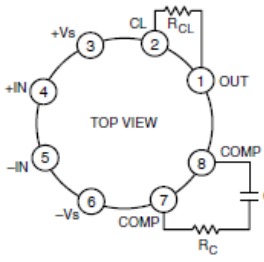

PHASE COMPENSATION

GAIN	C_C	R_C
1	68pf	100W
10	33pf	100W
20	15pf	100W
100	3.3pf	—

$R_{CL} = \frac{.7}{I_{LIM}}$

C_C RATED FOR FULL SUPPLY VOLTAGE

ABSOLUTE MAXIMUM RATINGS

SUPPLY VOLTAGE, $+V_S$ to $-V_S$	450V
OUTPUT CURRENT, source, sink	See SOA
POWER DISSIPATION, continuous @ T_C = 25°C	15W
INPUT VOLTAGE, differential	±25V
INPUT VOLTAGE, common mode	$\pm V_S$
TEMPERATURE, pin solder - 10s max	300°C
TEMPERATURE, junction[2]	150°C
TEMPERATURE, storage	–65 to +150°C
OPERATING TEMPERATURE RANGE, case	–55 to +125°C

SPECIFICATIONS

PARAMETER	TEST CONDITIONS[1]	PA88 MIN	PA88 TYP	PA88 MAX	PA88A MIN	PA88A TYP	PA88A MAX	UNITS
INPUT								
OFFSET VOLTAGE, initial			.5	2		.25	.5	mV
OFFSET VOLTAGE, vs. temperature	Full temperature range		10	30		5	10	µV/°C
OFFSET VOLTAGE, vs. supply			1	5		*	*	µV/V
OFFSET VOLTAGE, vs. time			75			*		µV/√kh
BIAS CURRENT, initial[3]			5	50		3	10	pA
BIAS CURRENT, vs. supply			.01			*		pA/V
OFFSET CURRENT, initial[3]			2.5	100		3	20	pA
INPUT IMPEDANCE, DC			10^{11}			*		Ω
INPUT CAPACITANCE			4			*		pF
COMMON MODE VOLTAGE RANGE[4]		$\pm V_S$–15			*			V
COMMON MODE REJECTION, DC	V_{CM} = ±90V	90	110		*	*		dB
NOISE	100kHz BW, R_S = 1KΩ, C_C = 15pf		2			*		µVrms
GAIN								
OPEN LOOP, @ 15Hz	R_L = 2KΩ, C_C = OPEN	96	111		*	*		dB
GAIN BANDWIDTH PRODUCT at 1MHz	R_L = 2KΩ, C_C = 15pf, R_C = 100Ω		2.1			*		MHz
POWER BANDWIDTH	R_L = 2KΩ, C_C = 15pf, R_C = 100Ω		6			*		kHz
PHASE MARGIN	Full temperature range		60			*		°
OUTPUT								
VOLTAGE SWING[4]	Full temp. range, I_O = ±75mA	$\pm V_S$–16	$\pm V_S$–14		*	*		V
VOLTAGE SWING[4]	Full temp. range, I_O = ±20mA	$\pm V_S$–10	$\pm V_S$–5.2		*	*		V
CURRENT, continuous	T_C = 85°C	±100				*		mA
SLEW RATE, A_V = 20	C_C = 15pf, R_C = 100Ω		8			*		V/µs
SLEW RATE, A_V = 100	C_C = OPEN		30			*		V/µs
CAPACITIVE LOAD, A_V = +1	Full temperature range	470			*			pf
SETTLING TIME to .1%	C_C = 15pf, R_C = 100Ω, 2V step		10			*		µs
RESISTANCE, no load	R_{CL} = 0		100			*		Ω
POWER SUPPLY								
VOLTAGE[6]	See note 6	±15	±200	±225	*	*	*	V
CURRENT, quiescent,			1.7	2		*	*	mA
THERMAL								
RESISTANCE, AC, junction to case[5]	Full temperature range, F > 60Hz			5.0			*	°C/W
RESISTANCE, DC, junction to case	Full temperature range, F < 60Hz			8.3			*	°C/W
RESISTANCE, junction to air	Full temperature range		30			*		°C/W
TEMPERATURE RANGE, case	Meets full range specifications	–25		+85	*		*	°C

NOTES: * The specification of PA88A is identical to the specification for PA88 in applicable column to the left.
1. Unless otherwise noted: T_C = 25°C, compensation = C_C = 68pF, R_C = 100Ω. DC input specifications are ± value given. Power supply voltage is typical rating.
2. Long term operation at the maximum junction temperature will result in reduced product life. Derate internal power dissipation to achieve high MTTF.
3. Doubles for every 10°C of temperature increase.
4. $+V_S$ and $-V_S$ denote the positive and negative power supply rail respectively.
5. Rating applies if the output current alternates between both output transistors at a rate faster than 60Hz.
6. Derate max supply rating .625 V/°C below 25°C case. No derating needed above 25°C case.

CAUTION The PA88 is constructed from MOSFET transistors. ESD handling procedures must be observed.
The internal substrate contains beryllia (BeO). Do not break the seal. If accidentally broken, do not crush, machine, or subject to temperatures in excess of 850°C to avoid generating toxic fumes.

POWER DERATING

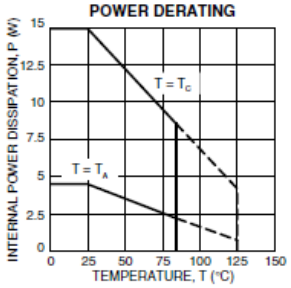

PHASE RESPONSE

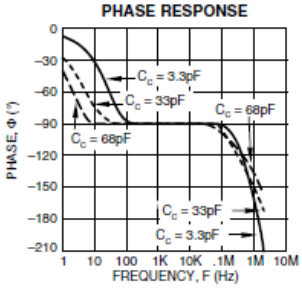

QUIESCENT CURRENT

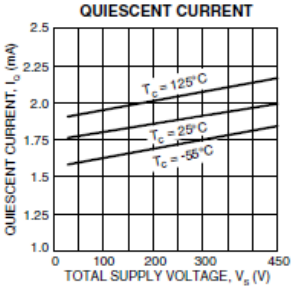

SMALL SIGNAL RESPONSE

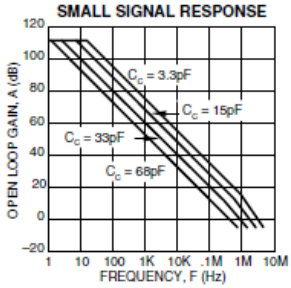

OUTPUT VOLTAGE SWING

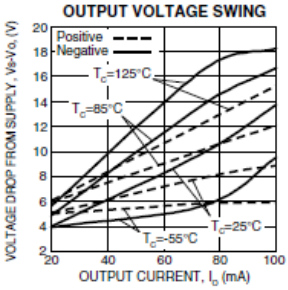

POWER RESPONSE

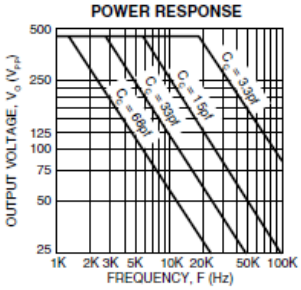

SLEW RATE

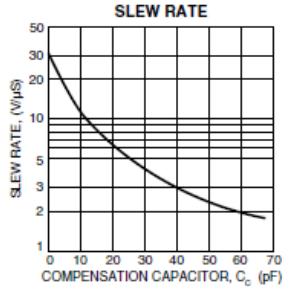

HARMONIC DISTORTION

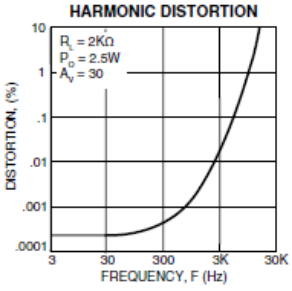

INPUT NOISE

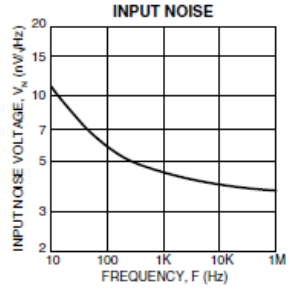

COMMON MODE REJECTION

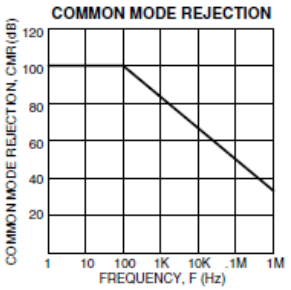

POWER SUPPLY REJECTION

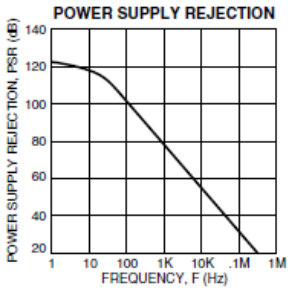

CURRENT LIMIT

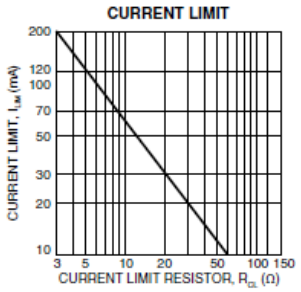

GENERAL

Please read Application Note 1 "General Operating Considerations" which covers stability, supplies, heat sinking, mounting, current limit, SOA interpretation, and specification interpretation. Visit www.apexmicrotech.com for design tools that help automate tasks such as calculations for stability, internal power dissipation, current limit; heat sink selection; Apex's complete Application Notes library; Technical Seminar Workbook; and Evaluation Kits.

CURRENT LIMIT

For proper operation, the current limit resistor (R_{CL}) must be connected as shown in the external connection diagram. The minimum value is 3.5 ohm, however for optimum reliability the resistor value should be set as high as possible. The value is calculated as follows; with the maximum practical value of 150 ohms.

$$R_{CL} = \frac{.7}{I_{LIM}}$$

SAFE OPERATING AREA (SOA)

The MOSFET output stage of this power operational amplifier has two distinct limitations:

1. The current handling capability of the MOSFET geometry and the wire bonds.
2. The junction temperature of the output MOSFETs.

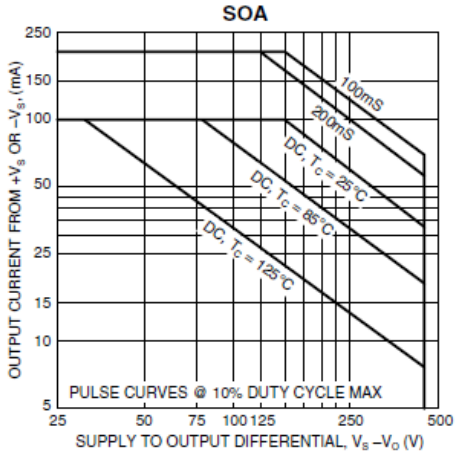

NOTE: The output stage is protected against transient flyback. However, for protection against sustained, high energy flyback, external fast-recovery diodes should be used.

INPUT PROTECTION

Although the PA88 can withstand differential input voltages up to ±25V, additional external protection is recommended, and required at total supply voltages above 300 volts. In most applications 1N4148 or 1N914 signal diodes are sufficient (D1, D2 in Figure 2a). In more demanding applications where low leakage or low capacitance are of concern 2N4416 or 2N5457-2N5459 JFETs connected as diodes will be required (Q1, Q2 in Figure 2b). In either case the input differential voltage will be clamped to ±.7V. This is sufficient overdrive to produce maximum power bandwidth.

POWER SUPPLY PROTECTION

Unidirectional zener diode transient suppressors are recommended as protection on the supply pins. The zeners clamp transients to voltages within the power supply rating and also clamp power supply reversals to ground. Whether the zeners are used or not, the system power supply should be evaluated for transient performance including power-on overshoot and power-off polarity reversal as well as line regulation.

Conditions which can cause open circuits or polarity reversals on either power supply rail should be avoided or protected against. Reversals or opens on the negative supply rail is known to induce input stage failure. Unidirectional transzorbs prevent this, and it is desirable that they be both electrically and physically as close to the amplifier as possible.

STABILITY

The PA88 has sufficient phase margin to be stable with most capacitive loads at a gain of 4 or more, using the recommended phase compensation.

The PA88 is externally compensated and performance can be tailored to the application. Use the graphs of small signal response and power response as a guide. The compensation capacitor C_C must be rated at 500V working voltage. An NPO capacitor is recommended. The compensation network C_CR_C must be mounted closely to the amplifier pins 7 and 8 to avoid spurious oscillation.

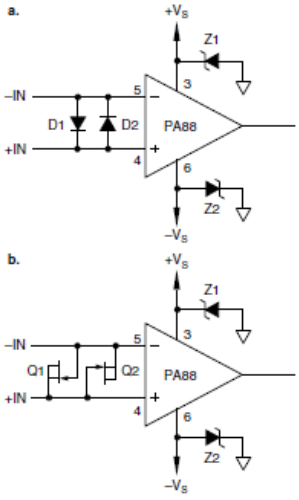

FIGURE 2. OVERVOLTAGE PROTECTION

PA88U REV M OCTOBER 2006

APPENDIX 2: Torus-Rod Studies

Geometric interpretation of a rotating and translating helix can be modified to simplify the analysis of local resistance acting on its surface. Force calculations for confined swimming action can benefit from such geometric reconstruction. For example, a rotating helix can be modeled as a combination of a torus and a rod with unit lengths depending on the attack angle of the helix itself (see Figs. A2.1-A2.3).

A CFD study based on a design space sweep for dimensions and proximity of well known geometries followed by a curve fit, in this case a surface fit, will yield a reliable alternative formulation. In this study the helix is assumed to be concentrically confined in a cylindrical channel of unit radius. Linearity of Stokes flow allows one to solve the flow field separately and superimpose the solutions (Happel and Brenner, 1965). Thus, the proposed local resistance matrix is:

$$\begin{bmatrix} c_t & & \\ & c_n & \\ & & c_b \end{bmatrix} = \begin{bmatrix} c_t^{rod}\cos(\zeta) + c_t^{torus}\sin(\zeta) & & \\ & c_n^{rod}\cos(\zeta) + c_n^{torus}\sin(\zeta) & \\ & & c_b^{rod}\cos(\zeta) + c_b^{torus}\sin(\zeta) \end{bmatrix}, \tag{A2.1}$$

where ζ is the attack angle of the helix (see Fig A2.1), and the local force coefficients are of the form

$$c_{\{t,n,b\}}^{\{rod,torus\}} = \frac{\pi\mu}{\left[a\ln\left(\frac{\mathrm{d}}{r_{tail}}\right)+b\ln\left(\frac{R_{ch}}{r_{tail}}\right)+c\left(\frac{\mathrm{d}}{R_{ch}}\right)^{d}+e\right]}, \tag{A2.2}$$

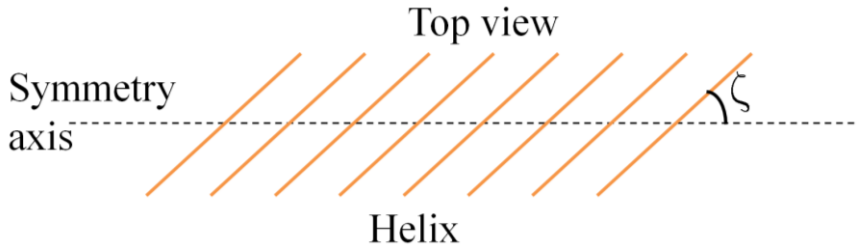

Figure A2.1: The attack angle: The helix is represented by inclined lines and the attack angle is the angle between inclined lines and the symmetry axis.

where constants $\{a,b,c,d,e\}$ are constants to be determined by surface fit analysis, μ is the dynamic viscosity, d is the local proximity to the channel walls, R_{ch} is the channel radius, and r_{tail} is the radius of the helical tail. The local proximity is not the shortest distance but the distance corresponding to the same quadrant of helix and channel as presented in Fig. A2.4. It is noted that the form presented in Eq. (A2.2) is determined by several trial-error steps on the solution of the surface fit study.

In Torus analysis simulations, open boundary conditions are set at the channel inlet and outlet boundaries. No-slip boundary condition is imposed on channel walls. Motion in tangential ,**t**, normal, **n**, and binormal, **b**, directions (see Fig. A2.2) of the torus are studied separately, with unit velocity boundary conditions imposed on its surface as $\{2\pi,1,1\}$, respectively. The fluid stress per unit length of the torus in {**t,n,b**} directions are calculated by (Landau and Lifshitz, 2005b):

$$\mathbf{F}_{\mathbf{nb}}^{torus} = \frac{1}{2\pi R_{torus}} \int_{S_{torus}} [-p\mathbf{I}+\boldsymbol{\tau}]_{\mathbf{tnb}}\, \mathrm{d}A, \tag{A2.3}$$

and

$$\mathbf{F}_{\mathbf{t}}^{torus} = \frac{1}{2\pi R_{torus}^2} \int_{S_{torus}} R_{torus} \times [-p\mathbf{I} + \boldsymbol{\tau}]_{\mathbf{t}} \, \mathrm{d}A, \tag{A2.4}$$

where R_{torus} is the major radius of the torus, p is the static pressure, $\boldsymbol{\tau}$ is the viscous stress tensor, A is the area and S_{torus} denotes the total surface area of the torus.

In Rod analysis simulations, periodic boundary conditions (COMSOL AB, 2010) are set at the channel inlet and outlet boundaries, where rod intersects perpendicularly to eliminate end effects. Periodic boundary conditions imply that the analyzed rod is only a short section of a much longer geometry. No-slip boundary condition is imposed on channel walls. Motion in tangential, **t**, normal, **n**, and binormal, **b**, directions (see Fig. A2.3) of the rod are studied separately, with unit velocity boundary conditions imposed on its surface as {1,1,1}, respectively. The fluid stress per unit length on acting on the surface of the rod are calculated by

$$\mathbf{F}_{\mathbf{tnb}}^{rod} = \frac{1}{\mathrm{L}_{rod}} \int_{S_{rod}} [-p\mathbf{I} + \boldsymbol{\tau}]_{\mathbf{tnb}} \, \mathrm{d}A, \tag{A2.5}$$

where L_{rod} is the length of the rod and channel, and S_{rod} is the total surface area of the rod.

The fluid domain is governed by steady incompressible Stokes equations subject to conservation of mass (See Eqs. (A2.6-A2.7)). Dynamic viscosity, μ, and density, ρ, of the fluid is set to 1 in order to scale the effect of viscosity. Second order Lagrangian tetrahedral elements are used with 150K and 60K degree-of-freedom for torus and rod studies, respectively. Solutions are obtained by PARDISO direct solver (Schenk and Gärtner, 2004) and each simulation requires approximately 10 minutes on an Intel Core i7 system with 4 GB of RAM. Corresponding fit surfaces and fit qualities, which are obtained by least square method with 95% confidence interval, are presented in Figs. A2.5-A2.10.

$$0 = -\nabla p + \mu \nabla^2 \mathbf{U}. \tag{A2.6}$$

$$\nabla \cdot \mathbf{U} = 0. \tag{A2.7}$$

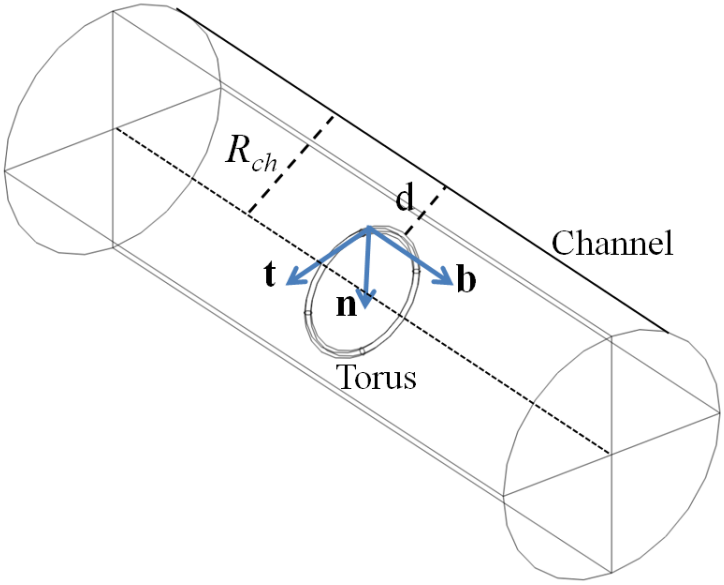

Figure A2.2: Concentric torus in the cylindrical channel. Tangential direction points the rigid-body rotation; binormal direction points the rigid-body translation along the symmetry axis; normal direction points rigid-body translation in radial direction.

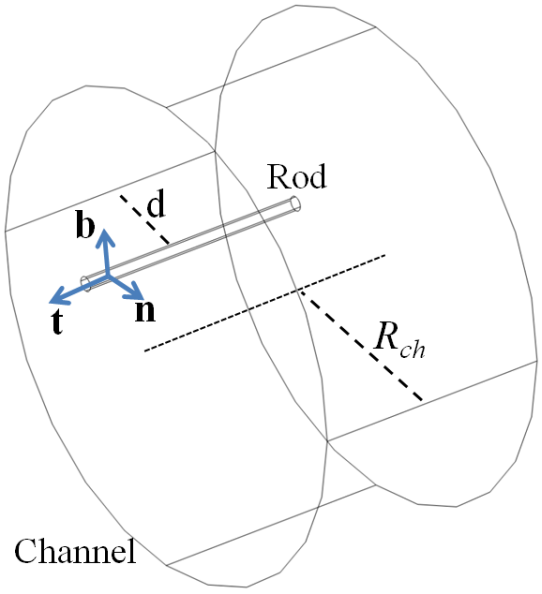

Figure A2.3: Rod in a channel with periodic boundary conditions. Tangential direction points the rigid-body translation along the symmetry axis; binormal direction points the azimuthal rigid-body translation; normal direction points rigid-body translation in radial direction.

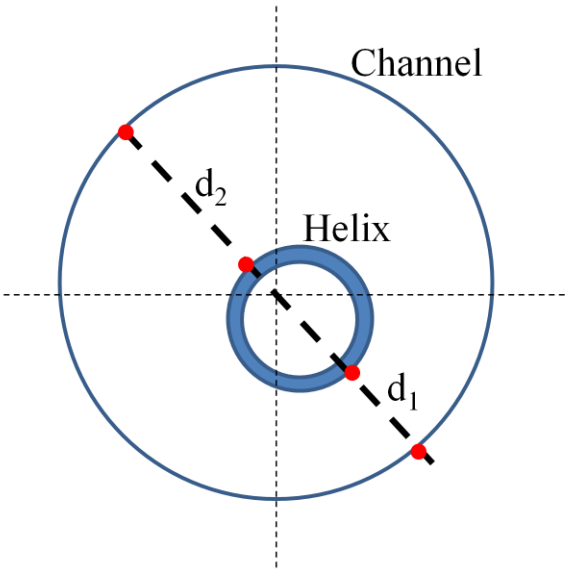

Figure A2.4: The local proximity of a helix parallel to the symmetry axis of the cylindrical channel, e.g. d_1 and d_2 as depicted in the figure above.

Design space is for this study is r_{tail} = {0.05 0.045 0.04 0.035 0.03 0.025 0.0125 0.01 0.0075 0.00625 0.005 0.003 0.0025} with d_1= {0.0670 0.0750 0.1000 0.1250 0.1500 0.1750 0.3000 0.4000 0.5000 0.6000 0.7000 0.8000}, and the coefficients determined by the fit study are:

$$\{a \quad b \quad c \quad d \quad e\}_{\mathbf{t}}^{rod} = \{1 \quad -0.5135 \quad -3 \quad 0.3 \quad 3\}, \tag{A2.8}$$

$$\{a \quad b \quad c \quad d \quad e\}_{\mathbf{n}}^{rod} = \{0.15 \quad 0.062 \quad 0.75 \quad 0.08333 \quad -0.8\}, \tag{A2.9}$$

$$\{a \quad b \quad c \quad d \quad e\}_{\mathbf{b}}^{rod} = \{0.6 \quad -0.335 \quad -3 \quad 0.2 \quad 2.75\}, \tag{A2.10}$$

$$\{a \quad b \quad c \quad d \quad e\}_{\mathbf{t}}^{torus} = \{0.15 \quad 0.05 \quad 0.237 \quad 6 \quad 0.05\}, \tag{A2.11}$$

$$\{a \quad b \quad c \quad d \quad e\}_{\mathbf{n}}^{torus} = \{0.0705 \quad 0.2 \quad 1.5 \quad 0.25 \quad -1.3\}, \tag{A2.12}$$

$$\{a \quad b \quad c \quad d \quad e\}_{\mathbf{b}}^{torus} = \{0.2 \quad -0.027 \quad 0.5 \quad 0.2 \quad -0.2\}, \tag{A2.13}$$

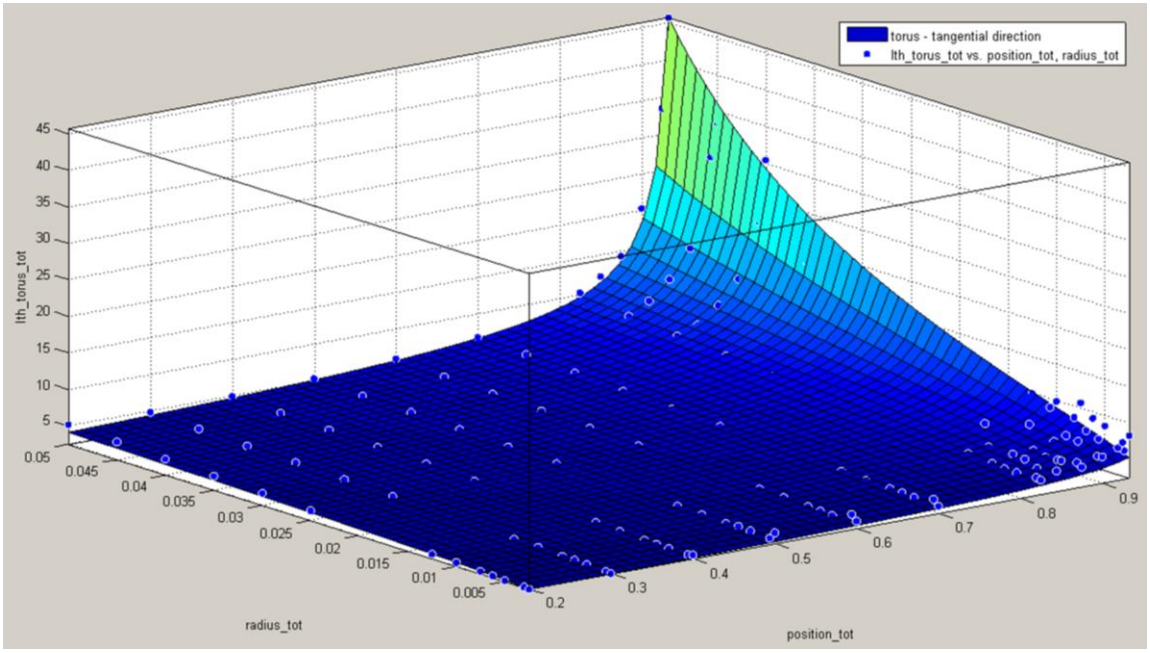

Figure A2.5: Torus rotation along the symmetry axis (tangential direction). Adjusted R-square = 0.9999, Root mean square (RMS) error = 0.07731.

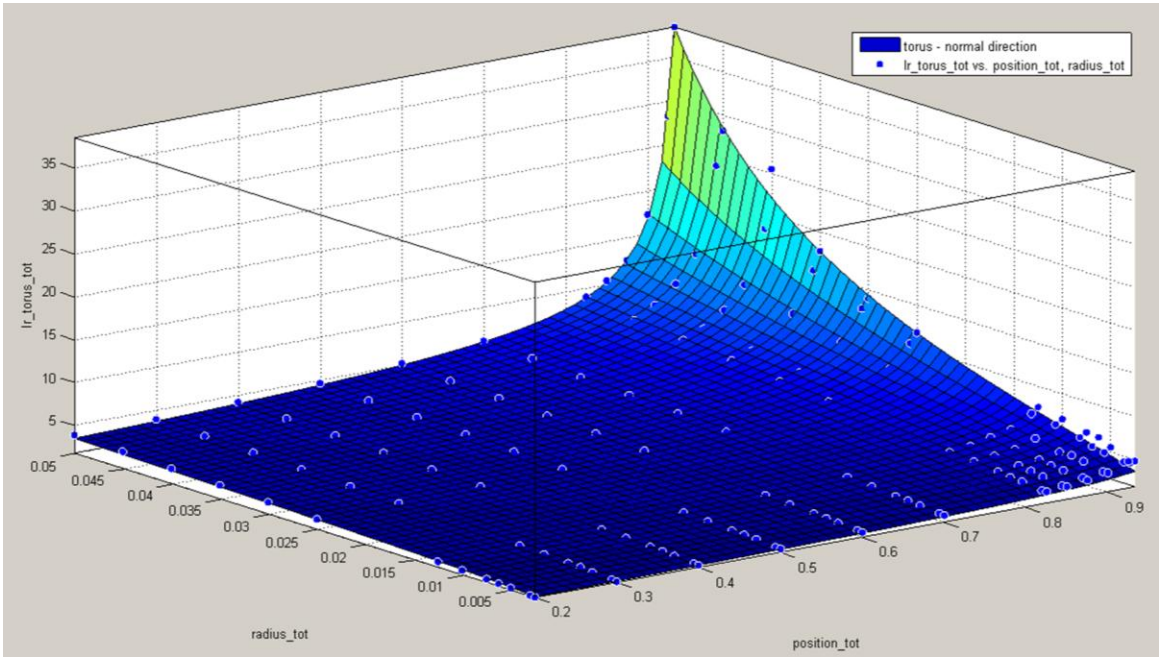

Figure A2.6: Torus translation in normal (radial) direction. Adjusted R-square = 0.9998, Root mean square (RMS) error = 0.06694.

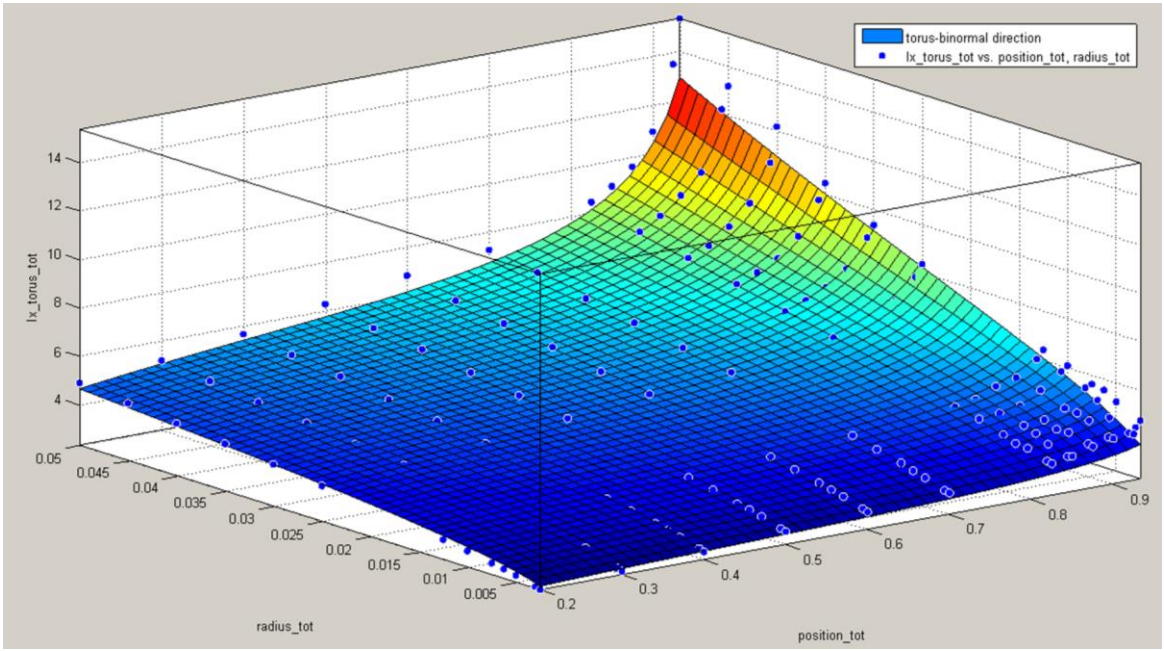

Figure A2.7: Torus translation in binormal (along the symmetry axis) direction. Adjusted R-square = 0.9998, Root mean square (RMS) error = 0.03626.

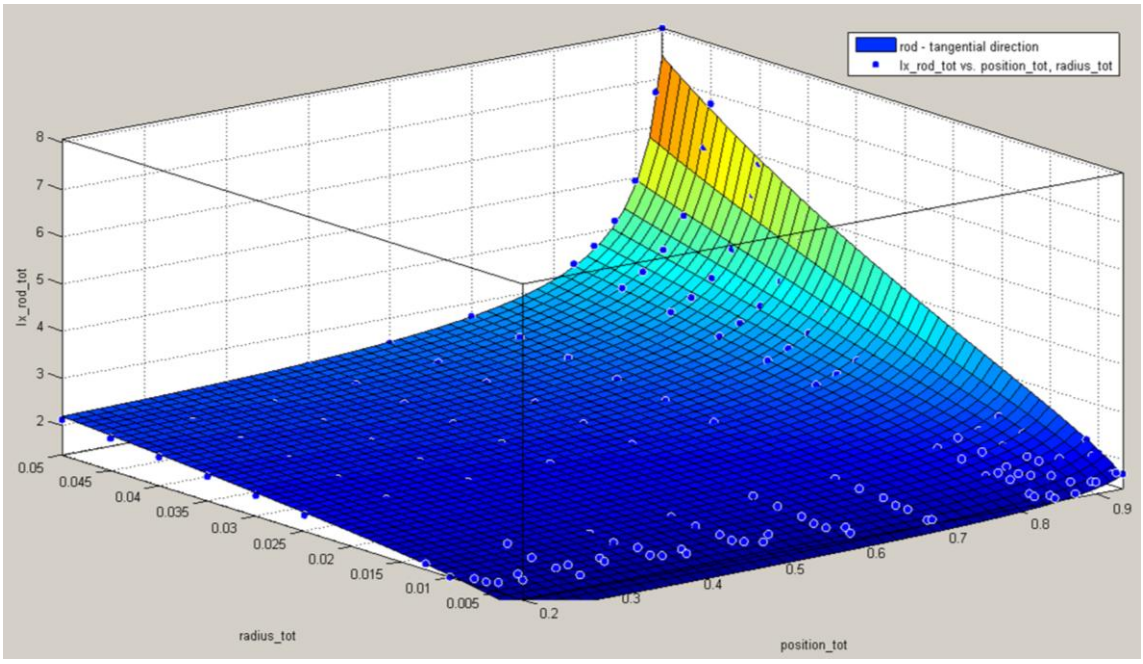

Figure A2.8: Rod translation in tangential (along the symmetry axis) direction. Adjusted R-square = 0.9998, Root mean square (RMS) error = 0.01689.

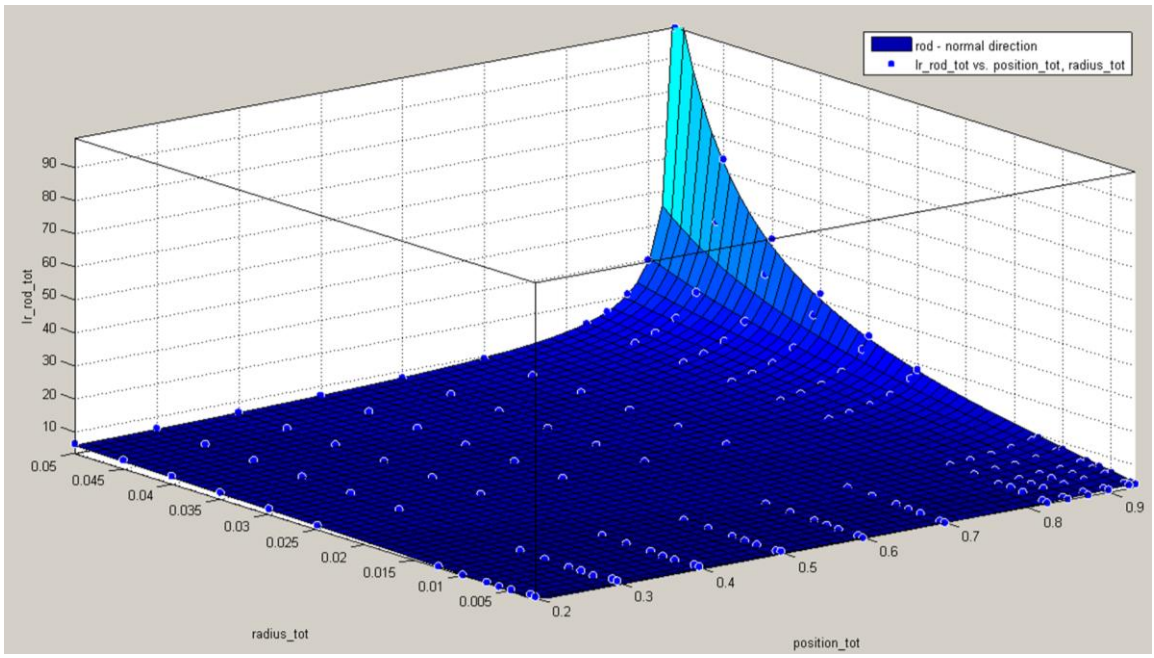

Figure A2.9: Rod translation in normal (azimuthal) direction. Adjusted R-square = 0.9999, Root mean square (RMS) error = 0.119.

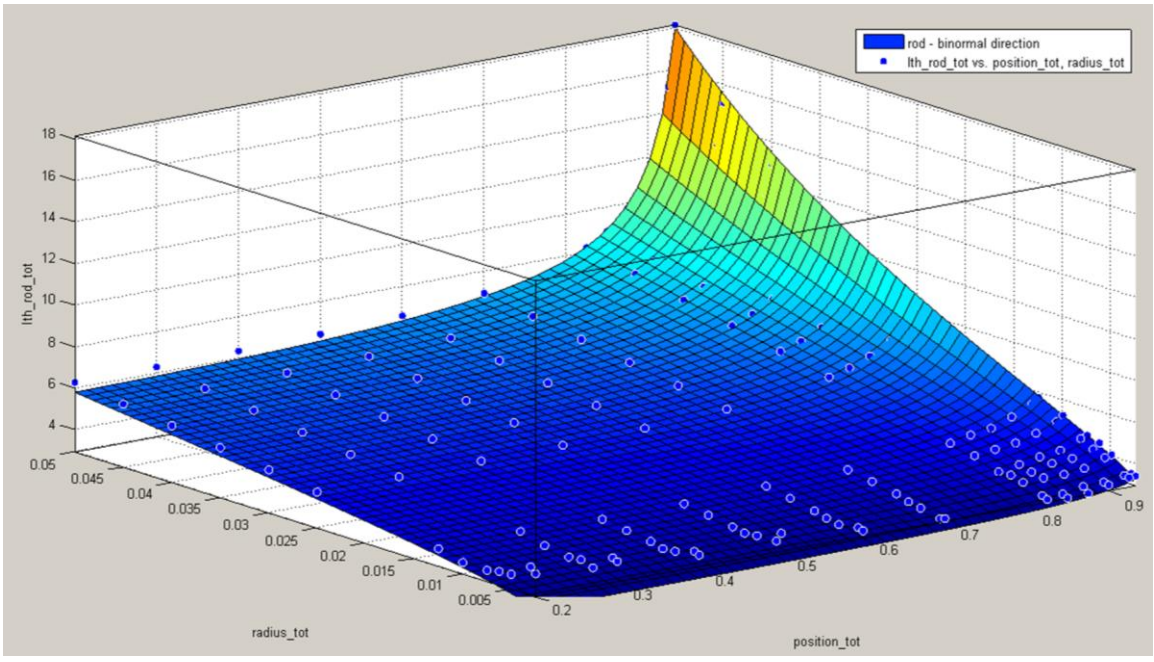

Figure A2.10: Rod translation in binormal (radial) direction. Adjusted R-square = 0.9997, Root mean square (RMS) error = 0.04382.

APPENDIX 3: Helical Tail Driving System Characteristics

The voltage drop and internal resistance of the battery used in helical robot is measured in order to formulate the voltage and total resistance as a function of motor current.

Measured battery current, battery resistance and battery voltage values are presented in Table A3.1. Figures A3.1 and A3.2 depict the fit curves for battery voltage and current. Figure A3.3 compares the fitted curve with a control set and open circuit voltage of the battery, which is 3.7 V. The control set is presented in Table A3.2. The fit equations are:

$$\mathrm{R}_{battery}(t) = 30e^{-54.6\mathrm{I}(t)} + e^{\mathrm{I}(t)} - 1.555\mathrm{I}(t), \tag{A3.1}$$

$$\mathrm{V}_{battery}(t) = 3.7 - 0.8\mathrm{I}(t), \tag{A3.2}$$

Table A3.1: Battery current and internal resistance values under applied dissipative loads.

Current (mA)	Battery Resistance (ohm)	Load (ohm)	Battery Voltage (V)
47	3.723	75	3.676
71	2.122	50	3.657
165	2.424	20	3.582
222	1.666	15	3.536
416	1.394	7.5	3.38
741	1.693	3.3	3.12
1180	2.135	1	2.77

Table A3.2: Control set.

Current (mA)	Battery Voltage (V)
640	3.2
420	3.38
240	3.52
130	3.61
45	3.68
30	3.69

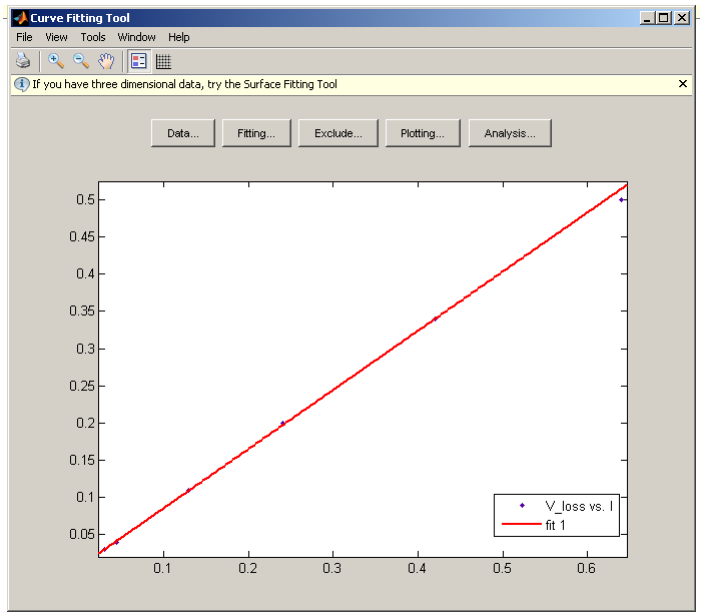

Figure A3.1: Fitted battery voltage curve.

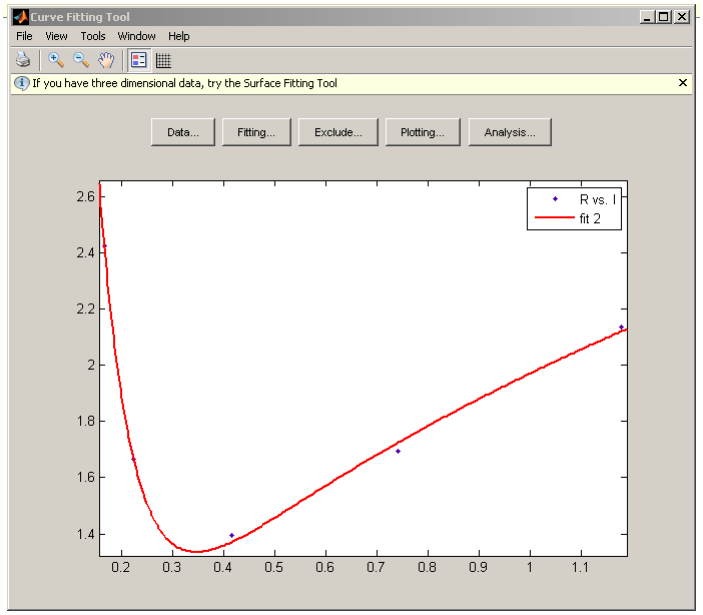

Figure A3.2: Fitted battery resistance curve.

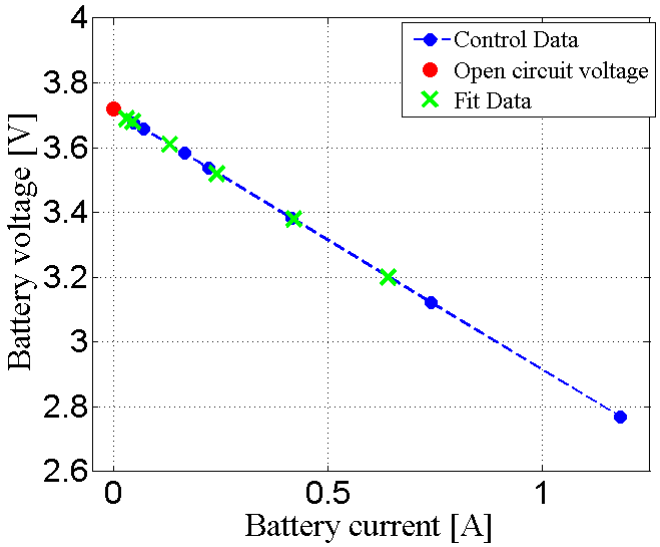

Figure A3.3: Battery voltage drop with motor current compared with open circuit voltage and control set.

Electromechanical properties of the coreless brushed DC-motor are calculated and measured as follows (see Table A3.3):

- The back-emf constant, K_b, is measured with a driver-driven motor arrangement. 0.02 A 0.3 V_{DC} is applied to the driver motor and driven motor is measured to generate 0.014 V at 1.1 Hz, which is measured with a laser tachometer. (See Fig. A3.4)
- The torque constant, K_m, is measured by a disk 2 cm in diameter and a 0.75 g mass is attached with a fishing line wrapped around it (See Fig. A3.5). The measured stall voltage and current values where the rotor cannot rotate the disk are 1.7 V and 0.1635 A. Km value is measured with assuming 9.81 m/s^2 for gravitational pull and using $K_m \cdot I$ = Stall Torque.
- The rotational friction constant of the motor, B_m, is determined with the help of K_m and measured "no load current" at a very slow rotation rate, which is registered by a laser tachometer. The no load current is found to be 0.03 A, and the corresponding rotation rate is 750 rpm. The friction torque on the motor is solely balanced by the magnetic torque induced by the windings and permanent magnet within the DC-motor, i.e. $K_m \cdot I_{no\text{-}load} = B_m \cdot \omega_m$.
- Other properties are determined by direct measurement with a digital multimeter.

Table A3.3: Electromechanical properties of coreless brushed DC-motor.

L_{motor} = 0.082 H
C_{motor} = 0.002 F
R_{motor} = 10.4 Ohm
K_b = 0.004 V·s/rad
K_m = 0.00045 N·m/A
B_m =7x10-7 N·m·s/rad @ 1 Hz
$I_{no\text{-}load}$ = 130 mA

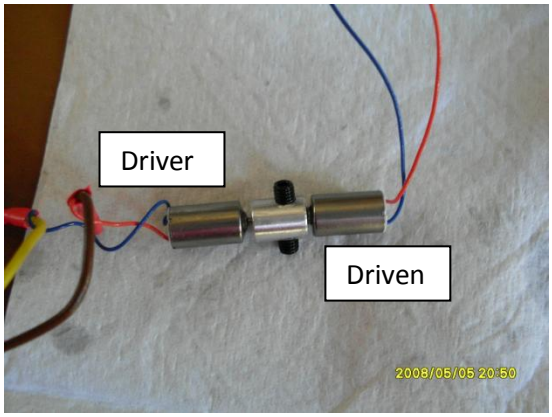

Figure A3.4: Back-EMF experiment: Driver and driven motors are mechanically coupled.

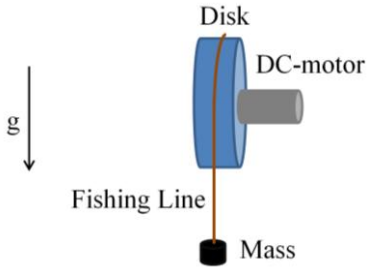

Figure A3.5: Torque constant experiment: Illustration of the experimental setup.

APPENDIX 4: Tail Resistance-Matrix in Open Form

The following MATLAB code is implemented to obtain the resistance matrix of a tail, which carries out helical wave propagations, in symbolic fashion. The deformation on the tail is written along the centerline of an inextensible cylindrical filament or wire.

```
syms x B w t b U Ct Cn Cb a W lam k L

% k: wave number (= 2*pi/lambda)
% x: position along the centerline of the filament or wire
% L: apparent tail length
% B wave amplitude
% w: angular rotation of the tail
% t: time
% a: ratio of apparent tail length to actual tail length
% Ct: local tangential resistive force coefficient
% Cn: local normal resistive force coefficient
% Cb: local bi-normal resistive force coefficient

% local position on tail:
p = [a*x; B*cos(w*t -k*a*x); B*sin(w*t -k*a*x)];

dpdx = simplify(diff(p,x)); %
d2pdx2 = simplify(diff(diff(p,x),x));
dpdx_len = simplify(sqrt(sum(dpdx.*dpdx)));

Tn = dpdx/dpdx_len; % local tangent

dpdx_c_d2pdx2 = simplify(cross(dpdx,d2pdx2));
dpdx_c_d2pdx2_len = ...
    simplify(sqrt(sum(dpdx_c_d2pdx2.*dpdx_c_d2pdx2)));

Bn = dpdx_c_d2pdx2/dpdx_c_d2pdx2_len; % local binormal

Nn = simplify(cross(Bn,Tn)); % local normal
```

```
R = [Tn Nn Bn];
C = diag([Ct Cn Cb]);
S = [0 -p(3,1) p(2,1); p(3,1) 0 -p(1,1); -p(2,1) p(1,1) 0];

RCR = simplify(R*C*R.');
RCRS = simplify( -RCR*S);
SRCR = simplify(S*RCR);
SRCRS = simplify( -S*RCR*S);

% position and time dependent resistance matrix:
dResistance = [RCR RCRS; SRCR SRCRS];

% Time dependent (6x6) resistance matrix
Resistance = int(dResistance,x,0,L);
```

Resultant symmetric full 6-by-6 resistance matrix elements, i.e. diagonals and the elements of the first row, are:

R_{11} = (L*(Cb*B^2*k^2 + Ct))/(B^2*k^2 + 1)

R_{12} = -(B*(Cb - Ct)*(cos(t*w - L*a*k) - cos(t*w)))/(a*(B^2*k^2 + 1))

R_{13} = -(B*(sin(t*w - L*a*k) - sin(t*w))*(Cb - Ct))/(a*(B^2*k^2 + 1))

R_{14} = (B^2*L*k*(Cb - Ct))/(B^2*k^2 + 1)

R_{15} = (B*Cb*L*k*sin(t*w - L*a*k) - B*Ct*L*k*sin(t*w - L*a*k))/(B^2*k^3 + k) - (B*Cb*cos(t*w - L*a*k) - 2*B*Ct*cos(t*w - L*a*k) - B*Cb*cos(t*w) + 2*B*Ct*cos(t*w) - B^3*Cb*k^2*cos(t*w - L*a*k) + B^3*Cb*k^2*cos(t*w))/(a*B^2*k^3 + a*k)

R_{16} = - (B*Cb*sin(t*w - L*a*k) - 2*B*Ct*sin(t*w - L*a*k) - B*Cb*sin(t*w) + 2*B*Ct*sin(t*w) - B^3*Cb*k^2*sin(t*w - L*a*k) + B^3*Cb*k^2*sin(t*w))/(a*B^2*k^3 + a*k) - (B*Cb*L*k*cos(t*w - L*a*k) - B*Ct*L*k*cos(t*w - L*a*k))/(B^2*k^3 + k)

R_{22} = ((Cb*L*k)/2 + (Cn*L*k)/2 + (B^2*Cn*L*k^3)/2 + (B^2*Ct*L*k^3)/2)/(k*(B^2*k^2 + 1)) + ((Cb*sin(2*t*w - 2*L*a*k))/4 - (Cn*sin(2*t*w - 2*L*a*k))/4 - (Cb*sin(2*t*w))/4 + (Cn*sin(2*t*w))/4 - (B^2*Cn*k^2*sin(2*t*w - 2*L*a*k))/4 + (B^2*Ct*k^2*sin(2*t*w - 2*L*a*k))/4 + (B^2*Cn*k^2*sin(2*t*w))/4 - (B^2*Ct*k^2*sin(2*t*w))/4)/(a*k*(B^2*k^2 + 1))

R_{33} = Cn*L - Cn*(L/2 - (sin(2*t*w - 2*L*a*k)/4 - sin(2*t*w)/4)/(a*k)) + (Cb*(L/2 - (sin(2*t*w - 2*L*a*k)/4 - sin(2*t*w)/4)/(a*k)))/(B^2*k^2 + 1) + (B^2*Ct*k^2*(L/2 - (sin(2*t*w - 2*L*a*k)/4 - sin(2*t*w)/4)/(a*k)))/(B^2*k^2 + 1)

R_{44} = (B^2*L*(Ct*B^2*k^2 + Cb))/(B^2*k^2 + 1)

R_{55} = (3*Cb*sin(2*t*w - 2*L*a*k) - 3*Cn*sin(2*t*w - 2*L*a*k) - 3*Cb*sin(2*t*w) + 3*Cn*sin(2*t*w) - 6*B^2*Cb*k^2*sin(2*t*w - 2*L*a*k) + 6*B^4*Cb*k^4*sin(2*t*w - 2*L*a*k) - 3*B^2*Cn*k^2*sin(2*t*w - 2*L*a*k) + 15*B^2*Ct*k^2*sin(2*t*w - 2*L*a*k) + 6*B^2*Cb*k^2*sin(2*t*w) - 6*B^4*Cb*k^4*sin(2*t*w) + 3*B^2*Cn*k^2*sin(2*t*w) - 15*B^2*Ct*k^2*sin(2*t*w) + 4*Cb*L^3*a^3*k^3 + 4*Cn*L^3*a^3*k^3 + 6*Cb*L*a*k*cos(2*t*w - 2*L*a*k) - 6*Cn*L*a*k*cos(2*t*w - 2*L*a*k) - 6*Cb*L^2*a^2*k^2*sin(2*t*w - 2*L*a*k) + 6*Cn*L^2*a^2*k^2*sin(2*t*w - 2*L*a*k) + 4*B^2*Cn*L^3*a^3*k^5 + 4*B^2*Ct*L^3*a^3*k^5 + 12*B^4*Cb*L*a*k^5 + 12*B^2*Ct*L*a*k^3 + 6*B^2*Cn*L^2*a^2*k^4*sin(2*t*w - 2*L*a*k) - 6*B^2*Ct*L^2*a^2*k^4*sin(2*t*w - 2*L*a*k) - 12*B^2*Cb*L*a*k^3*cos(2*t*w - 2*L*a*k) - 6*B^2*Cn*L*a*k^3*cos(2*t*w - 2*L*a*k) + 18*B^2*Ct*L*a*k^3*cos(2*t*w - 2*L*a*k))/(24*a*B^2*k^5 + 24*a*k^3)

R_{66} = (3*Cn*sin(2*t*w - 2*L*a*k) - 3*Cb*sin(2*t*w - 2*L*a*k) + 3*Cb*sin(2*t*w) - 3*Cn*sin(2*t*w) + 6*B^2*Cb*k^2*sin(2*t*w - 2*L*a*k) - 6*B^4*Cb*k^4*sin(2*t*w - 2*L*a*k) + 3*B^2*Cn*k^2*sin(2*t*w - 2*L*a*k) - 15*B^2*Ct*k^2*sin(2*t*w - 2*L*a*k) - 6*B^2*Cb*k^2*sin(2*t*w) + 6*B^4*Cb*k^4*sin(2*t*w) - 3*B^2*Cn*k^2*sin(2*t*w) + 15*B^2*Ct*k^2*sin(2*t*w) + 4*Cb*L^3*a^3*k^3 + 4*Cn*L^3*a^3*k^3 - 6*Cb*L*a*k*cos(2*t*w - 2*L*a*k) + 6*Cn*L*a*k*cos(2*t*w - 2*L*a*k) + 6*Cb*L^2*a^2*k^2*sin(2*t*w - 2*L*a*k) - 6*Cn*L^2*a^2*k^2*sin(2*t*w - 2*L*a*k) + 4*B^2*Cn*L^3*a^3*k^5 + 4*B^2*Ct*L^3*a^3*k^5 + 12*B^4*Cb*L*a*k^5 + 12*B^2*Ct*L*a*k^3 - 6*B^2*Cn*L^2*a^2*k^4*sin(2*t*w - 2*L*a*k) + 6*B^2*Ct*L^2*a^2*k^4*sin(2*t*w - 2*L*a*k) + 12*B^2*Cb*L*a*k^3*cos(2*t*w - 2*L*a*k) + 6*B^2*Cn*L*a*k^3*cos(2*t*w - 2*L*a*k) - 18*B^2*Ct*L*a*k^3*cos(2*t*w - 2*L*a*k))/(24*a*B^2*k^5 + 24*a*k^3)

APPENDIX 5: Numerical Methods and Formulae Used in Reduced-Order Hydrodynamic Model

Matrix inversions on square matrices are carried out by "Banachiewicz Identity Method" (Fujimoto, 2007). The method is based on partitioning a square matrix satisfying $\det(A) \neq 0$ into four sub-matrices as:

$$\mathbf{A} = \begin{bmatrix} \mathbf{E}_{n\times n} & \mathbf{F}_{n\times n} \\ \mathbf{G}_{n\times n} & \mathbf{H}_{n\times n} \end{bmatrix}_{2n\times 2n}, \tag{A5.1}$$

$$\mathbf{S} = \mathbf{H} - \mathbf{G}\mathbf{E}^{-1}\mathbf{F}, \tag{A5.2}$$

$$\mathbf{A}^{-1} = \begin{bmatrix} (\mathbf{E}^{-1} + \mathbf{E}^{-1}\mathbf{F}\mathbf{S}^{-1}\mathbf{G}\mathbf{E}^{-1}) & \mathbf{E}^{-1}\mathbf{F}\mathbf{S}^{-1} \\ -\mathbf{S}^{-1}\mathbf{G}\mathbf{E}^{-1} & \mathbf{S}^{-1} \end{bmatrix}_{2n\times 2n}. \tag{A5.3}$$

Local Frenet-Serret frame calculations are carried out by the following formulae (Hanson and Ma, 1994; Hanson and Ma, 1995):

$$\mathbf{T} = \frac{\mathrm{d}\mathbf{P}/\mathrm{d}x}{\left\|\mathrm{d}\mathbf{P}/\mathrm{d}x\right\|}, \tag{A5.4}$$

$$\mathbf{B} = \frac{\mathrm{d}\mathbf{P}/\mathrm{d}x \times \mathrm{d}^2\mathbf{P}/\mathrm{d}x^2}{\left\|\mathrm{d}\mathbf{P}/\mathrm{d}x \times \mathrm{d}^2\mathbf{P}/\mathrm{d}x^2\right\|}, \tag{A5.5}$$

$$\mathbf{N} = \mathbf{B} \times \mathbf{T}. \tag{A5.6}$$

The surface normal vector of the helical tail with B_o = 0.1 and λ = 2/3, i.e. base case design used in CFD-model, are presented in Fig. A5.1.

Quaternion calculations are carried out by the following formulae (Baraff, 2001):

$$\mathbf{q}(t = t_o) = \begin{bmatrix} q_{s0} & q_{v1} & q_{v2} & q_{v3} \end{bmatrix}, \tag{A5.7}$$

$$\boldsymbol{\Omega} = \begin{bmatrix} 0 & \Omega_y & \Omega_z \end{bmatrix}, \tag{A5.8}$$

$$\frac{\mathrm{d}q_{s0}}{\mathrm{d}t} = -\frac{\Omega_y q_{v2} + \Omega_z q_{v3}}{2}, \tag{A5.9}$$

$$\frac{\mathrm{d}}{\mathrm{d}t}\begin{bmatrix} q_{v1} \\ q_{v2} \\ q_{v3} \end{bmatrix} = q_{s0}\boldsymbol{\Omega} + \boldsymbol{\Omega} \times \begin{bmatrix} q_{v1} \\ q_{v2} \\ q_{v3} \end{bmatrix}, \tag{A5.10}$$

$$\mathbf{q}(t = t_o + \mathrm{d}t) = \begin{bmatrix} (q_{s0} + \mathrm{d}q_{s0}) & (q_{v1} + \mathrm{d}q_{v1}) & (q_{v2} + \mathrm{d}q_{v2}) & (q_{v3} + \mathrm{d}q_{v3}) \end{bmatrix}. \tag{A5.11}$$

Instantaneous rotation matrix between the swimmer frame and the lab frame is computed as follows:

$$\mathbf{R}_{11}^{sw \to lab} = 1 - 2(q_{v2}^2 + q_{v3}^2), \tag{A5.12}$$

$$\mathbf{R}_{12}^{sw \to lab} = 2(q_{v1}q_{v2} - q_{s0}q_{v3}), \tag{A5.13}$$

$$\mathbf{R}_{13}^{sw \to lab} = 2(q_{v1}q_{v3} - q_{s0}q_{v2}), \tag{A5.14}$$

$$\mathbf{R}_{21}^{sw \to lab} = 2(q_{v2}q_{v1} - q_{s0}q_{v3}), \tag{A5.15}$$

$$\mathbf{R}_{22}^{sw\to lab} = 1 - 2(q_{v1}^2 + q_{v3}^2), \tag{A5.16}$$

$$\mathbf{R}_{23}^{sw\to lab} = 2(q_{v2}q_{v3} - q_{s0}q_{v1}), \tag{A5.17}$$

$$\mathbf{R}_{31}^{sw\to lab} = 2(q_{v3}q_{v1} - q_{s0}q_{v2}), \tag{A5.18}$$

$$\mathbf{R}_{32}^{sw\to lab} = 2(q_{v3}q_{v2} - q_{s0}q_{v1}), \tag{A5.19}$$

$$\mathbf{R}_{33}^{sw\to lab} = 1 - 2(q_{v1}^2 + q_{v2}^2). \tag{A5.20}$$

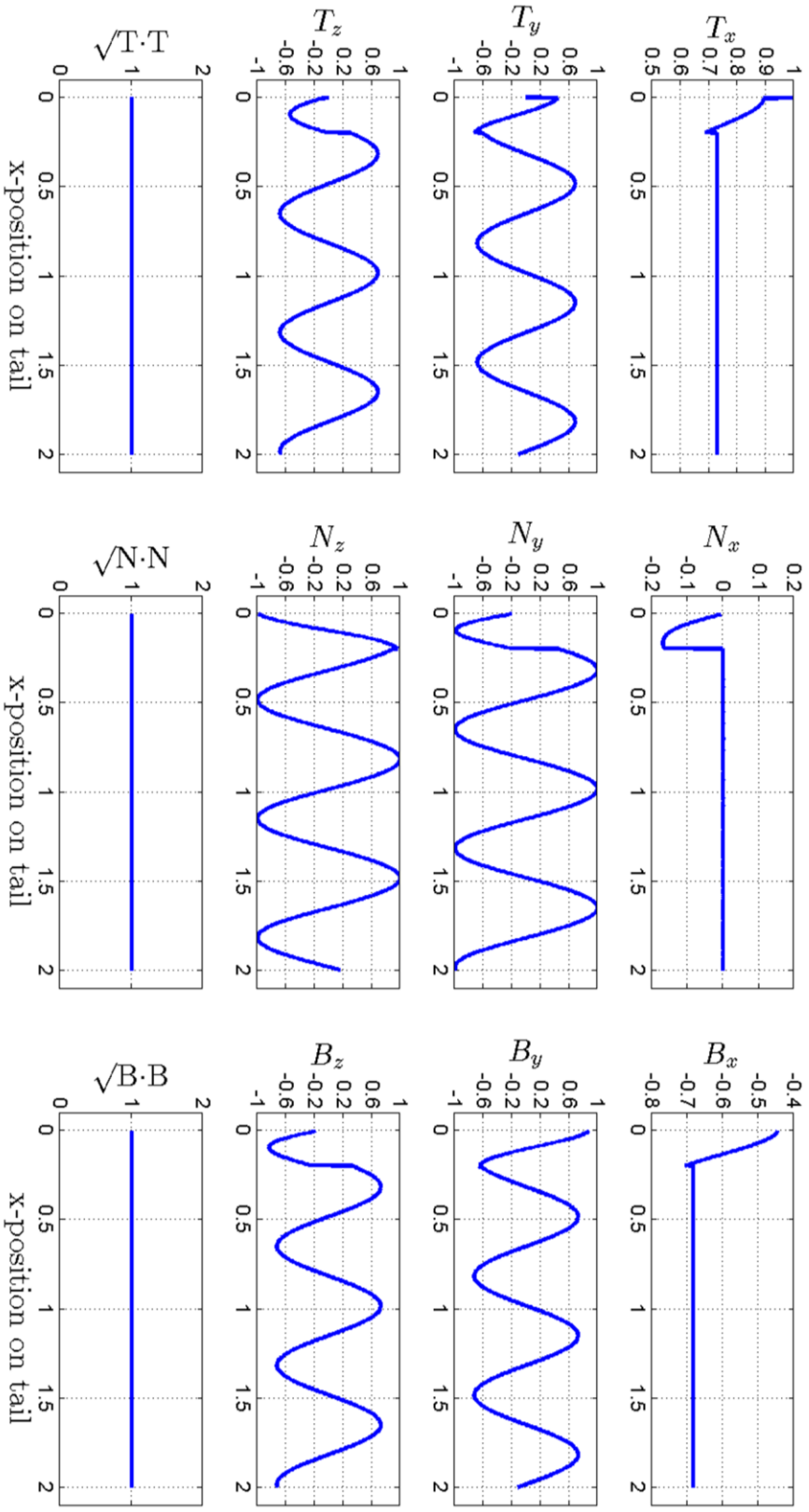

Figure A5.1: Surface normal vector of a right-handed helical tail: with B_o = 0.1 and λ = 2/3 (in dimensionless form).

APPENDIX 6: Experimental Measurements of the Robotic Prototype

Here are the results obtained by visual inspection by Microsoft Live Movie Maker application. Each table represents the experiments conducted with the picture of the tail it is following. The framed background is to demonstrate that the wave lengths and wave amplitudes have homogeneous distributions throughout the helical tail; however, unlike the background used in experiments, each small square is wider than 2 mm.

Each table shows the forward velocity of the swimmer (in mm/s), the body rotation rates (in Hz), and the rotation rates of the tail (in Hz), respectively. All measurements are carried out in the lab frame, i.e. the frame where the CCD camera is sitting on, and presented with mean value, standard deviation and 95% confidence intervals. The maximum and minimum values in are marked as outliers and not included in the comparative study presented in the chapter "IN-CHANNEL SWIMMING RESULTS".

In Table captions, for simplicity, experiment names are written in short form as:

- Horizontal wide channel with open ends: Wide channel
- Horizontal narrow channels with open ends: Narrow channel
- Horizontal narrow channels with closed ends: Closed channel
- Vertical wide channel with closed ends: Vertical channel
- Horizontal wide channel with closed ends: Horizontal channel

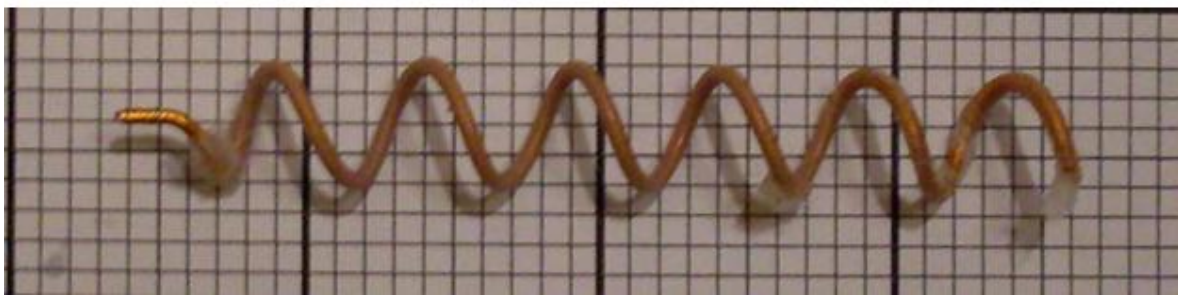

Figure A6.1: Tail with $N_\lambda = 6$; $B_o = 1.5$ mm; $m_{tail} = 1.15$ g.

Table A6.1.1: Wide channel experiment results with N_λ = 6; B_o = 1.5 mm; m_{tail} = 1.15 g.

t1 [s]	t2 [s]	disp [mm]	vel [mm/s]	mean	stdev	conf
1,27	22,77	10	0,465116279			
57,71	116,66	20	0,339270568			
0	1,27	1	0,787401575			
1,27	56,56	20	0,361729065			
63,74	86,21	10	0,445037828	0,479711063	0,161078848	0,141189241
		rot [1]	rotation rate[Hz]			
30,46	49,39	1	0,052826202			
49,39	63,63	1	0,070224719			
100,75	116,66	1	0,062853551			
214,08	230,51	1	0,060864273			
376,07	393,33	1	0,057937428	0,060941234	0,005739731	0,005031004
		rot [1]	rotation rate[Hz]			
393,4	394,7	1	0,769230769			
299,58	300,81	1	0,81300813			
209,88	211,04	1	0,862068966			
119,24	120,41	1	0,854700855			
459,11	460,61	1	0,666666667	0,793135077	0,07141826	0,062599714

Table A6.1.2: Narrow channel experiment results with N_λ = 6; B_o = 1.5 mm; m_{tail} = 1.15 g.

t1 [s]	t2 [s]	disp [mm]	vel [mm/s]	mean	stdev	conf
0	6,95	2	0,287769784			
6,95	13,46	2	0,307219662			
13,46	21,02	2	0,264550265			
21,02	29,03	2	0,24968789			
29,03	38,1	2	0,220507166	0,265946953	0,030035827	0,026327079
		rot [1]	rotation rate[Hz]			
0,23	15,4	1	0,065919578			
3,48	19,22	1	0,063532402			
6,65	22,98	1	0,061236987			
8,85	25,82	1	0,058927519			
10,25	27,35	1	0,058479532	0,061619204	0,002807217	0,002460589
		rot [1]	rotation rate[Hz]			
0,23	0,77	0,5	0,925925926			
0,77	1,23	0,5	1,086956522			
1,23	1,77	0,5	0,925925926			
1,77	2,23	0,5	1,086956522			
2,23	3,27	1	0,961538462	0,997460671	0,074221101	0,065056468

Table A6.1.3: Closed channel experiment results with N_λ = 6; B_o = 1.5 mm; m_{tail} = 1.15 g.

t1 [s]	t2 [s]	disp [mm]	vel [mm/s]	mean	stdev	conf
33,28	40,5	2	0,27700831			
31,08	48,6	4	0,228310502			
35,05	40,94	2	0,339558574			
40,5	49,78	2	0,215517241			
40,94	49,63	2	0,230149597	0,258108845	0,045771069	0,040119373
		rot [1]	rotation rate[Hz]			
1,33	11,08	1	0,102564103			
2,95	12,4	1	0,105820106			
4,15	13,6	1	0,105820106			
5,38	14,83	1	0,105820106			
6,43	16,05	1	0,103950104	0,104794905	0,001329908	0,001165694
		rot [1]	rotation rate[Hz]			
0,33	0,73	0,5	1,25			
0,73	1,1	0,5	1,351351351			
1,1	1,5	0,5	1,25			
1,5	1,87	0,5	1,351351351			
1,87	2,63	1	1,315789474	1,303698435	0,045727099	0,040080833

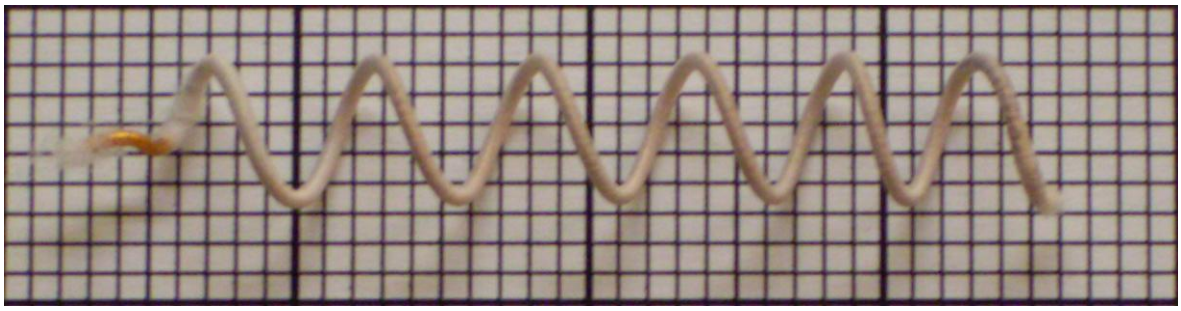

Figure A6.2: Tail with N_λ = 6; B_o = 2 mm; m_{tail} = 1.35 g.

Table A6.2.1: Wide channel experiment results with N_λ = 6; B_o = 2 mm; m_{tail} = 1.35 g.

t1 [s]	t2 [s]	disp [mm]	vel [mm/s]	mean	stdev	conf
0	39,74	14	0,352289884			
0	8,19	4	0,488400488			
4,05	39,42	12	0,339270568			
176,27	236,85	20	0,330141961			
115,32	135,62	10	0,492610837	0,400542748	0,073802988	0,064689983
		rot [1]	rotation rate[Hz]			
2,02	11,77	1	0,102564103			
11,77	23,34	1	0,086430424			
7,99	18,73	1	0,09310987			
18,73	30,86	1	0,082440231			
140,77	156,35	1	0,064184852	0,085745896	0,012754252	0,01117939
		rot [1]	rotation rate[Hz]			
0,23	0,97	0,5	0,675675676			
0,97	1,63	0,5	0,757575758			
1,63	2,27	0,5	0,78125			
87,38	88,21	0,5	0,602409639			
49,04	49,88	0,5	0,595238095	0,682429833	0,076764034	0,067285406

Table A6.2.2: Narrow channel experiment results with N_λ = 6; B_o = 2 mm; m_{tail} = 1.35 g.

t1 [s]	t2 [s]	disp [mm]	vel [mm/s]	mean	stdev	conf
0	15,18	4	0,263504611			
15,18	27,85	2	0,157853197			
27,85	41,85	2	0,142857143			
0	6,04	2	0,331125828			
6,04	15,33	2	0,215285253	0,222125206	0,069360641	0,060796165
		rot [1]	rotation rate[Hz]			
1,03	16,38	1	0,06514658			
3,09	18,72	1	0,063979527			
5,13	20,53	1	0,064935065			
6,72	22,37	1	0,063897764			
8,08	24,14	1	0,062266501	0,064045087	0,001019286	0,000893427
		rot [1]	rotation rate[Hz]			
0	0,77	0,5	0,649350649			
0,77	1,47	0,5	0,714285714			
1,47	2,23	0,5	0,657894737			
2,23	2,97	0,5	0,675675676			
2,97	3,73	0,5	0,657894737	0,671020303	0,023271026	0,020397579

Table A6.2.3: Closed channel experiment results with N_λ = 6; B_o = 2 mm; m_{tail} = 1.35 g.

t1 [s]	t2 [s]	disp [mm]	vel [mm/s]	mean	stdev	conf
127,85	136,51	2	0,230946882			
80,29	87,63	2	0,272479564			
121,83	127,85	2	0,332225914			
75,16	80,29	2	0,389863548			
36,11	41,54	2	0,368324125	0,318768007	0,059239632	0,051924873
		rot [1]	rotation rate[Hz]			
1,32	10,98	1	0,103519669			
2,74	12,11	1	0,106723586			
3,83	13,08	1	0,108108108			
4,89	14,07	1	0,108932462			
5,92	15,12	1	0,108695652	0,107195895	0,001991722	0,001745789
		rot [1]	rotation rate[Hz]			
0,43	1	0,5	0,877192982			
1	1,6	0,5	0,833333333			
1,6	2,13	0,5	0,943396226			
2,13	2,77	0,5	0,78125			
2,77	3,3	0,5	0,943396226	0,875713754	0,063061118	0,055274492

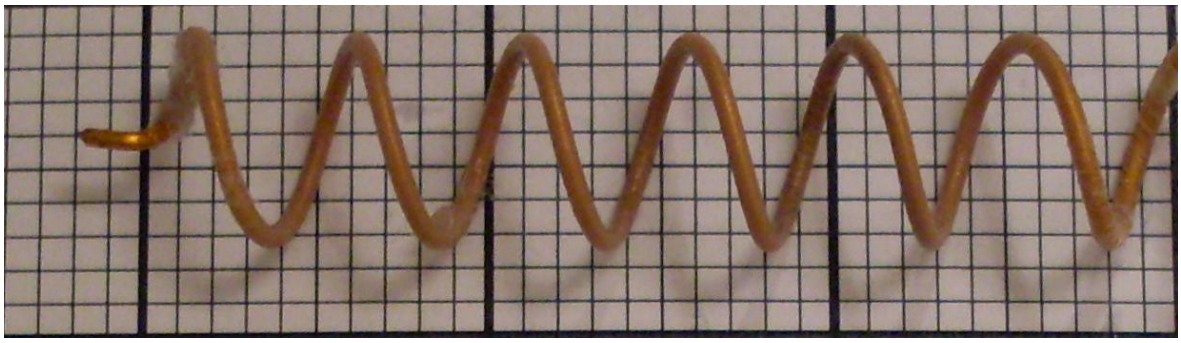

Figure A6.3: Tail with N_λ = 6; B_o = 2.5 mm; m_{tail} = 1.70 g.

Table A6.3.1: Wide channel experiment results with N_λ = 6; B_o = 2.5 mm; m_{tail} = 1.70 g.

t1 [s]	t2 [s]	disp [mm]	vel [mm/s]	mean	stdev	conf
0	41,25	8	0,193939394			
41,77	100,37	10	0,170648464			
100,37	158,66	10	0,171556013			
0	55,81	10	0,179179359			
0	112,33	20	0,178046826	0,178674011	0,008351718	0,007320469
		rot [1]	rotation rate[Hz]			
4,05	17,98	1	0,071787509			
60,78	75,54	1	0,067750678			
104,53	118,97	1	0,069252078			
133,74	148,58	1	0,067385445			
170,08	184,46	1	0,069541029	0,069143348	0,001561494	0,001368685
		rot [1]	rotation rate[Hz]			
18,5	21,2	1	0,37037037			
338,55	340,25	0,5	0,294117647			
99,75	102,42	1	0,374531835			
140,06	142,88	1	0,354609929			
179,68	182,51	1	0,35335689	0,349397334	0,028880112	0,025314069

Table A6.3.2: Narrow channel experiment results with N_λ = 6; B_o = 2.5 mm; m_{tail} = 1.70 g.

t1 [s]	t2 [s]	disp [mm]	vel [mm/s]	mean	stdev	conf
8,1	29,91	2	0,091701055			
29,91	68,22	2	0,05220569			
68,22	94,3	2	0,076687117			
94,3	121,85	2	0,072595281			
121,85	144,25	2	0,089285714	0,076494971	0,014142431	0,010403185
		rot [1]	rotation rate[Hz]			
2,29	15,95	1	0,073206442			
5,75	17,98	1	0,081766149			
7,81	20,33	1	0,079872204			
9,12	22,5	1	0,074738416			
10,43	24,23	1	0,072463768	0,076409396	0,003723034	0,003263323
		rot [1]	rotation rate[Hz]			
0,93	2,23	0,5	0,384615385			
2,23	3,33	0,5	0,454545455			
3,33	4,67	0,5	0,373134328			
4,67	5,8	0,5	0,442477876			
5,8	8,3	1	0,4	0,410954609	0,032056232	0,02809801

Table A6.3.3: Closed channel experiment results with N_λ = 6; B_o = 2.5 mm; m_{tail} = 1.70 g.

t1 [s]	t2 [s]	disp [mm]	vel [mm/s]	mean	stdev	conf
66,11	77,18	2	0,180668473			
80,13	146,69	8	0,120192308			
45,6	111,71	8	0,121010437			
50,17	66,11	2	0,125470514			
101,53	110,83	2	0,215053763	0,152479099	0,038658522	0,028437244
		rot [1]	rotation rate[Hz]			
0,96	9,23	1	0,120918984			
2,04	10,1	1	0,124069479			
3,1	11	1	0,126582278			
3,98	11,88	1	0,126582278			
5,24	12,99	1	0,129032258	0,125437056	0,002750701	0,002411052
		rot [1]	rotation rate[Hz]			
0	0,93	0,5	0,537634409			
0,93	1,77	0,5	0,595238095			
1,77	2,7	0,5	0,537634409			
2,7	3,6	0,5	0,555555556			
3,6	4,57	0,5	0,515463918	0,548305277	0,02668912	0,023393616

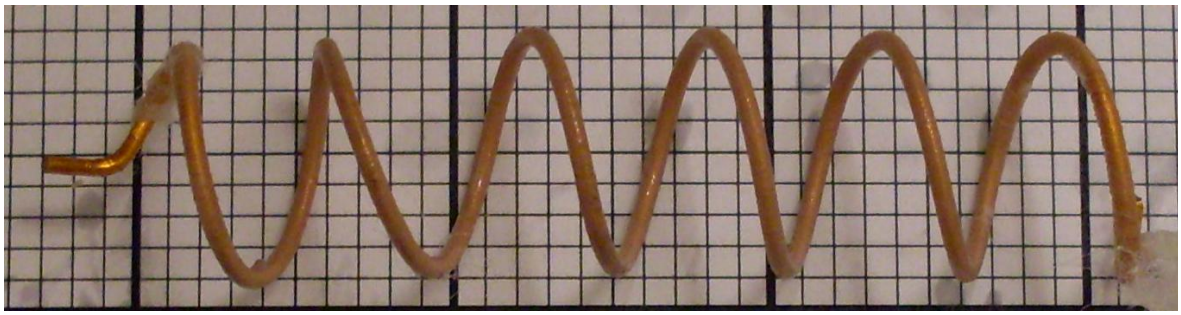

Figure A6.4: Tail with N_λ = 6; B_o = 3.5 mm; m_{tail} = 1.95 g.

Table A6.4.1: Wide channel experiment results with N_λ = 6; B_o = 3.5 mm; m_{tail} = 1.95 g.

t1 [s]	t2 [s]	disp [mm]	vel [mm/s]	mean	stdev	conf
3,03	102,57	20	0,200924252			
52,9	103,34	10	0,198255353			
59,76	155,05	18	0,188897051			
3,03	52,9	10	0,200521356			
3,13	50,37	10	0,211685013	0,200056605	0,007265932	0,006368753
		rot [1]	rotation rate[Hz]			
19,15	32,3	1	0,076045627			
46,44	75,01	2	0,0700035			
89,04	103,58	1	0,068775791			
141,43	155,46	1	0,071275837			
198,97	214,42	1	0,064724919	0,070165135	0,003670591	0,003217356
		rot [1]	rotation rate[Hz]			
3,9	5,97	0,5	0,241545894			
2,03	3,9	0,5	0,267379679			
7,9	10	0,5	0,238095238			
55,32	59,89	1	0,218818381			
5,97	7,9	0,5	0,259067358	0,24498131	0,016993073	0,014894811

Table A6.4.2: Narrow channel experiment results with N_λ = 6; B_o = 3.5 mm; m_{tail} = 1.95 g.

t1 [s]	t2 [s]	disp [mm]	vel [mm/s]	mean	stdev	conf
0	23,01	4	0,173837462			
0	54,12	6	0,110864745			
69,75	109,72	4	0,100075056			
0	8,26	2	0,242130751			
8,26	25,07	2	0,1189768	0,149176963	0,052989471	0,046446465
		rot [1]	rotation rate[Hz]			
0,47	12,27	1	0,084745763			
6,95	19,54	1	0,079428118			
4,28	16	1	0,085324232			
7,89	20,93	1	0,076687117			
2,83	14,01	1	0,089445438	0,083126133	0,004528238	0,003969103
		rot [1]	rotation rate[Hz]			
0,8	2,57	0,5	0,282485876			
2,57	4,67	0,5	0,238095238			
4,57	6,57	0,5	0,25			
6,57	8,8	0,5	0,224215247			
8,8	10,7	0,5	0,263157895	0,251590851	0,020111614	0,017628283

Table A6.4.3: Closed channel experiment results with N_λ = 6; B_o = 3.5 mm; m_{tail} = 1.95 g.

t1 [s]	t2 [s]	disp [mm]	vel [mm/s]	mean	stdev	conf
0	69,91	8	0,114432842			
0	8,24	2	0,242718447			
69,91	128,05	8	0,137598899			
36,24	52,4	2	0,123762376			
36,5	99,64	8	0,126702566	0,149043026	0,047417559	0,04156256
		rot [1]	rotation rate[Hz]			
0,9	11,42	1	0,095057034			
2,47	12,56	1	0,099108028			
3,56	13,39	1	0,1017294			
4,86	14,39	1	0,104931794			
6,02	15,37	1	0,106951872	0,101555626	0,004213564	0,003693284
		rot [1]	rotation rate[Hz]			
0,7	2,13	0,5	0,34965035			
2,13	3,7	0,5	0,318471338			
3,7	5,17	0,5	0,340136054			
5,17	6,67	0,5	0,333333333			
6,67	8,2	0,5	0,326797386	0,333677692	0,010728715	0,009403961

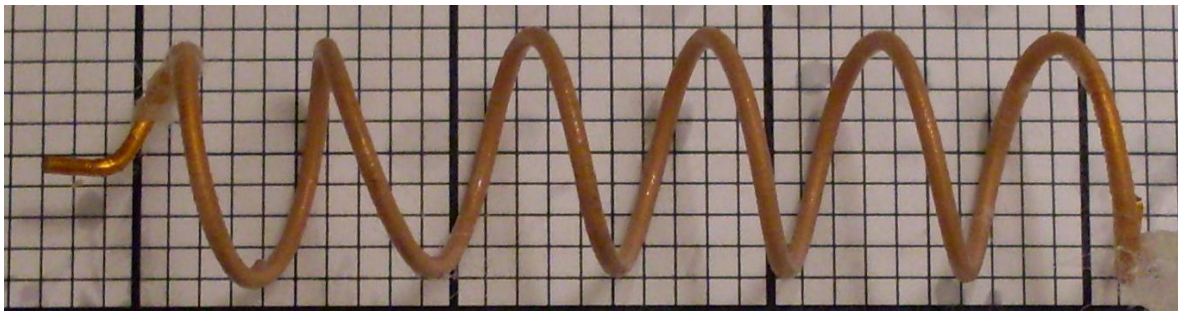

Figure A6.5: Tail with N_λ = 4; B_o = 1.5 mm; m_{tail} = 0.75 g.

Table A6.5.1: Wide channel experiment results with N_λ = 4; B_o = 1.5 mm; m_{tail} = 0.75 g.

t1 [s]	t2 [s]	disp [mm]	vel [mm/s]	mean	stdev	conf
6,79	20,37	10	0,736377025			
20,37	38,68	10	0,546149645			
38,68	62,3	10	0,423370025			
0	6,79	6	0,88365243			
7	87,09	40	0,499438132	0,617797452	0,168335585	0,147549934
		rot [1]	rotation rate[Hz]			
14,79	26,17	1	0,087873462			
52,83	67,42	1	0,068540096			
38,98	52,83	1	0,072202166			
26,17	38,98	1	0,078064012			
4,59	14,79	1	0,098039216	0,08094379	0,010759504	0,009430948
		rot [1]	rotation rate[Hz]			
203,11	204,11	1	1			
54,44	55,3	1	1,162790698			
88,07	89	1	1,075268817			
165,51	166,48	1	1,030927835			
214,63	215,6	1	1,030927835	1,059983037	0,056726439	0,049722002

Table A6.5.2: Narrow channel experiment results with N_λ = 4; B_o = 1.5 mm; m_{tail} = 0.75 g.

t1 [s]	t2 [s]	disp [mm]	vel [mm/s]	mean	stdev	conf
0	5,59	2	0,357781753			
5,59	11,34	2	0,347826087			
11,34	20,32	2	0,222717149			
0	20,32	6	0,295275591			
0	12,95	4	0,308880309	0,306496178	0,047935129	0,042016221
		rot [1]	rotation rate[Hz]			
3,97	18,99	1	0,066577896			
0,82	15,31	1	0,069013112			
6,55	22,45	1	0,062893082			
8,32	24,73	1	0,060938452			
9,59	26,2	1	0,060204696	0,063925448	0,003369027	0,002953029
		rot [1]	rotation rate[Hz]			
0,27	0,63	0,5	1,388888889			
0,63	1,13	0,5	1			
1,13	1,5	0,5	1,351351351			
1,5	2,03	0,5	0,943396226			
2,03	2,97	1	1,063829787	1,149493251	0,184509842	0,161727035

Table A6.5.3: Closed channel experiment results with N_λ = 4; B_o = 1.5 mm; m_{tail} = 0.75 g.

t1 [s]	t2 [s]	disp [mm]	vel [mm/s]	mean	stdev	conf
0,74	16,34	8	0,512820513			
4,12	17,37	6	0,452830189			
8,69	12,81	2	0,485436893			
0,74	4,12	2	0,591715976			
4,56	8,69	2	0,484261501	0,505413014	0,047147551	0,041325891
		rot [1]	rotation rate[Hz]			
0	10,78	1	0,092764378			
1,91	12,04	1	0,098716683			
3,8	13,28	1	0,105485232			
4,94	14,38	1	0,105932203			
6,1	15,49	1	0,106496273	0,101878954	0,005363379	0,004701122
		rot [1]	rotation rate[Hz]			
0,13	0,4	0,5	1,851851852			
0,4	0,67	0,5	1,851851852			
0,67	0,93	0,5	1,923076923			
0,93	1,2	0,5	1,851851852			
1,2	1,47	0,5	1,851851852	1,866096866	0,028490028	0,024972152

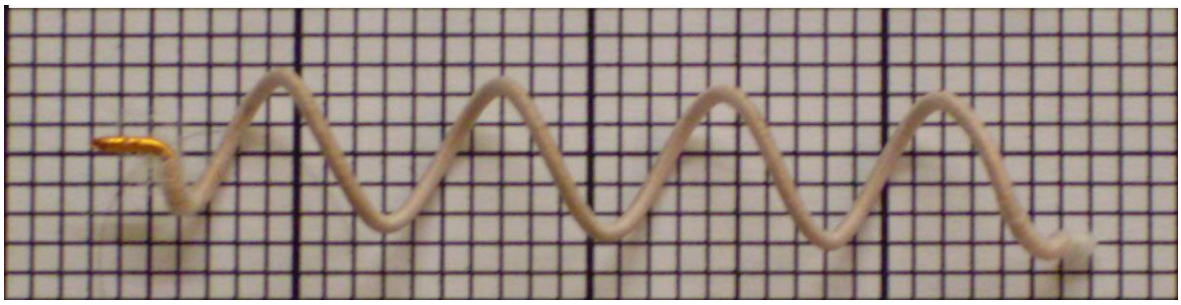

Figure A6.6: Tail with N_λ = 4; B_o = 2 mm; m_{tail} = 1.05 g.

Table A6.6.1: Wide channel experiment results with N_λ = 4; B_o = 2 mm; m_{tail} = 1.05 g.

t1 [s]	t2 [s]	disp [mm]	vel [mm/s]	mean	stdev	conf
0	20,87	16	0,766650695			
20,87	55,27	20	0,581395349			
7,68	54,68	30	0,638297872			
7,68	37,33	20	0,674536256			
7,68	20,58	10	0,775193798	0,687214794	0,074567732	0,065360298
		rot [1]	rotation rate[Hz]			
0,83	10,41	1	0,104384134			
10,41	21,26	1	0,092165899			
21,26	33,85	1	0,079428118			
5,09	15,06	1	0,100300903			
15,06	26,29	1	0,089047195	0,09306525	0,008756675	0,007675423
		rot [1]	rotation rate[Hz]			
2,1	2,67	0,5	0,877192982			
0,97	1,53	0,5	0,892857143			
2,67	3,23	0,5	0,892857143			
1,53	2,1	0,5	0,877192982			
0,37	0,97	0,5	0,833333333	0,874686717	0,021831142	0,019135488

Table A6.6.2: Narrow channel experiment results with N_λ = 4; B_o = 2 mm; m_{tail} = 1.05 g.

t1 [s]	t2 [s]	disp [mm]	vel [mm/s]	mean	stdev	conf
1,94	6,32	2	0,456621005			
6,32	10,14	2	0,523560209			
10,14	15,44	2	0,377358491			
15,44	20,73	2	0,378071834			
20,73	25,88	2	0,388349515	0,424792211	0,057496106	0,050396633
		rot [1]	rotation rate[Hz]			
0,6	14,85	1	0,070175439			
3,56	17,12	1	0,073746313			
5,95	19,41	1	0,074294205			
7,5	21,46	1	0,071633238			
8,66	22,89	1	0,070274069	0,072024653	0,001717692	0,001505595
		rot [1]	rotation rate[Hz]			
0,13	0,8	0,5	0,746268657			
0,8	1,43	0,5	0,793650794			
1,43	2,1	0,5	0,746268657			
2,1	2,77	0,5	0,746268657			
2,77	3,43	0,5	0,757575758	0,758006504	0,018352287	0,016086193

Table A6.6.3: Closed channel experiment results with N_λ = 4; B_o = 2 mm; m_{tail} = 1.05 g.

t1 [s]	t2 [s]	disp [mm]	vel [mm/s]	mean	stdev	conf
0	17,96	8	0,445434298			
17,96	38,27	8	0,393894633			
0	3,53	2	0,566572238			
25,31	38,12	6	0,468384075			
63,14	77,42	6	0,420168067	0,458890662	0,059313478	0,051989601
		rot [1]	rotation rate[Hz]			
1,1	9,71	1	0,116144019			
2,09	11,04	1	0,111731844			
3,09	12,17	1	0,110132159			
4,17	13,35	1	0,108932462			
5,25	14,42	1	0,109051254	0,111198347	0,00266928	0,002339684
		rot [1]	rotation rate[Hz]			
0,37	0,87	0,5	1			
0,87	1,37	0,5	1			
1,37	1,87	0,5	1			
1,87	2,4	0,5	0,943396226			
2,4	2,9	0,5	1	0,988679245	0,022641509	0,019845793

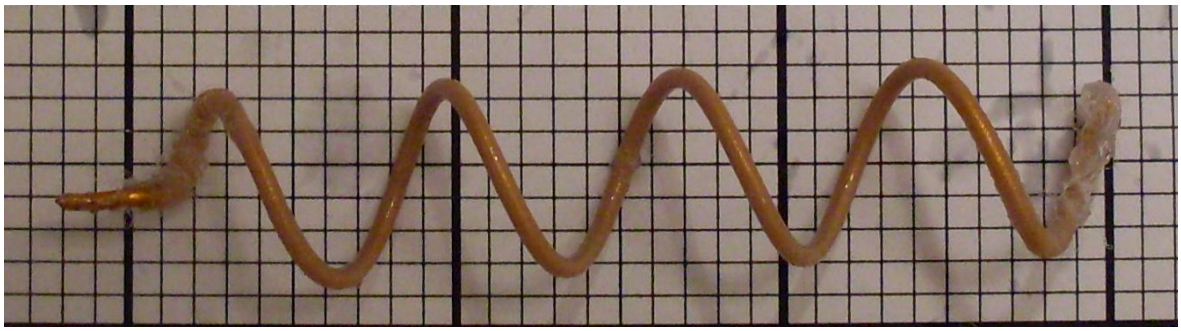

Figure A6.7: Tail with N_λ = 4; B_o = 2.5 mm; m_{tail} = 1.20 g.

Table A6.7.1: Wide channel experiment results with N_λ = 4; B_o = 2.5 mm; m_{tail} = 1.20 g.

t1 [s]	t2 [s]	disp [mm]	vel [mm/s]	mean	stdev	conf
1,61	27,55	12	0,462606014			
5,14	27,55	10	0,446229362			
27,55	53,6	10	0,383877159			
18,11	38,48	8	0,392734413			
53,6	60,06	2	0,309597523	0,399008894	0,053920493	0,047262528
		rot [1]	rotation rate[Hz]			
4,09	15,19	1	0,09009009			
15,19	27,56	1	0,080840744			
27,56	40,32	1	0,078369906			
40,32	53,42	1	0,076335878			
65,39	81,81	1	0,06090134	0,077307591	0,009456355	0,008288708
		rot [1]	rotation rate[Hz]			
0,53	2,6	1	0,483091787			
2,6	4,53	1	0,518134715			
4,53	6,53	1	0,5			
6,53	8,53	1	0,5			
0,06	2,67	1	0,383141762	0,476873653	0,048159036	0,04221248

Table A6.7.2: Narrow channel experiment results with N_λ = 4; B_o = 2.5 mm; m_{tail} = 1.20 g.

t1 [s]	t2 [s]	disp [mm]	vel [mm/s]	mean	stdev	conf
2,21	10,15	2	0,251889169			
10,15	17,94	2	0,256739409			
17,94	25,44	2	0,266666667			
25,44	35,14	2	0,206185567			
35,14	43,53	2	0,238379023	0,243971967	0,020975377	0,01838539
		rot [1]	rotation rate[Hz]			
1,93	16,18	1	0,070175439			
4,49	18,82	1	0,069783671			
6,32	21,03	1	0,067980965			
7,6	22,65	1	0,066445183			
8,78	23,94	1	0,065963061	0,068069664	0,001700393	0,001490433
		rot [1]	rotation rate[Hz]			
0,43	1,23	0,5	0,625			
1,23	2,2	0,5	0,515463918			
2,2	3,07	0,5	0,574712644			
3,07	4,07	0,5	0,5			
4,07	4,9	0,5	0,602409639	0,56351724	0,048500819	0,042512061

Table A6.7.3: Closed channel experiment results with N_λ = 4; B_o = 2.5 mm; m_{tail} = 1.20 g.

t1 [s]	t2 [s]	disp [mm]	vel [mm/s]	mean	stdev	conf
57,96	62,82	2	0,411522634			
26,48	30,89	2	0,453514739			
21,04	26,48	2	0,367647059			
41,9	47,32	2	0,36900369			
21,04	30,89	4	0,406091371	0,401555898	0,031714612	0,027798572
		rot [1]	rotation rate[Hz]			
1,18	9,15	1	0,125470514			
2,25	9,97	1	0,129533679			
3,38	11,03	1	0,130718954			
4,38	12,03	1	0,130718954			
0,07	8,17	1	0,12345679	0,127979778	0,002972359	0,00260534
		rot [1]	rotation rate[Hz]			
0,33	0,93	0,5	0,833333333			
0,93	1,63	0,5	0,714285714			
1,63	2,23	0,5	0,833333333			
0,33	1,63	1	0,769230769			
2,97	3,6	0,5	0,793650794	0,788766789	0,044553998	0,039052584

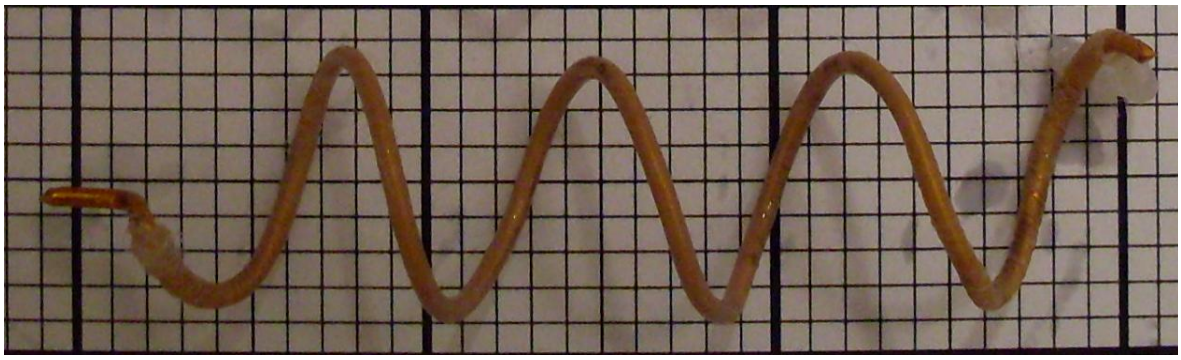

Figure A6.8: Tail with N_λ = 4; B_o = 3.5 mm; m_{tail} = 1.30 g.

Table A6.8.1: Wide channel experiment results with N_λ = 4; B_o = 3.5 mm; m_{tail} = 1.30 g.

t1 [s]	t2 [s]	disp [mm]	vel [mm/s]	mean	stdev	conf
1,87	60,85	16	0,271278399			
60,85	133,84	20	0,274010138			
133,84	176,93	10	0,232072407			
25,65	95,94	20	0,284535496			
95,94	173,2	20	0,258866166	0,264152521	0,018002754	0,015779819
		rot [1]	rotation rate[Hz]			
5,25	17,79	1	0,079744817			
0	11,16	1	0,089605735			
11,16	23	1	0,084459459			
23	36,02	1	0,076804916			
36,02	50,08	1	0,071123755	0,080347736	0,006334252	0,005552114
		rot [1]	rotation rate[Hz]			
1,07	3,93	1	0,34965035			
60,68	64,31	1	0,275482094			
99,71	103,45	1	0,267379679			
129,99	133,82	1	0,261096606			
51,08	54,78	1	0,27027027	0,2847758	0,032768338	0,028722187

Table A6.8.2: Narrow channel experiment results with N_λ = 4; B_o = 3.5 mm; m_{tail} = 1.30 g.

t1 [s]	t2 [s]	disp [mm]	vel [mm/s]	mean	stdev	conf
0	5,9	2	0,338983051			
5,9	40,53	10	0,288766965			
11,5	18,86	2	0,27173913			
0	19,01	6	0,315623356			
5,9	11,5	2	0,357142857	0,314451072	0,031336126	0,027466821
		rot [1]	rotation rate[Hz]			
0,6	14,88	1	0,070028011			
2,72	16,8	1	0,071022727			
5,45	18,57	1	0,076219512			
7,2	19,87	1	0,078926598			
8,67	21,01	1	0,081037277	0,075446825	0,004310341	0,003778111
		rot [1]	rotation rate[Hz]			
0,33	1,4	0,5	0,46728972			
1,4	2,7	0,5	0,384615385			
2,7	3,77	0,5	0,46728972			
3,77	5,1	0,5	0,37593985			
5,1	6,27	0,5	0,427350427	0,42449702	0,039035665	0,034215641

Table A6.8.3: Closed channel experiment results with N_λ = 4; B_o = 3.5 mm; m_{tail} = 1.30 g.

t1 [s]	t2 [s]	disp [mm]	vel [mm/s]	mean	stdev	conf
0	28,28	8	0,282885431			
16,05	37,85	8	0,366972477			
15,76	40,35	8	0,325335502			
25,18	49,78	8	0,325203252			
0	33,73	10	0,296471983	0,319373729	0,028951866	0,025376963
		rot [1]	rotation rate[Hz]			
0,5	9,2	1	0,114942529			
1,85	10,28	1	0,118623962			
3,09	11,15	1	0,124069479			
3,95	12,08	1	0,12300123			
4,86	13,06	1	0,12195122	0,120517684	0,003331871	0,00292046
		rot [1]	rotation rate[Hz]			
13,49	14,53	0,5	0,480769231			
14,53	15,63	0,5	0,454545455			
15,63	16,76	0,5	0,442477876			
16,76	17,89	0,5	0,442477876			
17,89	18,99	0,5	0,454545455	0,454963178	0,013986185	0,012259207

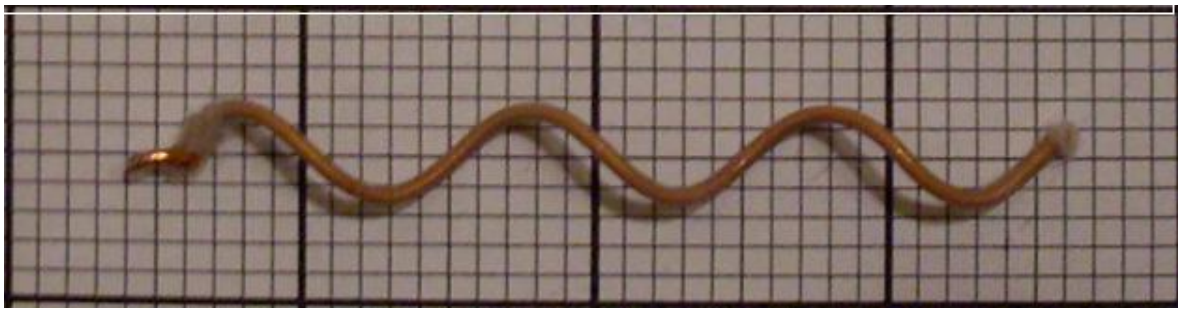

Figure A6.9: Tail with N_λ = 3; B_o = 1.5 mm; m_{tail} = 0.60 g.

Table A6.9.1: Wide channel experiment results with N_λ = 3; B_o = 1.5 mm; m_{tail} = 0.60 g.

t1 [s]	t2 [s]	disp [mm]	vel [mm/s]	mean	stdev	conf
6,75	29,39	20	0,883392226			
1,17	6,63	6	1,098901099			
16,96	28,65	10	0,855431993			
6,63	16,96	10	0,968054211			
0	6,63	8	1,206636501	1,002483206	0,132640155	0,116262086
		rot [1]	rotation rate[Hz]			
1,49	10,95	1	0,105708245			
10,95	21,28	1	0,096805421			
45,06	58,18	1	0,076219512			
21,28	32,72	1	0,087412587			
32,72	45,06	1	0,081037277	0,089436609	0,010662107	0,009345577
		rot [1]	rotation rate[Hz]			
0,1	0,6	1	2			
37,77	38,37	1	1,666666667			
0,6	1,07	1	2,127659574			
1,07	1,57	1	2			
1,57	2,07	1	2	1,958865248	0,154238607	0,135193615

Table A6.9.2: Narrow channel experiment results with N_λ = 3; B_o = 1.5 mm; m_{tail} = 0.60 g.

t1 [s]	t2 [s]	disp [mm]	vel [mm/s]	mean	stdev	conf
1,03	6,47	4	0,735294118			
6,47	20,88	10	0,693962526			
1,03	11,62	8	0,755429651			
3,53	6,32	2	0,716845878			
6,32	9,12	2	0,714285714	0,723163577	0,020783073	0,018216832
		rot [1]	rotation rate[Hz]			
0,6	9,46	1	0,112866817			
1,96	10,67	1	0,114810563			
3,2	11,75	1	0,116959064			
4,09	12,58	1	0,11778563			
4,89	13,38	1	0,11778563	0,116041541	0,001924563	0,001686923
		rot [1]	rotation rate[Hz]			
0	0,2	0,5	2,5			
0,2	0,4	0,5	2,5			
0,4	0,6	0,5	2,5			
0,6	0,8	0,5	2,5			
0,8	1	0,5	2,5	2,5	4,86475E-16	4,26407E-16

Table A6.9.3: Closed channel experiment results with N_λ = 3; B_o = 1.5 mm; m_{tail} = 0.60 g.

t1 [s]	t2 [s]	disp [mm]	vel [mm/s]	mean	stdev	conf
0	6,02	2	0,332225914			
66,17	72,48	2	0,316957211			
110,34	116,35	2	0,332778702			
14,09	20,1	2	0,332778702			
51,21	57,37	2	0,324675325	0,327883171	0,006268313	0,005494318
		rot [1]	rotation rate[Hz]			
0,79	12,18	1	0,087796313			
2,28	14,11	1	0,084530854			
3,6	15,67	1	0,082850041			
4,97	17,12	1	0,082304527			
6,18	18,34	1	0,082236842	0,083943715	0,002096841	0,001837929
		rot [1]	rotation rate[Hz]			
0,13	0,4	0,5	1,851851852			
0,4	0,63	0,5	2,173913043			
0,63	0,9	0,5	1,851851852			
0,9	1,13	0,5	2,173913043			
1,4	1,93	1	1,886792453	1,987664449	0,15260561	0,133762257

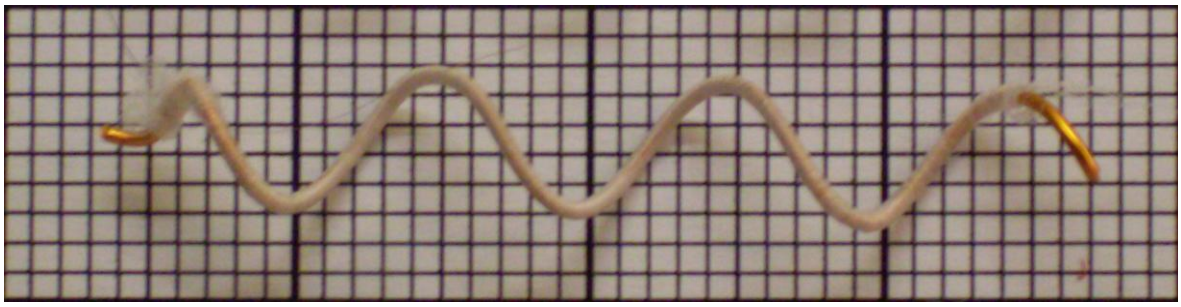

Figure A6.10: Tail with N_λ = 3; B_o = 2 mm; m_{tail} = 0.85 g.

Table A6.10.1: Wide channel experiment results with N_λ = 3; B_o = 2 mm; m_{tail} = 0.85 g.

t1 [s]	t2 [s]	disp [mm]	vel [mm/s]	mean	stdev	conf
0	21,33	20	0,937646507			
50,71	63,03	10	0,811688312			
51,32	74,46	20	0,864304235			
9,76	21,53	10	0,849617672			
158,38	187,66	20	0,683060109	0,829263367	0,083753615	0,073411932
		rot [1]	rotation rate[Hz]			
23,54	33,34	1	0,102040816			
62,09	69,13	1	0,142045455			
94,99	106,66	1	0,085689803			
146,11	155,06	1	0,111731844			
0,27	9,26	1	0,111234705	0,110548525	0,018353555	0,016087304
		rot [1]	rotation rate[Hz]			
0,67	1,23	0,5	0,892857143			
0,2	0,67	0,5	1,063829787			
1,23	1,67	0,5	1,136363636			
1,67	2,2	0,5	0,943396226			
2,2	2,63	0,5	1,162790698	1,039847498	0,105749286	0,092691633

Table A6.10.2: Narrow channel experiment results with N_λ = 3; B_o = 2 mm; m_{tail} = 0.85 g.

t1 [s]	t2 [s]	disp [mm]	vel [mm/s]	mean	stdev	conf
0,8	4,43	2	0,550964187			
4,43	7,69	2	0,613496933			
7,69	12,12	2	0,451467269			
12,12	15,67	2	0,563380282			
15,67	20,92	2	0,380952381	0,51205221	0,084020765	0,073646095
		rot [1]	rotation rate[Hz]			
0,9	13,86	1	0,077160494			
3,58	16,54	1	0,077160494			
5,95	19,95	1	0,071428571			
7,59	22,16	1	0,06863418			
8,74	23,47	1	0,067888663	0,07245448	0,004019627	0,003523294
		rot [1]	rotation rate[Hz]			
1	1,5	0,5	1			
1,5	1,93	0,5	1,162790698			
1,93	2,43	0,5	1			
2,43	2,93	0,5	1			
2,93	3,47	0,5	0,925925926	1,017743325	0,077991861	0,068361624

Table A6.10.3: Closed channel experiment results with N_λ = 3; B_o = 2 mm; m_{tail} = 0.85 g.

t1 [s]	t2 [s]	disp [mm]	vel [mm/s]	mean	stdev	conf
0,8	4,43	2	0,550964187			
4,43	7,69	2	0,613496933			
7,69	12,12	2	0,451467269			
12,12	15,67	2	0,563380282			
15,67	20,92	2	0,380952381	0,51205221	0,084020765	0,073646095
		rot [1]	rotation rate[Hz]			
0,9	13,86	1	0,077160494			
3,58	16,54	1	0,077160494			
5,95	19,95	1	0,071428571			
7,59	22,16	1	0,06863418			
8,74	23,47	1	0,067888663	0,07245448	0,004019627	0,003523294
		rot [1]	rotation rate[Hz]			
1	1,5	0,5	1			
1,5	1,93	0,5	1,162790698			
1,93	2,43	0,5	1			
2,43	2,93	0,5	1			
2,93	3,47	0,5	0,925925926	1,017743325	0,077991861	0,068361624

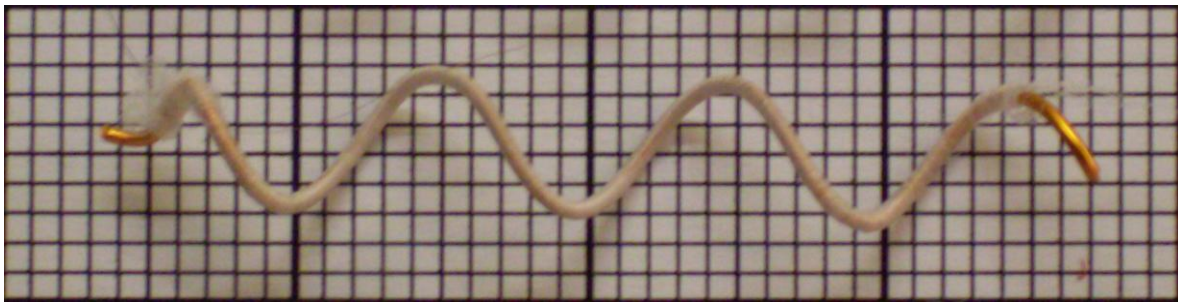

Figure A6.11: Tail with N_λ = 3; B_o = 2.5 mm; m_{tail} = 0.95 g.

Table A6.11.1: Wide channel experiment results with N_λ = 3; B_o = 2.5 mm; m_{tail} = 0.95 g.

t1 [s]	t2 [s]	disp [mm]	vel [mm/s]	mean	stdev	conf
0,81	8,76	8	1,006289308			
8,76	30,52	20	0,919117647			
30,52	55,86	20	0,789265983			
55,86	82	20	0,765110941			
19,09	42,46	20	0,855798032	0,867116382	0,087939905	0,077081309
		rot [1]	rotation rate[Hz]			
5,45	16,76	1	0,08841733			
16,76	28,53	1	0,084961767			
1,31	12,93	1	0,08605852			
12,93	24,41	1	0,087108014			
0	11,68	1	0,085616438	0,086432414	0,001213651	0,001063792
		rot [1]	rotation rate[Hz]			
2,73	3,33	0,5	0,833333333			
2,03	2,73	0,5	0,714285714			
1,47	2,03	0,5	0,892857143			
0,77	1,47	0,5	0,714285714			
0,17	0,77	0,5	0,833333333	0,797619048	0,071428571	0,062608753

Table A6.11.2: Narrow channel experiment results with N_λ = 3; B_o = 2.5mm; m_{tail} = 0.95 g.

t1 [s]	t2 [s]	disp [mm]	vel [mm/s]	mean	stdev	conf
1,62	6,03	2	0,453514739			
6,03	10,14	2	0,486618005			
10,14	14,4	2	0,469483568			
14,4	18,81	2	0,453514739			
18,81	24,99	2	0,323624595	0,437351129	0,058165226	0,050983132
		rot [1]	rotation rate[Hz]			
2,06	14,55	1	0,080064051			
4,49	17,2	1	0,078678206			
6,42	19,67	1	0,075471698			
7,87	21,46	1	0,073583517			
8,85	22,75	1	0,071942446	0,075947984	0,003041645	0,00266607
		rot [1]	rotation rate[Hz]			
0	0,57	0,5	0,877192982			
0,57	1,17	0,5	0,833333333			
1,17	1,77	0,5	0,833333333			
1,77	2,37	0,5	0,833333333			
2,37	2,97	0,5	0,833333333	0,842105263	0,01754386	0,015377588

Table A6.11.3: Closed channel experiment results with N_λ = 3; B_o = 2.5 mm; m_{tail} = 0.95 g.

t1 [s]	t2 [s]	disp [mm]	vel [mm/s]	mean	stdev	conf
1,91	19,54	8	0,45377198			
19,54	33,95	8	0,555170021			
27,63	42,03	8	0,555555556			
52,61	67,01	8	0,555555556			
60,1	74,65	8	0,549828179	0,533976258	0,04016097	0,035201995
		rot [1]	rotation rate[Hz]			
0,91	9,11	1	0,12195122			
1,99	10,14	1	0,122699387			
3,04	11,02	1	0,125313283			
4,26	11,86	1	0,131578947			
5,26	12,71	1	0,134228188	0,127154205	0,004897449	0,004292725
		rot [1]	rotation rate[Hz]			
0,17	0,67	0,5	1			
0,67	1,2	0,5	0,943396226			
1,2	1,7	0,5	1			
1,7	2,2	0,5	1			
2,2	2,7	0,5	1	0,988679245	0,022641509	0,019845793

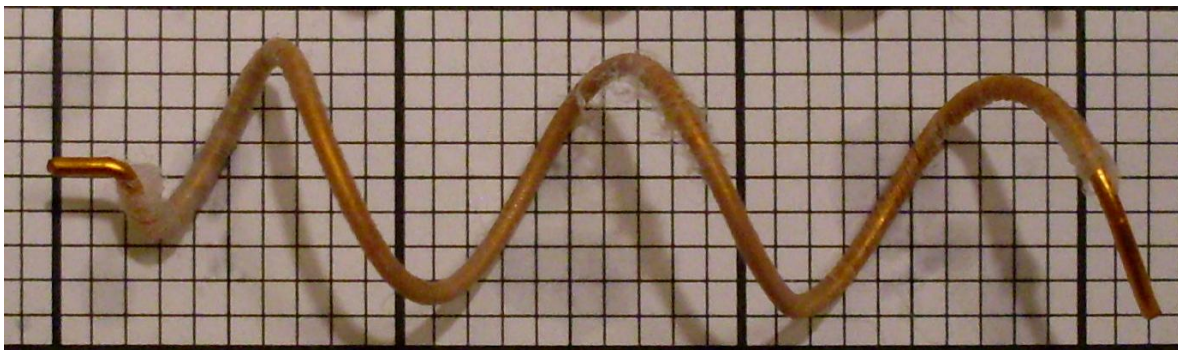

Figure A6.12: Tail with N_λ = 3; B_o = 3.5 mm; m_{tail} = 1.05 g.

Table A6.12.1: Wide channel experiment results with N_λ = 3; B_o = 3.5 mm; m_{tail} = 1.05 g.

t1 [s]	t2 [s]	disp [mm]	vel [mm/s]	mean	stdev	conf
0	25,94	18	0,693909021			
41,89	67,78	14	0,540749324			
10,42	23,83	10	0,745712155			
25,83	42,11	10	0,614250614			
25,83	60,34	20	0,579542162	0,634832655	0,074988816	0,065729388
		rot [1]	rotation rate[Hz]			
9,65	21,22	1	0,086430424			
5,13	16,28	1	0,089686099			
10,97	22,81	1	0,084459459			
7,24	18,6	1	0,088028169			
0	10,97	1	0,091157703	0,087952371	0,00235807	0,002066901
		rot [1]	rotation rate[Hz]			
1,27	2,43	0,5	0,431034483			
0,1	1,27	0,5	0,427350427			
4,9	6,17	0,5	0,393700787			
2,43	3,67	0,5	0,403225806			
3,67	4,9	0,5	0,406504065	0,412363114	0,014417634	0,012637381

Table A6.12.2: Narrow channel experiment results with N_λ = 3; B_o = 3.5mm; m_{tail} = 1.05 g.

t1 [s]	t2 [s]	disp [mm]	vel [mm/s]	mean	stdev	conf
4,14	33,99	8	0,2680067			
4,14	11,38	2	0,276243094			
11,38	17,44	2	0,330033003			
17,44	24,97	2	0,26560425			
24,97	33,69	2	0,229357798	0,273848969	0,032385025	0,028386205
		rot [1]	rotation rate[Hz]			
1,92	17,07	1	0,066006601			
4,73	19,21	1	0,069060773			
7,76	21,28	1	0,073964497			
9,57	23,5	1	0,071787509			
11,03	24,58	1	0,073800738	0,070924024	0,003030456	0,002656263
		rot [1]	rotation rate[Hz]			
0,97	1,77	0,5	0,625			
1,77	2,97	0,5	0,416666667			
2,97	3,8	0,5	0,602409639			
3,8	4,97	0,5	0,427350427			
0,99	2,99	1	0,5	0,514285347	0,086388406	0,075721385

Table A6.12.3: Closed channel experiment results with N_λ = 3; B_o = 3.5 mm; m_{tail} = 1.05 g.

t1 [s]	t2 [s]	disp [mm]	vel [mm/s]	mean	stdev	conf
25,89	28,98	2	0,647249191			
60,89	65,16	2	0,468384075			
5,44	9,56	2	0,485436893			
89,28	93,1	2	0,523560209			
22,65	25,89	2	0,617283951	0,548382864	0,071414391	0,062596323
		rot [1]	rotation rate[Hz]			
0,67	8,75	1	0,123762376			
1,6	9,85	1	0,121212121			
2,62	11	1	0,119331742			
3,56	11,91	1	0,119760479			
4,34	12,72	1	0,119331742	0,120679692	0,001689101	0,001480535
		rot [1]	rotation rate[Hz]			
0,53	1,33	0,5	0,625			
1,33	2,22	0,5	0,561797753			
2,22	3,06	0,5	0,595238095			
3,06	3,94	0,5	0,568181818			
3,94	4,77	0,5	0,602409639	0,590525461	0,023136361	0,020279542

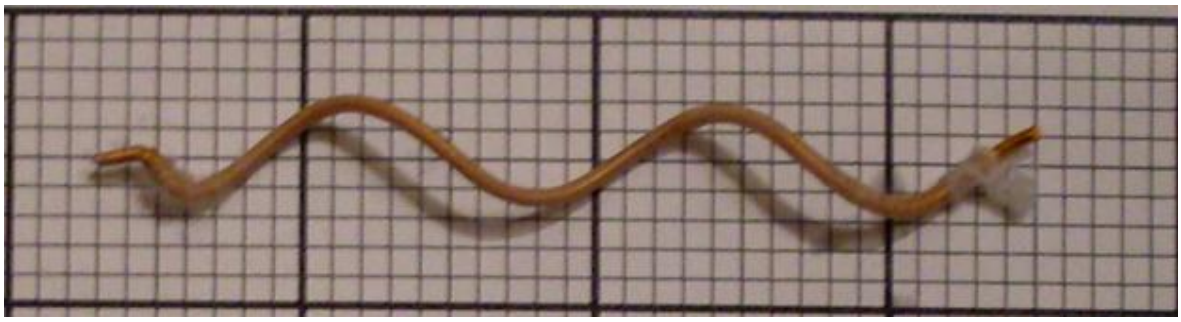

Figure A6.13: Tail with N_λ = 2.4; B_o = 1.5 mm; m_{tail} = 0.6 g.

Table A6.13.1: Wide channel experiment results with N_λ = 2.4; B_o = 1.5 mm; m_{tail} = 0.6 g.

t1 [s]	t2 [s]	disp [mm]	vel [mm/s]	mean	stdev	conf
5,5	28,87	20	0,855798032			
16,4	28,5	10	0,826446281			
28,5	41,09	10	0,794281176			
4,8	16,4	10	0,862068966			
0,93	4,8	4	1,033591731	0,874437237	0,083136843	0,072871317
		rot [1]	rotation rate[Hz]			
4,78	13,61	1	0,113250283			
13,61	22,64	1	0,110741971			
41,34	50,99	1	0,103626943			
89,87	99,7	1	0,1017294			
189,55	199,65	1	0,099009901	0,1056717	0,005426691	0,004756617
		rot [1]	rotation rate[Hz]			
1,4	2	1	1,666666667			
0,87	1,4	1	1,886792453			
9,94	10,54	1	1,666666667			
2	2,6	1	1,666666667			
0,33	0,87	1	1,851851852	1,747728861	0,099893461	0,08755887

Table A6.13.2: Narrow channel experiment results with N_λ = 2.4; B_o = 1.5mm; m_{tail} = 0.6 g.

t1 [s]	t2 [s]	disp [mm]	vel [mm/s]	mean	stdev	conf
0	10,9	8	0,733944954			
11,19	14,14	2	0,677966102			
0	3,39	2	0,589970501			
3,39	6,19	2	0,714285714			
6,19	8,54	2	0,85106383	0,71344622	0,084693094	0,074235406
		rot [1]	rotation rate[Hz]			
0	9,5	1	0,105263158			
1,77	10,72	1	0,111731844			
3,62	12,08	1	0,11820331			
4,73	13,22	1	0,11778563			
5,67	14,14	1	0,118063754	0,114209539	0,005094513	0,004465456
		rot [1]	rotation rate[Hz]			
0,27	0,73	1	2,173913043			
0,73	1,2	1	2,127659574			
1,2	1,67	1	2,127659574			
1,67	2,13	1	2,173913043			
2,13	2,6	1	2,127659574	2,146160962	0,02265948	0,019861545

Table A6.13.3: Closed channel experiment results with N_λ = 2.4; B_o = 1.5mm; m_{tail} = 0.6 g.

t1 [s]	t2 [s]	disp [mm]	vel [mm/s]	mean	stdev	conf
3,68	38,43	8	0,230215827			
38,43	71,12	8	0,244723157			
3,68	27,98	6	0,24691358			
3,68	45,35	10	0,239980802			
45,35	89,23	10	0,227894257	0,237945525	0,007632573	0,006690123
		rot [1]	rotation rate[Hz]			
0,3	10,24	1	0,100603622			
2,19	11,81	1	0,103950104			
3,42	13,18	1	0,102459016			
4,45	14,28	1	0,1017294			
5,5	15,2	1	0,103092784	0,102366985	0,001145206	0,001003799
		rot [1]	rotation rate[Hz]			
0,13	0,47	0,5	1,470588235			
0,47	0,8	0,5	1,515151515			
0,8	1,13	0,5	1,515151515			
1,13	1,47	0,5	1,470588235			
1,47	2,13	1	1,515151515	1,497326203	0,021831459	0,019135766

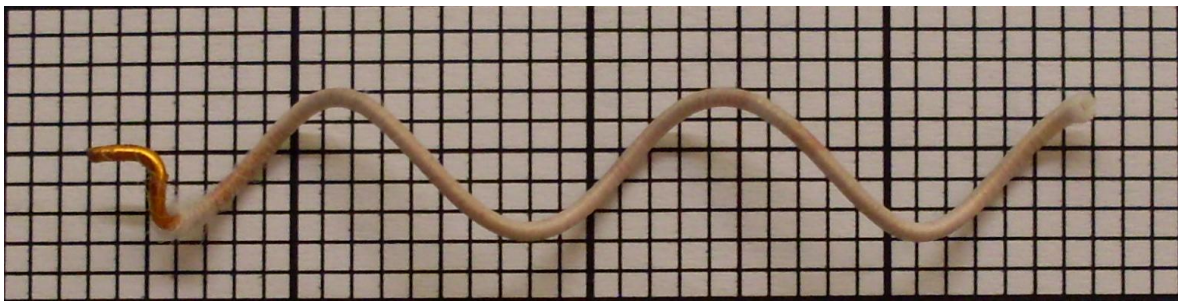

Figure A6.14: Tail with N_λ = 2.4; B_o = 2 mm; m_{tail} = 0.7 g.

Table A6.14.1: Wide channel experiment results with N_λ = 2.4; B_o = 2 mm; m_{tail} = 0.7 g.

t1 [s]	t2 [s]	disp [mm]	vel [mm/s]	mean	stdev	conf
0	16,35	20	1,22324159			
16,35	37,3	20	0,954653938			
25,83	47,83	20	0,909090909			
16,06	26,23	10	0,983284169			
7,08	25,83	20	1,066666667	1,027387455	0,110572181	0,096919009
		rot [1]	rotation rate[Hz]			
0,5	10,44	1	0,100603622			
69,35	77,65	1	0,120481928			
32,01	41,92	1	0,100908174			
140,07	147,65	1	0,131926121			
133,9	140,07	1	0,162074554	0,12319888	0,022813531	0,019996574
		rot [1]	rotation rate[Hz]			
1,8	2,23	1	2,325581395			
2,67	3,1	0,5	1,162790698			
0,57	1	0,5	1,162790698			
0,13	0,57	0,5	1,136363636			
1,37	1,8	0,5	1,162790698	1,390063425	0,467870951	0,410099435

Table A6.14.2: Narrow channel experiment results with N_λ = 2.4; B_o = 2 mm; m_{tail} = 0.7 g.

t1 [s]	t2 [s]	disp [mm]	vel [mm/s]	mean	stdev	conf
2,35	5,59	2	0,617283951			
5,59	9,85	2	0,469483568			
9,85	14,86	2	0,399201597			
14,86	19,12	2	0,469483568			
19,12	24,56	2	0,367647059	0,464619948	0,086066148	0,075438919
		rot [1]	rotation rate[Hz]			
0	13,09	1	0,076394194			
1,69	15,37	1	0,073099415			
3,53	17,13	1	0,073529412			
5,03	18,42	1	0,074682599			
6,63	19,51	1	0,077639752	0,075069074	0,00171836	0,001506181
		rot [1]	rotation rate[Hz]			
0,07	0,7	0,5	0,793650794			
0,7	1,17	0,5	1,063829787			
1,17	1,8	0,5	0,793650794			
1,8	2,27	0,5	1,063829787			
2,27	3,43	1	0,862068966	0,915406025	0,1237358	0,108457218

Table A6.14.3: Closed channel experiment results with N_λ = 2.4; B_o = 2 mm; m_{tail} = 0.7 g.

t1 [s]	t2 [s]	disp [mm]	vel [mm/s]	mean	stdev	conf
1,92	6,34	2	0,452488688			
6,34	10,32	2	0,502512563			
28,89	32,72	2	0,522193211			
35,81	40,09	2	0,46728972			
32,72	35,81	2	0,647249191	0,518346675	0,069029647	0,060506041
		rot [1]	rotation rate[Hz]			
0	9,6	1	0,104166667			
1,38	10,42	1	0,110619469			
2,72	11,27	1	0,116959064			
3,76	12,08	1	0,120192308			
4,72	13,02	1	0,120481928	0,114483887	0,006262074	0,005488849
		rot [1]	rotation rate[Hz]			
0,3	0,73	0,5	1,162790698			
0,73	1,13	0,5	1,25			
1,13	1,53	0,5	1,25			
1,53	1,93	0,5	1,25			
1,93	2,77	1	1,19047619	1,220653378	0,03699304	0,032425234

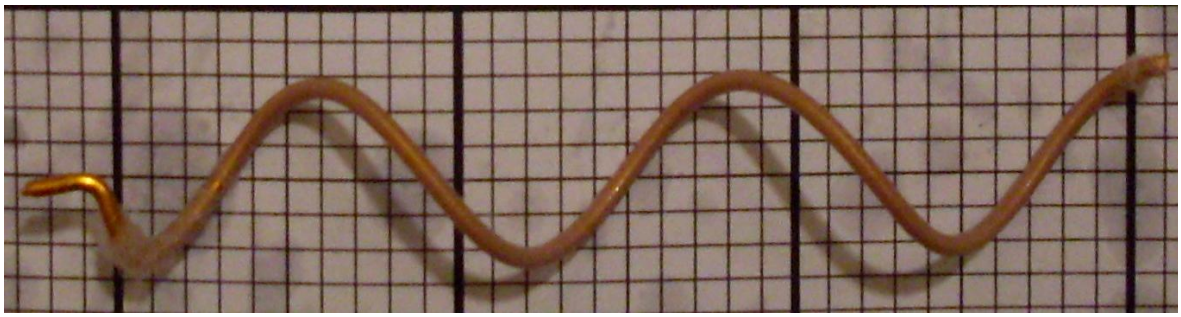

Figure A6.15: Tail with N_λ = 2.4; B_o = 2.5 mm; m_{tail} = 0.75 g.

Table A6.15.1: Wide channel experiment results with N_λ = 2.4; B_o = 2.5 mm; m_{tail} = 0.75 g.

t1 [s]	t2 [s]	disp [mm]	vel [mm/s]	mean	stdev	conf
1,47	8,04	8	1,217656012			
1,47	10,04	10	1,166861144			
1,47	16,56	16	1,060304838			
1,47	12,35	12	1,102941176			
1,47	31,07	30	1,013513514	1,112255337	0,072974862	0,063964111
		rot [1]	rotation rate[Hz]			
0,39	10,39	1	0,1			
10,3	20,86	1	0,09469697			
14,04	24,84	1	0,092592593			
32,06	41,98	1	0,100806452			
0,3	10,3	1	0,1	0,097619203	0,003325694	0,002915046
		rot [1]	rotation rate[Hz]			
8,69	9,26	0,5	0,877192982			
9	9,54	0,5	0,925925926			
3,41	4,57	1	0,862068966			
11,4	12,56	1	0,862068966			
12,56	13,76	1	0,833333333	0,872118035	0,030421259	0,026664919

Table A6.15.2: Narrow channel experiment results with N_λ = 2.4; B_o = 2.5mm; m_{tail} = 0.75 g.

t1 [s]	t2 [s]	disp [mm]	vel [mm/s]	mean	stdev	conf
3,54	7,67	2	0,484261501			
7,67	14,6	3	0,432900433			
14,6	19,9	2,5	0,471698113			
19,9	25,8	2	0,338983051			
0	3,54	2	0,564971751	0,45856297	0,073639253	0,064546465
		rot [1]	rotation rate[Hz]			
0,1	12,34	1	0,081699346			
1,85	13,86	1	0,083263947			
3,69	15,66	1	0,083542189			
5,67	17,58	1	0,083963056			
7,5	19,17	1	0,085689803	0,083631668	0,001282406	0,001124058
		rot [1]	rotation rate[Hz]			
0,27	0,93	0,5	0,757575758			
0,93	1,57	0,5	0,78125			
1,57	2,2	0,5	0,793650794			
2,2	2,9	0,5	0,714285714			
2,9	3,57	0,5	0,746268657	0,758606184	0,0277793	0,024349182

Table A6.15.3: Closed channel experiment results with N_λ =2.4; B_o =2.5mm; m_{tail} = 0.75 g.

t1 [s]	t2 [s]	disp [mm]	vel [mm/s]	mean	stdev	conf
0	11,63	8	0,687876182			
26,36	39,24	8	0,621118012			
29,45	43	8	0,590405904			
32,69	46,97	8	0,56022409			
62,58	75,68	8	0,610687023	0,614062242	0,042350544	0,037121206
		rot [1]	rotation rate[Hz]			
0,23	8,82	1	0,116414435			
1,5	10,08	1	0,116550117			
2,67	11,31	1	0,115740741			
3,71	12,17	1	0,11820331			
4,55	13,13	1	0,116550117	0,116691744	0,000813173	0,000712765
		rot [1]	rotation rate[Hz]			
0,4	0,83	0,5	1,162790698			
0,83	1,3	0,5	1,063829787			
1,3	1,73	0,5	1,162790698			
1,73	2,2	0,5	1,063829787			
2,2	3,1	1	1,111111111	1,112870416	0,044265406	0,038799626

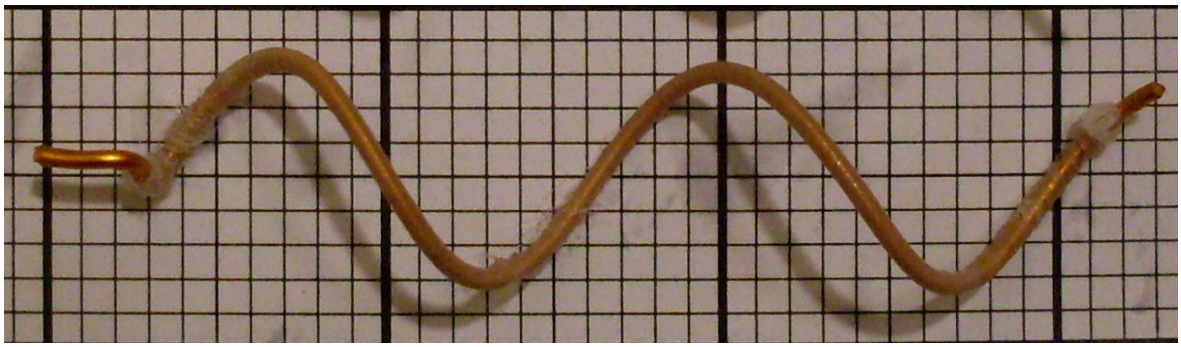

Figure A6.16: Tail with N_λ = 2.4; B_o = 3.5 mm; m_{tail} = 0.85 g.

Table A6.16.1: Wide channel experiment results with N_λ = 2.4; B_o = 3.5mm; m_{tail} = 0.85 g.

t1 [s]	t2 [s]	disp [mm]	vel [mm/s]	mean	stdev	conf
1,68	23,26	20	0,926784059			
10,2	33,36	20	0,863557858			
10,2	21,6	10	0,877192982			
0	10,2	10	0,980392157			
21,36	33,36	10	0,833333333	0,896252078	0,051773901	0,045380992
		rot [1]	rotation rate[Hz]			
0	10,99	1	0,090991811			
10,99	22,42	1	0,087489064			
22,42	33,89	1	0,087183958			
5,12	16,41	1	0,088573959			
16,41	27,86	1	0,087336245	0,088315007	0,001424904	0,001248961
		rot [1]	rotation rate[Hz]			
48,08	50,19	1	0,473933649			
50,19	52,32	1	0,469483568			
52,32	54,41	1	0,4784689			
54,41	56,46	1	0,487804878			
56,46	58,51	1	0,487804878	0,479499175	0,0073528	0,006444895

Table A6.16.2: Narrow channel experiment results with N_λ = 2.4; B_o =3.5 mm; m_{tail} =0.85 g.

t1 [s]	t2 [s]	disp [mm]	vel [mm/s]	mean	stdev	conf
1,33	5,01	2	0,543478261			
5,01	8,1	2	0,647249191			
8,1	12,22	2	0,485436893			
12,22	17,23	2	0,399201597			
1,33	8,98	4	0,522875817	0,519648352	0,080669821	0,070708916
		rot [1]	rotation rate[Hz]			
0,59	11,93	1	0,088183422			
2,95	10,49	1	0,132625995			
4,57	15,91	1	0,088183422			
6,22	18,1	1	0,084175084			
7,14	19,64	1	0,08	0,094633584	0,019236187	0,016860952
		rot [1]	rotation rate[Hz]			
0,62	1,26	0,5	0,78125			
1,26	2,09	0,5	0,602409639			
2,09	2,72	0,5	0,793650794			
2,72	3,56	0,5	0,595238095			
3,56	4,26	0,5	0,714285714	0,697366848	0,084900392	0,074417108

Table A6.16.3: Wide channel experiment results with N_λ = 2.4; B_o = 3.5 mm; m_{tail} = 0.85g.

t1 [s]	t2 [s]	disp [mm]	vel [mm/s]	mean	stdev	conf
0	16,34	8	0,489596083			
16,34	30,02	8	0,584795322			
24,14	37,97	8	0,578452639			
48,42	61,82	8	0,597014925			
6,18	24,14	8	0,445434298	0,539058654	0,060356813	0,052904107
		rot [1]	rotation rate[Hz]			
0,53	8,43	1	0,126582278			
1,6	9,3	1	0,12987013			
2,78	10,27	1	0,133511348			
3,86	11,02	1	0,139664804			
4,69	11,9	1	0,138696255	0,133664963	0,005017983	0,004398375
		rot [1]	rotation rate[Hz]			
0,3	0,93	0,5	0,793650794			
0,93	1,6	0,5	0,746268657			
1,6	2,23	0,5	0,793650794			
2,23	2,9	0,5	0,746268657			
2,9	3,5	0,5	0,833333333	0,782634447	0,033039486	0,028959854

From here on, represented are the observations of the experiments carried out with wide channel having closed ends; in vertical and horizontal orientations with respect to gravitational pull. Same experimental procedure is followed, except for vertical experiments where the swimmer was not in contact with the channel walls and swimming against the gravitational pull. The tail length and tail weight, i.e. m_{tail}= 1.25 g, are fixed for the helices used in vertical experiments.

Figure A6.17: Tail with λ = 15.5 mm; B_o = 2.5 mm; L_{tail} = 130 mm.

Table A6.17.1: Vertical experiment results with λ = 15.5 mm; B_o = 2.5 mm; L_{tail} = 130 mm.

t1 [s]	t2 [s]	disp [mm]	vel [mm/s]	mean	stdev	conf
146,83	150,2	2	0,59347181			
150,2	153,27	2	0,651465798			
126,33	145,81	10	0,513347023			
157,27	161,24	2	0,503778338			
144,08	146,83	2	0,727272727	0,597867139	0,084420725	0,073996668
		rot [1]	rotation rate[Hz]			
147,13	157,02	1	0,101112235			
149,58	159,68	1	0,099009901			
162,02	172,01	1	0,1001001			
168,34	178,3	1	0,100401606			
155,7	165,9	1	0,098039216	0,099732612	0,001084054	0,000950197
		rot [1]	rotation rate[Hz]			
146,83	147,33	1	2			
157,53	158,1	1	1,754385965			
165,28	165,85	1	1,754385965			
171,56	172,12	1	1,785714286			
136,93	137,53	1	1,666666667	1,792230576	0,111212697	0,097480436

Table A6.17.2: Horizontal experiment results with λ = 15.5 mm; B_o=2.5 mm; L_{tail} = 130 mm.

t1 [s]	t2 [s]	disp [mm]	vel [mm/s]	mean	stdev	conf
24,13	29,73	2	0,357142857			
33,01	Şub.00	2	0,337837838			
6,43	12,66	2	0,321027287			
12,66	18,39	2	0,34904014			
18,39	24,13	2	0,348432056	0,342696036	0,012449875	0,010912596
		rot [1]	rotation rate[Hz]			
40,77	57,81	1	0,058685446			
57,81	75,01	1	0,058139535			
32,43	49,45	1	0,058754407			
49,45	66,83	1	0,057537399			
13,31	30,28	1	0,058927519	0,058408861	0,000509292	0,000446406
		rot [1]	rotation rate[Hz]			
38,6	39,56	1	1,041666667			
39,56	40,5	1	1,063829787			
40,5	41,43	1	1,075268817			
41,43	42,4	1	1,030927835			
42,4	43,36	1	1,041666667	1,050671955	0,016310456	0,014296482

Figure A6.18: Tail with λ = 10 mm; B_o = 2.5 mm; L_{tail} = 88 mm.

Table A6.18.1: Vertical experiment results with λ =10 mm; B_o =2.5 mm; L_{tail} =88 mm.

t1 [s]	t2 [s]	disp [mm]	vel [mm/s]	mean	stdev	conf
561,25	605,52	10	0,225886605			
605,52	648,13	10	0,234686693			
516,16	561,25	10	0,221778665			
469,61	516,16	10	0,214822771			
605,52	652,79	10	0,211550666	0,22174508	0,008203452	0,007190511
		rot [1]	rotation rate[Hz]			
581,94	590,31	1	0,119474313			
590,31	598,8	1	0,11778563			
598,8	607,17	1	0,119474313			
607,17	615,66	1	0,11778563			
615,66	624,17	1	0,117508813	0,11840574	0,000878322	0,000769869
		rot [1]	rotation rate[Hz]			
595,86	596,53	1	1,492537313			
596,53	597,2	1	1,492537313			
597,2	597,83	1	1,587301587			
597,83	598,5	1	1,492537313			
598,5	599,16	1	1,515151515	1,516013009	0,036704573	0,032172386

Table A6.18.2: Horizontal experiment results with λ = 10 mm; B_o = 2.5 mm; L_{tail} = 88 mm.

t1 [s]	t2 [s]	disp [mm]	vel [mm/s]	mean	stdev	conf
0	26,31	6	0,228050171			
26,31	51,25	10	0,40096231			
51,25	68,05	8	0,476190476			
35,92	41,23	2	0,376647834			
41,23	46,33	2	0,392156863	0,374801531	0,080999608	0,070997982
		rot [1]	rotation rate[Hz]			
50,05	63,29	1	0,075528701			
23,48	36,61	1	0,076161462			
17,43	30,33	1	0,07751938			
33,87	47,09	1	0,075642965			
47,09	60,23	1	0,076103501	0,076191202	0,000708816	0,000621294
		rot [1]	rotation rate[Hz]			
16	16,97	1	1,030927835			
16,97	17,9	1	1,075268817			
17,9	18,9	1	1			
18.Oca	19,87	1	1,030927835			
19,87	20,87	1	1	1,027424897	0,027632705	0,024220688

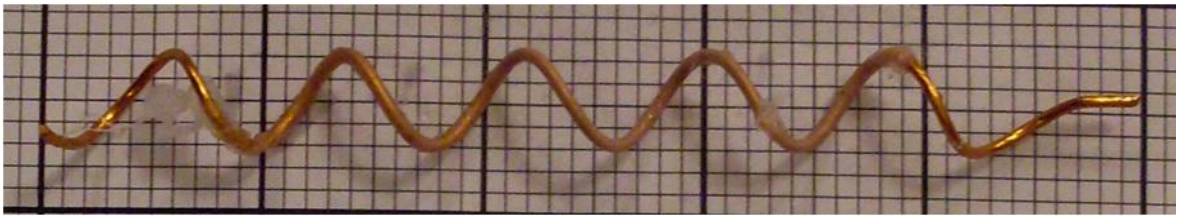

Figure A6.19: Tail with λ = 16 mm; B_o = 4.5 mm; L_{tail} = 93 mm.

Table A6.19.1: Vertical experiment results with λ = 16 mm; B_o = 4.5 mm; L_{tail} = 93 mm.

t1 [s]	t2 [s]	disp [mm]	vel [mm/s]	mean	stdev	conf
1000,98	1037,77	10	0,271812993			
1037,77	1073,64	10	0,2787845			
1073,64	1107,47	10	0,295595625			
1107,47	1144,46	10	0,270343336			
927,49	964,9	10	0,267308206	0,276768932	0,010137671	0,008885897
		rot [1]	rotation rate[Hz]			
1044,75	1052,55	1	0,128205128			
1052,55	1060,35	1	0,128205128			
1060,35	1068,22	1	0,127064803			
1068,22	1075,99	1	0,128700129			
1075,99	1083,76	1	0,128700129	0,128175063	0,000597641	0,000523846
		rot [1]	rotation rate[Hz]			
3,69	4,76	1	0,934579439			
4,76	5,79	1	0,970873786			
5,79	6,86	1	0,934579439			
6,86	7,92	1	0,943396226			
7,92	8,99	1	0,934579439	0,943601666	0,014057116	0,012321379

Table A6.19.2: Horizontal experiment results with λ = 16 mm; B_o = 4.5 mm; L_{tail} = 93 mm.

t1 [s]	t2 [s]	disp [mm]	vel [mm/s]	mean	stdev	conf
17,3	20,79	2	0,573065903			
20,79	Oca.00	2	0,607902736			
24,08	27,91	2	0,522193211			
27,91	30,64	2	0,732600733			
30,64	35,02	2	0,456621005	0,578476717	0,092375351	0,080969077
		rot [1]	rotation rate[Hz]			
34,78	49,14	1	0,069637883			
49,14	62,41	1	0,07535795			
62,41	74,16	1	0,085106383			
25,3	39,51	1	0,070372977			
39,51	53,39	1	0,07204611	0,074504261	0,005655536	0,004957205
		rot [1]	rotation rate[Hz]			
51,22	52,82	1	0,625			
52,82	54,46	1	0,609756098			
54,46	56,06	1	0,625			
56,06	57,66	1	0,625			
57,66	59,26	1	0,625	0,62195122	0,006097561	0,00534465

Figure A6.20: Tail with λ = 12 mm; B_o = 4.5 mm; L_{tail} = 60 mm.

Table A6.20.1: Vertical experiment results with λ = 12 mm; B_o = 4.5 mm; L_{tail} = 60 mm.

t1 [s]	t2 [s]	disp [mm]	vel [mm/s]	mean	stdev	conf
1000,98	1037,77	10	0,271812993			
1037,77	1073,64	10	0,2787845			
1073,64	1107,47	10	0,295595625			
1107,47	1144,46	10	0,270343336			
927,49	964,9	10	0,267308206	0,276768932	0,010137671	0,008885897
		rot [1]	rotation rate[Hz]			
1044,75	1052,55	1	0,128205128			
1052,55	1060,35	1	0,128205128			
1060,35	1068,22	1	0,127064803			
1068,22	1075,99	1	0,128700129			
1075,99	1083,76	1	0,128700129	0,128175063	0,000597641	0,000523846
		rot [1]	rotation rate[Hz]			
3,69	4,76	1	0,934579439			
4,76	5,79	1	0,970873786			
5,79	6,86	1	0,934579439			
6,86	7,92	1	0,943396226			
7,92	8,99	1	0,934579439	0,943601666	0,014057116	0,012321379

Table A6.20.2: Horizontal experiment results with λ = 12 mm; B_o = 4.5 mm; L_{tail} = 60 mm.

t1 [s]	t2 [s]	disp [mm]	vel [mm/s]	mean	stdev	conf
1422,08	1459,89	10	0,264480296			
1459,89	1502,58	10	0,234246896			
1502,58	1541,64	10	0,256016385			
1541,64	1579,77	10	0,262260687			
1502,58	1557,7	14	0,253991292	0,254199111	0,010696993	0,009376156
		rot [1]	rotation rate[Hz]			
1531,83	1539,54	1	0,129701686			
1539,54	1547,2	1	0,130548303			
1547,2	1554,91	1	0,129701686			
1554,91	1562,57	1	0,130548303			
1562,57	1570,34	1	0,128700129	0,129840021	0,000684245	0,000599756
		rot [1]	rotation rate[Hz]			
1,29	2,42	1	0,884955752			
2,42	3,49	1	0,934579439			
3,49	4,59	1	0,909090909			
4,59	5,69	1	0,909090909			
5,69	6,79	1	0,909090909	0,909361584	0,015695889	0,0137578

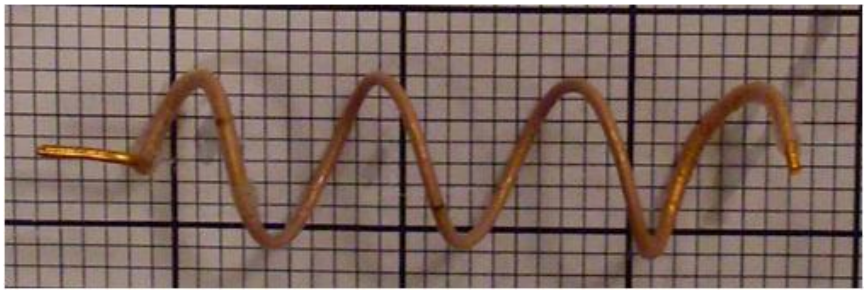

Figure A6.21: Tail with λ = 15 mm; B_o = 7.5 mm; L_{tail} = 56 mm.

Table A6.21.1: Vertical experiment results with λ = 15 mm; B_o = 7.5 mm; L_{tail} = 56 mm

t1 [s]	t2 [s]	disp [mm]	vel [mm/s]	mean	stdev	conf
594,84	599,72	2	0,409836066			
599,72	605,42	2	0,350877193			
605,42	610,6	2	0,386100386			
591,02	594,84	2	0,523560209			
585,88	591,02	2	0,389105058	0,411895782	0,058959774	0,051679571
		rot [1]	rotation rate[Hz]			
586,95	593,82	1	0,145560408			
592,06	598,91	1	0,145985401			
598,91	605,89	1	0,143266476			
5,89	12,74	1	0,145985401			
9,32	16,3	1	0,143266476	0,144812832	0,001272096	0,001115021
		rot [1]	rotation rate[Hz]			
7,28	9,05	1	0,564971751			
5,55	7,28	1	0,578034682			
3,82	5,55	1	0,578034682			
2,05	3,82	1	0,564971751			
0,28	2,05	1	0,564971751	0,570196924	0,006399503	0,005609309

Table A6.21.2: Horizontal experiment results with λ = 15 mm; B_o = 7.5 mm; L_{tail} = 56 mm

t1 [s]	t2 [s]	disp [mm]	vel [mm/s]	mean	stdev	conf
27,48	52,02	4	0,162999185			
27,48	35,23	2	0,258064516			
35,23	52,02	2	0,119118523			
52,02	59,28	2	0,275482094			
18,48	27,87	2	0,212992545	0,205731373	0,058282881	0,051086259
		rot [1]	rotation rate[Hz]			
25,52	34,92	1	0,106382979			
34,92	44,23	1	0,107411386			
44,23	53,19	1	0,111607143			
53,19	61,15	1	0,125628141			
29,76	39,23	1	0,105596621	0,111325254	0,007445988	0,006526577
		rot [1]	rotation rate[Hz]			
28,24	31,64	1	0,294117647			
31,64	35,07	1	0,29154519			
35,07	38,61	1	0,282485876			
38,61	42,11	1	0,285714286			
42,11	45,57	1	0,289017341	0,288576068	0,004123099	0,00361399

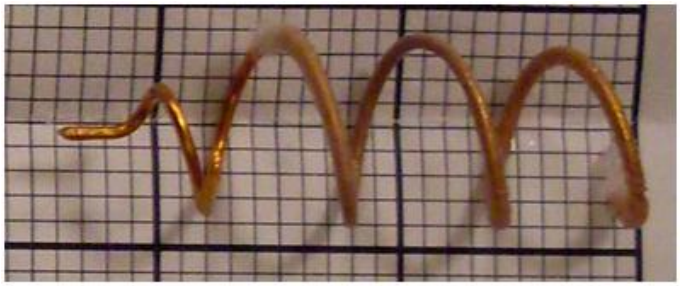

Figure A6.22: Tail with λ = 11 mm; B_o = 7.5 mm; L_{tail} = 42 mm.

Table A6.22.1: Vertical experiment results with λ = 11 mm; B_o = 7.5 mm; L_{tail} = 42 mm

t1 [s]	t2 [s]	disp [mm]	vel [mm/s]	mean	stdev	conf
614,3	623,45	2	0,218579235			
623,45	631,77	2	0,240384615			
631,77	643,08	2	0,17683466			
643,08	652,53	2	0,211640212			
652,53	661,57	2	0,221238938	0,213735532	0,02076536	0,018201306
		rot [1]	rotation rate[Hz]			
642,08	649,14	1	0,141643059			
649,14	656,33	1	0,139082058			
645,75	652,84	1	0,141043724			
638,66	645,75	1	0,141043724			
629,72	636,91	1	0,139082058	0,140378925	0,001081266	0,000947754
		rot [1]	rotation rate[Hz]			
628,95	630,65	1	0,588235294			
630,65	632,45	1	0,555555556			
627,18	628,95	1	0,564971751			
632,46	634,22	1	0,568181818			
634,22	635,96	1	0,574712644	0,570331413	0,010875816	0,009532898

Table A6.22.2: Horizontal experiment results with λ = 11 mm; B_o = 7.5 mm; L_{tail} = 42 mm

t1 [s]	t2 [s]	disp [mm]	vel [mm/s]	mean	stdev	conf
59,01	92,83	10	0,295683028			
92,83	132,52	10	0,251952633			
01.Şub	73,79	10	0,24230676			
43,25	87,36	12	0,272047155			
5,57	13	2	0,269179004	0,266233716	0,018363994	0,016096454
		rot [1]	rotation rate[Hz]			
42,95	53,26	1	0,09699321			
53,26	62,23	1	0,11148272			
62,23	71,2	1	0,11148272			
71,2	79,53	1	0,120048019			
79,53	87,68	1	0,122699387	0,112541211	0,008983561	0,007874294
		rot [1]	rotation rate[Hz]			
28,54	31,74	1	0,3125			
31,74	35,01	1	0,305810398			
35,01	38,51	1	0,285714286			
38,51	42,18	1	0,272479564			
7,9	10,67	1	0,36101083	0,307503016	0,030306144	0,026564019

From here on, represented are the observations of the experiments carried out with wide horizontal channel having closed ends. Selected tails, which are used in horizontal channel experiments, are stripped in order to study the effect of enhanced lubrication effect on the forward swim of the bio-inspired robotic prototype.

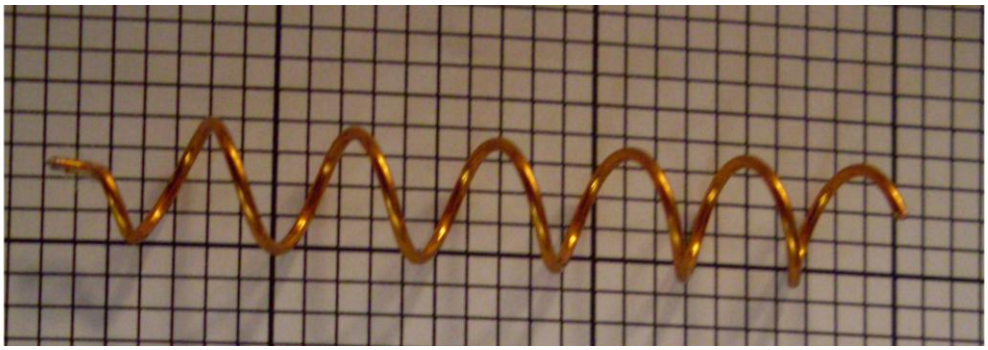

Figure A6.23: Tail with λ = 10 mm; B_o = 2 mm; L_{tail} = 60 mm; no cloth.

Table A6.23.1: Horizontal experiment results with λ = 10 mm; B_o = 2 mm; L_{tail} = 60 mm; no cloth.

t1 [s]	t2 [s]	disp [mm]	vel [mm/s]	mean	stdev	conf
0,00	4,19	2,00	0,477326969			
4,19	9,82	2,00	0,355239787			
25,62	30,41	2,00	0,417536534			
15,80	20,47	2,00	0,428265525			
20,47	25,62	2,00	0,388349515	0,413343666	0,040828601	0,035787189
		rot [1]	rotation rate[Hz]			
4,55	28,25	1,00	0,042194093			
7,66	31,72	1,00	0,04156276			
11,61	35,80	1,00	0,041339396			
14,49	39,03	1,00	0,040749796			
17,12	41,78	1,00	0,0405515	0,041279509	0,000588366	0,000515716
		rot [1]	rotation rate[Hz]			
0,13	2,07	1,00	0,515463918			
2,07	4,07	1,00	0,5			
4,07	6,03	1,00	0,510204082			
6,03	8,00	1,00	0,507614213			
8,00	10,00	1,00	0,5	0,506656442	0,00599485	0,005254621

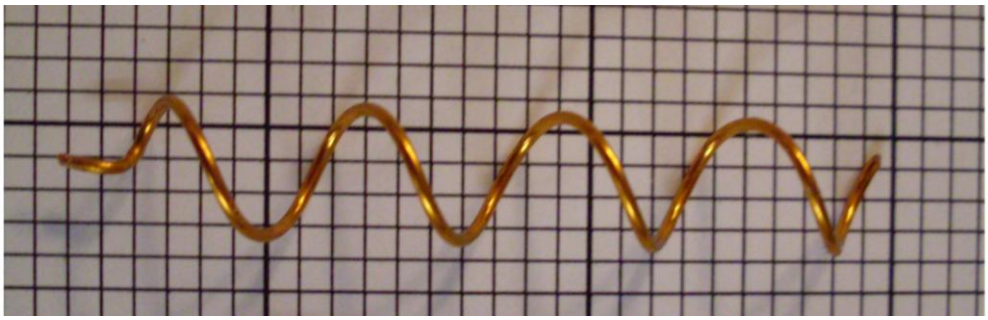

Figure A6.24: Figure with λ = 15 mm; B_o = 2 mm; L_{tail} = 60 mm; no cloth.

Table A6.24.1: Horizontal experiment results with λ = 15 mm; B_o = 2 mm; L_{tail} = 60 mm; no cloth.

t1 [s]	t2 [s]	disp [mm]	vel [mm/s]	mean	stdev	conf
17,38	20,76	2,00	0,591715976			
3,26	6,52	2,00	0,613496933			
6,52	9,65	2,00	0,638977636			
9,65	12,91	2,00	0,613496933			
14,69	17,38	2,00	0,743494424	0,64023638	0,053755062	0,047117524
		rot [1]	rotation rate[Hz]			
2,29	25,70	1,00	0,042716788			
7,12	30,89	1,00	0,042069836			
0,00	23,77	1,00	0,042069836			
10,74	35,00	1,00	0,041220115			
13,17	37,77	1,00	0,040650407	0,041745396	0,000725127	0,00063559
		rot [1]	rotation rate[Hz]			
0,07	1,83	1,00	0,568181818			
1,83	3,60	1,00	0,564971751			
3,60	5,40	1,00	0,555555556			
5,40	7,23	1,00	0,546448087			
7,23	9,03	1,00	0,555555556	0,558142554	0,007714537	0,006761966

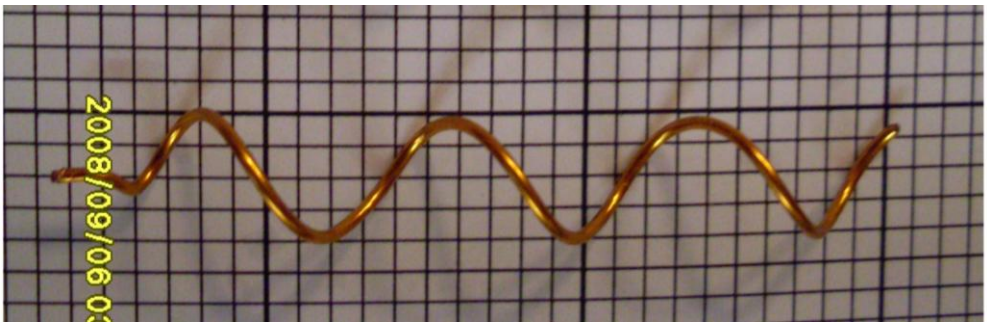

Figure A6.25: Figure with λ = 20 mm; B_o = 2 mm; L_{tail} = 60 mm; no cloth.

Table A6.25.1: Horizontal experiment results with λ = 20 mm; B_o = 2 mm; L_{tail} = 60 mm; no cloth.

t1 [s]	t2 [s]	disp [mm]	vel [mm/s]	mean	stdev	conf
19,95	23,29	2,00	0,598802395			
4,66	7,52	2,00	0,699300699			
7,52	11,35	2,00	0,522193211			
11,35	14,21	2,00	0,699300699			
0,96	11,36	7,00	0,673076923	0,638534786	0,068836293	0,060336563
		rot [1]	rotation rate[Hz]			
3,34	28,07	1,00	0,040436717			
8,24	33,56	1,00	0,039494471			
13,30	38,22	1,00	0,040128411			
15,05	40,97	1,00	0,038580247			
17,22	43,12	1,00	0,038610039	0,039449977	0,000761293	0,00066729
		rot [1]	rotation rate[Hz]			
0,00	1,27	1,00	0,787401575			
1,27	2,60	1,00	0,751879699			
2,60	3,93	1,00	0,751879699			
3,93	5,30	1,00	0,729927007			
5,30	6,63	1,00	0,751879699	0,754593536	0,01847647	0,016195043

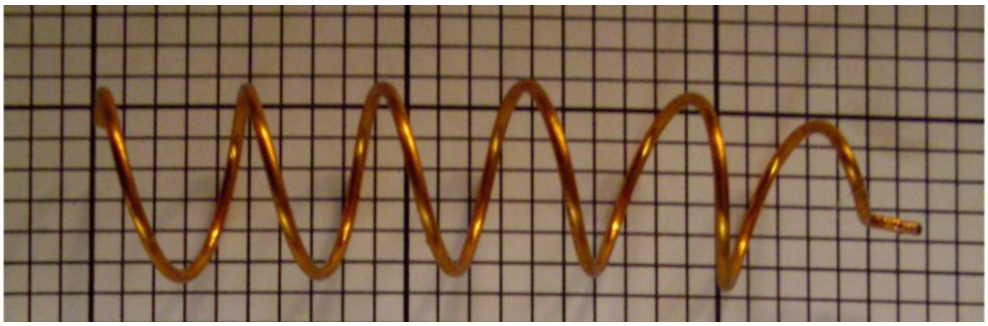

Figure A6.26: Tail with λ = 10 mm; B_o = 3.5 mm; L_{tail} = 60 mm; no cloth.

Table A6.26.1: Horizontal experiment results with λ = 10 mm; B_o = 3.5 mm; L_{tail} = 60 mm; no cloth.

t1 [s]	t2 [s]	disp [mm]	vel [mm/s]	mean	stdev	conf
36,39	41,40	2,00	0,399201597			
10,74	15,39	2,00	0,430107527			
15,39	21,84	2,00	0,310077519			
21,84	30,31	2,00	0,236127509			
30,31	36,39	2,00	0,328947368	0,340892304	0,06845031	0,059998239
		rot [1]	rotation rate[Hz]			
3,34	26,01	1,00	0,04411116			
7,28	30,07	1,00	0,043878894			
10,74	34,25	1,00	0,042535091			
1,07	23,74	1,00	0,04411116			
15,27	38,90	1,00	0,042319086	0,043391078	0,000794592	0,000696478
		rot [1]	rotation rate[Hz]			
2,12	6,80	1,00	0,213675214			
6,80	11,69	1,00	0,204498978			
11,69	16,67	1,00	0,200803213			
16,67	21,60	1,00	0,202839757			
0,00	4,33	1,00	0,230946882	0,210552809	0,011107316	0,009735813

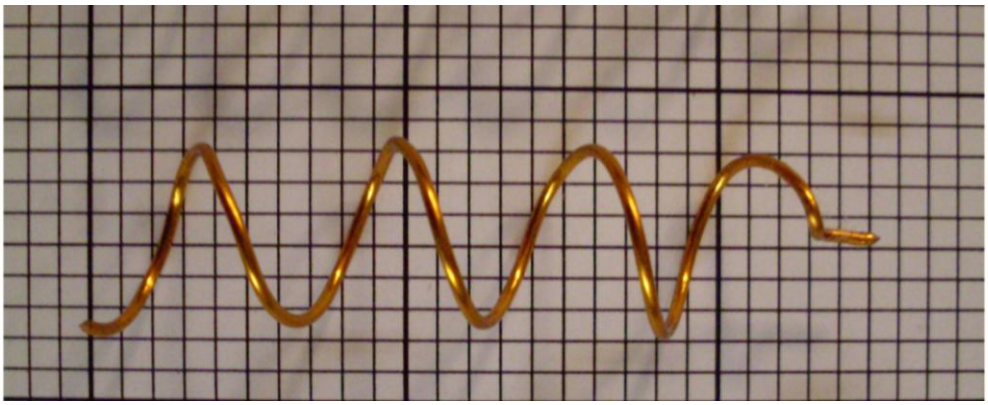

Figure A6.27: Tail with λ = 15 mm; B_o = 3.5 mm; L_{tail} = 60 mm; no cloth.

Table A6.27.1: Horizontal experiment results with λ = 15 mm; B_o = 3.5 mm; L_{tail} = 60 mm; no cloth.

t1 [s]	t2 [s]	disp [mm]	vel [mm/s]	mean	stdev	conf
2,63	6,56	2,00	0,508905852			
23,63	27,56	2,00	0,508905852			
11,93	16,23	2,00	0,465116279			
16,23	19,69	2,00	0,578034682			
19,69	23,63	2,00	0,507614213	0,513715376	0,036283144	0,031802993
		rot [1]	rotation rate[Hz]			
1,07	23,63	1,00	0,044326241			
4,89	27,56	1,00	0,04411116			
7,76	30,78	1,00	0,043440487			
10,54	33,96	1,00	0,042698548			
13,13	36,63	1,00	0,042553191	0,043425926	0,000717087	0,000628543
		rot [1]	rotation rate[Hz]			
1,10	4,44	1,00	0,299401198			
4,44	7,74	1,00	0,303030303			
7,74	11,04	1,00	0,303030303			
11,04	14,60	1,00	0,280898876			
14,60	18,07	1,00	0,288184438	0,294909024	0,008872365	0,007776827

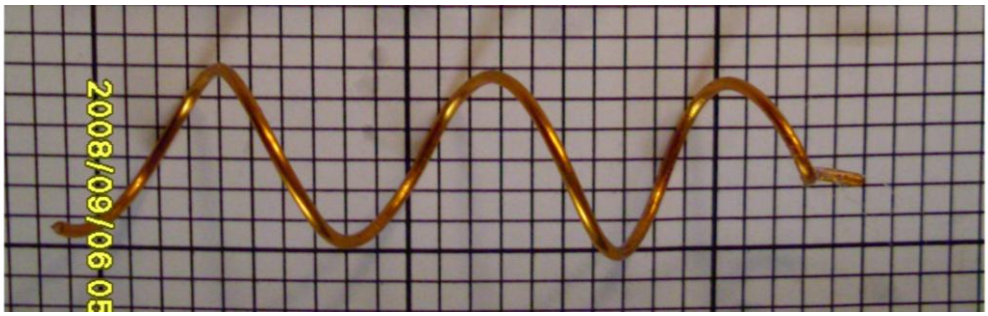

Figure A6.28: Tail with λ = 20 mm; B_o = 3.5 mm; L_{tail} = 60 mm; no cloth.

Table A6.28.1: Horizontal experiment results with λ = 20 mm; B_o = 3.5 mm; L_{tail} = 60 mm; no cloth.

t1 [s]	t2 [s]	disp [mm]	vel [mm/s]	mean	stdev	conf
0,96	4,07	2,00	0,643086817			
4,07	7,07	2,00	0,666666667			
7,07	10,06	2,00	0,668896321			
31,26	34,73	2,00	0,576368876			
13,77	16,65	2,00	0,694444444	0,649892625	0,040198095	0,035234536
		rot [1]	rotation rate[Hz]			
1,79	26,11	1,00	0,041118421			
9,46	34,49	1,00	0,039952058			
5,15	29,94	1,00	0,040338846			
13,77	38,81	1,00	0,039936102			
16,65	41,68	1,00	0,039952058	0,040259497	0,000455559	0,000399308
		rot [1]	rotation rate[Hz]			
1,37	4,17	1,00	0,357142857			
4,17	6,98	1,00	0,355871886			
6,98	9,70	1,00	0,367647059			
9,70	12,49	1,00	0,358422939			
12,49	15,26	1,00	0,36101083	0,360019114	0,004175863	0,003660238

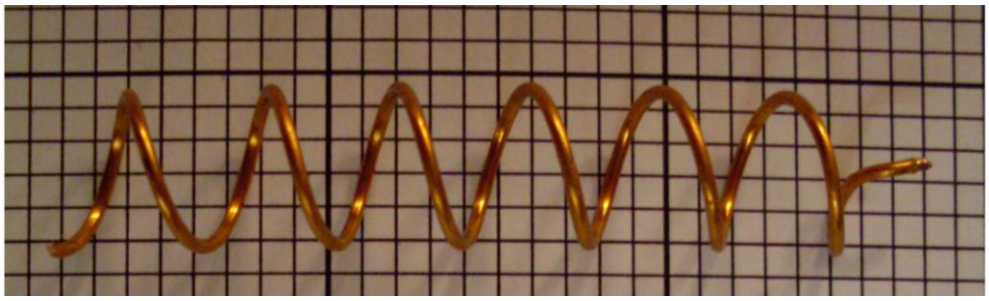

Figure A6.29: Tail with λ = 10 mm; B_o = 2.5 mm; L_{tail} = 60 mm; no cloth.

Table A6.29.1: Horizontal experiment results with λ = 10 mm; B_o = 2.5 mm; L_{tail} = 60 mm; no cloth.

t1 [s]	t2 [s]	disp [mm]	vel [mm/s]	mean	stdev	conf
46,87	53,31	2,00	0,310559006			
6,92	13,12	2,00	0,322580645			
13,12	19,44	2,00	0,316455696			
19,44	25,88	2,00	0,310559006			
25,88	32,08	2,00	0,322580645	0,316547	0,005376434	0,004712566
		rot [1]	rotation rate[Hz]			
2,03	23,26	1,00	0,047103156			
5,96	28,03	1,00	0,045310376			
9,42	31,49	1,00	0,045310376			
13,24	35,30	1,00	0,045330916			
11,33	33,39	1,00	0,045330916	0,045677148	0,000713063	0,000625016
		rot [1]	rotation rate[Hz]			
0,53	3,37	1,00	0,352112676			
3,37	6,23	1,00	0,34965035			
6,23	9,17	1,00	0,340136054			
9,17	12,17	1,00	0,333333333			
12,17	15,17	1,00	0,333333333	0,341713149	0,007925644	0,006947006

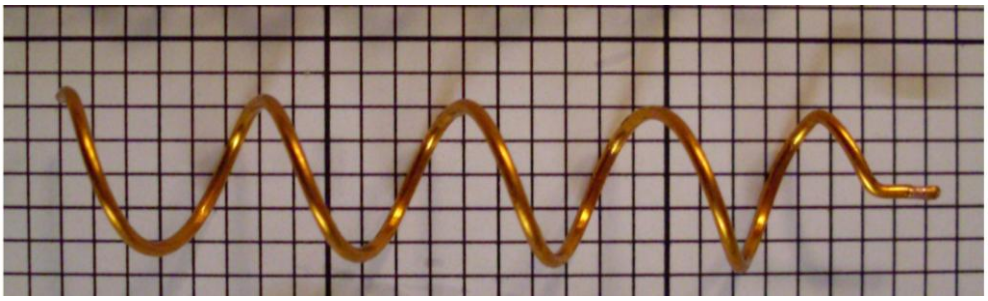

Figure A6.30: Tail with λ = 15 mm; B_o = 2.5 mm; L_{tail} = 60 mm; no cloth.

Table A6.30.1: Horizontal experiment results with λ = 15 mm; B_o = 2.5 mm; L_{tail} = 60 mm; no cloth.

t1 [s]	t2 [s]	disp [mm]	vel [mm/s]	mean	stdev	conf
8,52	25,85	12,00	0,692440854			
5,27	8,26	2,00	0,668896321			
8,26	11,13	2,00	0,696864111			
26,44	29,56	2,00	0,641025641			
8,52	25,85	12,00	0,692440854	0,678333556	0,021082481	0,01847927
		rot [1]	rotation rate[Hz]			
2,51	27,83	1,00	0,039494471			
6,94	32,22	1,00	0,039556962			
9,93	35,42	1,00	0,039231071			
12,56	38,05	1,00	0,039231071			
14,60	40,33	1,00	0,038865138	0,039275743	0,00024475	0,000214529
		rot [1]	rotation rate[Hz]			
0,90	3,11	1,00	0,452488688			
3,11	5,37	1,00	0,442477876			
5,37	7,63	1,00	0,442477876			
7,63	9,90	1,00	0,440528634			
9,90	12,21	1,00	0,432900433	0,442174701	0,00624954	0,005477862

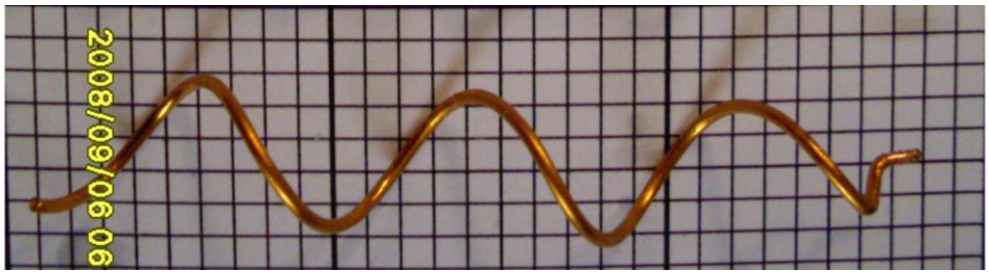

Figure A6.31: Tail with λ = 20 mm; B_o = 2.5 mm; L_{tail} = 60 mm; no cloth.

Table A6.31.1: Horizontal experiment results with λ = 20 mm; B_o = 2.5 mm; L_{tail} = 60 mm; no cloth.

t1 [s]	t2 [s]	disp [mm]	vel [mm/s]	mean	stdev	conf
1,07	3,10	2,00	0,985221675			
3,10	4,78	2,00	1,19047619			
4,78	6,80	2,00	0,99009901			
6,80	8,95	2,00	0,930232558			
8,95	11,10	2,00	0,930232558	1,005252398	0,096119364	0,08425079
		rot [1]	rotation rate[Hz]			
0,00	26,02	1,00	0,038431975			
8,00	35,34	1,00	0,036576445			
11,10	38,56	1,00	0,036416606			
4,42	31,40	1,00	0,037064492			
21,25	49,18	1,00	0,035803795	0,036858663	0,000883797	0,000774668
		rot [1]	rotation rate[Hz]			
0,60	2,27	1,00	0,598802395			
2,27	3,94	1,00	0,598802395			
3,94	5,66	1,00	0,581395349			
5,66	7,33	1,00	0,598802395			
7,33	9,07	1,00	0,574712644	0,590503036	0,010381951	0,009100014

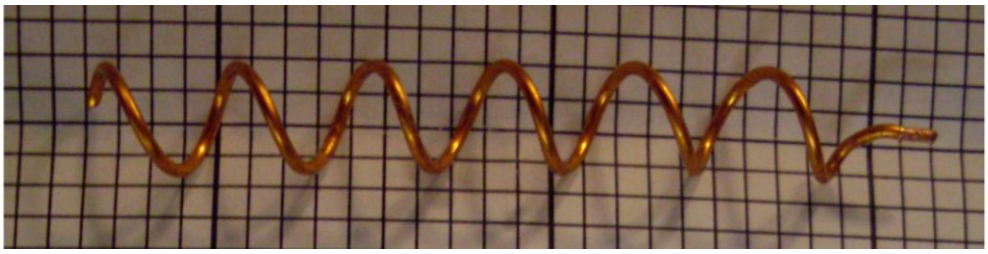

Figure A6.32: Tail with λ = 10 mm; B_o = 1.5 mm; L_{tail} = 60 mm; no cloth.

Table A6.32.1: Horizontal experiment results with λ = 10 mm; B_o = 1.5 mm; L_{tail} = 60mm; no cloth.

t1 [s]	t2 [s]	disp [mm]	vel [mm/s]	mean	stdev	conf
2,86	27,19	12,00	0,493218249			
8,71	13,00	2,00	0,466200466			
13,00	17,65	2,00	0,430107527			
17,65	21,94	2,00	0,466200466			
2,86	12,88	7,00	0,698602794	0,510865901	0,095988018	0,084135661
		rot [1]	rotation rate[Hz]			
1,31	22,78	1,00	0,046576619			
5,25	26,60	1,00	0,046838407			
11,69	33,75	1,00	0,045330916			
14,07	35,78	1,00	0,046061723			
5,01	26,95	1,00	0,045578851	0,046077303	0,000571732	0,000501136
		rot [1]	rotation rate[Hz]			
0,43	1,86	1,00	0,699300699			
1,86	3,22	1,00	0,735294118			
3,22	4,58	1,00	0,735294118			
4,58	5,98	1,00	0,714285714			
5,98	7,39	1,00	0,709219858	0,718678901	0,014397355	0,012619606

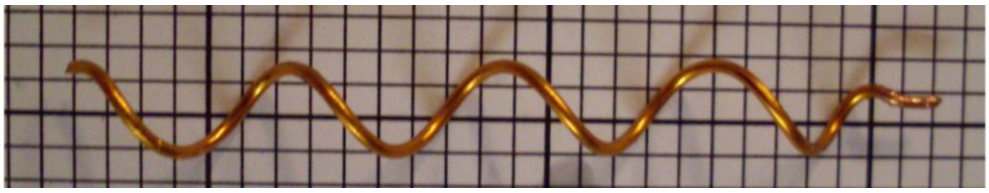

Figure A6.33: Tail with λ = 15 mm; B_o = 1.5 mm; L_{tail} = 60 mm; no cloth.

Table A6.33.1: Horizontal experiment results with λ = 15 mm; B_o = 1.5 mm; L_{tail} = 60mm; no cloth.

t1 [s]	t2 [s]	disp [mm]	vel [mm/s]	mean	stdev	conf
1,44	35,23	25,00	0,739863865			
5,89	9,26	2,00	0,59347181			
9,26	12,50	2,00	0,617283951			
12,50	15,51	2,00	0,664451827			
15,36	18,48	2,00	0,641025641	0,651219419	0,050245895	0,04404166
		rot [1]	rotation rate[Hz]			
0,36	27,17	1,00	0,037299515			
5,05	31,62	1,00	0,037636432			
9,26	36,04	1,00	0,037341299			
11,78	38,59	1,00	0,037299515			
14,09	40,85	1,00	0,037369208	0,037389194	0,000126416	0,000110806
		rot [1]	rotation rate[Hz]			
0,43	1,37	1,00	1,063829787			
1,37	2,30	1,00	1,075268817			
2,30	3,23	1,00	1,075268817			
3,23	4,17	1,00	1,063829787			
4,17	5,10	1,00	1,075268817	1,070693205	0,005603957	0,004911995

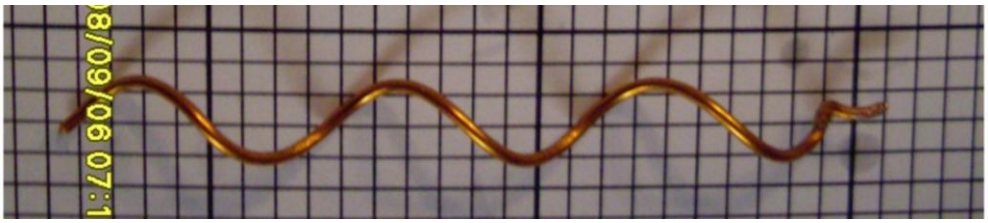

Figure A6.34: Tail with λ = 20 mm; B_o = 1.5 mm; L_{tail} = 60 mm; no cloth.

Table A6.34.1: Horizontal experiment results with λ = 20 mm; B_o = 1.5 mm; L_{tail} = 60mm; no cloth.

t1 [s]	t2 [s]	disp [mm]	vel [mm/s]	mean	stdev	conf
0,83	6,80	4,00	0,67001675			
6,92	9,90	2,00	0,67114094			
0,83	3,94	2,00	0,643086817			
3,94	6,80	2,00	0,699300699			
6,80	10,14	2,00	0,598802395	0,65646952	0,033875897	0,029692987
		rot [1]	rotation rate[Hz]			
0,00	31,25	1,00	0,032			
3,94	35,54	1,00	0,03164557			
9,06	40,55	1,00	0,031756113			
18,84	50,81	1,00	0,031279324			
14,31	46,04	1,00	0,031515916	0,031639385	0,000240248	0,000210583
		rot [1]	rotation rate[Hz]			
0,00	0,83	1,00	1,204819277			
0,83	1,63	1,00	1,25			
1,63	2,47	1,00	1,19047619			
2,47	3,27	1,00	1,25			
3,27	4,07	1,00	1,25	1,229059094	0,026045244	0,022829244

APPENDIX 7: Prescribed ALE-Mesh Implementation for Unbounded Viscous Medium Study

Arbitrary Lagrangian-Eulerian method (Duarte *et al*., 2004) is used to handle mesh deformation in time-dependent swimmer simulations. The rigid-body translation vector of the swimmer and the stretch effect of its tail on the surrounding mesh require mesh deformation, i.e. node displacement, handled between moving and stationary boundaries. The mesh nodes on the swimmer surface move with the swimmer, whereas the mesh nodes on the channel boundaries stay stationary at all times.

One can set the commercial package COMSOL to solve the mesh deformations at the expense of increased degree-of-freedom to solve and further numerical stiffness introduced to the problem. However, a more safe approach is to prescribe the mesh deformation within the fluid domain as a geometric function of the channel and swimmer boundaries. To be more precise, nodes inside a certain volume around the swimmer moves with the swimmer, while the translation effect linearly fades towards the channel boundaries outside that volume. Prescribed mesh deformation is demonstrated in Fig. A7.1.

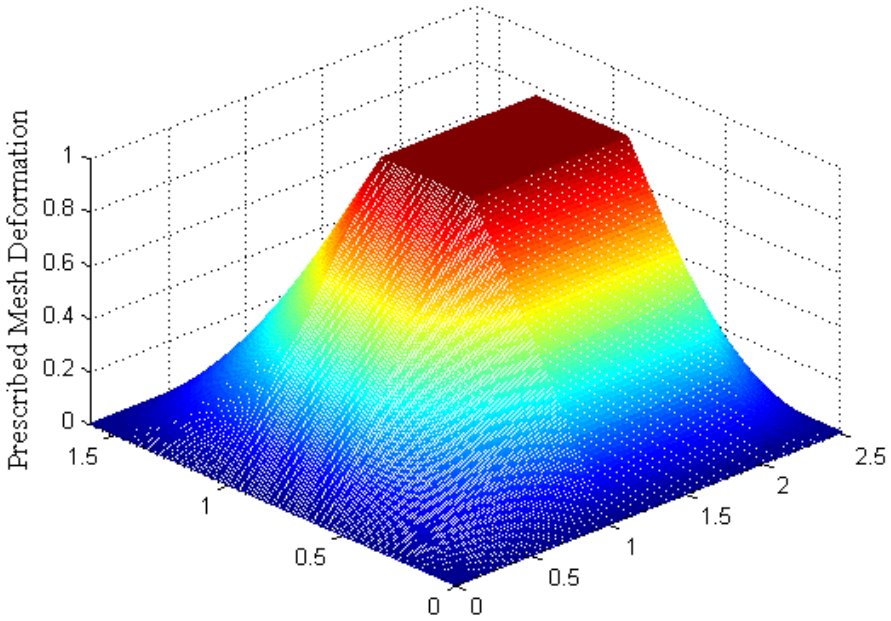

Figure A7.1: Prescribed mesh deformation for rigid-body translations: The red zone moves with the swimmer and stretching effect fades towards the channel boundaries.

A similar prescribed mesh deformation is formulated for the wave propagation on the tail, either rotation or deformation. Thus, as a result of superimposed deformation effect, mesh nodes on the tail deform with the tail, and simultaneously translate with the swimmer. The wave propagation effect dies out immediately at the revolute joint between body and tail; however, fades linearly towards the prescribed volume undergoing rigid-body translations with the swimmer. Prescribed mesh deformation on the tail is depicted in Fig. A7.2. The overall prescribed mesh deformation zones are illustrated in Fig. A7.3: for the sake of clarity, the zones presented are calculated for a planar wave propagating swimmer with zero instantaneous lateral translation.

Lastly, Fig. A7.4 presents the meshing on the tail boundaries and stretching effect on the mesh near a boundary carrying out planar wave propagations. Further detail on mesh deformation can be found in (Duarte *et al*., 2004; Tabak, 2007b; COMSOL AB, 2010).

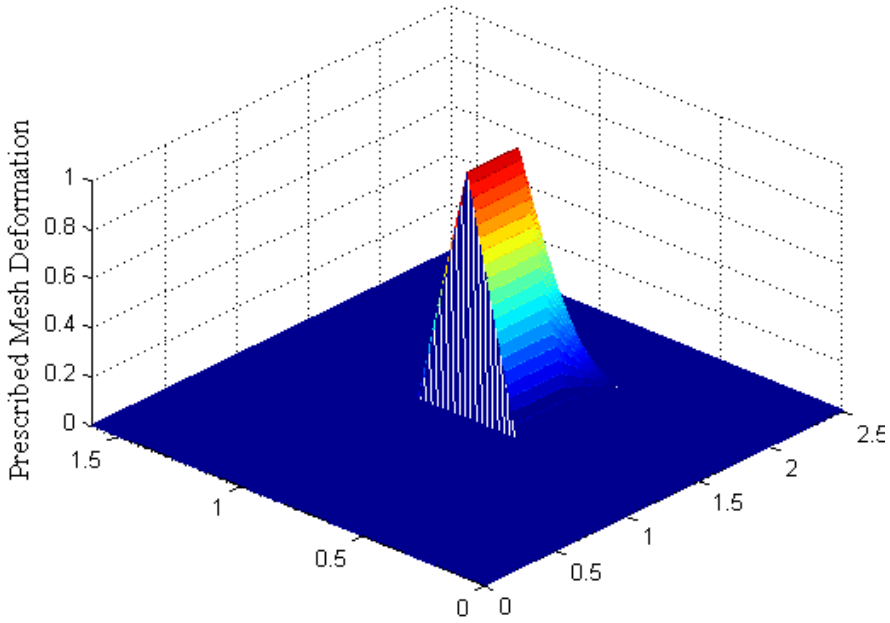

Figure A7.2: Mesh deformation for wave propagation: The red zone moves with the tail boundaries and stretching effect fades away from it; however, abruptly halts at the joint between the body and tail.

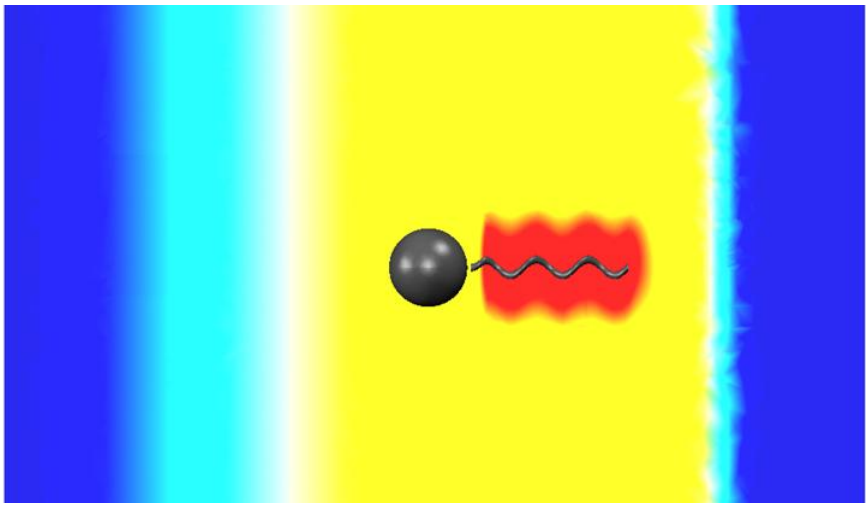

Figure A7.3: Superimposed mesh deformation zones illustrated on a slice with a swimmer propagating plane waves.

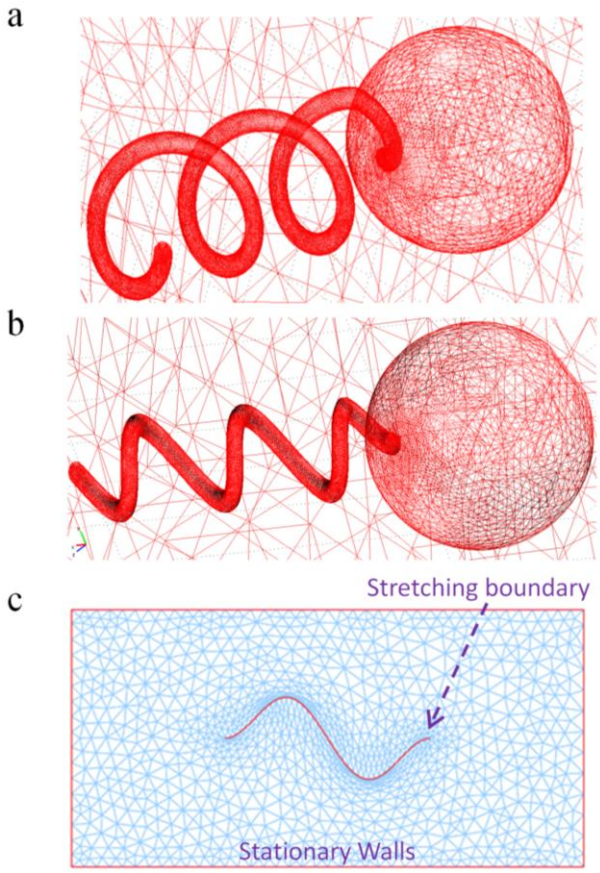

Figure A7.4: Boundary meshing: Swimmer mesh for helical wave propagation (a); swimmer mesh for planar wave propagation (b); deforming mesh with respect to a waving boundary confined with stationary boundaries (c).

APPENDIX 8: Stokeslet-Based Solutions Presented by Lighthill and the Asymptotic Solutions of Stokesian Flows Presented by Felderhof

Stokeslet functions, S, represent the spatial effect of point forces known as singularities in radial and azimuthal (transverse) directions, and can be embedded in the governing equation for a Stokesian flow as depicted in Eq. (8.1) (Lighthill, 1976). Stokeslet based analysis presented by Lighthill (1976), which was carried out for an isolated helical swimmer without a body in an unbounded medium, includes periodic integrals of the form, which are depicted in Fig. A8.1. Here, the flow field was postulated in terms of the Stokeslets so that the force field induced by the unit length of the rotating tail was obtained in symbolic form as follows (Lighthill, 1976):

$$\mathrm{S} - \nabla p + \mu \nabla^2 \mathbf{U} = 0 \,. \tag{A8.1}$$

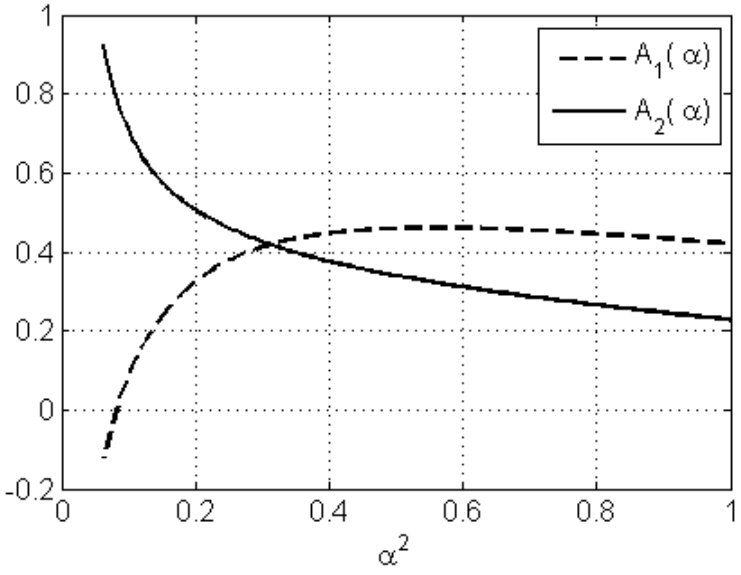

Figure A8.1: Periodic integrals $A_1(\alpha)$ and $A_2(\alpha)$ with respect to α^2.

$$\phi = \left[\alpha^2\theta^2 + 2(1-\alpha^2)(1-\cos(\theta))\right]^{3/2}, \tag{A8.2}$$

$$\varepsilon = 5.2\,\frac{r_{tail}\alpha}{\lambda}, \tag{A8.3}$$

$$A_1(\alpha) = \ln\varepsilon + \int_{\varepsilon}^{\infty} \frac{\theta\sin(\theta)}{\phi}\,d\theta, \tag{A8.4}$$

$$A_2(\alpha) = \ln\varepsilon + \int_{\varepsilon}^{\infty} \frac{\sin^2(\theta)}{\phi}\,d\theta. \tag{A8.5}$$

Furthermore, Lighthill has extended the analysis for helical swimmers with a body to compensate in the hydrodynamic stress analysis, also referred as c_x approach in this text based on the selected direction of swim. His method provided a set of equations to directly calculate the forward velocity and body rotation rate assuming lateral velocities are negligible. The correction functions are formulated as follows:

$$C_U = \frac{1}{\left(1+0.5\frac{D_{T,x}\psi D_{body}}{L_{tail}}\right)}, \tag{A8.6}$$

$$C_\Omega = \left(1+0.5\frac{D_{T,x}\Psi D_{body}}{L_{tail}}\right)C_U, \tag{A8.7}$$

$$\begin{aligned}\Psi = 1.5\,[&2-\alpha^2-3\alpha^{-1}+2\alpha^{-1}\ln(kL_{tail})-(1+\alpha^2)\ln(\varepsilon)-2A_3(\alpha)\\ &-(1-\alpha^2)A_1(\alpha)]\end{aligned}, \tag{A8.8}$$

$$\psi = \Psi - 1.5\alpha^2(1-\alpha^2)\left[-1-\ln(\varepsilon)+A_1(\alpha)\right]^2\chi, \tag{A8.9}$$

$$\chi = \frac{1}{\left[-(1-\alpha^2)-(2-\alpha^2)\ln(\varepsilon)+\alpha^2 A_1(\alpha)+2(1-\alpha^2)A_2(\alpha)\right]}, \tag{A8.10}$$

$$A_3(\alpha) = -\frac{\ln(a^2)}{\alpha} + \ln\varepsilon + \int_{-a}^{-\varepsilon} \frac{0.5}{\phi^{1/3}}\, d\theta + \int_{\varepsilon}^{a} \frac{0.5}{\phi^{1/3}}\, d\theta, \tag{A8.11}$$

with an integration limit of

$$a = \pi L_{tail} / \lambda \tag{A8.12}$$

where α is the ratio of apparent length to actual length of the tail, $D_{T,x}$ is the translational drag coefficient of the swimming robot's body in the **x**-axis, and $k=2\pi/\lambda$. Here, $A_{\{1,2,3\}}$ are periodic integrals of the flow fields signified by local Stokeslet functions throughout the tail, χ is the dimensionless helix torque, Ψ and ψ are velocity reduction functions, C_U and C_Ω are translation and rotation rate corrections. Exact forms of the integrals, $A_{\{1,2,3\}}$, can be found in (Lighthill, 1976). The periodic integral A_3 is depicted in Fig. A8.2.

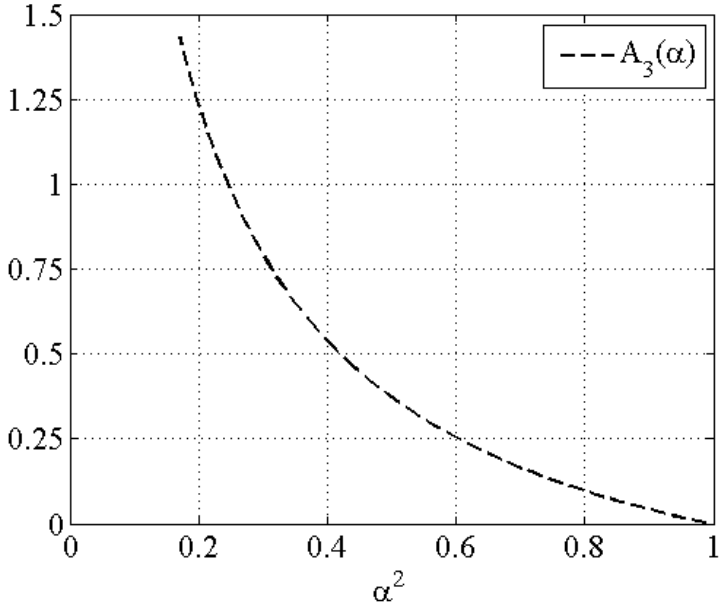

Figure A8.2: Periodic integral $A_3(\alpha)$ with respect to α^2.

Felderhof's (2010) analysis, which is based on representation of induced flow fields with harmonic flow field equations, is focused on rotating infinite length bodies with helical geometries confined to cylindrical channels filled with viscous fluids. The induced flow field between channel walls of radius R_{ch} and a helical body of minor radius r_{tail} and major radius of B_o, which is rotating with an angular frequency of ω, is represented by modified Bessel functions of the first kind, $I_{\{0,1\}}$, and modified Bessel functions of the second kind, $K_{\{0,1\}}$, (Bowman, 1958) embedded in the coefficient matrix obtained by boundary conditions as follows:

$$A_{11}=(kI_0(kr_{tail})-I_1(kr_{tail})/r_{tail})\sin(kx-\omega t), \tag{A8.13}$$

$$A_{12}=(-kK_0(kr_{tail})-K_1(kr_{tail})/r_{tail})\sin(kx-\omega t), \tag{A8.14}$$

$$A_{13}=I_1(kr_{tail})\sin(kx-\omega t)/r_{tail}, \tag{A8.15}$$

$$A_{14}=K_1(kr_{tail})\sin(kx-\omega t)/r_{tail}, \tag{A8.16}$$

$$A_{15}=\left(\left(k^2+\frac{2}{r_{tail}^2}\right)I_1(kr_{tail})-kI_0(kr_{tail})/r_{tail}\right)r_{tail}\sin(kx-\omega t), \tag{A8.17}$$

$$A_{16}=\left(\left(k^2+\frac{2}{r_{tail}^2}\right)K_1(kr_{tail})-kK_0(kr_{tail})/r_{tail}\right)r_{tail}\sin(kx-\omega t), \tag{A8.18}$$

$$A_{21}=(kI_0(kR_{ch})-I_1(kR_{ch})/R_{ch})\sin(kx-\omega t), \tag{A8.19}$$

$$A_{22}=(-kK_0(kR_{ch})-K_1(kR_{ch})/R_{ch})\sin(kx-\omega t), \tag{A8.20}$$

$$A_{23}=I_1(kR_{ch})\sin(kx-\omega t)/R_{ch}, \tag{A8.21}$$

$$A_{24}=K_1(kR_{ch})\sin(kx-\omega t)/R_{ch}\,, \tag{A8.22}$$

$$A_{25}=\left(\left(k^2+\frac{2}{R_{ch}^2}\right)I_1(kR_{ch})-kI_0(kR_{ch})/R_{ch}\right)R_{ch}\sin(kx-\omega t)\,, \tag{A8.23}$$

$$A_{26}=\left(\left(k^2+\frac{2}{R_{ch}^2}\right)K_1(kR_{ch})-kK_0(kR_{ch})/R_{ch}\right)R_{ch}\sin(kx-\omega t)\,, \tag{A8.24}$$

$$A_{31}=I_1(kr_{tail})\cos(kx-\omega t)/r_{tail}\,, \tag{A8.25}$$

$$A_{32}=K_1(kr_{tail})\cos(kx-\omega t)/r_{tail}\,, \tag{A8.26}$$

$$A_{33}=(kI_0(kr_{tail})-I_1(kr_{tail})/r_{tail})\cos(kx-\omega t)\,, \tag{A8.27}$$

$$A_{34}=(-kK_0(kr_{tail})-K_1(kr_{tail})/r_{tail})\cos(kx-\omega t)\,, \tag{A8.28}$$

$$A_{35}=A_{33}-A_{31}, \tag{A8.29}$$

$$A_{36}=A_{34}-A_{32}\,, \tag{A8.30}$$

$$A_{41}=I_1(kR_{ch})\cos(kx-\omega t)/R_{ch}\,, \tag{A8.31}$$

$$A_{42}=K_1(kR_{ch})\cos(kx-\omega t)/R_{ch}\,, \tag{A8.32}$$

$$A_{43}=(kI_0(kR_{ch})-I_1(kR_{ch})/R_{ch})\cos(kx-\omega t)\,, \tag{A8.33}$$

$$A_{44}=(-kK_0(kR_{ch})-K_1(kR_{ch})/R_{ch})\cos(kx-\omega t)\,, \tag{A8.34}$$

$$A_{45}=A_{43}-A_{41}, \tag{A8.35}$$

$$A_{46}=A_{44}-A_{42}, \tag{A8.36}$$

$$A_{51}=I_1(kr_{tail})k\cos(kx-\omega t), \tag{A8.37}$$

$$A_{52}=K_1(kr_{tail})k\cos(kx-\omega t), \tag{A8.38}$$

$$A_{53}=0, \tag{A8.39}$$

$$A_{54}=0, \tag{A8.40}$$

$$A_{55}=k^2 r_{tail} I_0(kr_{tail})\cos(kx-\omega t), \tag{A8.41}$$

$$A_{56}=-k^2 r_{tail} K_0(kr_{tail})\cos(kx-\omega t), \tag{A8.42}$$

$$A_{61}=I_1(kR_{ch})k\cos(kx-\omega t), \tag{A8.43}$$

$$A_{62}=K_1(kR_{ch})k\cos(kx-\omega t), \tag{A8.44}$$

$$A_{63}=0, \tag{A8.45}$$

$$A_{64}=0, \tag{A8.46}$$

$$A_{65}=k^2 R_{ch} I_0(kR_{ch})\cos(kx-\omega t), \tag{A8.47}$$

$$A_{66}=-k^2 R_{ch} K_0(kR_{ch})\cos(kx-\omega t), \tag{A8.48}$$

and inverse of the coefficient matrix is used to calculate:

$$A_{n1} = A_{11}^{-1} B_o \omega \sin(kx - \omega t) + A_{13}^{-1} B_o \omega \cos(kx - \omega t), \tag{A8.49}$$

$$A_{n2} = A_{21}^{-1} B_o \omega \sin(kx - \omega t) + A_{23}^{-1} B_o \omega \cos(kx - \omega t), \tag{A8.50}$$

$$A_{n3} = A_{31}^{-1} B_o \omega \sin(kx - \omega t) + A_{33}^{-1} B_o \omega \cos(kx - \omega t), \tag{A8.51}$$

$$A_{n4} = A_{41}^{-1} B_o \omega \sin(kx - \omega t) + A_{43}^{-1} B_o \omega \cos(kx - \omega t), \tag{A8.52}$$

$$A_{n5} = A_{51}^{-1} B_o \omega \sin(kx - \omega t) + A_{53}^{-1} B_o \omega \cos(kx - \omega t), \tag{A8.53}$$

$$A_{n6} = A_{61}^{-1} B_o \omega \sin(kx - \omega t) + A_{63}^{-1} B_o \omega \cos(kx - \omega t), \tag{A8.54}$$

which are used to calculate the amplitude of the velocity components as:

$$\begin{aligned} v_1 = & k \cos(kx - \omega t)\{A_{n1}(kI_0(kr_{tail}) - I_1(kr_{tail})/r_{tail}) + A_{n2}(-kK_0(kr_{tail}) - K_1(kr_{tail})/r_{tail}) \\ & + A_{n5}\left[2(kI_0(kr_{tail}) - I_1(kr_{tail})/r_{tail}) + r_{tail}\left(\left(k^2 + \frac{2}{r_{tail}^2}\right)I_1(kr_{tail}) - kI_0(kr_{tail})/r_{tail}\right)\right] \\ & + A_{n6}\left[2(-kK_0(kr_{tail}) - K_1(kr_{tail})/r_{tail}) + r_{tail}\left(\left(k^2 + \frac{2}{r_{tail}^2}\right)K_1(kr_{tail}) - kK_0(kr_{tail})/r_{tail}\right)\right]\} \end{aligned}, \tag{A8.55}$$

$$\begin{aligned} v_2 = -k \sin(kx - \omega t)\big[& A_{n1} I_1(kr_{tail}) + A_{n2} K_1(kr_{tail}) \\ & + A_{n5}(I_1(kr_{tail}) + r_{tail}(kI_0(kr_{tail}) - I_1(kr_{tail})/r_{tail})) \\ & + A_{n6}(K_1(kr_{tail}) + r_{tail}(-kK_0(kr_{tail}) - K_1(kr_{tail})/r_{tail}))\big] \end{aligned}, \tag{A8.56}$$

and finally used to express the time-dependent forward velocity equation (see Eq. (A8.57)). Forward velocity equation will be normalized in time-domain to determine the average forward propulsion velocity of a helical swimmer concentrically confined in a cylindrical channel filled with a viscous fluid:

$$U_x(t) = \Upsilon_x^{-1}(\mathrm{v}_1 \mathrm{B}_o \cos(kx - \omega t) - \mathrm{v}_2 \mathrm{B}_o \sin(kx - \omega t)/r_{tail}), \quad \text{(A8.57)}$$

where Υ_x is the interaction coefficient added later on, which is taking the dissipating effect of the presence of the body into account.

BIBLIOGRAPHY

Abbott, J.J., Lagomarsion, M.C., Zhang, L., Dong, L., Nelson, B.J., "How should microrobots swim?", The International Journal of Robotic Research, Vol. 28, No. 11-12, pp. 1434-1447, 2009.

Alexander, G.P., Yeomans, J.M., "Hydrodynamic interactions at low Reynolds number", Experimental Mechanics, Vol. 50, pp. 1283-1292, 2010.

Andreev, V.M., Kaventsky, A.G., Kalinovsky, V.S., Khvostikov, Larionov, V.R., Rumyantsev, V.D., Shvarts, M.Z., Yakimova, E.V., Ustinov, V.A., "Tritium-powered betacells based on $Al_x Ga_{1-x} As$", Transactions of IEEE, pp.1253-1256, 2000.

Apex Microtechnology Corporation, High voltage power operational amplifiers data sheet, 2006, http://www.cirrus.com/en/pubs/proDatasheet/PA88U_P.pdf, Retrieved from World Wide Web on 07.01.2012.

Arena, P., Bonomo, C., Fortuna, L., Frasca, M., Graziani, S., "Design and control of an IPMC wormlike robot", IEEE Transactions on Systems, Man, and Cybernetics, Part B: Cybernetics, Vol. 36, No. 5, pp. 1044-1052, 2006.

Armitage, J.P., Pitta, T.P., Vigeant, M.A.-S., Packer, H.L., Ford, R.M., "Transformations in flagellar structure of Rhodobacter *sphaeroids* and possible relationship to changes in swimming speed", Journal of Bacteriology, Vol. 181, No. 16, pp. 4825-4833, 1999.

Balasubramanian, S., Kagan, D., Hu, C.-M.J., Campuzano, S., Lobo-Castañon, M.J., Lim, N., Kang, D.Y., Zimmerman, M., Zhang, L., Wang, J., "Micromachine-enabled capture and isolation of cancer cells in complex media", Angewandte Chemie International Edition, Vol. 50, Issue 18, pp. 4161-4164, 2011.

Baraff, D., "Physically based modeling, rigid body simulation", Course Notes, ACM SIGGRAPH, 2001.

Batchelor, G.K., "An Introduction to Fluid Dynamics", Cambridge University Press, USA, Ch. 4, 2005.

Bates, J.B., Gruzalski, G.R., Luck, C.F., "Rechargeable solid state lithium microbatteries", In: The IEEE Conference on Micro Electro Mechanical Systems, Fort Lauderdale, FL, USA, 7-10 February, 1993.

Behkam, B., Sitti, M., "E. *Coli* inspired propulsion for swimming microrobots", In: The ASME International Mechanical Engineering Congress and Exposition, Anaheim CA, USA, 13-19 November 2004.

Behkam, B., Sitti, M., "Design methodology for biomimetic propulsion of miniature swimming robots", ASME Journal of Dynamic Systems, Measurement, and Control, Vol. 128, No. 1, pp. 36-43, 2006a.

Behkam, B., Sitti, M., "Towards hybrid swimming microrobots: bacteria assisted propulsion of polystyrene beads", In: The 28th IEEE Annual International Conference on Engineering in Medicine and Biology Society, 30 August - 3 September, 2006b.

Behkam B., Sitti, M., "Bacterial flagella-based propulsion and on/off motion control of microscale objects", Applied Physics Letters, Vol. 90, 023902(3pp), 2007.

Belovs, M., Cébers, A., "Nonlinear dynamics of semiflexible magnetic filaments in an AC magnetic field", Physical Review, Series E, Vol. 73, 2006.

Berg, H.C., "Random Walks in Biology", Princeton University Press, USA, Ch. 1, 1993.

Berg, H.C., "Motile behavior of bacteria", Physics Today, Vol. 53, Issue 1, pp. 24-29, 2000.

Berg, H.C., "The rotary motor of bacterial flagella", Annual Review of Biochemistry, Vol. 72, pp. 19-54, 2003.

Bermejo, S., Ortega, P., Jimenez, J.J., Castaner, L., "Response of c-Si PV arrays under monochromatic light for MEMS power supply", Journal of Micromechanics and Microengineering, Vol. 15, pp. 1446-1453, 2005.

Berry, R.M., Berg, H.C., "Torque generated by the bacterial flagellar motor close to stall", Biophysical Journal, Vol. 71, pp. 3501-3510, 1996.

Bhalerao, S.A., Chaudhary, A.V., Deshmukh, R.B., Patrikar, R.M., "Powering wireless sensor nodes using ambient RF energy", In: The IEEE Conference on Systems, Man, and Cybernetics, Taipei, Taiwan, 8-11 October, 2006.

Blake, J.R., "Singularities of viscous flow. Part II: Applications to slender body theory", Journal of Engineering Mathematics, Vol. 8, No. 2, pp. 113-124, 1974.

Blanchard, J., Henderson, D., Lal, A., "A nuclear microbattery for MEMS devices", Final Scientific/Technical Report, U.S. Department of Energy Award No. DE-FG07-99ID13781, 2002.

Bogue, R., "The development of medical microrobots: A review of progress", Industrial Robot: An International Journal, Vol. 35, Issue 4, pp. 294-299, 2008.

Bonilla, F.A., Kleinfelter, N., Cushman, J.H., "Microfluidic aspects of adhesive microbial dynamics: A numerical exploration of flow-cell geometry, Brownian dynamics, and sticky boundaries", Advances in Water Resources, Vol. 30, pp. 1680-1695, 2007.

Bourot, J.M., "On the numerical computation of the optimum profile in Stokes flow", Journal of Fluid Mechanics, Vol. 65, No. 3, pp. 513-515, 1974.

Bowman, F., "Introduction to Bessel Functions", Dover Publications, Inc., New York, Ch 3, 1958.

Braum, J., Fermvik, L., Stenback, A., "Theory and performance of a tritium battery for the microwatt range", Journal of Physics, Series E: Scientific Instruments, Vol. 6, pp. 727-731, 1973.

Brennen, C., Winet, H., "Fluid mechanics of propulsion by cilia and flagella", Annual Review of Fluid Mechanics, Vol. 9, pp. 339-398, 1977.

Brokaw, C.J., "Non-sinusoidal bending waves of sperm flagella", The Journal of Experimental Biology, Vol. 43, pp. 155-169, 1965.

Brokaw, C.J., "Effects of increased viscosity on the movements of some invertebrate spermatozoa", The Journal of Experimental Biology, Vol. 45, pp. 113-139, pp. 113-139, 1966.

Brown, M.T., Delalez, N.J., Armitage, J.P., "Protein dynamics and mechanisms controlling the rotational behavior of the bacterial flagellar motor", Current Opinion in Microbiology, Vol. 14, pp. 734-740, 2011.

Bruck, S., "Interactions of synthetic and natural surfaces with blood in the physiological environment", Journal of Biomedical Materials Research, Part A, Vol. 11, No. 1, pp. 1-21, 1977.

Camassa, R., Leiterman, T.J., Mclaughlin, R.M., "Trajectory and flow properties for a rod spinning in a viscous fluid. Part 1: An exact solution", Journal of Fluid Mechanics, Vol. 612, pp. 153-200, 2008.

Cappelleri, D.J., Frecker, M.I., Simpson, T.W., "Design of a PZT bimorph actuator using a metamodel-based approach", Transactions of ASME, Vol. 124, pp. 354-357, 2002.

Chakraborty, A., Gopalakrishnan, S., Kausel, E., "Wave propagation analysis in inhomogeneous piezo-composite layer by the thin-layer method", International Journal for Numerical Methods in Engineering, Vol. 54, pp. 567-598, 2005.

Chattopadhyay, S., Wu, X.-L., "The effect of long-range hydrodynamic interaction on the swimming of a single bacterium", Biophysical Journal, Vol. 96, pp. 2023-2028, 2009.

Chen, B., Jiang, S., Liu, Y., Yang, Y., Chen, S., "Research on the kinematic properties of a sperm-like swimming micro robot", Journal of Bionic Engineering, Vol. 7, pp. S123-S129, 2010.

Cheng, Y.-T., Lin, L., Najafi, K., "A hermetic glass-silicon package formed using localized aluminum/silicon-glass bonding", Journal of Microelectromechanical Systems Vol. 10, No. 3, pp. 392-399, 2001.

Childress, S., "Mechanics of Swimming and Flying", Cambridge University Press, NY, Ch. 4, 1981.

Chwang, A.T., Wu, T.Y.-T., "Hydromechanics of low-Reynolds-number flow. Part2: Singularity method for Stokes flows", Journal of Fluid Mechanics, Vol. 67, Part 4, pp. 787-815, 1975.

Cipparrone, G., Hernandez, R.J., Pagliusi, P., Provenzano, C., "Magnus force effect in optical manipulation", Physical Review, Series A, Vol. 84, No. 1, 015802 (4pp), 2011.

Corkidi, C., Taboada, B., Wood, C.D., Guerrero, A., Darszon, A., "Tracking sperm in three-dimensions", Biochemical and Biophysical Research Communications, Vol. 373, pp. 125-129, 2008.

Costabel, M., “Principles of boundary element methods”, Finite Elements in Physics Course Notes, Lausanne, 1-10 September, 1986.

Crenshaw, H.C., “A new look at locomotion in microorganisms: Rotating and translating”, American Zoologist, Vol. 36, pp. 608-618, 1996.

De la Torre, J.G., Bloomfield, V.A., “Hydrodynamic theory of swimming of flagellated microorganisms,” Biophysical Journal, Vol. 20, pp. 49-67, 1977.

Döpper, J., Clemens, M., Ehrfeld, W., Jung, S., Kämper, K.-P., Lehr, H., “Micro gear pumps for dosing of viscous fluids”, Journal of Micromechanics and Microengineering, Vol. 7, pp. 230-232, 1997.

Dreyfus, R., Baudry, J., Roper, M.L., Fermigier, M., Stone, H.A., Bibette, J., “Microscopic artificial swimmers”, Nature, Vol. 437, No. 6, pp. 862-865, 2005.

Duarte, F., Gormaz, R., Natesan, S., “Arbitrary Lagrangian-Eulerian method for Navier-Stokes equations with moving boundaries”, Computer Methods in Applied Mechanics and Engineering, Vol. 193, pp. 4819-4836, 2004.

Duplantier, B., “Brownian motion, “diverse and undulating””, Progress in Mathematical Physics, Vol. 47, pp. 201-293, 2006.

Durrani, A., Hayward, J. A., Chapman, D., "Biomembranes as model for polymer surfaces. II. The synthesis of reactive species for covalent coupling of phosphorylcholine to polymer surface", Biomaterials, Vol. 7, pp. 121-125, 1986.

Edd, J., Payen, S., Rubinsky, B., Stoller, M.L., Sitti, M., “Biomimetic propulsion for a swimming surgical micro-robot”, In: IEEE/RSJ International Conference on Intelligent Robotics and Systems, Las Vegas, USA, October 2003.

Edwards, C., Postlethwaite, I., “Anti-windup and bumpless transfer schemes”, In: The UKACC International Conference on Control, University of Exeter, UK, 2-5 September, 1996.

Edwards, C., Postlethwaite, I., “Anti-windup and bumpless-transfer schemes”, Automatica, Vol. 34, Issue. 2, pp. 199-120, 1998.

Einstein, A., “Investigations on the Theory of the Brownian Movement”, Dover Publications, Inc., USA, 1956.

Erman, A.G., Yesilyurt, S., "Swimming of onboard-powered autonomous robots in viscous fluid filled channels", In: The IEEE International Conference on Mechatronics, Istanbul, Turkey, 13-15 April, 2011.

Fantastic Voyage, The Movie, Twentieth Century Fox Film Corporation, 1966, http://www.imdb.com/title/tt0060397/, Retrieved from World Wide Web on 07.01.2012.

Fatikow, S., Rembold, U., "Microsystem Technology and Microrobotics", Springer, Berlin, Ch. 8, 1997.

Fauci, L.J., McDonald, A., "Sperm motility in the presence of boundaries", Bulletin of Mathematical Biology, Vol. 57, No. 5, pp. 659-699, 1995.

Fauci, L.J., "A computational model of the fluid dynamics of undulatory and flagellar swimming", American Zoologist, Vol. 36, pp. 599-607, 1996.

Fawcett, D.W., "A comparative view of sperm ultrastructure", Biology of Reproduction Supplement, Vol. 2, pp. 90-127, 1970.

Felderhof, B.U., "Swimming at low Reynolds number of a cylindrical body in a circular tube", Physics of Fluids, Vol. 22, No. 11, 113604 (6pp), 2010.

Feynman, R.P., "There's plenty of room at the bottom", Journal of Microelectromechanical Systems, Vol. 1, No. 1, pp. 60-66, 1992.

Feynman, R.P., "Infinitesimal machinery", Journal of Microelectromechanical Systems, Vol. 2, No. 1, pp. 4-14, 1993.

Fountain, T.W.R., Kailat, P.V., Abbott, J.J., "Wireless control of magnetic helical microrobots using a rotating-permanent-magnet manipulator", In: The IEEE International Conference on Robotics and Automation, Anchorage, Alaska, USA, 3-8 May, 2010.

Friedrich, B.M., Riedel-Kruse, I.H., Howard, J., Jülicher, F., "High-precision tracking of sperm swimming fine structure provides strong test of resistive force theory", The Journal of Experimental Biology, Vol. 213, pp. 1226-1234, 2010.

Frymier, P.D., Ford, R.M., Berg, H.C., Cummings, P.T., "Three-dimensional tracking of motile bacteria near a solid planar surface", Proceedings of the National Academy of Science, Vol. 92, pp. 195-199, 1995.

Frymier, P.D., Ford, R.M., "Analysis of bacterial swimming speed approaching a solid-liquid interface", Bioengineering, food, and natural products. AIChE Journal, Vol. 43, No. 5, pp. 1341-1347, 1997.

Fujimoto, T., "The Banachiewicz identity and inverse positive matrices", Fukuoka University Review of Economics, Vol. 51, No.4, pp. 309-315, 2007.

Gadelha, C., Wickstead, B., Gull, K., "Flagellar and ciliary beating in trypanosome motility", Cell Motility and the Cytoskeleton, Vol. 64, pp. 629-643, 2007.

Garstecki, P., Tierno, P., Weibel, D.B., Sagués, F., Whitesides, G.M., "Propulsion of flexible polymer structures in a rotating magnetic field", Journal of Physics: Condensed Matter, Vol. 21, 204110(8pp), 2009.

Gauger, E., Stark, H., "Numerical study of a microscopic artificial swimmer", Physical Review, Series E, Vol. 74, 021907, 2006.

Ghosh, A., Fischer, P.: Controlled Propulsion of Artificial Magnetic Nanostructured Propellers, Nano Letters, Vol. 9, pp. 2243-2245, 2009.

Gray, J., Hancock, G.J., "The propulsion of sea-urchin spermatozoa", The Journal of Experimental Biology, Vol. 32, pp. 802-814, 1955.

Gibbons, I.R., "Cilia and flagella of eukaryotes", The Journal of Cell Biology, Vol. 91, No 3, Part 2, pp. 107s-124s, 1981.

Gibbons, I.R., Gibbons, B.H., "Transient flagellar waveforms during intermittent swimming in sea urchin sperm. I. Wave patterns", Journal of Muscle Research and Cell Motility, Vol. 1, pp. 31-59, 1980.

Gibbons, I.R., Gibbons, B.H., "Transient flagellar waveforms during intermittent swimming in sea urchin sperm. II. Analysis of tubule sliding", Journal of Muscle Research and Cell Motility, Vol. 2, pp. 83-130, 1981.

Goldstein, J., Newbury, D., Joy, D., Lyman, C., Echlin, P., Lifshin, E., Sawyer, L., Michael, J., "Scanning Electron Microscopy and X-ray Microanalysis, Third Edition", Springer, USA, Ch. 2, 2007.

Gurarie, E., Grünbaum, D., Nishizaki, M.T., "Estimating 3D movements from 2D observations using a continuous model of helical swimming", Bulletin of Mathematical Biology, Vol. 73, No. 6, pp. 1358-1377, 2011.

Gorbet, M.B., Sefton, M.V., "Biomaterial-associated thrombosis: Roles of coagulation factors, complement, platelets and leukocytes", Biomaterials, Vol. 25, No. 26, pp. 5681-5703, 2004.

Goto, T., Masuda, S., Terada, K., Takano, Y., "Comparison between observation and boundary element analysis of bacterium swimming motion", JSME International Journal, Vol. 44, pp. 958-963, 2001.

Hakim, R.M., "Complement activation by biomaterials", Cardiovascular Pathology, Vol. 2, pp. 187S- 197S, 1992.

Hsu, T.R., "MEMS & Microsystems: Design and Manufacture", McGraw Hill Higher Education, New York, Ch. 6 & 9, 2002.

Hancock, G.J., "The self-propulsion of microscopic organisms through liquids", Proceedings of the Royal Society of London, Series A, Vol. 217, No. 1128, pp. 96-121, 1953.

Hsu, C.-Y., Dillon, R., "A 3D motile rod-shaped monotrichous bacterial model", Bulletin of Mathematical Biology, Vol. 71, pp. 1228-1263, 2009.

Higdon, J.J.L., "A hydrodynamic analysis of flagellar propulsion", Journal of Fluid Mechanics, Vol. 90, pp. 685-711, 1978.

Higdon, J.J.L., "The hydrodynamics of flagellar propulsion: helical waves", Journal of Fluid Mechanics, Vol. 94, No. 2, pp. 331-351, 1979.

Higdon, J.J.L., Muldowney, G.P., "Resistance functions for spherical particles, droplets and bubbles in cylindrical channels", Journal of Fluid Mechanics, Vol. 298, pp. 193-210, 1995.

Hanson, A.J., Ma, H., "Visualizing flow with quaternion frames", In: The IEEE Computer Society Conference on Visualization '94, Washington DC, USA, 17-21 Oct 1994.

Hanson, A.J., Ma, H., "Quaternion frame approach to streamline visualization", IEEE Transactions on Visualization and Computer Graphics, Vol. 1, No. 2, pp. 164-174, 1995.

Hanson, S.R., "Blood coagulation and blood-materials interactions", Biomaterials Science Second Edition, Ratner, B.D., Hoffman, A.S., Schoen, F.J., Lemons, J.E., Ed., Elsevier Academic Press, China, 2004.

Happel, J., Brenner, H., "Low Reynolds Number Hydrodynamics", Prentice-Hall, N.J, Ch. 3&7, 1965.

Hensten-Petersen, A., Jacobsen, N., "Systemic toxicity and hypersensivity", Biomaterials Science Second Edition, Ratner, B.D., Hoffman, A.S., Schoen, F.J., Lemons, J.E., Ed., Elsevier Academic Press, China, 2004.

Hill, J., Kalkancı, O., McMurry, J.L., Koser, H., "Hydrodynamic surface interactions enable *Escherichia* coli to seek efficient routes to swim upstream", Physical Review Letters, Vol. 98, Issue 6, 068101 (4pp), 2007.

Hinojosa, F.A., Martel, S., "Suggested shape for a first generation endovascular untethered microdevice prototype", In: The IEEE 27th Annual Conference on Engineering in Medicine and Biology, Shanghai, China, 1-4 September, 2005.

Honda, T., Arat, K.I., Ishiyama, K., "Micro swimming mechanisms propelled by external magnetic fields", IEEE Transactions on Magnetics, Vol. 32, No. 5, pp. 5085-5087, 1996.

Howse, J.R., Jones, R.A.L., Ryan, A.J., Gough, T., Vafabakhsh, R., Golestanian, R., "Self-motile colloidal particles: From directed propulsion to random walk", Physical Review Letters, Vol. 99, 2007.

Huang, M.-S., Li, C.-J., Yu, J.-C., Huang, Y.M., Hsieh, L.C., "Robust parameter design of micro-injection molded gears using a LIGA-like fabricated mold insert", Journal of Materials and Processing Technology, Vol. 209, pp. 5690-5701, 2009.

Huba, M., "Open flexible P-controller design," In: The 12th IEEE International Workshop on Advanced Motion Control, Sarajevo, Bosnia and Herzegovina, 25-27 March, 2012a.

Huba, M., "Modular disturbance observer based constrained PI-controller design," In: The 12th IEEE International Workshop on Advanced Motion Control, Sarajevo, Bosnia and Herzegovina, 25-27 March, 2012b.

Innerspace, The Movie, Warner Bros., 1987, http://www.imdb.com/title/tt0060397/, Retrieved from World Wide Web on 07.01.2012.

Jain, A., David, G.W., Oppenheim, I.J., "MEMS ultrasonic transducer for monitoring of steel structures", Proceedings of SPIE, Vol. 4696, pp. 256-264, 2002.

James, D.F., "Boger fluids", Annual Review of Fluid Mechanics, Vol. 41, pp. 129-142, 2009.

Jeon, Y.B., Sood, R., Jeong, J.-H., Kim, S.-G., "MEMS power generator with transverse mode thin film PZT", Sensors and Actuators, Series A, Vol. 122, Issue 1, pp.16-22, 2005.

Jiang, B., Smith, J.R., Philipose, M., Roy, S., Sundara-Rajan, K., Mamishev, A.V., "Energy scavenging for inductively coupled passive RFID systems", IEEE Transactions on Instrumentation and Measurement, Vol. 56, No. 1, pp. 118-125, 2007.

Jiles, D., "Introduction to Magnetism and Magnetic Materials, 2nd Edition.", Chapman & Hall, London, UK, 1998.

Jin, Y., Wang, Z.F., Lim, P.C., Pan, D.Y., Wei, J., Wong, C.K., "MEMS vacuum packaging technology and applications", In: The 5th Electronics Packaging Technology Conference, Singapore, December 2003.

Johnson, R.E., "An improved slender-body theory for Stokes flow", Journal of Fluid Mechanics, Vol. 99, No. 2, pp. 411-431, 1980.

Johnson, R.E., Brokaw, C.J., "Flagellar hydrodynamics. A comparison between resistive-force theory and slender-body theory", Biophysical Journal, Vol. 25, pp. 113-127, 1979.

Johnson, R.J., "Complement activation during extracorporal therapy: Biochemistry, cell biology and clinical relevance", Nephrology Dialysis Transplantation, Vol. 9, pp. 36-45, 1994.

Jordan, C.E., "Coupling internal and external mechanics to predict swimming behavior: A general approach?", American Zoologist, Vol. 36, pp. 710-722, 1996.

Jung, K., Nam, J., Choi, H., "Investigations on actuation characteristics of IPMC artificial muscle actuator", Sensors and Actuators, Series A, Vol. 107, pp. 183-192, 2003.

Keller, J.B., Rubinow, S.I., "Swimming of flagellated microorganisms", Biophysical Journal, Vol. 16, pp. 151-170, 1976.

Kim, J., Chiao, M, Lin, L., "Ultrasonic bonding of In/Au and Al/Al for hermetic sealing of MEMS packaging", Proceedings of the IEEE Micro Electro Mechanical Systems, pp. 415-418, 2002.

Kim, B., Kim, D.-H., Jung, J., Park, J.-O., "A biomimetic undulatory tadpole robot using ionic polymer-metal composite actuators", Smart Materials and Structures, Vol. 14, No. 6, pp 1579-1585, 2004.

Kim, B., Lee, M.G., Lee, Y.P., Kim, Y., Lee, G., "An earthworm-like micro robot using shape memory alloy actuator", Sensors and Actuators, Series A, Vol. 125, pp. 429-437, 2006.

Koehl, M.A.R., "When does morphology matter?", Annual Review of Ecology and Systematics, Vol. 27, pp. 501-542, 1996.

Kosa, G., Shoham, M., Zaaroor, M., "Propulsion method for swimming microrobots", IEEE Transactions on Robotics, Vol. 23, No. 1, pp. 137-150, 2007.

Koz, M., Yesilyurt, S., "Simulations of microflows induced by rotation of spirals in microchannels", In: SPIE-Photonics West: MOEMS-MEMS, San Jose CA, USA 19-24 Jan, 2008.

Kragic, D., Christensen, H.I., "Survey on visual servoing for manipulation", Technical Report, ISRN KTH/NA/P--02/01--SE CVAP259, January, 2002.

Kubby, J., "Hybrid integration of light emitters and detector with SOI based Micro-Opto-Electro-Mechanical Systems (MOEMS)", Proceedings of SPIE, Vol. 4293, pp. 32-45, 2001.

Lagomarsino, M.C., Capuani, F., Lowe, C.P., "A simulation study of the dynamics of a driven filament in an Aristotelian fluid", Journal of Theoretical Biology, Vol. 224, pp. 215-224, 2003.

Lal, A., Bilbao y León, R.M., Guo, H., Li, H., Santanam, S., Yao, R., Blanchard, J., Henderson, D., "A nuclear microbattery for MEMS devices", In: The 9th International Conference on Nuclear Engineering, Nice, France, 8-12 April, 2001.

Lal, A., Blanchard, J., “The daintiest dynamos [nuclear microbatteries]”, Spectrum, IEEE, Vol. 41, Issue 9, pp. 36-41, 2004.

Landau, L.D., Lifshitz, E.M., “Theory of Elasticity”, Elsevier, China, Ch. 3, 2005a.

Landau, L.D., Lifshitz, E.M., “Fluid Mechanics, Second Edition”, Elsevier Butterworth-Heinemann, China, Ch. 2 & 20 & 24, 2005b.

Larm, O., Larsson, R., Olsson, P., "A new non-thrombogenic surface prepared by selective covalent binding of heparin via a modified reducing terminal residue", Biomaterials, Medical Devices, and Artificial Organs, Vol. 11, pp. 161-173, 1983.

Laser, D.J., Santiago, J.G., “A review of micropumps”, Journal of Micromechanics and Microengineering, Vol. 14, pp.R35 –R64, 2004.

Lauga, E., Powers, T.R., “The hydrodynamics of swimming microorganisms”, Reports on Progress in Physics, Vol. 72, No. 9, 096601 (36pp), 2009.

Lauga, E., DiLuzio, W.R., Whitesides, G.M., Stone, H.A., “Swimming in circles: motion of bacteria near solid boundaries”, Biophysical Journal, Vol. 90, pp. 400-412, 2006.

Li, N., Cannon, M.C., “Gas vesicle genes identified in *Bacillus megaterium* and functional expression in *Escherichia coli*”, Journal of Bacteriology, Vol. 180, No. 9, pp. 2450-2458, 1998.

Lighthill, J., “Mathematical Biofluiddynamics”, Society for Industrial and Applied Mathematics, USA, Ch. 3, 1975.

Lighthill, J., “Flagellar hydrodynamics: The John von Neumann lecture, 1975”, SIAM Review, Vol. 18, No. 2, pp. 161-230, 1976.

Lighthill, J., “Helical distributions of Stokeslets”, Journal of Engineering Mathematics, Vol. 30, pp. 35-78, 1996a.

Lighthill, J., “Reinterpreting the basic theorem of flagellar hydrodynamics”, Journal of Engineering Mathematics, Vol. 30, pp. 25-34, 1996b.

Lim, S.M., Lee, S., Park, H.C., Yoon, K.J., Goo, N.S., “Design and demonstration of a biomimetic wing section using a lightweight piezo-composite actuator (LIPCA)”, Smart Materials and Structures, Vol. 14, pp. 496-503, 2005.

Liron, N., Shahar, R., “Stokes flow due to a Stokeslet in a pipe”, Journal of Fluid Mechanics, Vol. 86, Part 4, pp 727-744, 1978.

Liu, W., Menciassi, A., Scapellato, S., Dario, P., Chen, Y., “A biomimetic sensor for a crawling minirobot”, Robotics and Autonomous Systems, Vol. 54, pp. 513-528, 2006.

Liu, B., Powers, T.R., Breuer, K.S., “Force-free swimming of a model helical flagellum in viscoelastic fluids”, Proceedings of the National Academy of Sciences (PNAS), Vol. 108, no. 49, pp. 19516-19520, 2011.

Lobaskin, V., Lobaskin, D., Kulić I.M., “Brownian dynamics of a microswimmer”, The European Physical Journal Special Topics, Vol. 157, pp. 149-156, 2008.

Loechel, B., Goettert, J., Gruetzner, G., Bednarzik, M., Waberski, C., Ahrens, G., Engelke, R., Singh, V., Degen, R., Kirsch, U., “Extreme aspect ratio NiFe gear wheels for the production of commercially available Micro Harmonic Drive® gears”, Microsystem Technologies, Vol. 14, pp. 1675-1681, 2008.

Lovalenti, P.M., Brady, J., “The hydrodynamic force on a rigid particle undergoing arbitrary time-dependent motion at small Reynolds number”, Journal of Fluid Mechanics, Vol. 256, pp. 561-605, 1993a.

Lovalenti, P.M., Brady, J., “The force on a sphere in a uniform flow with small-amplitude oscillations at finite Reynolds number”, Journal of Fluid Mechanics, Vol. 256, pp. 607-614, 1993b.

Lu, J., Kovalgin, A.Y., Schmitz, J., “Modeling of an integrated electromagnetic generator for energy scavenging”, In: 10th Annual Workshop on Semiconductor Advances for Future Electronics and Sensors (SAFE), Veldhoven, Netherlands, 29-30 November, 2007.

Machadoi L.G., Savi, M.A., “Medical applications of shape memory alloys”, Brazilian Journal of Medical and Biological Research, Vol. 36, pp. 683-691, 2003.

Mahadevan, L., Matsudaira, P., “Motility powered by supramolecular springs and ratchets”, Science, Vol. 288, pp. 95-99, 2000.

Mahoney, A.W., Sarrazin, J.C., Bamberg, E., Abbott, J.J., “Velocity control with gravity compensation for magnetic helical microswimmers”, Advanced Robotics, Vol. 25, pp. 1007-1028, 2011.

Mallouk, T.E., Sen, A., “Powering nanorobots”, Scientific American, Vol. 300, pp. 72-77, 2009.

Manghi, M., Schlagberger, X., Netz, R. R., “Propulsion with a rotating elastic nanorod”, Physical Review Letters, Vol. 96, Issue 6, 068101(6pp), 2006.

Maniyeri, R., Suh, Y.K., Kang, S., Kim, M.J., “Numerical study on the propulsion of a bacterial flagellum in a viscous fluid using an immersed boundary method”, Computers and Fluids, Vol. 62, pp. 13-24, 2012.

Martel, S., Felfoul, O., Mathieu, J.B., Chanu, A., Tamaz, S., Mohammadi, M., Mankiewicz, M., Tabatabaei, S.N., “MRI-based medical nanorobotic platform for the control of magnetic nanoparticles and flagellated bacteria for target interventions in human capillaries”, International Journal of Robotic Research, Vol. 28, pp. 1169-1182, 2009.

Mathieu, J.B., Beaudoin, G., Martel, S., “Method of propulsion of a ferromagnetic core in the cardiovascular system through magnetic gradients generated by an MRI system”, IEEE Transactions on Biomedical Engineering, Vol. 53, No. 2, pp. 292-299, 2006.

Merrill, E.W., Salzman, E.W., "Polyethylene oxide as a biomaterial", American Society of Artificial Internal Organs, Vol. 6, pp. 60-64, 1983.

Mirkovic, T., Zacharia, N.S., Scholes, G.D., Ozin, G.A., “Fuel for thought: chemically powered nanomotors out-swim nature’s flagellated bacteria”, ACS Nano, Vol. 4, No. 4, pp. 1782-1789, 2010.

Mitchell, R.N., “Innate and adaptive immunity: the immune response to foreign materials”, Biomaterials Science Second Edition, Ratner, B.D., Hoffman, A.S., Schoen, F.J., Lemons, J.E., Ed., Elsevier Academic Press, China, 2004.

Moireau, P., Xiao, N., Astorino, M., Figueroa, C.A., Chapelle, D., Taylor, C.A., Gerbeau, J.F., “External tissue support and fluid-structure simulation in blood flows”, Biomechanics and Modeling in Mechanobiology, Vol. 11, pp. 1-18, 2012.

Munson, B.R., Young, D.F., Okiishi, T.H., “Fundamentals of Fluid Mechanics, 4th Edition”, John Wiley & Sons, USA, Ch. 6, 2002.

Nasser-Nemat, S., “Micromechanics of actuation of ionic polymer-metal composites”, Journal of Applied Physics, Vol. 92, No. 5, 2002.

Nasser-Nemat, S., Li, J.Y., "Electromechanical response of ionic polymer-metal composites", Journal of Applied Physics, Vol. 87, No. 7, pp. 3321-3331, 2000.

Nasseri, S., Thien, N.P., "Geometric optimization of a micromachine with spiral tail immersed in viscous medium", Computational Mechanics, Vol. 20, pp. 267-271, 1997.

Nelson, B.J., Kaliakatsos, I.K., Abbott, J.J., "Microrobots for minimally invasive medicine", Annual Review of Biomedical Engineering, Vol. 12, pp. 55-85, 2010.

Newbury, K., "Characterization, Modeling, and Control of Ionic Polymer Transducers", PhD Thesis submitted to Mechanical Engineering Department Virginia Polytechnic Institute and State University, 2003.

Nielsen, O.M., Arana, L.R., Baertsch, C.D., Jensen, K.F., Schmidt, M.A., "A thermophotovoltaic micro-generator for portable power applications", In: The 12th International Conference on Solid State Sensors, Actuators and Microsystems, Boston, 8-12 June, 2003.

Nguyen, N.-T., Wereley, S., "Fundamentals and Applications of Microfluidics 2nd Ed.", Artech House, Inc., USA, Ch 3, 2006.

Oberhammer, J., Niklaus, F., Stemme, G., "Sealing of adhesive bonded devices on wafer level", Sensors and Actuators, Series A, Vol. 110, pp. 407-412, 2004.

Odar, F., Hamilton, W.S., "Forces on a sphere accelerating in a viscous fluid", Journal of Fluid Mechanics, Vol. 18, No.2, pp. 302-314, 1964.

Ogata, K., "Modern Control Engineering, Third Edition", Prentice-Hall, Inc., NJ, Ch 3, 1997.

Olsson, H., Åström, K.J., de Wit, C.C., Gäfvert, M., Lischinsky, P., "Friction models and friction compensation", European Journal of Control, Vol. 4, No. 3, pp. 176-195, 1997.

Otsuka, K., Ren, X., "Recent developments in the research of shape memory alloys", Intermetallics, Vol. 7, pp. 511-528, 1999.

Peppas, N.A., Huang, Y., Torres-Lugo, M., Ward, J.H., Zhang, J., "Physicochemical foundations and structural design of hydrogels in medicine and biology", Annual Review of Biomedical Engineering, Vol. 2, pp. 9-29, 2000.

Perrin, F., “Mouvement Brownien d’un ellipsoïde (I). Dispersion diélectrique pour des molecules ellipsoïdales”, Le Journal de Physique et Le Radium, Série 7, Vol. 5, pp. 497-511, 1934.

Perrin, F., “Mouvement Brownien d’un ellipsoïde (II). Rotation libre et dépolarisation des fluorescences. Translation et diffusion de molecules ellipsoïdales”, Le Journal de Physique et Le Radium, Série 7, Vol. 7, pp. 1-11, 1936.

Peskin, C.S., “The immersed boundary method”, Acta Numerica, Vol. 11, pp. 479-517, 2002.

Phan-Thien, N., Tran-Cong, T., Ramia, M., “A boundary-element analysis of flagellar propulsion”, Journal of Fluid Mechanics, Vol. 184, pp. 533-549, 1987.

Piezo Systems, Inc., Catalog # 7B, 2007, http://www.piezo.com/catalog.html, Retrieved from World Wide Web on 08.01.2008.

Piefort, V., “Finite element modelling of piezoelectric active structures”, PhD dissertation submitted to Faculty of Applied Sciences, Universite Libre De Bruxelles, 2001.

Purcell, E.M., “Life at low Reynolds number”, American Journal of Physics, Vol. 45, No. 1, pp. 3-11, 1977

Purcell, E.M., “The efficiency of propulsion by a rotating flagellum”, Proceedings of the National Academy of Sciences USA, Vol. 94, pp. 11307-11311, 1997.

Qin, F.-H., Huang, W.-X., Sung, H.J., “Simulation of small swimmer motions driven by tail/flagellum beating”, Computers and Fluids, Vol.55, pp.109-17, 2012.

Ramia, M., Tullock, D.L., Phan-Thien, N., “The role of hydrodynamic interaction in the locomotion of microorganisms”, Biophysical Journal, Vol. 65, pp. 755-778, 1993.

Rapaport, D.C., “Microscale swimming: the molecular dynamics approach”, Physical Review Letters, Vol. 99, Issue 23, 238101(4pp) 2007.

Ravid, S., Eisenbach, M., “Minimal requirements for rotation of bacterial flagella”, Journal of Bacteriology, Vol. 158, no. 3, pp. 1208-1210, 1984.

Raz, O., Avron, J.E., "Swimming, pumping and gliding at low Reynolds numbers", New Journal of Physics, Vol. 9, pp. 437-445, 2007.

Remes, R., Williams, D.F., "Immune response in biocompatibility", Biomaterials, Vol. 13, pp. 731-43, 1992.

Rogers, M.S., Sniegowski, J.J., Miller, S.L., LaVigne, G.F., "Designing and operating electrostatically driven microengines", In: The 44th International Instrumentation Symposium, Reno, Nevada, USA, 3-7 May, 1998.

Roper, M., Dreyfus, R., Baudry, J., Fermigier, M., Bibette, J., Stone, H.A., "Do magnetic micro-swimmers move like eukaryotic cells?", Proceedings of the Royal Society, Series A, Vol. 464, pp. 877-904, 2008.

Rusu, M., Ursu, M., Rusu, D., "Poly(vinyl chloride) and Poly(e-caprolactone) blends for medical use", Journal of Thermoplastic Composite Materials, Vol. 19, pp. 173-190, 2006.

Saito, M., Kitamura, N., Terauchi, M., "Ultrasonic manipulation of locomotive microorganisms and evaluation of their activity", Journal of Applied Physics, Vol. 92, No. 12, pp. 7581-7586, 2002.

Sakar, M.S., Steager, E.B., Kim, D.H., Julius, A.A., Kim, M.J., Kumar, V., Pappas, H.J., "Modelling, control and experimental charactrerization of microrobots", The International Journal of Robotic Research, Vol. 30, No. 6, pp. 647-658, 2011.

Salvagnini, C., "Thrombin inhibitors grafting on polyester membranes for the preparation of blood-compatible materials", PhD Dissertation submitted to Université Catholique de Louvain, France, 2005.

Schenk, O., Gärtner, K., "Solving unsymmetric sparse systems of linear equations with PARDISO", Future Generation Computer Systems, Vol. 20, No. 3, pp. 475-487, 2004.

Serre, C., Perez-Rodriguez, A., Fondevilla, N., Morante, J.R., Montserrat, J., Esteve, J., "Vibrational energy scavenging with Si technology electromagnetic inertial microgenerators", Microsystem Technologies, Vol. 13, pp. 1655-1661, 2007.

Shampire, L.F., Gordon, M.K., "Computer Solution of Ordinary Differential Equations: The Initial Value Problem", Oxford University Press, USA, 1985.

Shechter, E., Martel, S., "Principle of motion control of bacterial micro-robots using oxygen gradients", In: The IEEE/ASME International Conference of Advanced Intelligent Mechatronics, Montreal, Canada, 6-9 July, 2010.

Shum, H., Gaffney, E.A., Smith, D.J., "Modelling bacterial behavior close to a no-slip plane boundary: the influence of bacterial geometry", Proceedings of the Royal Society A, Vol. 466, No. 2118, pp. 1725-1748, 2010.

Siauve, N., Scorretti, R., Burais, N., Nicolas, L., Nicolas, A., "Electromagnetic fields and human body: a new challenge for the electromagnetic field computation", The International Journal for Computation and Mathematics in Electrical and Electronics Engineering, Vol. 22, No. 3, pp. 457-469, 2003.

Sleigh, M.A., "International series of monographs on pure and applied biology v12: the biology of cilia and flagella", Kerkut, G.A., General Editor, Pergamon Press LTD., Newyork, Ch. 4, 1962.

Spagnolie, S.E., Lauga, E., "The Optimal Elastic Flagellum", Physics of Fluids, Vol. 22, 031901 (15pp), 2010.

Spagnolie, S.E., Lauga, E., "Hydrodynamics of self-propulsion near a boundary: Predictions and accuracy of far-field approximations", Journal of Fluid Mechanics, Vol. 700, pp. 105-147, 2012.

Spong, M.W., Vidyasagar, M., "Robot Dynamics and Control", John Wiley & Sons, USA, Ch. 7, 1989.

Stolarski, T.A., "Tribology in Machine Design", Butterworth-Heinemann, Great Britain, Ch. 5, 1990.

Sun, Y., Fry, S.N., Potasek, D.P., Bell, D.J., Nelson, B.J., "Characterizing fruit fly behavior using a microforce sensor with a new comb-drive configuration", Journal of Microelectromechanical Systems, Vol. 14, No. 1, pp. 4-11, 2005.

Tabak, A.F., Yesilyurt, S., "Numerical analysis of a planar wave propagation based micropropulsion system", In: The ASME International Mechanical Engineering Congress and Exposition, Seattle WA, USA, 11-15 November, 2007a.

Tabak, A.F., "Simulation based experiments of travelling-plane-wave-actuator micropumps and microswimmers", MSc dissertation submitted to Faculty of Engineering and Natural Sciences, Sabanci University, Istanbul, 2007b.

Tabak, A.F., Yesilyurt, S., "Simulation-based analysis of flow due to traveling-plane-wave deformations on elastic thin-film actuators in micropumps", Microfluidics and Nanofluidics, Vol. 4, No. 6, pp. 489-500, 2008.

Tabak, A.F., Yesilyurt, S., "Modeling and simulations of the motion of bio-inspired micro swimming robots," In: The ASME First Global Congress on Nanoengineering for Medicine and Biology, Houston, TX, USA, 7-10 February, 2010a.

Tabak, A.F., Yesilyurt, S., "Validated reduced order models for simulating trajectories of bio-inspired artificial micro-swimmers", In: The ASME 3rd Joint US-European Fluids Engineering Summer Meeting and 8th International Conference on Nanochannels, Microchannels, and Minichannels, Montreal, Canada, 1-5 August, 2010b.

Tabak, A.F., Temel, F.Z., Yesilyurt, S., "Comparison on experimental and numerical results for helical swimmers inside channels", In: The IEEE/RSJ International Conference on Intelligent Robots and Systems, San Francisco CA, USA, 25-30 September, 2011.

Tabak, A.F., Yesilyurt, S., "Experiment-based kinematic validation of numeric modeling and simulated control of an untethered biomimetic microrobot in channel", In: The 12th IEEE International Workshop on Advanced Motion Control, Sarajevo, Bosnia and Herzegovina, 25-27 March, 2012a.

Tabak, A.F., Yesilyurt, S., "Experiments on in-channel swimming of an untethered biomimetic robot with different helical tails", In: The 4th IEEE RAS/EMBS International Conference on Biomedical Robotics and Biomechatronics, Rome, Italy, 24-27 June, 2012b.

Tadokoro, S., Fukuhara, M., Bar-Cohen, Y., Oguro, K., Takamori, T., "A CAE approach in application of Nafion-Pt composite (ICPF) actuators: analysis for surface wipers of NASA MUSES-CN nanorovers", Proceedings of SPIE Smart Structures and Materials 2000: Electroactive Polymer Actuators and Devices, Vol. 3987, pp. 262-272, 2000.

Takano,Y., Goto, T., "Numerical analysis of small deformation of flexible helical flagellum of swimming bacteria", JSME International Journal, Series C, Vol. 46, No. 4, pp. 1234-1240, 2003.

Taylor, B.L., Zhulin, I.B., "In search of higher energy: metabolism-dependent behavior in bacteria", Molecular Biology, Vol. 28, No. 4, pp. 683-690, 1998.

Taylor, G., “Analysis of the swimming of microscopic organisms”, Proceedings of the Royal Society of London, Series A, Vol. 209, pp. 447-461, 1951.

Teramura, Y., Kaneda, Y., Totani, T., Iwata, H., “Behavior of synthetic polymers immobilized on cell membrane”, Biomaterials, Vol. 29, pp. 1345-1355, 2008.

Thaokar, R.M., “Hydrodynamic interaction between two rotating tori”, The European Physical Journal, Series B, Vol. 61, pp. 47-58, 2008.

van der Sman, R.G.M., “Drag force on spheres confined on the center line of rectangular microchannels”, Journal of Colloid and Interface Science, Vol. 351, pp. 43-49, 2010.

van der Sman, R.G.M., “Effects of confinement on hydrodynamic interaction between a suspended sphere and stationary objects”, Computers and Fluids, Vol. 58, pp. 63-69, 2012.

Wang, Z., Hang, G., Li, J., Wang, Y., Xiao, K., “A micro-robot fish with embedded SMA wire actuated flexible biomimetic fin”, Sensors and Actuators, Series A: Physical, Vol. 144, pp. 354-360, 2008.

Washizu, M., Kurahashi, Y., Iochi, H., Kurosawa, O., Aizawa, S.-I., Kudo, S., Magariyama, Y., Hotani, H., “Dielectric measurement of bacterial motor characteristics”, IEEE Transactions on Industry Applications, Vol. 29, No. 2, 1993.

Watari, N., Larson, R.G., “The hydrodynamics of a run-and-tumble bacterium propelled by polymorphic helical flagella”, Biophysical Journal, Vol. 98, pp. 12-17, 2010.

White, M.F., “Viscous fluid flow, third edition” McGraw-Hill, New York, Ch 3, 2006.

Wiggins, C.H., Goldstein, R.E., “Flexive and propulsive dynamics of elastica at low Reynolds number”, Physical Review Letters, Vol. 80, No. 17, pp. 3879-3882, 1998.

Wise, K.D., “Integrated sensors, MEMS, and microsystems: Reflections on a fantastic voyage”, Sensors and Actuators, Series A: Physical, Vol. 136, Issue 1, pp. 39-50, 2007.

Woolley, D.M., Vernon, G.G., “A study of helical and planar waves on Sea Urchin sperm flagella, with a Theory of How They are Generated”, The Journal of Experimental Biology, Vol. 204, pp. 1333-1345, 2001.

Xiaoming, W., Yi, Y., Ping, Z.Y., Xing, Z.N., Tianling, R., Liu, L., "MEMS piezoelectric acoustic transducer", Integrated Ferroelectrics, Vol. 89, No.1, pp. 150-159, 2007.

Yang, H., Pan, C.-T., Chou, M.-C., "Ultra-fine machining tool/molds by LIGA technology", Journal of Micromechanics and Microengineering, Vol. 11, pp. 94-99, 2001.

Yeatman, E.M., "Rotating and gyroscopic MEMS energy scavenging", In: The IEEE International Workshop on Wearable and Implantable Body Sensor Networks, Cambridge, Massachusetts, USA, 3-5 April, 2006.

Yoon, K.J., Park, K.H., Lee, S.K., Goo, N.S., Park, H.C., "Analytical design model for a piezo-composite unimorph actuator and its verification using lightweight piezo-composite curved actuators", Smart Materials and Structures, Vol. 13, pp. 459-467, 2004.

Young, K.D., "The selective value of bacterial shape", Microbiology and Molecular Biology Reviews, Vol. 70, No. 3, pp. 660-703, 2006.

Yu, T.S., Lauga, E., Hosoi, A.E., "Experimental investigations of elastic tail propulsion at low Reynolds number", Physics of Fluids, Vol. 18, Issue. 9, 091701 (4pp), 2006a.

Yu, T.S., Lauga, E., Hosoi, A.E., "Experimental investigations of elastic tail propulsion at low Reynolds number", HML Report Number 06-P-01, 23 August, 2006b.

Zeidan, F.Y., Andres, L.S., Vance, J.M., "Design and application of squeeze film dampers in rotating machinery", In: The 25th Turbomachinery Symposium, Houston, TX, USA, 17-19 September, 1996.

Zhang, L., Abbott J.J., Dong, L., Kratochvil, B.E., Bell, D., Nelson, B.J., "Artificial bacterial flagella: fabrication and magnetic control", Applied Physics Letters, Vol. 94, No. 6, 064107 (3pp), 2009.

Zhang, L., Peyer, K.E., Nelson, B.J., "Artificial bacterial flagella for micromanipulation", Lab on a Chip, Vol. 10, pp. 2203-2215, 2010.